Synthesis of Dendronic Raman Markers and Raman Investigations of Polarons in Lead Halide Perovskites and Host-Guest Interactions in ZIFs

A thesis

Submitted for the Degree of

DOCTOR OF PHILOSOPHY

in the Faculty of Science

by

Priyanka Jain

Chemistry and Physics of Materials Unit

Jawaharlal Nehru Centre for Advanced Scientific Research

Bengaluru-560064, India

March 30, 2022

To my Parents and Brother...

Declaration

I hereby declare that the matter embodied in the thesis entitled "**Synthesis of Dendronic Raman Markers and Raman Investigations of Polarons in Lead Halide Perovskites and Host-Guest Interactions in ZIFs**" is the result of investigations carried out by me at the Chemistry and Physics of Materials Unit, Jawaharlal Nehru Centre for Advanced Scientific Research, Bangalore, India under the supervision of **Prof. Chandrabhas Narayana** and it has not been submitted elsewhere for the award of any degree or diploma.

In keeping with the general practice in reporting the scientific observations, due acknowledgements have been made whenever the work described is based on the findings of other investigators. Any omission that might have occurred due to oversight or error in judgement is regretted.

Bengaluru-560064, India

March 30, 2022

Priyanka Jain

Certificate

I hereby certify that the matter embodied in this thesis entitled **"Synthesis of Dendronic Raman Markers and Raman Investigations of Polarons in Lead Halide Perovskites and Host-Guest Interactions in ZIFs"** has been carried out by **Priyanka Jain** at Chemistry and Physics of Materials Unit, Jawaharlal Nehru Centre for Advanced Scientific Research, Bangalore, India under my supervision and it has not been submitted elsewhere for the award of any degree or diploma.

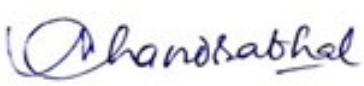

Bengaluru-560064, India
March 30, 2022

Prof. Chandrabhas Narayana
(Research Supervisor)

Acknowledgements

I take this opportunity to express my gratitude to all the people who have motivated, inspired and supported me throughout my Ph.D.

First and foremost I extend my gratitude to my research supervisor, **Prof. Chandrabhas Narayana** for giving me the opportunity to work with him and guiding me here at JNCASR. I am extremely grateful to him for providing me with good collaborations which enhanced my research experience. I am also grateful to him for giving me enough freedom to carry my research work. I thank him for his patience, belief, and positive attitude towards me in various aspects of my research work. I thank you Sir.

I am also thankful to Prof. A Sundaresan for attending to all the needs of Light scattering lab and immense support.

I would like to also thank Dr. Sridhar Rajaram for allowing me to be a part of Polymer lab, guidance, and support. The time in his lab made me confident as a synthetic chemist while carrying my research work.

I am deeply indebted to my senior **Dr. Gayatri Kumari**, for providing immense positiveness and motivating me to pursue my research. I am extremely grateful to her for all her guidance with my Ph.D work, ideas, and many many fruitful discussions which enhanced my research experience tremendously.

I am grateful to be part of this institution where I heard and met several great scientist whose enthusiasm and zeal for science have always motivated me. I am also thankful for the excellent facilities that are provided here, for carrying out my research work smoothly.

I express my warm thanks to Dr. Ranjani Viswanatha and Prof. Swapan K. Pati for the wonderful collaborations. I am thankful to them for teaching me important aspects

of research. I would also like to acknowledge their students, Dr. Pradeep K R and Ms. Madhulika Mazumder for extensive work and discussions to shape the research work well. I am also grateful to Dr. Boby Joseph at Elettra, Trieste, Italy for the synchrotron XRD measurements and fruitful discussions.

I thank all the course instructors at JNC and IISc, Prof. N. Chandrabhas, Prof. A. Sundaresan, Prof. S. M. Shivaprasad, Prof. S. Narasimhan, Prof. U. V. Waghmare, Dr. N. S. Vidhyadhiraja, and Prof. T. N. Gururow for their informative courses and friendly environment.

I would like to thank past and present CPMU chairperson, Prof. S. Balasubramanian, Prof. N. Chandrabhas, and Prof. A Sundaresan for excellent facilities in the department.

I would like to extend my gratitude to Dr. Premakumar Yanda, Abhishek Garg, Dr. Ranjan Sasmal, Srinath Kompella, Dr. Susheela, Dr. Subhajit Laha, and Darshan Chalapathi for various kinds of help and discussions.

I would like to acknowledge CSIR and JNCASR for fellowship.

I would like to extend my gratitude to Shobha Ma'am and Sushmitha for great company, amazing food, and all the laughter whenever we meet.

I must thank all my past lab mates, Dr. Gayatri, Dr. Partha, Dr. Dhanya, Dr. Sorb, Dr. Sayan, Dr. Rajaji, Dr. Kamali, Priyank, Dr. Shantanu, Sunami, Suhas, Samyabrata and all the summer and project students for their various helps and useful discussions during my tenure and maintain a friendly atmosphere in the lab. My special thanks to Dr. Ramana, Dr. Arjun, Ramesh, and Anusha for my time and all the help in polymer lab. It would be incomplete without thanking my present lab mates, friends, and fierce women, **Divya, Janaky, and Anjana** for being a great support system here at JNCASR. I deeply thank them.

I thank all my friends at JNCASR, especially **Prem**, Divya, Swati, Abhijit, Pradeep, Rajendra, Shivaram, and Ravi for their company in various activities and always being there for me. I also thank Anusha, Deepak, Vyabhav, Malay, Usha, and Ganesh for making my journey memorable.

I would like to thank my friends outside JNCASR, especially all the wonderful women

in my life, from school: **Karuna, Nandita, Kriti Pal**, Mehak; from College: **Kriti Seth**, Ankita, Akshaya, and my other friends Prayank, Sanchit, and Ayush for their immense support, believe in me, and constant encouragement. I would like to also thank my family members especially my cousin Megha and niece Aadya for always being there for me.

Finally, I would like to thank my parents, **Mrs. Sushma Jain**, the strongest woman I know and **Mr. Deepak Jain** and my brother, **Prashant Jain** for their unconditional love, support, and all the freedom to pursue all my endeavours.

Preface

This thesis utilizes Raman spectroscopic technique to probe and understand the structural disorder in lead halide perovskites (LHPs) and molecular interactions in zeolitic imidazolate frameworks (ZIFs) which makes them promising candidates for various applications. Also, it explores the synthesis of dendronic markers for surface-enhanced Raman spectroscopy (SERS) applications. **Chapter 1** gives a brief introduction on the theory of Raman scattering, SERS, and SERS of thiol molecules. Also, the theory of the Raman spectral analysis in the low-frequency and molecular regions have been presented which includes, lattice vibrations, anharmonicity in phonons, electron-phonon coupling, effect of molecular guest adsorption on structure, and their interactions on Raman spectra.

Chapter 2 discusses the various experimental methods used in this thesis.

Chapter 3 accounts for the Raman spectroscopic investigations carried on a series of undoped $CsPbX_3$ (where X = Cl, Br) nanocrystals and Mn-doped counterparts of the same. In **Chapter 3A**, all the Raman modes were assigned for changing Cl to Br ratio in the systems. The LO_2 and the TO_2 modes of the system was utilized to deduce the structural homogeneity and nature of octahedra in the system. In **Chapter 3B**, a new vibrational lattice mode at 132 $cm^{\breve{}1}$ due to polaronic distortion upon photoinduction was investigated. From the DFT studies, we have shown that the polaronic states are dominated by the B-site cation in the perovskite structure, but it is the strong covalent overlap of the halide which determines its stability. These results underscore that the persisting knowledge of the Pb-X stretching modes playing a dominant role in polaron formation in LHPs is incomplete. Further, the polaronic behaviour was studied over a sample space in this family of material and the stability of it was discussed with structural modifications. This elucidation to map polaronic signatures with excellent spatial reso-

lution using traditional Raman spectroscopy can be used as a simple tool to understand the structural changes and their impacted electronic properties and thus design superior devices using it for in situ applications.

Chapter 4 describes microscopical molecular changes and gas adsorption behaviour in ZIFs using Raman spectroscopy. This chapter dealt with computational assignments of the peaks to address and understand the results obtained from the Raman studies. Hence, the computational methods and detailed assignments are discussed in **Appendix A**. In **chapter 4A**, the temperature evolution of ZIF-4 was studied with and without the guest molecules. Fascinating results were obtained with rare observation of N_2 adsorption under ambient conditions. From critical analysis of the Raman spectra for ZIF-4 with temperature, it was found that non-covalent interactions resulted in new phase transition, structural changes with guest interaction. In **chapter 4B**, temperature-dependent Raman studies under N_2 was performed on ZIF-67. The studies revealed two types of adsorption of N_2 on ZIF-67 explaining the unusual uptake of gas adsorption in ZIF-67, inspite of structural limitations as opposed to the well-known ZIF-8 system.

Chapter 5 demonstrates the synthesis of dendrons with thiophenol groups on their periphery which is called the Raman marker. The Raman marker was utilized as a SERS analyte and a 100-fold enhancement in the detection limit was observed by constraining more number of Raman-active molecules in a dendronic framework. This strategy broadens the applicability of SERS, as these analyte molecules can be just mixed or drop-casted on any kind of SERS substrate.

Chapter 6 provides the summary of the thesis work and outlook for the present work.

Contents

List of Publications

1. *Designing Dendronic-Raman Markers for Sensitive Detection using Surface-enhanced Raman Spectroscopy*
   Priyanka Jain, Robi Sankar Patra, Sridhar Rajaram, and Chandrabhas Narayana,
   RSC Advances, 2019, 9, 28222-28227

2. *Polaronic Signatures in Doped and Undoped Cesium Lead Halide Perovskite Nanocrystals through a Photoinduced Raman Mode*
   Priyanka Jain, Madhulika Mazumder, K. R. Pradeep, Ranjani Viswanatha, Swapan K. Pati, and Chandrabhas Narayana,
   ACS Applied Materials and Interfaces, 2022, 14 (4), 5567-5577

3. *Are the Mixed Halide Perovskite NCs ($CsPbX_3$ (X = Cl, Br)) Structurally Homogeneous?*
   Priyanka Jain, K. R. Pradeep, Ranjani Viswanatha, and Chandrabhas Narayana
   Manuscript under preparation

4. *Non-covalent interactions triggering structural changes and gas uptake in ZIF-4 microscrystals*
   Priyanka Jain, Gayatri Kumari, and Chandrabhas Narayana
   Manuscript under preparation

5. *Role of Metal Ion facilitating N_2 adsorption in ZIF-67: A Raman Study*
   Priyanka Jain and Chandrabhas Narayana
   Manuscript under preparation

Other Publications

1. *Interfacial tetrazine click chemistry mediated assembly of multifunctional colloidosomes*

   Meenakshi Pahwa, **Priyanka Jain**, Nilanjana Das Saha, Chandrabhas Narayana, and Sarit S. Agasti,

   Chemical Communications, 2021, 57, 9534-9537

2. *Harvesting Delayed Fluorescence in Perovskite Nanocrystals Using Spin-Forbidden Mn d States*

   Pradeep K. R., Debdipto Acharya, **Priyanka Jain**, Kushagra Gahlot, Anur Yadav, Andrea Camellini, Margherita Zavelani-Rossi, Giulio Cerullo, Chandrabhas Narayana, Shobhana Narasimhan, and Ranjani Viswanatha,

   ACS Energy Letters 2020, 5, 2, 353–359

3. *Phase Transitions in Materials*

   Divya Chalapathi, **Priyanka Jain**, and Chandrabhas Narayana,

   Advances in the Chemistry and Physics of Materials, pp. 249-274, World Scientific, 2019

Chapter 1

Introduction

A painting by an old master is a valuable, irreplaceable product, so valuable that highly skilled artists spend months replicating them. These replicas are so close to the real thing that it's nearly impossible to tell them apart. Indeed, some of these artisans are so skilled that they can create a new painting in the manner of an ancient artist and mislead almost everyone, which will be of more value than the forger's original work. In the art world, this is a big issue. Where there are chemical tests that can determine if the paints are old or fresh, it requires a sizable amount of materials. However, the laser paired with the spectroscope gave promising results. A hundred-thousandth of a square inch of pigment surface was vaporised using the laser's incredibly narrow beam. The spectroscope, which can study even the vapour from a microscopic specimen, was able to analyse this tiny sample, which was invisible to the naked eye. The painting under scrutiny was a portrait of an elderly woman attributed to the Maitre de Bruges, a 15th-century Flemish artist. It was all a ruse. In most cases, the use of this combination does not even require touching an object. (Excerpt drawn from Ref. [1])

Almost everything that scatters, absorbs, emits, or reflects light qualifies as a target probe. A spectroscope discovered the element helium in the sun in 1868, years before it was discovered on Earth. All types of elemental analysis from identifying to finding out the constituents can be achieved from atomic or molecular spectroscopy. The word "spectroscopy" is derived from the Latin "spectron," which means "spirit" or "ghost," and the Greek "$\sigma\kappa o\pi\iota\varepsilon\nu$" which means "to see". These roots are significant because,

in molecular spectroscopy, light is used to probe the matter, but the molecules themselves are never seen; only their action on the light is seen. "Of all the tools that have been applied to the study of the detailed structure of matter, it can fairly be said that spectroscopy has been applied in more ways to more problems, and has produced more fundamental information than any other," said Robert B. Leighton, professor of physics at the California Institute of Technology.

Vibrational spectroscopy has emerged as an effective technique to probe molecules irrespective of their environment and study their structure and dynamics of it. The spectrum can be used as a "fingerprint" because every molecule has a characteristic vibrational feature. This makes the technique superior in molecular detection, sensing, and characterisation. Although both Infrared and Raman spectroscopy provide vital information about the molecular vibrations, only the latter has been employed in this thesis and will be discussed in detail in this chapter.

1.1 Raman Scattering

Raman Spectroscopy is named after an Indian physicist, C. V. Raman, who was popular in the study of optics and acoustics worldwide while working at Calcutta University. The study of vibrations and sounds of stringed instruments such as Indian veena, tambura, and violin were his speciality. It was his first trip to London in 1921, where the deep blue colour of the Mediterranean kept him fascinated, however being unable to accept Lord Rayleigh's explanation of reflection of light resulting in the blue colour. Shortly after that, Raman was able to show that indeed it was the scattering of the sunlight by water molecules that gave rise to the blue colour of the ocean. This is where he became obsessed with light scattering, and his group started working extensively on it, mainly on light scattering by liquids.

On March 16, 1928, at a lecture in South Indian Science Association in Bangalore, Prof. C. V. Raman announced his new finding with the words, "I propose this evening to speak to you on a new kind of radiation or light emission from atoms and molecules." Sir C.V. Raman and K. S. Krishnan showed from their experiments for the first time, that when a beam of a visible light passed through a liquid, a fraction of this light was scattered

in a different colour (inelastic scattering) while most of it being Rayleigh scattered. By carrying the experiment on almost 60 different liquids it was determined that the nature of this light (energy/intensity) was dependent on the nature of the liquid used [2]. The Nobel prize in Physics, 1930 was awarded to C.V Raman for this discovery and it was named after him as 'Raman effect".

The importance of the Raman effect was recognized not only as a physicists tool but more so as a chemist's tool. The Raman effect is a weak scattering phenomenon, where only one in a million scattered photons are inelastically scattered. With the advent of lasers, the Raman effect became the principal method of nondestructive chemical analysis for both organic and inorganic compounds. Moreover, over the years, techniques such as resonant Raman, surface-enhanced Raman spectroscopy (SERS), tip-enhanced Raman spectroscopy (TERS), and others have proven to address the issue of weak inelastic scattering and making the Raman effect significant as an analytical tool. (Excerpts drawn from Ref. [3])

In this thesis, Raman spectroscopy has been used as a primary tool in understanding and probing various aspects of structure-property relationship in materials and even synthesizing new molecules for SERS applications. Hence, this chapter overviews the theory of Raman scattering, SERS, and SERS of thiol molecules. Also, the theory of the Raman spectral analysis in the low-frequency and molecular regions have been presented which includes, lattice vibrations, anharmonicity in phonons, electron-phonon coupling, effect of molecular guest adsorption on structure, and their interactions on Raman spectra. Lastly, highlights of the thesis work are described.

1.1.1 Classical Theory of Raman Scattering

When a molecule is subjected to an electric field, $\vec{E}$, the molecule is distorted due to a charge separation (positive charge of nuclei and negative charge of electrons), thus making the molecule polarised which creates an induced dipole moment, $\vec{P}$. This induced dipole moment is thus dependent upon the electric field and can be given by the relation,

$$\vec{P} = \alpha \cdot \vec{E}, \tag{1.1}$$

where α is the intrinsic polarizability of the molecule. α is a tensor which can be represented as

$$\begin{bmatrix} \alpha_{xx} & \alpha_{xy} & \alpha_{xz} \\ \alpha_{yx} & \alpha_{yy} & \alpha_{yz} \\ \alpha_{zx} & \alpha_{zy} & \alpha_{zz} \end{bmatrix}$$

In an oscillating electric field of the frequency, ν_0, the magnitude of the electric field is given as

$$E = E_0 \cos 2\pi\nu_0 t \tag{1.2}$$

Therefore, under these conditions, the resultant magnitude of the induced dipole will vary with time as

$$P = \alpha \cdot E = \alpha E_0 \cos 2\pi\nu_0 t \tag{1.3}$$

Thus, this oscillating dipole leads to a secondary radiation, with a frequency equivalent to the incident radiation. This major component of radiation is termed elastic or Rayleigh scattering. Now, the molecule comprises internal degrees of freedom which will modulate the polarizability in an oscillating field. Hence, a molecule with N atoms shall have 3N degrees of freedom being transitional, rotational, and vibrational in nature. Polarizability is a function of nuclear coordinates and vibrational frequencies of molecules. Let q_v be the normal coordinate of vibration whose coordinate as a function of time is given as

$$q_v = q_v^0 \cos 2\pi\nu_v t \tag{1.4}$$

where ν_v gives the frequency of q_v^{th} vibration. Thus, the equation of polarizability will be modified to

$$\alpha = \alpha_0 + \left(\frac{\partial\alpha}{\partial q_v}\right)_0 q_v + \cdots \tag{1.5}$$

where α_0 is the polarizability at the equilibrium position. The electrical harmonic approximation is applied here, which assumes that the displacements of the molecular vibrations involved are small making the higher orders other than that the first power of q_v trivial [4].

Substituting q_v from the equation 1.4 in the equation 1.5, we get

$$P = \alpha_0 E_0 2\pi\nu_0 t + \left(\frac{1}{2}\right) E_0 q_v^0 \left(\frac{\partial\alpha}{\partial q_v}\right)_0 [\cos 2\pi(\nu_0 + \nu_v)t + cos2\pi(\nu_0 - \nu_v)t] \tag{1.6}$$

This is the final equation of polarizability, with the first term of equation 1.6 being Rayleigh scattered ($\nu = \nu_0$). But the important ones here are the second and the third terms describing the Raman scattering (or inelastic scattering). Here, the frequency of oscillating dipole is either more ($\nu_0 + \nu_v$) or less ($\nu_0 - \nu_v$) than the incident light frequency, known as Anti-stokes and Stokes line, respectively. We look again at the equation 1.6, where it is evident that we obtain a finite term of these inelastic components, only when the change in polarizability is non-zero during the vibration, *i.e.* $\left(\frac{\partial \alpha}{\partial q_v}\right)_0 \neq 0$.

Although the classical theory described here predicts well the frequency of vibration and dictates the selection rule, it cannot precisely determine the intensities obtained. Hence, necessitates an explanation of Raman scattering using quantum mechanics.

1.1.2 Quantum Theory of Raman Scattering

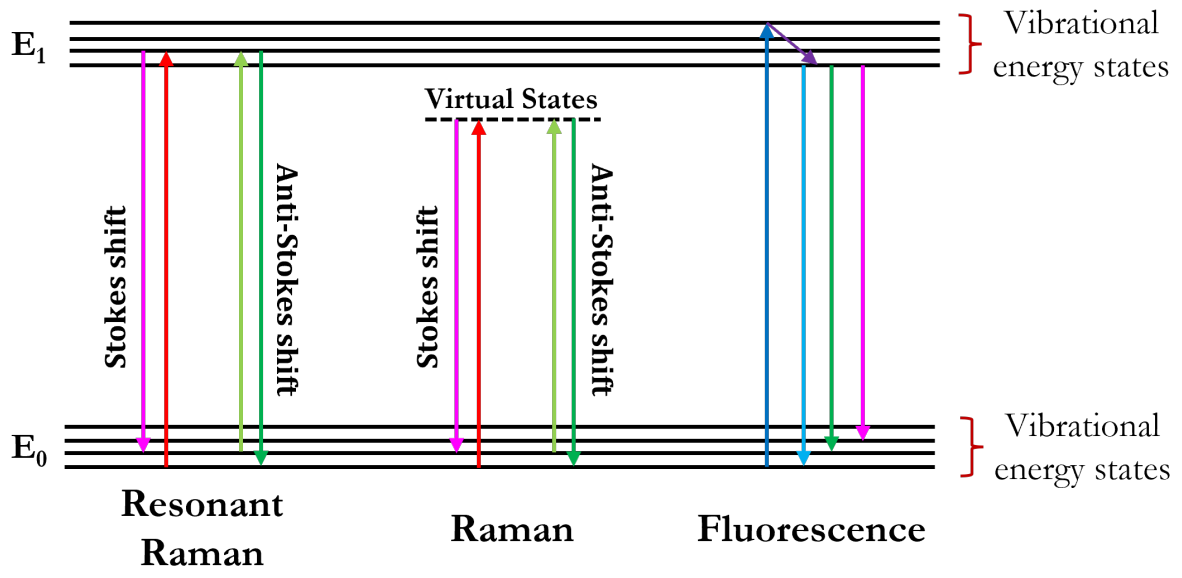

Figure 1.1: Energy level diagram describing Raman, Resonant Raman, and Fluorescence

To avoid tedious calculations, the molecule is treated quantum mechanically while the electromagnetic field is treated classically in the quantum approach. The time-independent Schrödinger equation determines the quantized energy levels of molecules. Raman scattering is a two-photon process, where an excitation of an electron occurs from $|i\rangle$ to $|r\rangle$ and an emission of an electron occurs from state $|r\rangle$ to $|f\rangle$, simultaneously. This process is accompanied by the release of photons, which are largely of the same energy,

and a few are of greater (anti-Stokes) or lesser energy (Stokes) as shown in the Figure 1.1. As seen in the figure, the virtual state is the intermediate state which is referred to as $|r\rangle$. It is virtual or intermediate by virtue of not being a solution to the Schrödinger equation. The phenomenon of scattering is explained quantum mechanically by transition probabilities from an initial state $|i\rangle$ to a final state $|f\rangle$ under a perturbation, in this instance electromagnetic radiation. An aspect of Raman polarizability can be shown as [5] for a particular transition.

$$\alpha_{kl} = \frac{1}{\hbar} \sum_{r \neq i,f} \left\{ \frac{\langle f|p_k|r\rangle\langle r|p_l|i\rangle}{\omega_r - \omega_i - \omega_L - i\Gamma_r} + \frac{\langle f|p_l|r\rangle\langle r|p_k|i\rangle}{\omega_r - \omega_f + \omega_L + i\Gamma_r} \right\} \tag{1.7}$$

p_k and p_l are dipole moment operators, and the summation is over all possible states $|r\rangle$ of energy $\hbar\omega_r$ and width $2\hbar\Gamma_r$ (with exception of the initial and final state). The states $|i\rangle$, $|f\rangle$, and $|r\rangle$ are vibronic (mixed electronic/vibrational) states of the molecule, and ω_L is the incident laser's angular frequency. According to equation 1.7, at least one component of the transition polarisability tensor must be non-zero for any vibrational transition $|i\rangle$ to $|f\rangle$ to be Raman active, defining the Raman scattering selection rule. It is important to note that the intensity of any transition is not taken into account when establishing the selection rule. As a result, it's possible that an allowed transition is missed experimentally because of its low intensity.

Raman modes are defined by (a) the frequency of the scattered light, which determines the peak position, (b) the depolarization ratio (the ratio of intensity in perpendicular and parallel directions), which indicates the molecule's symmetry, and (c) the scattering cross-section, which characterises the intensity qualitatively. The scattering cross-section for a normal mode m with an excitation frequency of Ω_L is shown below and given by [32],

$$\frac{d\sigma_m}{d\Omega} = \frac{\hbar\omega_R^4}{1440\pi^2 \left(\epsilon_0\right)^2 c^4 \omega_k} \left(1 + n_k^B\left(T\right)\right) L_M R_k \tag{1.8}$$

where $\omega_R = \omega_0 - \omega_k$, L_M is the local field correction and $n_k^B\left(T\right)$ is the Bose factor. R_k is the Raman activity given by

$$R_k = 45\bar{\alpha}_k^{'2} + 7\bar{\gamma}_k^{'2} \tag{1.9}$$

where $\bar{\alpha}_k^{'}$ and $\bar{\gamma}_k^{'}$ are the isotropic and anisotropic invariants of Raman tensor.

The overall intensity of the scattered light (4π solid angle) averaged over all the orientations of the molecule is [6]

$$I_{if} = \frac{2^7\pi^5}{9c^4} I_0 \left(\nu_0 + \nu_{if}\right)^4 \sum_{k,l} \left|\left(\alpha_{kl}\right)_{if}\right|^2 \tag{1.10}$$

where I_0, ν_0, and c are the intensity, frequency of the incident light, and the velocity of light, respectively. The summation belongs to the molecule normal coordinate over k = x, y, z and l = x, y, z. The intensity of scattered light is proportional to the frequency of incident light from equation 1.10. Raman signal enhances by 5 to 10 times, as the incident laser frequency approaches electronic transition frequency. This phenomenon is known as pre-resonance Raman. Preresonance Raman is advantageous in the cases of fluorescent molecules, where a good Raman signal intensity can be achieved without interference from the fluorescent background. Whereas, when ω_L is equal to the real electronic transition, then, the denominator of the first term in polarizability tensor (equation 1.7) diminishes. Hence, an enormous increase in the first term occurs resulting in the enhancement of Raman band intensities by three to five orders of magnitude [7]. This phenomenon is referred to as Resonance Raman scattering is shown in Figure 1.1. However, the resonance Raman condition does not reach infinity because Γ_r (which is proportional to the lifetime of excited state), keeps a finite first term in polarizability tensor.

For a collection of N molecules, the intensity of scattered radiation is dependent on more factors such as, the occupation of the vibronic state, m. The probability of this occupation of vibrational levels is defined using the Bose-Einstein statistics. Although the majority of the molecules at a certain temperature occupy the lowest vibrational level, a few occupy higher vibrational states also. This occupancy is quantifiable and increases at higher temperatures. It is defined as the ratio of Stokes and anti-Stokes intensity,

$$\frac{I_{Stokes}}{I_{anti\text{-}Stokes}} = \frac{\left(\tilde{\nu}_0 - \tilde{\nu}_m\right)^4}{\left(\tilde{\nu}_0 + \tilde{\nu}_m\right)^4} exp\left\{hc_0\tilde{\nu}_m/kT\right\} \tag{1.11}$$

where ν_m is the vibrational wavenumber.

1.2 Surface-enhanced Raman scattering (SERS)

Raman spectroscopy has been proven as a vital tool to study various aspects of materials. However, it cannot be forgotten that it is a weak phenomenon resulting in limitations of the technique in a lot of different systems, where molecules are perhaps low in concentration or prone to degradation in harsh laser conditions. Such systems include biomolecules, organic molecules, or even stable organic-inorganic molecules which are used as Raman tags in analytical quantities. Hence, necessitating alternatives for this spectroscopy tool to widen its applications. For this purpose, various techniques have been developed, one of them being SERS. A metal nanostructure is an integral component of SERS which enables the enhancement of a Raman signal by several orders of magnitude. Here, the metal nanoparticles are commonly noble metals such as gold, silver, and copper, however, even other metals like aluminium, lithium, and sodium also show weaker SERS signals. But the first question is, how does SERS work? SERS is based on the phenomenon of enhancing the Raman signal intensity from a molecule using surface plasmons which are adsorbed on/near the surface of metal nanoparticles. When an electromagnetic radiation falls onto the surface of these metal nanostructures, surface plasmons get excited. Surface plasmons are the collective oscillation of these electrons on the surface of the metal. When these surface plasmons have a frequency that matches with the incident radiation, the phenomenon is called surface plasmon resonance. Moreover, when the dimension of the plasmonic structure is less than the wavelength of light (nanostructures), then an oscillating dipole is produced creating a localized electromagnetic radiation close to the surface of the metal nanostructures shown in Figure 1.2. When the molecules are placed in the proximity of this metal surface, it experiences an enhanced electromagnetic field from both the incident as well as Raman scattered light leading to the phenomenon called surface-enhanced Raman scattering.

Fleischmann et al. was the first group that observed SERS on roughened electrodes [8] and was later shown by many other groups [9, 10]. With the advent of SERS, the application of Raman spectroscopy has been vital for characterisation, detection, and sensing of molecules. Analyte molecules as low as 10^{-15} M have also been detected using SERS [11, 12, 13]. This is mainly because, the scattering cross-section of the molecule gets fairly enhanced as compared to fluorescence, being 10^{-30} cm^2 per molecule in non-resonant Ra-

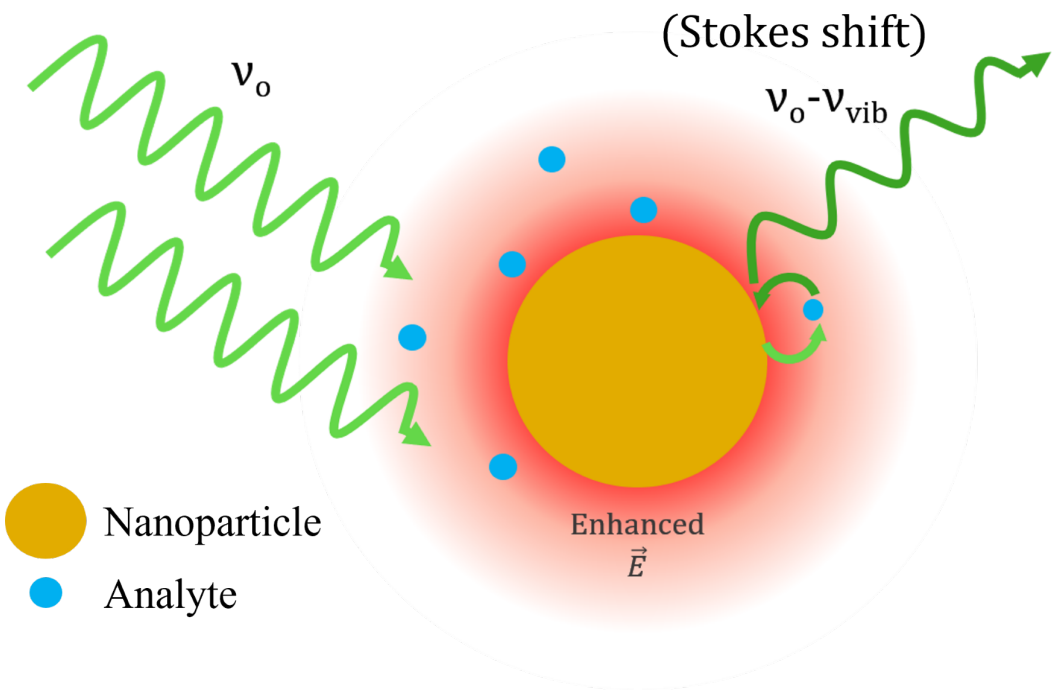

Figure 1.2: Schematic of SERS phenomenon

man to 10^{-17} cm^2 per molecule under SERS conditions [14]. Although still understanding of the complete picture of SERS is limited, there are two well-accepted mechanisms used, namely electromagnetic and chemical enhancement. The electromagnetic enhancement is based on a mechanism involving the enhancement of the local electric field generated [15]. Whereas, the chemical enhancement mainly involves enhancing the polarizability of the molecule in question. This can be achieved by alterations in the chemical environment with processes like charge-transfer processes and resonant intermediates [15]. Both the mechanisms are described briefly in the next two paragraphs.

1.2.1 Electromagnetic Enhancement (EM)

The electromagnetic enhancement is the major component of the SERS enhancement (up to 10^{10}) and as discussed, it involves contributions from local field enhancement as well as re-radiation enhancement. To take both into account, the Drude model of electrical conduction can be implied. According to it, metals are considered to be periodic static positive charges in a pool of electrons, a momentary displacement of which will create a dipole. The induced dipole oscillates with its own frequency thus generating an electric

field. When a molecule is placed in this electric field, it experiences $E_t = E_0 + E_{loc}$, where E_0 is the incident field and E_{loc} is the local field created by surface plasmons. This local field is dependent on the radius of the nanoparticle, r, distance of the molecule from its centre, d, and dielectric constant of the metal, ϵ along with the incident electric field. Thus, E_{loc} can be given by,

$$E_{loc} = \frac{\epsilon - \epsilon_0}{\epsilon + 2\epsilon_0} \left(\frac{r}{r+d} \right)^3 E_0 \tag{1.12}$$

The total electric field experienced by the molecule induces a dipole, μ_i (proportional to E_t and polarizability tensor, α). Molecular vibrations upon excitation with E_t produces elastic and inelastic frequencies. In the case of stokes shift, the outgoing field will be given by $E_o = E_D + E_{en}$, where E_D is the red-shifted field and E_{en} is the elastic scattering component from the dipole in the molecule itself.

Hence, the field enhancement will take into account the enhanced incoming field and the enhanced outgoing field, and the magnitude of it will depend on the ratio of the field amplitudes E_t/E_0 and E_o/E_0 respectively. Thus, the SERS electromagnetic enhancement is given by,

$$G_{SERS} = |A(\nu_L)|^2 |A(\nu_S)|^2 = \left| \frac{\epsilon(\nu_L) - \epsilon_0}{\epsilon(\nu_L) + 2\epsilon_0} \right|^2 \left| \frac{\epsilon(\nu_S) - \epsilon_0}{\epsilon(\nu_S) + 2\epsilon_0} \right|^2 \left(\frac{r}{r+d} \right)^{12} \tag{1.13}$$

where $A(\nu_L)$ and $A(\nu_S)$ are the amplitudes for laser and Raman scattered field respectively. From equation 1.13, G_{SERS} is equal to the fourth power of the local electromagnetic field and is large when resonance is achieved between the scattered and plasmons field. The enhancement factor is further influenced in specific geometries of nanostructures, which has localized areas of high enhancement known as "hotspots". Hotspots can be formed within closely spaced nanostructures, for example, a pelletized colloidal solution of nanoparticles containing the molecules to be studied. This hotspot formation becomes crucial especially at ultralow concentration, which has made single-molecule detection using SERS possible [16, 17].

1.2.2 Chemical Enhancement (CM)

Between the electromagnetic and chemical enhancement, it is the latter that is not as well understood. SERS enhancement of pyridine was observed to be much stronger than

the enhancement of water, and Jean Maire and Van Duyne argued that this observation cannot be only attributed to the EM effect [10]. It has a smaller contribution of about $10^2 - 10^3$ as compared to EM enhancement but is significant. According to the research so far, certain interactions between the molecule and the surface, such as covalency, charge transfer, or exchange, govern the extent of CM effects [18, 19, 20]. A transitory transfer of hot electrons or holes from the metal into the adsorbed molecules, or charge transfer resonances between metal and molecules, occurs during metal-ligand complexation. Many attempts have been made over the years to establish theories for the SERS effect that might contain all contributions, such as studies by Lombardi et al. based on Herzberg-Teller correlations [21, 22]. However, it was realized that the CM contribution of each molecule in SERS is different and investigating these effects would be acceptable if the isolation and quantification were carried for each contribution. Experimentally, certain methods have been developed to estimate the CM contribution of Raman scattering: 1) SERS and Raman spectra, their respective mode intensities are obtained. 2) A mode is chosen as standard which is unaffected by CM and used to normalize the spectrum. 3) Then the intensity difference between SERS and normalized Raman spectra are used to estimate the CM enhancement of each Raman mode [23]. However, there are certain prerequisites for the results to be reliable: the EM effect on all modes should be uniform, the standard mode should be completely independent of the CM, CM effects should be seen on all the molecules which must be bound to the metal surface [23].

Although challenging with numerous open ends, advanced approaches have been developed and groups have been able to show quantification of the CM effect using organic molecules such as malachite green, rhodamine 6G. But, the most widely used molecules for the same has been thiol based molecules which are electronically coupled to the metal and this coupling is largely affected by whether the system is physisorbed or chemisorbed.

1.2.3 SERS of thiol molecules

Thiol moieties are commonly used as end groups when the substrate is a noble metal owing to the strong affinity of sulphur to metals [24, 25]. In the cartoon depicted in Figure 1.3, the affinity of gold (Au) and a molecule substituted with a thiol moeity is depicted. In the 1990s, SERS provided the first evidence of the dissociative nature

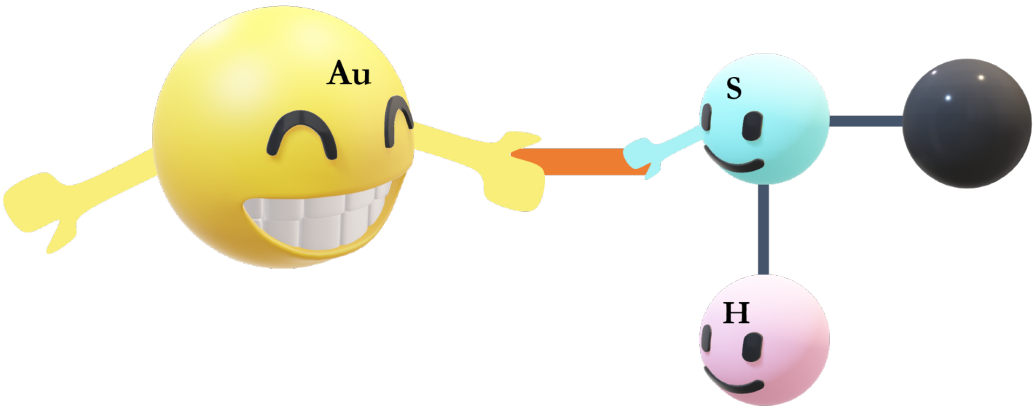

Figure 1.3: Representative picture for Au-thiol affinity

of adsorption of thiols such as thiophenol, benzylthiol, and others with gold (Au) and argued that they interact with the metal through sulphur [26]. Hence, the interactions of thiols and disulfides with Au surfaces in aqueous solutions has been studied using SERS, especially self-assembled monolayers (SAMs). More recent reports conveyed that the SAMs formed in aqueous solution because Au-thiol chemistry is more physisorbed than chemisorbed. As discussed in the previous section, there are more open ends in understanding the chemical enhancement factor of SERS, however, the Au-thiol chemistry is being exploited using SERS extensively, not only in the previously mentioned molecules but in a myriad of natural products such as antibiotics, antimicrobial, aesthetics, and others with a wide range of bioactivities [25]. SERS is being used as a simple and fast tool to detect thiol-containing compounds without much purification steps and also differentiate in the chemical environment they are in. In **Chapter 5** of this thesis, the synthesis of new Raman markers (thiol based dendronic molecules) has been carried out for SERS applications. Although, there exist better Raman scattering molecules such as rhodamine 6G as compared to molecules such as thiophenol, this Au-thiol chemistry, ease-of-synthesis, and handling of these materials over the complex dyes motivated the synthesis for new thiol-based compounds.

1.3 Raman spectrum Analysis

Raman spectroscopy is a non-destructive technique that can be used on a wide range of materials to probe the structure of a material. The basic Raman mode parameters such as band position, line-width, and intensity of a peak in the spectrum provide unique information. To simplify, firstly the band position gives information about the chemical structure, phase, polymorphism, and others. The line-width of a band provides deeper information such as intrinsic stress/strain, structural disorder, and others. Finally, the intensity of the peaks gives an idea about the concentration and distribution of chemical species in a system. In a typical Raman spectrum, peaks appear from different regions of a molecule, for example, the Raman spectrum of an organics molecule (thiophenol derivative synthesized in Chapter 5) is shown in Figure 1.4. The analysis of the entire spectra can seem overwhelming, however, it can be divided into specific regions for simplicity. The high-frequency region above 2500 cm^{-1} belongs to the internal modes of the stretching frequencies such as S-H, O-H, C-H, and N-H. This region is highly sensitive to any interactions that occur within the molecules or with the external environment, especially hydrogen bonding. The region between 400-1700 cm^{-1} belongs to the group frequencies, such as ring breathing, deformation, in- and out-of-plane stretching and bending modes and others. In this region, a large number of modes appear, mainly belonging to the backbone of molecules, but each molecule has a different spectrum in this region and is thus known as the "fingerprint" region. Finally, the low-frequency region is an extremely important region, especially for solid-state physics. It mainly focuses on the lattice or the external modes of materials, where crystal vibrations (or phonons) reveal various properties of a material such as elastic properties, thermal, and electric conductivity of the materials.

All the Raman mode parameters are extremely sensitive towards the local environment changes and external stimuli such as temperature, pressure, and pH. This results in shifting, broadening, and appearance/disappearance of the modes. Specific changes occur in the different materials depending on the purpose of the study which could alter the structure and thus the properties of the materials. Qualitatively, reducing temperature lowers lattice volumes by stiffening of bonds and ordered structure. Mechanical characterstics are influenced by operating temperature. At high temperatures, the thermal

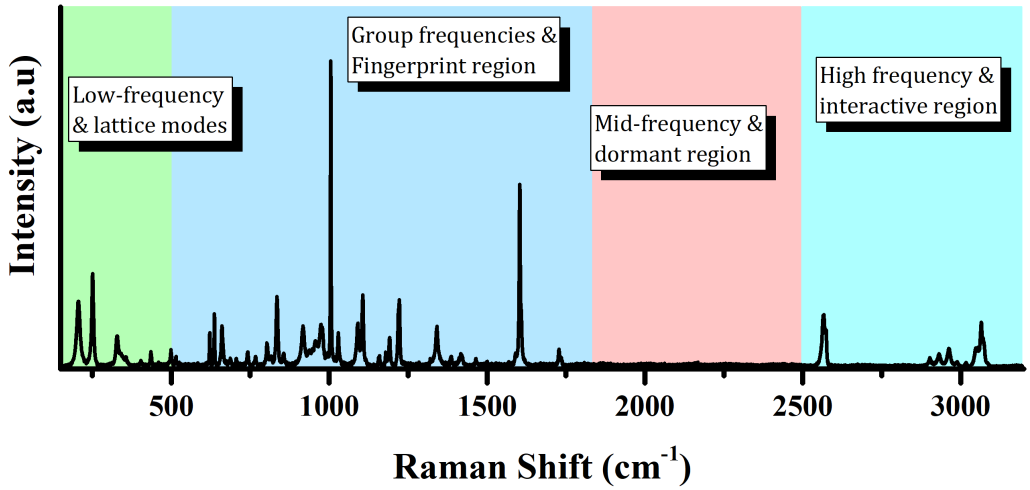

Figure 1.4: Raman spectra of an organic molecule (Benzyl-4-mercaptobenzoate synthesized in Chapter 5). The spectrum depicts different regions obtained in a typical Raman spectrum from a small molecule. Different regions provide specific information about the structure of the molecule.

vibrations and phonon interactions increase, thus invoking the anharmonic component of bonding force. In this thesis, temperature has been used as the primary parameter to study structural homogeneity, electron-phonon coupling, phase transition, and gas adsorption in materials. Different regions of the Raman spectra as described from Figure 1.4 have different implications in materials. Thus, the focus of the next sections will be to understand fundamentals of lattice vibrations, lattice-electron couplings, anharmoncity in phonons, and structural effects upon guest adsorption and interactions in molecules.

1.3.1 Lattice Vibrations

A phonon is defined as the collective vibration of atoms in a crystal. These vibrations can be derived using the phonon dispersion relation, which gives a relation between the angular frequency of the phonon, ω as a function of momentum of the phonon, k [27]. When two or more charged particles move in opposite directions with the centre of mass at rest in a primitive cell, they are called optical phonons. When the two lattices move in opposite directions, this mode has the maximum energy for wavelength infinity or k=0.

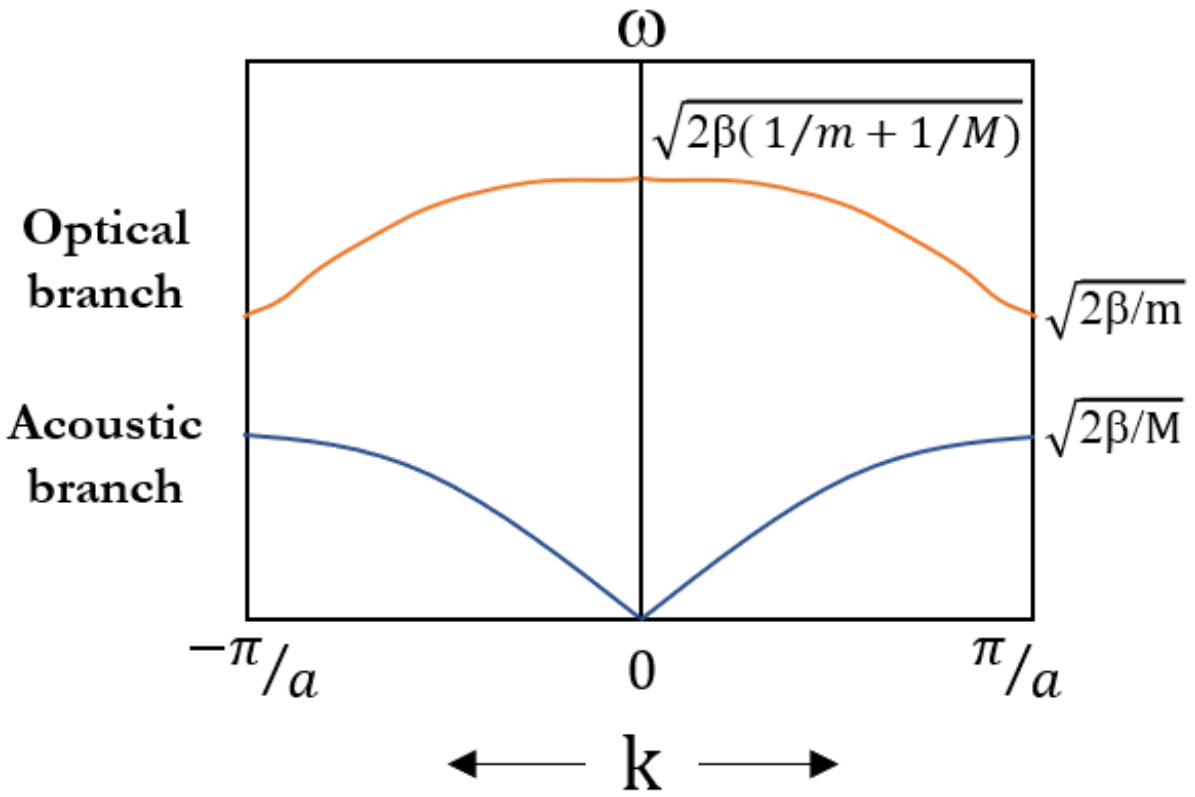

Figure 1.5: Dispersion relation of phonons for a diatomic linear lattice showing the optical and acoustical branches.

Considering a diatomic lattice with masses m and M. The equations of motion for an atom with masses 'm' and 'M' respectively, can be given by,

$$m\frac{\partial^2 U_{2n}}{\partial t^2} = \beta\left(U_{2n+1} - 2U_{2n} + U_{2n-1}\right) \tag{1.14}$$

$$M\frac{\partial^2 U_{2n+1}}{\partial t^2} = \beta\left(U_{2n+2} - 2U_{2n+1} + U_{2n}\right) \tag{1.15}$$

$$U_{2n} = A\exp^{i(2nka\pm\omega t)} \tag{1.16}$$

$$U_{2n+1} = A\exp^{i((2n+1)ka\pm\omega t)} \tag{1.17}$$

where, β is the force constant between two nearest-neighboring planes. Thus for a diatomic lattice, the solution will be,

$$\omega^2 = \beta\left(\frac{1}{m}+\frac{1}{M}\right) \pm \beta\sqrt{\left(\frac{1}{m}+\frac{1}{M}\right)^2 - \frac{4\sin^2\left(\frac{ka}{2}\right)}{Mm}} \tag{1.18}$$

The plot of the solution is shown in the Figure 1.5. The curve that begins at ω=0 and k=0, increases linearly and saturates at the edge of the Brillouin zone. This branch is rightly known as the acoustic branch because of its representation of an elastic wave or sound. The upper branch is called the optical branch, which as shown in the Figure 1.5 has a non-zero frequency given by $\omega = \sqrt{2\beta\,(1/m + 1/M)}$, which does not change significantly with k.

In acoustic mode, the molecules oscillate as a rigid body shown in Figure 1.6, whereas in the optical mode, the two atoms move in & out-of-phase in such a way that the centre of mass remains fixed.

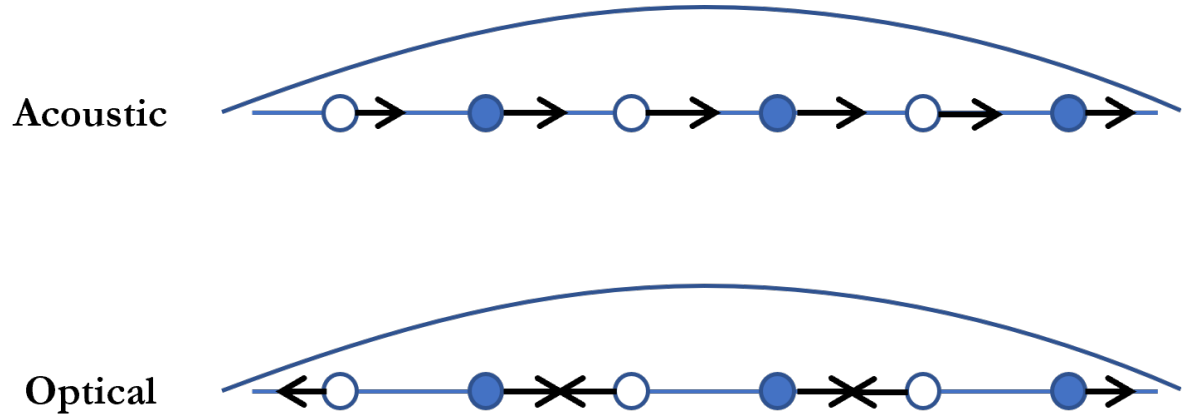

Figure 1.6: Schematic representation of acoustic and optical oscillation in a diatomic linear lattice

The above understanding can be extended to a three-dimensional lattice and will be discussed qualitatively. In a monoatomic lattice, each unit cell contains a single atom and the equation of motion of each of these atoms will be given by

$$u = A\exp^{i(ka-\omega t)} \tag{1.19}$$

where k describes the wavelength and direction of propagation, A specifies the amplitude as well as the direction of the vibration. Hence, u determines the polarization of the wave. The polarization can be longitudinal, where $A \parallel k$ or transverse, where $A \perp k$.

Upon substituting the equation 1.19 into the equation of motion, the equation will be obtained in all three directions for component A, which will be coupled together into a 3 x 3 matrix. Three different dispersion relations or curves will be obtained from the

roots of the equation, passing through the origin. Thus, the branches will be acoustic. When k lies in a direction of high symmetry, the polarization will be different in the three branches, two of them being transverse and one being longitudinal in nature. However, along with non-symmetry directions, one cannot obtain pure branches and thus have a mixed character.

Further extending the discussion to a unit cell containing say N atoms per unit cell, 3N dispersion curves will form. Out of the 3N dispersion curves, 3 will be acoustic while 3N-3 will be optical branches. Where the classification of the acoustic branches does not change, the optical branches can be described as longitudinal and transverse optical (LO and TO) branches, when q lies along a high symmetry direction.

The lattice vibrations were explained using classical theory until now, however, a phonon is described as the quantum of lattice vibration. Hence, to invoke the quantum theory, the energy levels of the harmonic oscillators need to be quantized. It is known that the allowed energy levels of the harmonic oscillators can be written as,

$$E = \left(n + \frac{1}{2}\right)\hbar\omega \tag{1.20}$$

where n is a quantum number. Upon comparing the classical (**equation 1.19**) and quantum (**equation 1.20**) solutions of the energy of a normal vibration in a one-dimensional lattice, the energy of the vibrational mode over time will equate to,

$$E = \frac{1}{2}M\omega^2A^2 = \left(n + \frac{1}{2}\right)\hbar\omega \tag{1.21}$$

It is observed that the amplitude and frequency of vibration are related to the phonon occupation of the mode, where only discrete values are allowed. A lattice with N atoms in a unit cell is described by 3N independent oscillators as discussed previously. Hence, the total vibrational energy of the crystal will be the summation of the energies of the individual modes. Now, phonons interact with other particles such as photons, electrons, and neutrons. There exist selection rules for allowed transitions between quantum states in crystals. In a crystal, the elastic scattering of a photon is governed by the wavevector selection rule $\boldsymbol{k'} = \boldsymbol{k} + \boldsymbol{G}$, where G is the vector in reciprocal space, k is the wavevector for incident photon, and k' is the wavevector for the scattered photon. This equation can act as a prerequisite for the conservation of momentum, where the momentum of

the lattice will be -$\hbar$G. In the case of inelastic scattering, the selection rule is given by $\boldsymbol{k'} = \boldsymbol{k} \pm \boldsymbol{q} + \boldsymbol{G}$. In the case of the first-order inelastic scattering process, the crystal vibrations very close to the Brillouin zone centre, i.e. q $\sim$ 0 gets excited. The Brillouin zone centre is known as the Γ point. The second-order Raman describes the phonon density of states (PDOS) since, at higher-order, the individual phonon wave-vector can span through the entire length till the first Brillouin zone.

1.3.2 Anharmonicity in phonons

In solids, phonons are not exclusive and generally coupled/interact with other particles and quasiparticles like electrons, polarons, magnons, and other phonons. As a result, the harmonic model is not enough to explain temperature-induced frequency or linewidth changes in Raman spectra in real crystals because in harmonic approximations, they are considered to be independent, and there is no change in PDOS with time. Moreover, even the changes in properties such as thermal expansion, temperature variations of elastic constants and compressibility cannot be explained by the same [28]. Hence, for a real system, at T $\neq$ 0, due to phonon-phonon interactions (anharmonicity), the phonon occupation number n_k varies. By the Bose-Einstein distribution, the dependence of the two can be given by $n_k = 1/\exp^{(\hbar\omega(k))/KT} - 1$ where K is Boltzmann's constant. Phonon-phonon interactions and the collisions of particles in a thermodynamic system are analogous. In this analogy, phonon relaxation time (τ_{ph}), i.e. the time elapsed between collisions, is simply the lifetime of the phonons. It is noteworthy that the finite width (Γ) of the Raman lines is a consequence of 1) the anharmonicity and 2) the lifetime of the phonons (inversely proportional).

In a cubic anharmonic process, where a third term is added to the harmonic potential, possibilities of a phonon decay into two other phonons or merging of two phonons into a single phonon can occur. Correspondingly, the modified phonon linewidth and frequency can be described as [29],

$$\omega(T) = \omega_0 + CT + B_1 \left(1 + \frac{2}{\exp\left(\hbar\omega/2K_BT\right) - 1}\right) \tag{1.22}$$

$$\Gamma(T) = \Gamma_0 + B_2 \left(1 + \frac{2}{\exp\left(\hbar\omega/2K_BT\right) - 1}\right) \tag{1.23}$$

where ω_0 and Γ_0 are intrinsic frequency and linewidth of the phonon at absolute zero temperature, B_1 and B_2 are the respective cubic anharmonic constants, and C explains the thermal expansion coefficient. Here, temperature causes an implicit frequency shift described by CT as the thermal volume expansion. Additionally, an explicit contribution of the thermal population of vibrational levels is reflected in the third term of equation 1.22.

When a system is subjected to varying temperatures, it alters the average position of the atoms and distance in the energies of these levels. Hence the phonon population correlated with each normal mode is affected and thereby the phonon occupation number of the system. The temperature changes the phonon population which affects the PDOS, which is a critical parameter for any real system [28].

1.3.3 Electron-phonon coupling: Polaron

One of the fundamental interactions of quasiparticles in solids is electron-phonon coupling (EPC), apart from coulomb interaction. EPC has a significant contribution in various physical processes. For example, lattice vibrations in metals couple to low-energy electronic excitations strongly which influence their transport and thermodynamic properties such as resistivity, thermal conductivity, superconductivity, and phonon dispersion [30].

A polaron is a quasiparticle, where an electron interacts with the atoms in a solid, displacing them from their equilibrium positions. This effectively screens the electron (phonon-cloud), increasing its effective mass, and decreasing the electron mobility. It was first proposed by Lev Landau [31] and then later by Solomon Pekar [32]. The Bloch spectrum, which comprises allowed and prohibited bands, is the energy spectrum of an electron travelling in a periodic potential of a crystal lattice. An electron with energy within an allowed band moves like a free electron but has a different effective mass than an electron in a vacuum. The interaction between electrons and these displacements in the lattice is known as electron-phonon coupling. Lev Landau outlined in his 1933 paper one conceivable scenario, which included the creation of a lattice defect, such as an F-center, and the trapping of the electron by this defect [31]. Solomon Pekar presented a different scenario, in which the electron is dressed with lattice polarization (a cloud of virtual polar phonons) [32]. This type of electron, together with the deformation it

causes, flows freely through the crystal, but with a higher effective mass [33]. This new entity formed by the carrier together with the induced polarization is called a polaron is shown in the Figure 1.7 coined by Pekar. An active field of research revolves around theoretical work, namely solving Fröhlich (based on scattering of LO phonon with charge carrier) and Holstein Hamiltonian (based on interaction with molecular phonons), which is focused on finding exact numerical solutions for one or two electrons interacting in a large crystal lattice.

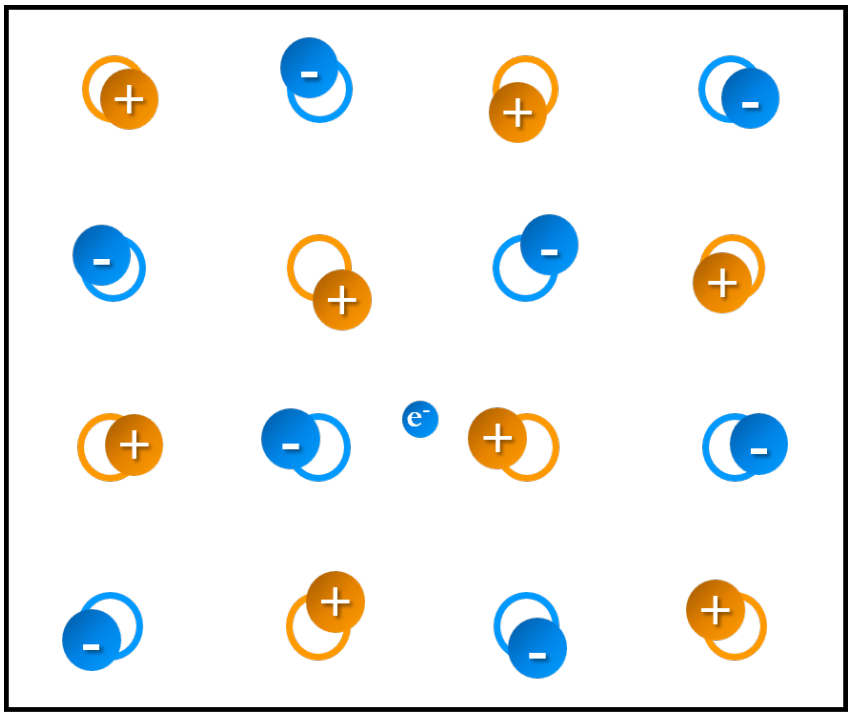

Figure 1.7: Picture how to visualize a polaron. (inspiration taken from [34]). In an ionic crystal or a polar semiconductor, a conduction electron repels negative ions while attracting positive ions. There is a self-induced potential that operates on the electron and changes its physical properties.

The EPC to optical phonons is the subject of polaron research. The reason for this is that the strength of the short-range coupling is determined by the relative displacements between the atom hosting the carrier and its neighbours because these displacements modulate the carrier's onsite energy and hopping integrals (assuming long-range interactions are screened) [35]. Acoustic phonons are gapless, making them easy to excite; nevertheless, because they describe the "in-phase" motion of neighbouring atoms, the associated relative displacements are vanishingly small, resulting in very weak EPC. Op-

tical phonons, on the other hand, describe "antiphase" atomic motion [36], resulting in huge relative displacements and a substantially larger EPC. Electron coupling with lattice deformation are weak in covalent semiconductors, thus polaron formation is not possible. The electrostatic interaction with induced polarisation is strong in polar semiconductors, and polarons occur at low temperatures if the polaron concentration is low and the screening is ineffective. Molecular crystals, where the interaction with molecular vibrations is substantial, are another class of materials where polarons are found [37]. Polarons are crucial to the experimental study of a wide range of materials because the formation of polarons can substantially lower electron mobility in semiconductors. Organic semiconductors are also responsive to polaronic effects, which is essential for the creation of organic solar cells that are effective in charge transport. Polarons are also useful for understanding the optical conductivity of these materials.

Both IR and Raman spectroscopy has been used as a powerful tool for *in-situ* investigation of charge carriers in electronic devices based on conducting polymers with the latter having an added advantage of exceptional spatial resolution [38, 39]. A few examples of understanding polaronic effects using Raman spectroscopy include spectral changes in the intensity ratio of specific Raman modes related to carrier concentration in organic conducting polymers,[40, 41] observation of periodic broad modes up to 8^{th} order in Raman in 2D semiconducting magnet,[42] and changes in scattering response upon small to large polaron with phase transition in perovskite manganese-oxides [43]. Low-frequency Raman measurements combined with first-principles molecular dynamics (MD) have been carried out to discuss the local polar fluctuations in $MAPbBr_3$ and $CsPbBr_3$ inhibiting carrier recombination.[44]. In **Chapter 3** of this thesis, evidence of polaron and its behaviour in cesium lead halide perovskite nanocrystals using micro-Raman spectroscopy will be discussed.

1.3.4 Effect of molecular guests on structure: Porous Materials

In porous materials, specifically metal organic frameworks (MOFs) or zeolitic imidazolate frameworks (ZIFs), guest molecules play a significant role. Guest molecules are any molecules which can be inserted in the framework of these porous materials such as gases (N_2, Ar, CH_4, and other hydrocarbons) or small molecules (DMF, H_2O, and others)

which are commonly used as solvents for the synthesis of such MOFs/ZIFs. The insertion or removal of guest molecules can thus act as a driving force for various responsive behaviours such as towards temperature, pressure, or electric field because it alters the chemical potential of the system. In simpler words, they create a noticeable stress/strain on the structure of the system often causing guest induced or stimuli induced deformation/expansion/collapsing of the framework but not necessarily changing the structure of the system. For example, in some cases, removal of the sample also known as activating a porous material at high temperature lead to a structural change in the case of ZIF-7 which could be reversed by CO_2 adsorption with breathing phenonmenon [45]. This structural change is well observed in X-ray diffraction. A schematic representation of breathing of framework upon guest insertion/removal is shown in Figure 1.8. Another example is the gate-opening of ZIF-8, which was first shown by N_2 adsorption alone and predicted to be accompanied by rearrangement in the framework with small unit cell expansion [46]. These results were confirmed by both single crystal XRD and Raman spectroscopy to be a gradual gate-opening in ZIF-8 leading to N_2 adsorption [47, 48]. Vibrational spectroscopy is undoubtedly a powerful tool in monitoring the structural evolution of these porous systems with external stimuli.

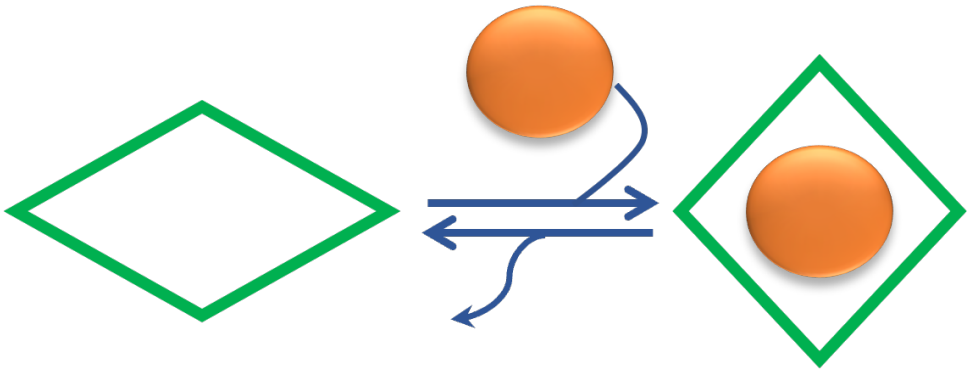

Figure 1.8: Breathing of a porous framework upon guest insertion/removal. Schematic inspired from [49].

Thermodynamically, when temperature is used as a stimuli, the free energy of the system can be given by $\Delta G = \Delta H_{dispersion} - T\Delta S_{vibrational}$, where the balance between the dispersion interactions and vibrational entropy determines the ZIF configuration. Many groups have discussed the effect of this competition on the low-frequency modes in ZIF-8 and ZIF-7. Low-frequency modes (< 100 cm^{-1}, also known as the rigid unit

modes (RUMs) have unique spectral signatures upon changes in the lattice occurring due to deformation of the network, rotation of linkers, or gas adsorption [50]. These RUMs mainly correspond to twisting/rocking of the linker modes without a change in the Zn-N distance. Depending on the open or close form of the framework, the interatomic distances will change which will then affect their electron density, bond strengths and hence the vibrational frequency. In a closed pore, electron density overlap between the neighbouring moieties will be greater than that of an open pore which will result in an increase in the intensity of the rigid unit modes and stiffening of these modes due to decrease in vibrational entropy [50]. In **Chapter 4**, the changes upon different perturbations on the RUM will be discussed to determine the configuration of the ZIF framework, along with other spectral changes in the molecular modes as well as guest characterstic peaks upon adsorption. These adsorptions result in geometric distortion of framework or guest molecules often accompanied by guest-host interactions or framework interactions (non-bonding) which can be identified in the vibrational spectrum. Hence, in the next section we discuss what types of interactions can be present and how does it affect a vibrational spectra.

1.3.5 Effect of Non-bonding interactions in molecules

Coulomb, van der Waals (VDW), and chemical interactions are the three basic types of interactions between atomic and molecular systems [51]. VDW interactions are classified into dipole-dipole, dipole-induced dipole, induced-dipole-induced dipole, and dispersion forces in the decreasing order of their strength. Dispersion forces are the weakest forces which mainly describe the interactions between non-polar gases and arise due to temporary polarization of the atom/molecule. Chemical interactions are also further classified into covalent, ionic, donor-acceptor, and hydrogen bonding (H-bond). Each of these interactions is based on the well-known interaction of atomic or molecular orbitals. The varying degrees of orbital overlap and the distribution of electron density on them (orbital occupancy) reflect the chemical interaction's specific architecture. The chemical interaction is directional, but the Coulomb and van der Waals contacts are isotropic. This is the fundamental distinction between them. The variety of structures that emerge during chemical interaction is a result of directionality. Although H-bond energy is the weakest

among all types of chemical bonds it is about an order of magnitude higher than VDW energy.

Non-bonding interactions play an essential role in the field of biology, chemistry, and biochemistry. Although weak in nature, they establish the structures and properties of liquids, biological molecules, and molecular crystals [52]. Water and DNA are the best examples in nature that highlight the importance of non-bonding interactions, rather hydrogen bonding in science. Hydrogen bonding is known to determine crystal structure, solvation processes, nonlinear optical responses in solid state materials, and the macroscopic properties of gases and condensed phase materials. Moderately strong hydrogen bonding is the most prevalent and well-studied class of interactions, which includes N-H$\cdots$N, N-H$\cdots$O, O-H$\cdots$N, O-H$\cdots$O, and other related interactions between fragments (with no charge) with distances typically ranging from 1.5 to 2.2 Å[53]. Electrostatic interactions dominate the structures that result from this type of interaction in neutral biological molecules. Weak C-H$\cdots$N, C-H$\cdots$O, and C-H$\cdots\pi$ interactions (also known as weak hydrogen bonds) are usually longer than 2.2 Å. These weaker H-bonds are not as directional as the stronger forms of H-bonds but have a significant impact on observables, such as a 10 % shift in peak positions in the pure molecular liquid's vibrational spectrum on average [53]. Vibrational spectroscopy is an effective tool for studying the effects of non-bonding interactions because changes in the Raman/IR spectra of interacting molecules determine accurately which bonds and atoms are affected. In addition, the amount and nature of shift observed in peak positions or broadening of the modes even underpin the extent of the interaction.

In a typical signature of H-bond, due to the stretching mode of the donor molecule, which corresponds to an elongated bond, the peak intensity increases as well as the peak shifts to lower energy. This spectral pattern is usually referred to as a redshift, despite the fact that it is not technically accurate [54]. Although most H-bonding follows typical trends, a few of them do not. C-H$\cdots\pi$ interactions is one of the non-traditional weak H-bonding, where a blue-shift in the C-H stretching frequencies is observed followed by a decrease in the intensity [54, 55]. These interactions typically range between 2.6-3.0 Å, the C-H bond may point to the centre of the ring, and the CHX angle is close to linearity as shown in the Figure 1.9. The C-H bond length shortens upon complexation which leads

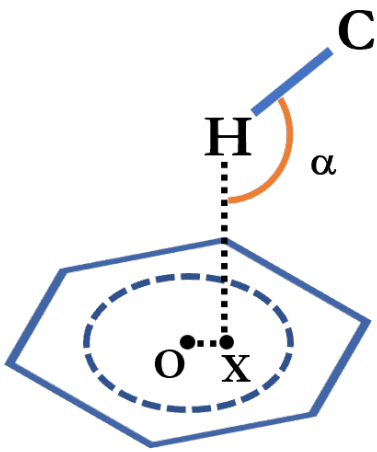

Figure 1.9: Illustration of C-H$\cdots\pi$ interaction

to a higher C-H stretching mode [56]. The predominant interaction that stabilizes it is majorly dispersion rather than electrostatic or charge transfer interaction, thus making C-H$\cdots\pi$ interactions less directional in nature, unlike strong H-bonds. Although weak, the C-H stretching vibration can undergo a significant blue-shift ($\sim$ 4-31 cm^{-1}) because they will never be present as a singular interaction. A large number of such interactions with possibilities of multiple sites (also less directional) are present, thus significantly influencing the structure of a material [56, 55].

In **Chapter 4**, the Raman spectral evolution in ZIF systems will be discussed with guests as well as temperature changes. Since there are a large number of atoms in ZIFs, they result in a large number of vibrational modes which makes it difficult to spot the changes upon specific interactions and finding the origin of it becomes even more challenging. Thus, to obtain any reliable information on temperature or adsorbate-induced alterations, it is primary to identify broad sources of interactions in these systems. A few of these interactions such as dispersive and C-H$\cdots\pi$ interactions will be central point of discussion. The effects of their presence with and without guest molecules with temperature will be discussed extensively. The riveting results from the Raman spectral changes of the structure underscored the presence of these non-bonding interactions essential to show guest adsorption as well as stabilise an empty pore in ZIF systems.

1.4 Highlights of the thesis

In this thesis, Raman and temperature dependent Raman spectroscopy has been used in studying various aspects of structure-property relationship in certain materials and synthesis of thiol based markers for SERS applications. The introduction and motivation to the systems used are described along with the chapters. Here, the important results are briefly described.

1. Solid solution formation and Pb environments have been explored in cesium lead mixed halide ($CsPbX_3$, where X=Cl, Br) perovskite nanocrystals (NCs) using the LO_2 mode and the TO_2 mode in $CsPbX_3$ NCs.

2. A new polaronic peak at 132 cm^{-1} was discovered below 273 K in $CsPbX_3$ and Mn-doped counterparts and its stability in the family of materials was investigated.

3. ZIF-4(DS): Temperature evolution of ZIF framework and structural changes were explored in ZIF-4 under guest-free and guest conditions. An open to narrow pore transition in absence of guests and an adsorption-induced transition in guest environment have been discovered. Gas adsorption (N_2 and CO_2) were presented for the first time under ambient conditions marked by their characterstic frequencies in Raman spectrum. The adsorption sites in ZIF-4 were proposed experimentally using Raman studies.

4. ZIF-67(DS): Temperature dependent Raman studies revealed two types of N_2 adsorption in ZIF-67 and the adsorption sites were discussed.

5. Three new dendronic thiol-based molecules were synthesized for SERS applications.

References

[1] H. Hellman, *Spectroscopy.* US Atomic Energy Commission, Division of Technical Information, (1968).

[2] C. V. Raman and K. S. Krishnan, "A new type of secondary radiation," *Nature*, vol. 121, no. 3048, pp. 501–502, (1928).

[3] American Chemical Society International Historic Chemical Landmarks, "The Raman Effect," (1998).

[4] D. A. Long and D. Long, *The Raman effect: a unified treatment of the theory of Raman scattering by molecules*, vol. 8. Wiley Chichester, (2002).

[5] E. Le Ru and P. Etchegoin, *Principles of Surface-Enhanced Raman Spectroscopy: and related plasmonic effects.* Elsevier, (2008).

[6] A. C. Albrecht, "On the theory of raman intensities," *The Journal of chemical physics*, vol. 34, no. 5, pp. 1476–1484, (1961).

[7] J. R. Ferraro, *Introductory raman spectroscopy.* Elsevier, (2003).

[8] M. Fleischmann, P. J. Hendra, and A. J. McQuillan, "Raman spectra of pyridine adsorbed at a silver electrode," *Chemical physics letters*, vol. 26, no. 2, pp. 163–166, (1974).

[9] M. G. Albrecht and J. A. Creighton, "Anomalously intense raman spectra of pyridine at a silver electrode," *Journal of the american chemical society*, vol. 99, no. 15, pp. 5215–5217, (1977).

[10] D. L. Jeanmaire and R. P. Van Duyne, "Surface raman spectroelectrochemistry: Part i. heterocyclic, aromatic, and aliphatic amines adsorbed on the anodized silver electrode," *Journal of electroanalytical chemistry and interfacial electrochemistry*, vol. 84, no. 1, pp. 1–20, (1977).

[11] P. P. Patra and G. P. Kumar, "Single-molecule surface-enhanced raman scattering sensitivity of ag-core au-shell nanoparticles: revealed by bi-analyte method," *The journal of physical chemistry letters*, vol. 4, no. 7, pp. 1167–1171, (2013).

[12] K. Kneipp, Y. Wang, R. R. Dasari, and M. S. Feld, "Approach to single molecule detection using surface-enhanced resonance raman scattering (serrs): a study using rhodamine 6g on colloidal silver," *Applied Spectroscopy*, vol. 49, no. 6, pp. 780–784, (1995).

[13] S. Yang, X. Dai, B. B. Stogin, and T.-S. Wong, "Ultrasensitive surface-enhanced raman scattering detection in common fluids," *Proceedings of the National Academy of Sciences*, vol. 113, no. 2, pp. 268–273, (2016).

[14] K. Kneipp, Y. Wang, H. Kneipp, L. T. Perelman, I. Itzkan, R. R. Dasari, and M. S. Feld, "Single molecule detection using surface-enhanced raman scattering (sers)," *Physical review letters*, vol. 78, no. 9, p. 1667, (1997).

[15] A. Campion and P. Kambhampati, "Surface-enhanced raman scattering," *Chemical society reviews*, vol. 27, no. 4, pp. 241–250, (1998).

[16] S. M. Stranahan and K. A. Willets, "Super-resolution optical imaging of single-molecule sers hot spots," *Nano letters*, vol. 10, no. 9, pp. 3777–3784, (2010).

[17] E. Le Ru, P. Etchegoin, and M. Meyer, "Enhancement factor distribution around a single surface-enhanced raman scattering hot spot and its relation to single molecule detection," *The Journal of chemical physics*, vol. 125, no. 20, p. 204701, (2006).

[18] K. Kneipp, "Chemical contribution to sers enhancement: an experimental study on a series of polymethine dyes on silver nanoaggregates," *The Journal of Physical Chemistry C*, vol. 120, no. 37, pp. 21076–21081, (2016).

[19] A. Otto, "The 'chemical'(electronic) contribution to surface-enhanced raman scattering," *Journal of Raman Spectroscopy*, vol. 36, no. 6-7, pp. 497–509, (2005).

[20] C. Boerigter, U. Aslam, and S. Linic, "Mechanism of charge transfer from plasmonic nanostructures to chemically attached materials," *ACS nano*, vol. 10, no. 6, pp. 6108–6115, (2016).

[21] J. R. Lombardi, R. L. Birke, T. Lu, and J. Xu, "Charge-transfer theory of surface enhanced raman spectroscopy: Herzberg–teller contributions," *The Journal of chemical physics*, vol. 84, no. 8, pp. 4174–4180, (1986).

[22] J. R. Lombardi and R. L. Birke, "A unified approach to surface-enhanced raman spectroscopy," *The Journal of Physical Chemistry C*, vol. 112, no. 14, pp. 5605–5617, (2008).

[23] B. Liu, B. Thielert, A. Reutter, R. Stosch, and P. Lemmens, "Quantifying the contribution of chemical enhancement to sers: A model based on the analysis of light-induced degradation processes," *The Journal of Physical Chemistry C*, vol. 123, no. 31, pp. 19119–19124, (2019).

[24] P. Giulia, "A not-so-strong bond," *Nature Reviews. Materials*, vol. 4, no. 4, pp. 226–226, (2019).

[25] Y. Hong, R. Wang, Z. Jiang, Z. Cong, and H. Song, "Rapid sers detection of thiol-containing natural products in culturing complex," *International journal of analytical chemistry*, vol. 2020, (2020).

[26] R. L. Garrell, C. Szafranski, and W. Tanner, "Surface-enhanced raman spectroscopy of thiols and disulfides," in *Raman and Luminescence Spectroscopies in Technology II*, vol. 1336, pp. 264–271, International Society for Optics and Photonics, (1990).

[27] N. W. Ashcroft, N. D. Mermin, *et al.*, "Solid state physics," (1976).

[28] G. Lucazeau, "Effect of pressure and temperature on raman spectra of solids: anharmonicity," *Journal of Raman Spectroscopy*, vol. 34, no. 7-8, pp. 478–496, (2003).

[29] M. Balkanski, R. Wallis, and E. Haro, "Anharmonic effects in light scattering due to optical phonons in silicon," *Physical Review B*, vol. 28, no. 4, p. 1928, (1983).

[30] R. Heid, "15 electron-phonon coupling," *The Physics of Correlated Insulators, Metals, and Superconductors*.

[31] L. D. Landau, "Electron motion in crystal lattices," *Phys. Z. Sowjet.*, vol. 3, p. 664, (1933).

[32] S. Pekar, "Zhetf 16 (1946) 341," *J. Phys.(USSR)*, vol. 10, p. 347, (1946).

[33] L. Landau and S. Pekar, "Effective mass of a polaron," *Zh. Eksp. Teor. Fiz*, vol. 18, no. 5, pp. 419–423, (1948).

[34] Wikipedia contributors, "Polaron — Wikipedia, the free encyclopedia," 2022. [Online; accessed 28-March-2022].

[35] D. J. Marchand and M. Berciu, "Effect of dispersive optical phonons on the behavior of a holstein polaron," *Physical Review B*, vol. 88, no. 6, p. 060301, (2013).

[36] G. D. Mahan, *Many-particle physics*. Springer Science & Business Media, (2013).

[37] H. Fröhlich, H. Pelzer, and S. Zienau, "Xx. properties of slow electrons in polar materials," *The London, Edinburgh, and Dublin Philosophical Magazine and Journal of Science*, vol. 41, no. 314, pp. 221–242, (1950).

[38] Y. Furukawa, "Vibrational spectroscopy of conducting polymers: Fundamentals and applications," *Handb. Vib. Spectrosc.*, (2006).

[39] D. Mihailovic, "Photoinduced polaron signatures in infrared spectroscopy," in *Polarons in Advanced Materials*, pp. 547–567, Springer, (2007).

[40] C. Francis, D. Fazzi, S. Grimm, F. Paulus, S. Beck, S. Hillebrandt, A. Pucci, and J. Zaumseil, "Raman spectroscopy and microscopy of electrochemically and chemically doped high-mobility semiconducting polymers," *J. Mater. Chem. C*, vol. 5, no. 25, pp. 6176–6184, (2017).

[41] J. Yin, Z. Wang, D. Fazzi, Z. Shen, and C. Soci, "First-principles study of the nuclear dynamics of doped conjugated polymers," *J. Phys. Chem. C*, vol. 120, no. 3, pp. 1994–2001, (2016).

[42] W. Jin, H. H. Kim, Z. Ye, G. Ye, L. Rojas, X. Luo, B. Yang, F. Yin, J. S. A. Horng, S. Tian, *et al.*, "Observation of the polaronic character of excitons in a two-dimensional semiconducting magnet cri 3," *Nat. Commun.*, vol. 11, no. 1, pp. 1–7, (2020).

[43] S. Yoon, H. L. Liu, G. Schollerer, S. Cooper, P. Han, D. Payne, S.-W. Cheong, and Z. Fisk, "Raman and optical spectroscopic studies of small-to-large polaron crossover in the perovskite manganese oxides," *Phys. Rev. B*, vol. 58, no. 5, p. 2795, (1998).

[44] O. Yaffe, Y. Guo, L. Z. Tan, D. A. Egger, T. Hull, C. C. Stoumpos, F. Zheng, T. F. Heinz, L. Kronik, M. G. Kanatzidis, *et al.*, "Local polar fluctuations in lead halide perovskite crystals," *Phys. Rev. Lett.*, vol. 118, no. 13, p. 136001, (2017).

[45] C. Cuadrado-Collados, J. Fernández-Català, F. Fauth, Y. Q. Cheng, L. L. Daemen, A. J. Ramirez-Cuesta, and J. Silvestre-Albero, "Understanding the breathing phenomena in nano-zif-7 upon gas adsorption," *Journal of Materials Chemistry A*, vol. 5, no. 39, pp. 20938–20946, (2017).

[46] D. Fairen-Jimenez, S. Moggach, M. Wharmby, P. Wright, S. Parsons, and T. Duren, "Opening the gate: framework flexibility in zif-8 explored by experiments and simulations," *Journal of the American Chemical Society*, vol. 133, no. 23, pp. 8900–8902, (2011).

[47] J.-P. Zhang, A.-X. Zhu, and X.-M. Chen, "Single-crystal x-ray diffraction and raman spectroscopy studies of isobaric n 2 adsorption in sod-type metal–organic zeolites," *Chemical Communications*, vol. 48, no. 93, pp. 11395–11397, (2012).

[48] G. Kumari, K. Jayaramulu, T. K. Maji, and C. Narayana, "Temperature induced structural transformations and gas adsorption in the zeolitic imidazolate framework zif-8: A raman study," *The Journal of Physical Chemistry A*, vol. 117, no. 43, pp. 11006–11012, (2013).

[49] R.-B. Lin, S. Xiang, W. Zhou, and B. Chen, "Microporous metal-organic framework materials for gas separation," *Chem*, vol. 6, no. 2, pp. 337–363, (2020).

[50] K. T. Butler, P. Vervoorts, M. G. Ehrenreich, J. Armstrong, J. M. Skelton, and G. Kieslich, "Experimental evidence for vibrational entropy as driving parameter of flexibility in the metal–organic framework zif-4 (zn)," *Chemistry of Materials*, vol. 31, no. 20, pp. 8366–8372, (2019).

[51] B. A. Kolesov, "Hydrogen bonds: Raman spectroscopic study," *International Journal of Molecular Sciences*, vol. 22, no. 10, p. 5380, (2021).

[52] A. M. Wright, A. A. Howard, G. S. Tschumper, and N. I. Hammer, "Raman spectroscopic investigations of noncovalent interactions between pyrimidine and hydrogen bonded networks," in *AIP Conference Proceedings*, vol. 1267, pp. 852–853, American Institute of Physics, (2010).

[53] A. A. Howard, G. S. Tschumper, and N. I. Hammer, "Effects of hydrogen bonding on vibrational normal modes of pyrimidine," *The Journal of Physical Chemistry A*, vol. 114, no. 25, pp. 6803–6810, (2010).

[54] S. A. McDowell, "Redshift and blueshift of the ar–h vibrational stretching frequency in complexes of farh and acetylene," *The Journal of chemical physics*, vol. 122, no. 20, p. 204309, (2005).

[55] S. Tsuzuki and A. Fujii, "Nature and physical origin of ch/π interaction: significant difference from conventional hydrogen bonds," *Physical Chemistry Chemical Physics*, vol. 10, no. 19, pp. 2584–2594, (2008).

[56] R. JIONG, "A theoretical study of ch... x (x= o, n, s, p and pi) interactions," (2007).

Chapter 2

Experimental Methods

In this thesis, temperature-dependent Raman spectroscopy and SERS have been used extensively to study perovskite materials, ZIFs, and dendronic Raman markers. Moreover, organic as well as solvothermal synthesis was carried followed by necessary characterisations. In this chapter, the instrumental setups, synthesis methods and characterisation tools will be discussed.

2.1 Raman spectrometer

All the Raman spectroscopic or SERS studies discussed in the thesis were carried on a LabRam HR Evolution spectrometer shown in Figure 2.1. Excitation lasers of λ = 633 nm with source powers of 17 mW were used focused through a 50 X objective lens (N.A. = 0.5) onto the sample such that, it experiences a power of $\sim$ 5 mW. The LabRam setup contains edge filters with steep cut-offs. As a result, Raman spectra were obtained starting from 50 cm^{-1}. Before the experiment commences, calibration was carried out using the auto-calibration mode on a Si sample used as the reference.

Figure 2.2 represents the optical path the laser light follows from its source to the detector. The laser light enters the main optical path after passing through a max-line filter (to remove any laser glows or other unnecessary wavelengths of light) and passes through an opening (S1) to a neutral density (ND) filter (F2). At F2, a specific ND filter helps to control the laser power that is being incident on the sample, which can be changed

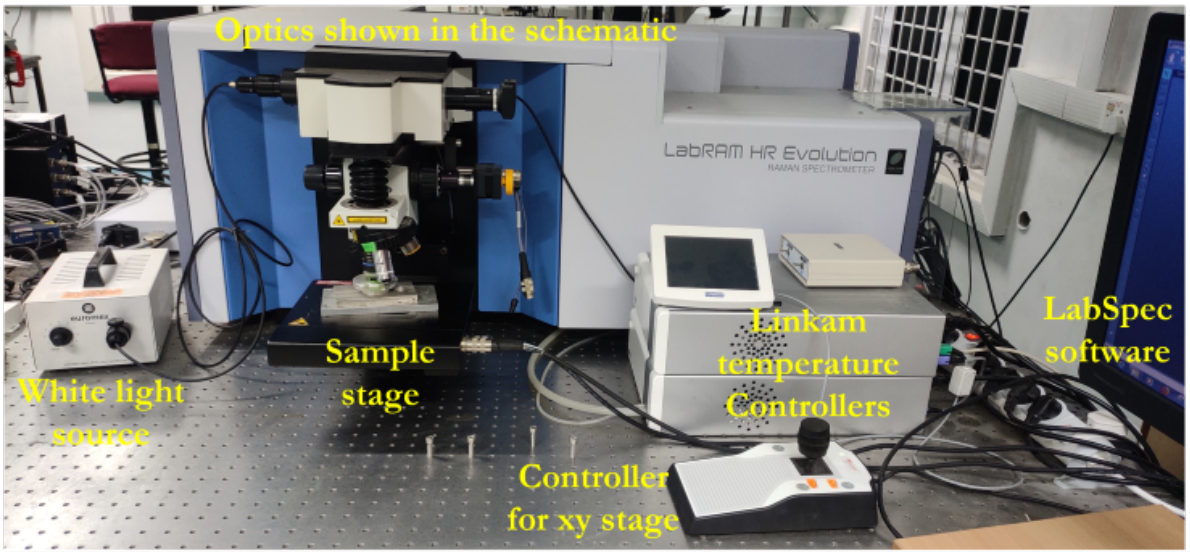

Figure 2.1: LabRam HR Evolution Raman spectrometer

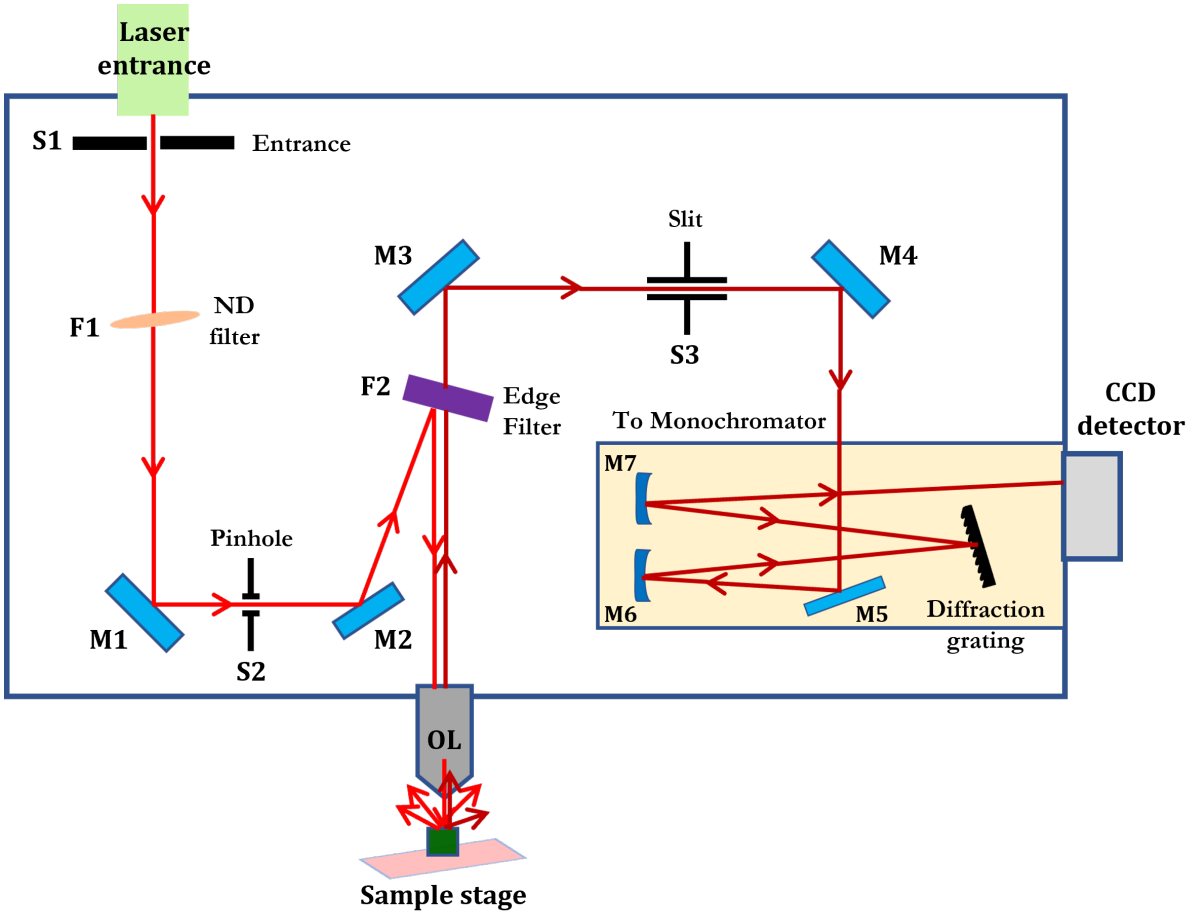

Figure 2.2: Schematic representation of the optical path inside the LabRam HR Evolution

using the software. Further, this light falls onto a mirror, M2 and reflects onto another mirror, M3 via a pinhole (S2). The placement of M3 is such that the reflected beam falls on the edge filter (F3) at a specific angle. The F3 reflects the light into the microscope because the edge filter is designed to reflect the light below a cut-off wavelength. Inside the microscope, the light reflects through a series of mirrors, which is finally focused onto the sample using an objective. The sample is placed on a motorised XYZ stage which is brought in focus of the light through the objective using the joystick shown in the Figure 2.1. A white light source connected to the setup with a camera attachment facilitates viewing of the optical image of the sample on the computer. The motorised XYZ stage together with camera attachment helps to not only focus the sample properly but also choose various sample spots in a large area for better experimental control. For example, in this thesis, temperature-dependent studies (298 - 77 K) were possible at about 20 spots at each temperature.

F3 reflects all Rayleigh scattered light while transmitting Stokes Raman scattered rays (wavelength higher than the cut-off). These scattered rays flow through the slit (S3) after being reflected by a mirror, M4. On reflection from the M5 mirror, this beam enters the monochromator. The incident scattered light reflects from the mirror, M6 and is incident onto a convex mirror, M7 inside the monochromator. The diffraction grating now receives the reflected light. In this spectrometer, you can choose between 600, 1200, or 1800 grooves/mm diffraction gratings. Depending on the wavelengths, the scattered light is dispersed into distinct beams at different angles. A convex mirror, M8 collimates all diffracted light onto a CCD detector. The incident photons are converted into a readable Raman spectrum by the air-cooled CCD detector.

2.2 Temperature-dependent measurements

A significant part of this thesis discusses temperature-dependent measurements, which are mainly carried under N_2 atmosphere discussed in chapter 3 and chapter 4. However, a small part of chapter 4A also discusses temperature-dependent studies performed under vacuum. Both the measurement methods are discussed subsequently.

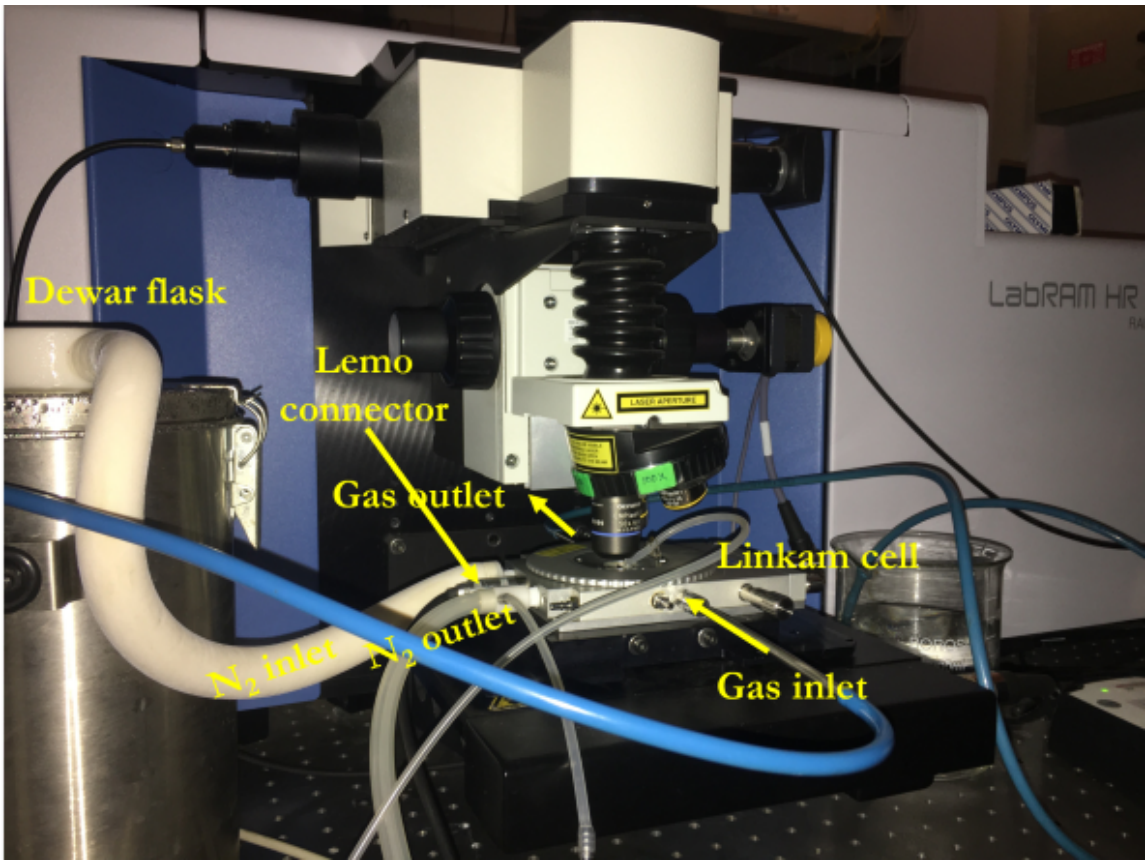

Figure 2.3: Linkam setup employed for temperature-dependent Raman studies under gas conditions

2.2.1 Measurements performed on Linkam THMS heating and freezing stage system

The temperature-dependent Raman measurements under inert (or gas) atmosphere were performed in a Linkam THMS600 system. The system is equipped with a THMS600 stage, T95 ThinkPad system controller, and LN95 liquid nitrogen cooling pump shown in Figure 2.1. The stage is mounted onto the labRamHR using a double-sided adhesive tape to keep the linkam stage anchored during the experiments. A temperature sweep can be performed from -196 °C (with LN95) up to 600 °C with a least scale value of 0.1 °C at variable ramp rate. Although the highest ramp rate of 150 °C per minute can be achieved, for all the presented work it was always kept between 5-10 °C per minute. This ensured both lesser equilibration time after reaching the desired temperature and avoiding large movement of the spot under consideration. Additionally, below 0 °C, condensation of moisture occurs on the viewing window because of the temperature gradient between

outside and inside the cell. To prevent this, recycled hot nitrogen is blown on the surface connected to the N_2 outlet shown in Figure 2.3

The linkam cell (THMS600 stage) can be connected to the gas line using two quick-fit ports shown in Figure 2.3, serving as a gas inlet and outlet for purging gases inside the cell. This setup proves itself useful in looking at various gases, namely N_2, Ar, and CO_2 and not just N_2 in the cases of ZIFs systems.

2.2.2 Measurements performed on cryostat s50

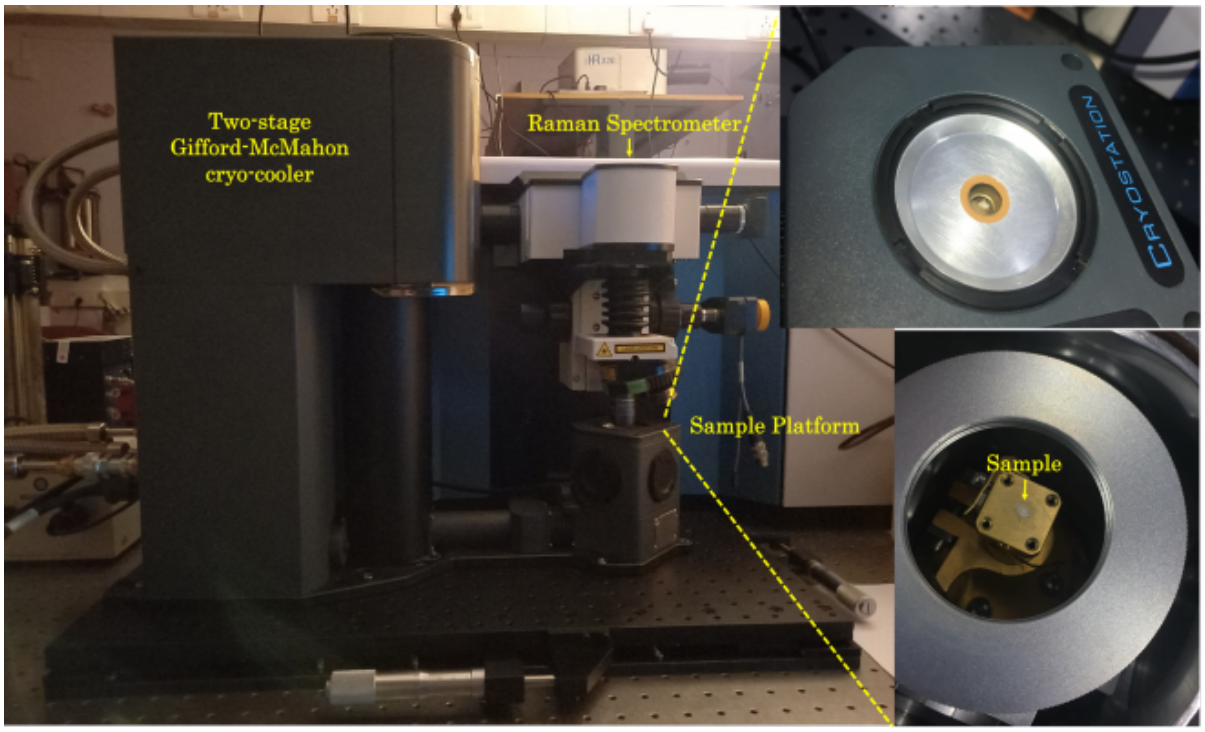

Figure 2.4: Cryostation s50 employed for temperature-dependent Raman studies under vacuum

The temperature-dependent Raman measurements under vacuum were performed in a cryostation s50 system. It comprises the compressor, a control unit, a cryostat and sample chamber, and a laptop with a user interface computer. Using this setup, temperatures up to 3 K can be achieved from 298 K under a high vacuum.

In the cryostat, a two-stage Gifford-McMahon cryocooler is located which provides the main cooling shown in the Figure 2.4. This cryo-cooler is connected to a separate variable-flow He compressor, together with maintaining a closed-loop flow of He. There

are two principal stages in the cryo-cooler, with separate thermometers to monitor temperature and heaters to warm up. The two stages are connected to different regions of the sample chamber. The sample chamber consists of a platform to mount the sample, the configurable sample holder, a radiation shield surrounding it, and the outer window assembly keeping the system completely isolated as shown in the Figure 2.5. Stage 1 is thermally coupled to the radiation shield which is mounted around the inner sample chamber and stage 2 with the platform. Before cooling commences, a vacuum pump inside the control unit evacuates the air from the sample chamber up to 2 mTorr. High vacuum is achieved with cryopumping charcoal adsorbers, which removes any vapour in the vacuum space. Finally, the thermometers attached to each component, platform, stage, and sample holder ensures the desired temperatures which are monitored by the control unit.

The sample mount comprises the damper and sample mount holder. The damper ensures reduced vibrations. The sample mount has been mounted vertically for our studies. Once the sample mount and sample thermometer is placed onto the sample chamber, the sample was mounted on the stage using a double-sided low-T adhesive tape. Then the radiation shield is placed over it followed by its lid which is finally isolated using vacuum housing and lid. The height of the sample mount holder was adjusted such that once the sample is placed, it does not touch the outer housing.

2.3 Organic Synthesis

An essential part of this thesis also deals with synthesizing new organic compounds for SERS applications. Now, during the synthesis of these materials, many of the organic compounds, reactants, as well as final products used are sensitive towards moisture and/or oxygen and pyrophoric in nature. Hence, there is a need to isolate these air-sensitive compounds from the atmosphere and be handled in a controlled environment, typically in an atmosphere of nitrogen or argon.

Common vacuum/inert gas manifold systems used in an organic laboratory are called Schlenk lines. It is a dual manifold as shown in Figure 2.6 , with a gas line and a vacuum line. The gas line is connected to a direct gas inlet which goes through a column and can

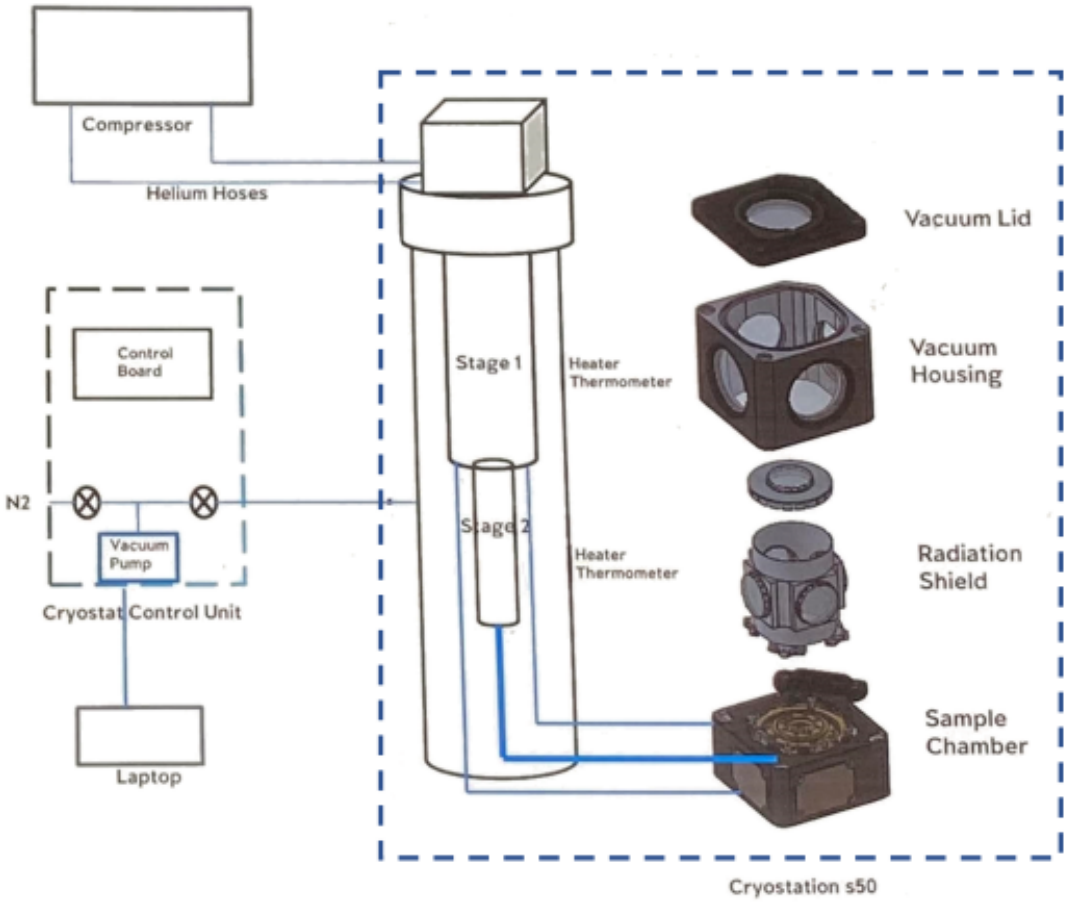

Figure 2.5: Schematic of the block diagram for the cryostation assembly with the focus on mainly the cryostat. The detached mounting assembly is required along with the sample mount. This diagram was obtained from the cryostation s50 user manual provided by Montana instruments.

be controlled at specific ports as labelled in the Figure 2.6. The gas outlet is connected to an oil bubbler (the bubbling speed of the gas also helps regulate the flow of the gas in these ports. The other column is for the vacuum line, where it is connected with a solvent trap (for collecting released solvents during evacuation) dipped in a Dewar flask to condense evaporated solvents and a vacuum pump. This manifold can be easily incorporated with glassware with quick-fits and connectors attached to the tubing through the ports.

As much as carrying the synthesis of new materials in a controlled environment is important, it is more important to use pure starting materials from solvents to chemical substances. Typically in a chemistry lab, one can find solvents such as methanol, acetonitrile, dichloromethane and others used in reactions or for purification. The most

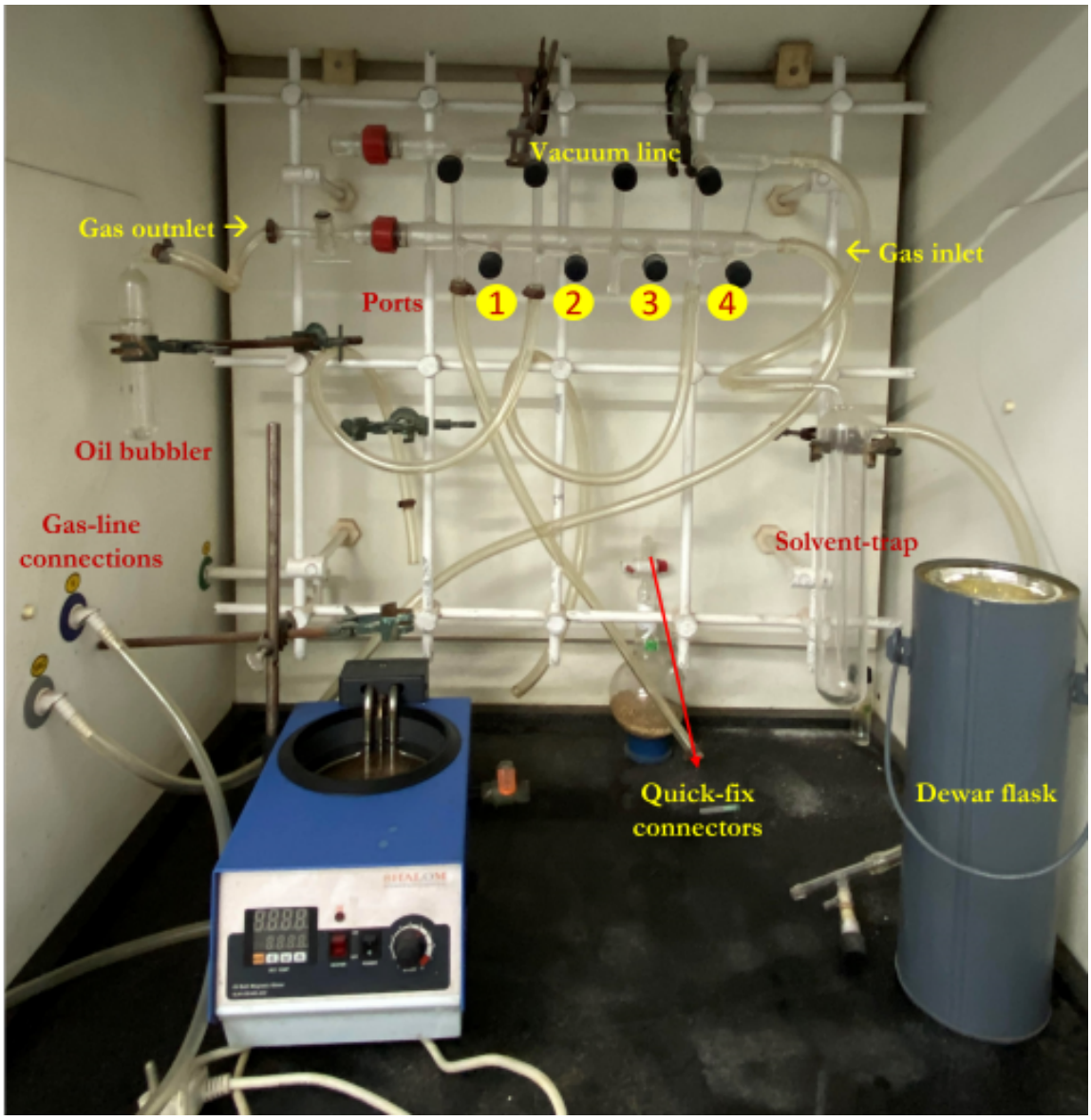

Figure 2.6: Photograph of the Schlenk line setup used labelling the components of the manifold

common impurity is water in them. Similarly, chemical substances obtained from industries contain impurities like unreacted starting materials, intermediates, by-products, isomers and related compounds. Purity is a matter of degree and is relative in a sense. During any synthesis, the question should be whether the substance is pure enough for the intended purpose. The most common purification methods include distillation (including fractional distillation in the standard atmosphere or reduced pressure, steam distillation), crystallization, and other methods. To remove moisture from common solvents, storing them in activated molecular sieves is a common practice which is also rejuvenated regularly. In chapter 5, almost all solvents used were distilled (using the book of "Purification

of Laboratory Chemicals") and the main starting material of Bis-MPA was purified by azeotropic distillation using dean stark apparatus.

Another important aspect during synthesis is to monitor the progress of the reaction and isolation of the pure product. Here, is where chromatography has played a significant role in the daily life of an organic chemist. It is widely used in purifying small amounts of organic mixtures. Chromatography is based on the differential distribution of various components (on the basis of polarity and mass) in a mixture between the mobile phase and the stationary phase. The primary rule is to determine the nature of the mobile phase required for the separation. A common technique used in this thesis is thin-layer chromatography (TLC) where the mobile phase travels up to the stationary phase (the adsorbent) shown in Figure 2.7. Silica is used as the adsorbent on an aluminium sheet. The reaction mixture is spotted, dipped in a solvent or mixture of solvents, and allowed to move through the plate. Later, the plate is visualized by dipping it in a reagent (here $KMnO_4$ solution) that results in coloured products upon heating. (shown in Figure 2.7b) The course of the reaction can be monitored using TLC as shown in Figure 2.7c, where the intensity of the product increases or the disappearance of other starting materials/by-products with time is observed. It is important to set these TLC parameters during the course of the reaction to establish conditions for column chromatography for isolation of the product of the reaction.

In this work, the flash column chromatography used was packed using a dry method (Silica gel of mesh size 230–400) and the substance was placed on top of the column. The solvent was run down it, the fractions were collected, and monitored using the TLC silica gel 60 F_{254}. (shown in Figure 2.7a) After the completion of the column, the fractions containing products of a similar source were combined (like fractions shown in 2.7c), the solvent evaporated using a rotary evaporator and dried under vacuum. ^{1}H Nuclear magnetic resonance (NMR) for all the products is carried and once the final products are achieved, characterisation is completed by recording and analysing ^{13}C NMR and high-resolution mass spectroscopy (HRMS) also. ^{1}H and ^{13}C NMRs was recorded on a Fourier transform NMR spectrometer (400 MHz for ^{1}HNMR and 125 MHz for ^{1}3CNMR). Mass spectrometry was carried out using the Q-TOF instrument for HRMS. The final products obtained were further used for SERS studies.

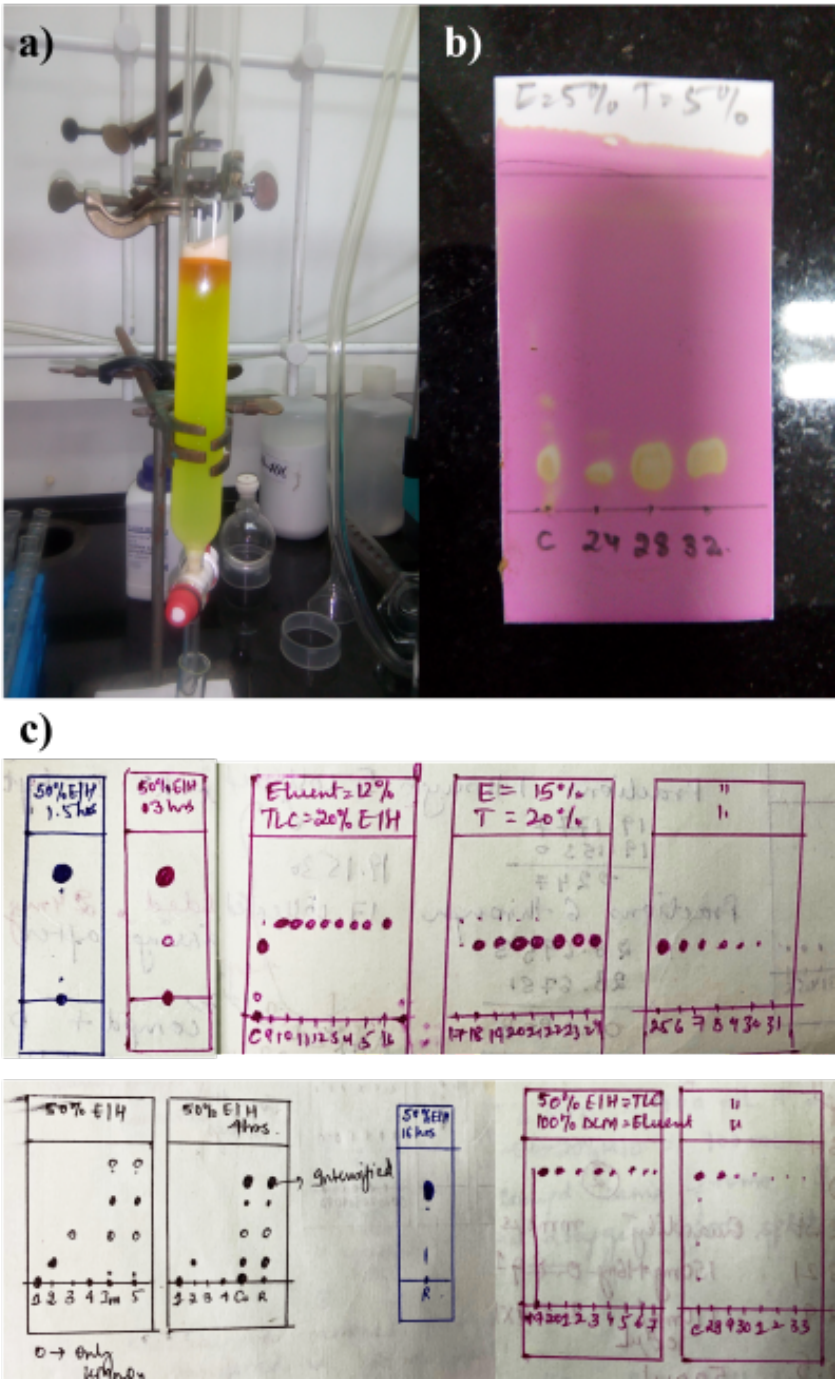

Figure 2.7: Photographs of chromatography at various stages in an organic synthesis a) Flash column chromatography showing the elution of one of the components of a mixture. b) A TLC plate right after visualization using $KMnO_4$ solution. c) Handwritten notes of the obtained TLC monitoring the course of the reaction and obtained during/after flash column chromatography from the fractions. Please note that all the snapshots are independent of each other and do not belong to the same reaction but give an idea about the process being discussed in this section.

Chapter 3

Perovskite Nanocrystals*

3.1 Introduction

Perovskite is a class of materials that has a chemical formula ABX_3, where the letter A denotes the inorganic or organic cation, B stands for a divalent metal cation, and X stands for halide anion as shown in Figure 3.1. The three-dimensional structural motif of ideal cubic perovskite can be viewed as a cube with the B-cation is at the centre of the cube, surrounded by six X ions arranged in an octahedral geometry at the cube's face centres, while the A-cation is at the cube's corners. The electrostatic interaction between the A-site cations and the anionic B-X framework stabilises the structure of perovskite. One of the key factors that affect the physical properties of a perovskite material is the distortion in its structure, which can be caused by a variety of factors, such as a size mismatch between the A and B cations, doping in the halide site, or electronic effects like Jahn-Teller distortion. Such internal stress lead to a cooperative rotation of the BX_6 octahedra and a concomitant change of the A-cation position, resulting in the formation of lower symmetry structures in orthorhombic, tetragonal, rhombohedral, and monoclinic phases.

This work was carried in collaboration with Quantum Dot lab and Advanced Quantum Theory lab, JNCASR. The samples were obtained from **Dr. Pradeep KR, who carried the XRD and PL characterisations. First principle DFT calculations were carried by **Ms. Madhulika** The results obtained are used in this thesis only for complete understanding of the work.*

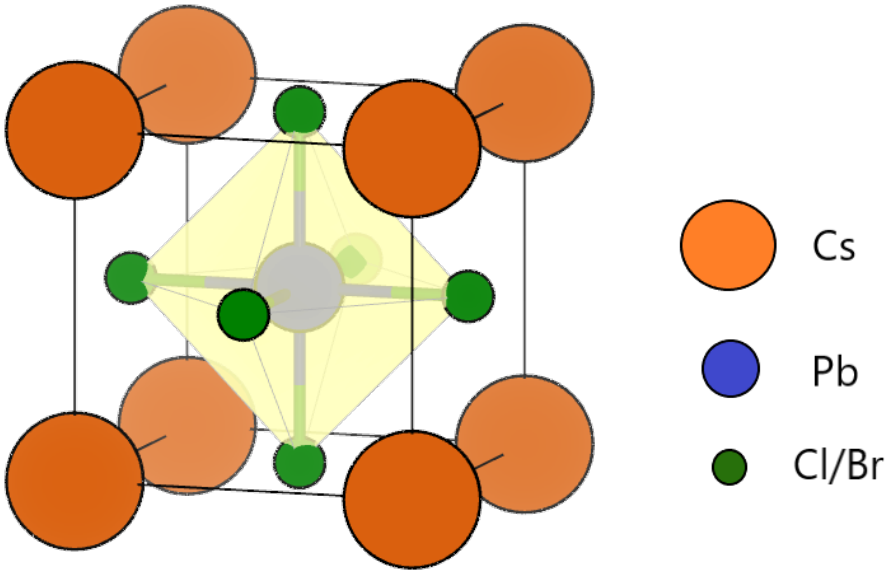

Figure 3.1: Perovskite structure of $CsPbX_3$ (where X = Cl/Br) with cubic symmetry

Colloidally synthesized cesium lead halides ($CsPbX_3$, where X = Cl, Br, I) nanocrystals (NCs) are promising candidates for light emitting applications. The solution processability and cost effectiveness of these NCs has brought enormous attention among the scientific community. Moreover, these materials possess extremely high photoluminescence and sharp absorption edges. The wide tunability of these perovskite NCs over the entire visible range can be accomplished using variation in halide compositions [1]. Owing to their extraordinary electronic and optical properties, great deal of work is being carried in thin-films for for optoelectronic [2, 3] and photovoltaic applications [4, 5]. However, like any other material, there are shortcomings related to it, which limits the use of them. A few examples are such as, light-induced phase segregation affecting the stability of these NCs under ambient conditions, [6] and inability to maintain an optically active cubic phase [1]. Hence, there has been an overwhelming need to study the structure-property correlations in order to fully exploit the scope of these materials.

Although there are various aspects to look at, in the next two parts of this chapter we will be mainly focusing on two aspects which will be introduced briefly with their sections. In Chapter 3A, the question being addressed is, if the mixed halide perovskites form alloys/solid-solution or are phase segregated? In Chapter 3B, the focus of the work revolves around the polaronic origin of a new Raman mode appearing below ambient conditions.

$CsPbX_3$ (X=Cl,Br)	Composition of Br
P1	0.0
P2	24.7
P3	51.4
P4	72.1
P5	86
P6	100

Table 3.1: Compositions of NCs from P1 to P6

3.2 Experimental section

All Raman measurements were carried out on LabRam HR Evolution, Horiba using a He-Ne laser of 633 nm excitation wavelength and a grating of 1800 grooves/mm. The laser power was 5-6 mW at the sample, when focused using a 50X objective lens (NA = 0.5). Accumulation time for each spectrum recorded was 120 s. Samples were mounted on the linkam stage and heated up to 313 K. The chamber was purged for a few minutes with nitrogen gas using the linkam (LNP95) pump and brought back to room temperature.

For the Raman studies, samples were prepared from P1 to P6, with P1 being $CsPbCl_3$, P6= $CsPbBr_3$, P2, P3 and P4 are mixed halide NCs with increasing Br concentration. The compositions of all the NCs are listed in Table 3.1. 1 mL of the sample was dispersed in hexanes, centrifuged with an equal volume of methyl acetate for 3 minutes at 10000 rpm. The residue was dissolved in minimum volume (about 100 μL) of hexanes, dropped gradually in 2 μL drops, and dried on a silicon substrate. The dried spot was used for temperature-dependent experiments. For each sample, at least ten different x, y coordinates were measured on the dried spot at each temperature. Raman Spectra were normalized by carrying out an area normalization for the region 50-400 cm^{-1}.

Chapter 3A

Are the Mixed Halide Perovskite NCs ($CsPbX_3$ (X = Cl, Br)) Structurally Homogeneous?†

Summary

The present chapter revealed clear Raman spectral changes in the peak shifts and shapes obtained from $CsPbX_3$ NCs of various compositions. The mixed halide systems were found to be homogeneously alloyed from the photoluminescence, X-ray diffraction, and Raman spectroscopy. The systematic red-shift of the LO_2 mode of the NCs with changing composition was an excellent marker for the formation of a solid solution. The analysis of the TO_2 mode revealed the presence of Cl-rich octahedra and Br-rich octahedra in P2 (25 % Br) and P5 (86 % Br) NCs respectively. The presence of more than one type of octahedra was suggested in more mixed compositions suggesting a formation of more than one solid solutions. Raman spectroscopy was used as a vital tool in revealing various aspects of local structural homogeneity in the $CsPbX_3$ NCs.

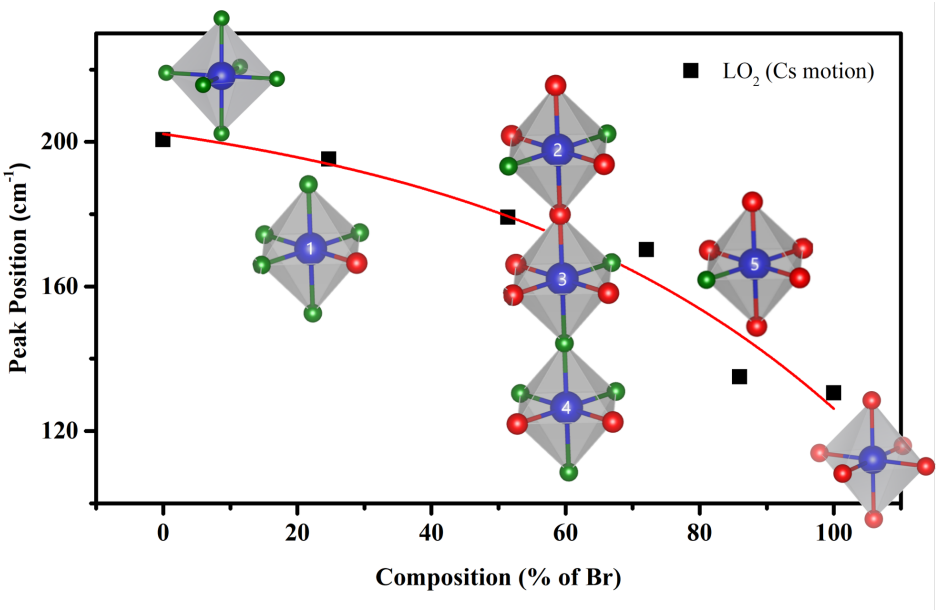

†*Manuscript under preparation*

3.3 Motivation for the work

The building blocks of the perovskites NCs include the octahedra, and the nature of the octahedra in the mixed halide systems. The studies on it helps to answer the questions in phase segregation such as identifying the channels facilitating ion migration and dynamics of phase segregation in the lead halide octahedra. This differentiates between alloys (more than one solid solution) and solid solution with several possibilities in the octahedra for individual halide compositions.

Diffraction based methods, mainly X-ray diffraction is the primary tool for structural characterisation and understanding for most of the mixed halide hybrid perovskite till date [7]. However, the use is limited to providing a global picture but not a microscopic/atomic one. Rosales et al. recently used solid state nuclear magnetic resonance (NMR) spectroscopy to explore the phase segregation and alloying nature of organolead mixed halide perovskite, however the microstructure and extent of alloying in the mixed halides are still unclear [8]. Using one and two-dimensional NMR spectroscopy, Karmakar et al. detected seven different Pb octahedral environments in Br/Cl mixed halide perovskites [9]. Solid state NMR spectroscopy is an exceptional tool for probing the local chemical environment of NMR active nuclei, but it cannot provide detailed local structural information around the atoms, such as lead-halide bond distances and octahedral arrangements. In this regard, there is a recent Raman study that investigated temperature evolution of $CsPbCl_3$, $CsPbBr_3$, and $CsPbI_3$ NCs which revealed important results on structural and thermal decomposition of the materials locally [10] In another study, the complete degradation of $CH_3NH_3PbI_3$ to PbI_2 under laser illumination was explained owing to the excellent lateral resolution and sensitivity of the technique [11].

With this motivation, Raman spectroscopy is used as the primary tool to understand the structural homogeneity and the nature of the octahedra in the mixed halide systems. Taking advantage of the lattice dynamics being coupled and perturbed by any local/global changes in the perovskite NCs, a Raman study will be of great advantage in the present research.

3.4 Results and Discussions

3.4.1 Synthesis and characterisation of $CsPbX_3$ NCs

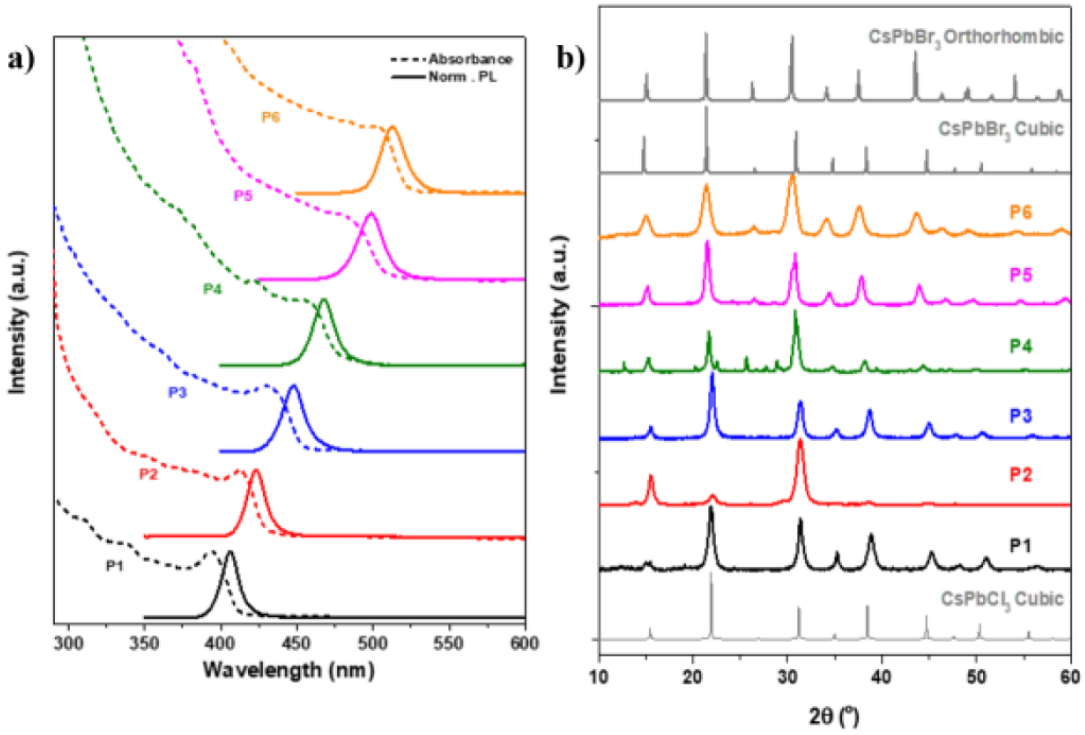

Figure 3.2: Characterisation of $CsPbX_3$ NCs from P1 to P6 displaying a) Absorption and PL emission spectra b) XRD patterns of the synthesized NCs along with the reported bulk structures of $CsPbCl_3$ and $CsPbBr_3$

A series of pure and mixed halide perovskite NCs (P1-P6) following the hot injection method was synthesized by starting with stoichiometric mixture lead halide salts using method described in ref. [12]. Figure 3.2a displays the photoluminescence spectra of the perovskite NCs over various compositions. Pristine $CsPbCl_3$ (P1) NCs emit near UV-blue PL (λ = 404 nm) whereas pristine $CsPbBr_3$ (P6) emits bright green PL (λ = 512 nm). PL emission of the mixed halide perovskites (P2 to P5) ranges between 404 to 512 nm. This periodic shifting of the mixed halide perovskites from P1 towards P6 suggests systematic Br incorporation in the nanocrystals.

These results echoed with the crystal structure, where powder XRD measurements were performed at 298 K of the drop casted films of samples P1 to P6. As shown in Figure 3.2b, the XRD pattern for the P1 NCs matches with the cubic $CsPbCl_3$ bulk

structure and the P6 NCs matched better with the reported structure of $CsPbBr_3$ in the orthorhombic symmetry than the cubic one. The XRD patterns for the $CsPb(Cl/Br)_3$ (P2-P5) displays a periodic shift in the peaks due to a change of halide composition. These results corroborate a formation of an alloyed structure, especially with the absence of a mixture of peaks originating from the individual $CsPbCl_3$ and $CsPbBr_3$ structures in the samples from P2 to P5. Additionally, a linear behaviour of the peak positions in the XRD patterns was also observed for these NCs, strongly inclining towards a solid solution behaviour. One of the reasons for successful alloying is the smaller lattice mismatch between cubic $CsPbCl_3$ and orthorhombic $CsPbBr_3$ (4.5 %) that does not lead to phase-segregation [8]. While detailed analysis on the XRD provided information on the crystal structure of mixed halide perovskites, XRD techniques are limited to the macroscopic scale. Local structural changes arising from intrinsic or extrinsic perturbations in the systems cannot be understood by a global technique such as XRD or PL. Hence, the focus of the next section will be on Raman spectroscopy.

3.4.2 Raman Investigation on P1-P6 NCs

Raman spectroscopic studies were carried out on a drop-casted sample from 298 K to 77 K similar to XRD studies. The Raman spectra obtained at 298 K are stacked in Figure 3.3a. It is clearly observable that the spectra are broad and modes are degenerate primarily because of near-cubic symmetry (cubic in the case of $CsPbCl_3$ and orthorhombic in the case of $CsPbBr_3$ [13]) and nano-size of the samples. Additionally, thermal effects dominate at 298 K. The assignment of the modes become difficult at such temperatures, taking into account the thermal effects and added parameter of mixed halide compositions. The effect is clearly seen in Figure 3.3a, where the Raman spectra obtained especially for P3 and P4 NCs has a broad background type feature with no resolvable peaks. Therefore, no useful analysis of microscopic structure can be carried out. Keeping this in mind, the Raman data was analysed at 77 K, where thermal effects are reduced. Low-temperature XRD measurements were carried to confirm the absence of any phase transition between 298 to 77 K. Moreover, there are reported photoinduced effects of ion migrations that suppress in these LHPs at low temperatures [14]. Hence, analysis of the Raman spectra becomes easier and more reliable for understanding the microstructure of these NCs. A gradual

$CsPbX_3$ (X=Cl,Br)	Composition of Br	Mode Assignments		
		TO_2	TO_3	LO_2
P1	0.0	70, 87	108, 119	200
P2	24.7	68, 82	106, 117	195
P3	51.4	69, 82	111, 137	179
P4	72.1	67, 84	108, 138	170
P5	86	66	74, 79	135
P6	100	66	73, 80	130

Table 3.2: Compositions of NCs from P1 to P4 along with Band Assignments

shift of all the phonon modes was observed to a lower wavenumber ongoing from P1 to P6 NCs (Figure 3.3b). As the NCs are becoming Br-rich, it is intuitive to observe such a red-shift with increasing effective mass of Br resulting in lower bond energy. This observation resonates with the results obtained from PL emission as well. But for any further analysis, it is important to assign these normal modes of different NCs compositions.

3.4.2.1 Assignment of Modes for P1 to P6 NCs

For bulk $CsPbCl_3$, the $Pm\bar{3}m$ space group has $3T_{1u}$ active optical phonons [15, 16, 17]. Each of the T_{1u} comprises a TO mode and an LO mode. Each TO mode is doubly degenerate. Thus, for the O_h representation, a total of 9 modes are reported in this phase and completely resolvable at cryogenic temperatures. Now, from Raman and resonant Raman studies carried on $CsPbCl_3$, these vibrations have been associated with $PbCl_6$ octahedra or Cs^+ ion motion. The peaks corresponding to TO_1 (32, 35 cm^{-1}) and TO_2 (72, 90 cm^{-1}) are associated with the vibrations of $PbCl_6^-$ octahedra, whereas TO_3 (110, 121 cm^{-1}) and LO_2 ($\sim$200 cm^{-1}) being related to the motions of Cs^+ ions. The Raman data reported for bulk $CsPbCl_3$ matched well with the spectra obtained for P1 ($CsPbCl_3$) NCs. Since the O_h representation of one family of perovskites remains the same, we will expect the same number of modes and implications of the external modes in other compositions as well. Hence, all the normal modes were assigned along the lines of the reported bulk structure of $CsPbCl_3$ and listed in the Table 3.2 from the Figure 3.4. The

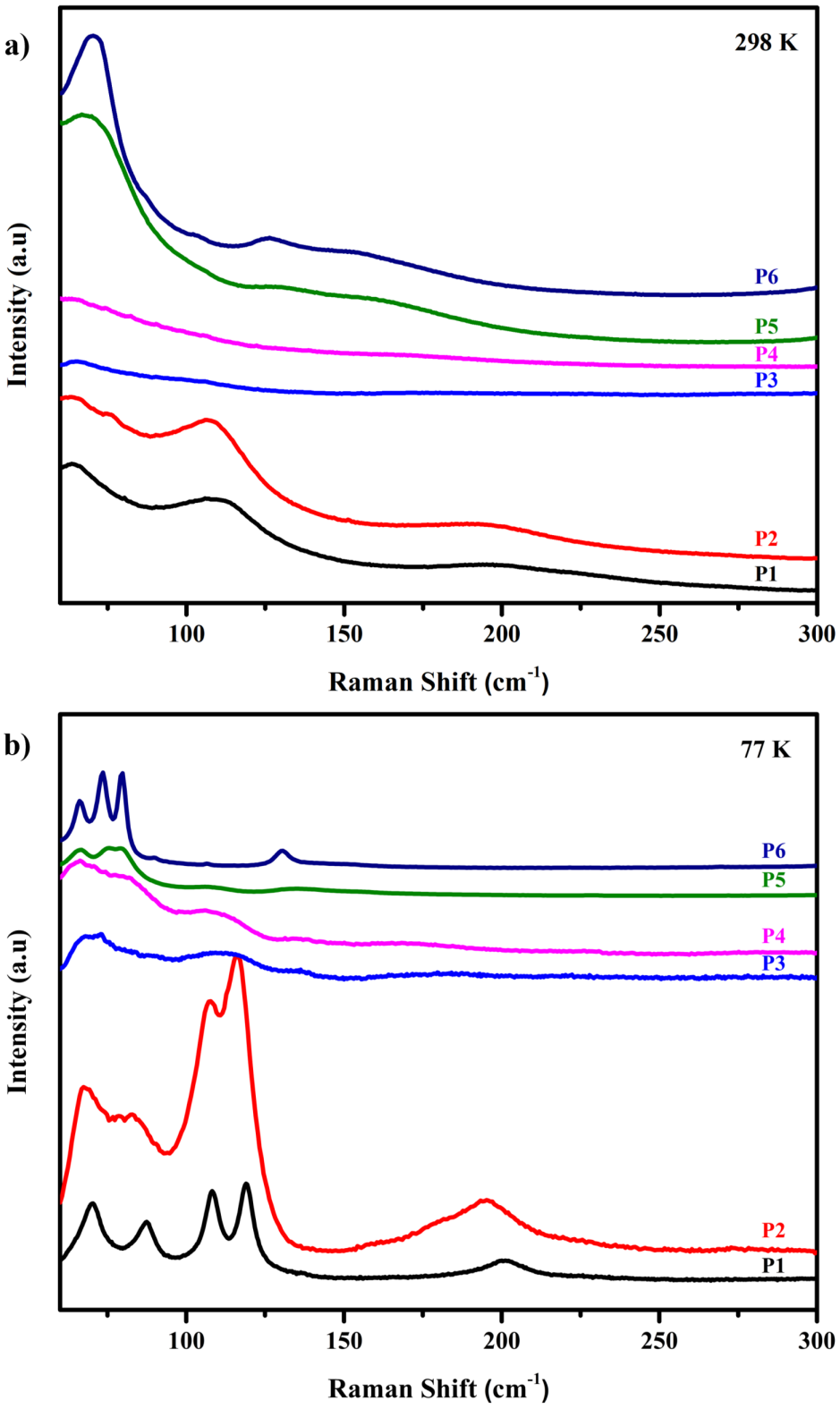

Figure 3.3: Raman spectra of $CsPbX_3$ NCs stacked for compositions P1 to P6 at a) 298 K and b) 77 K

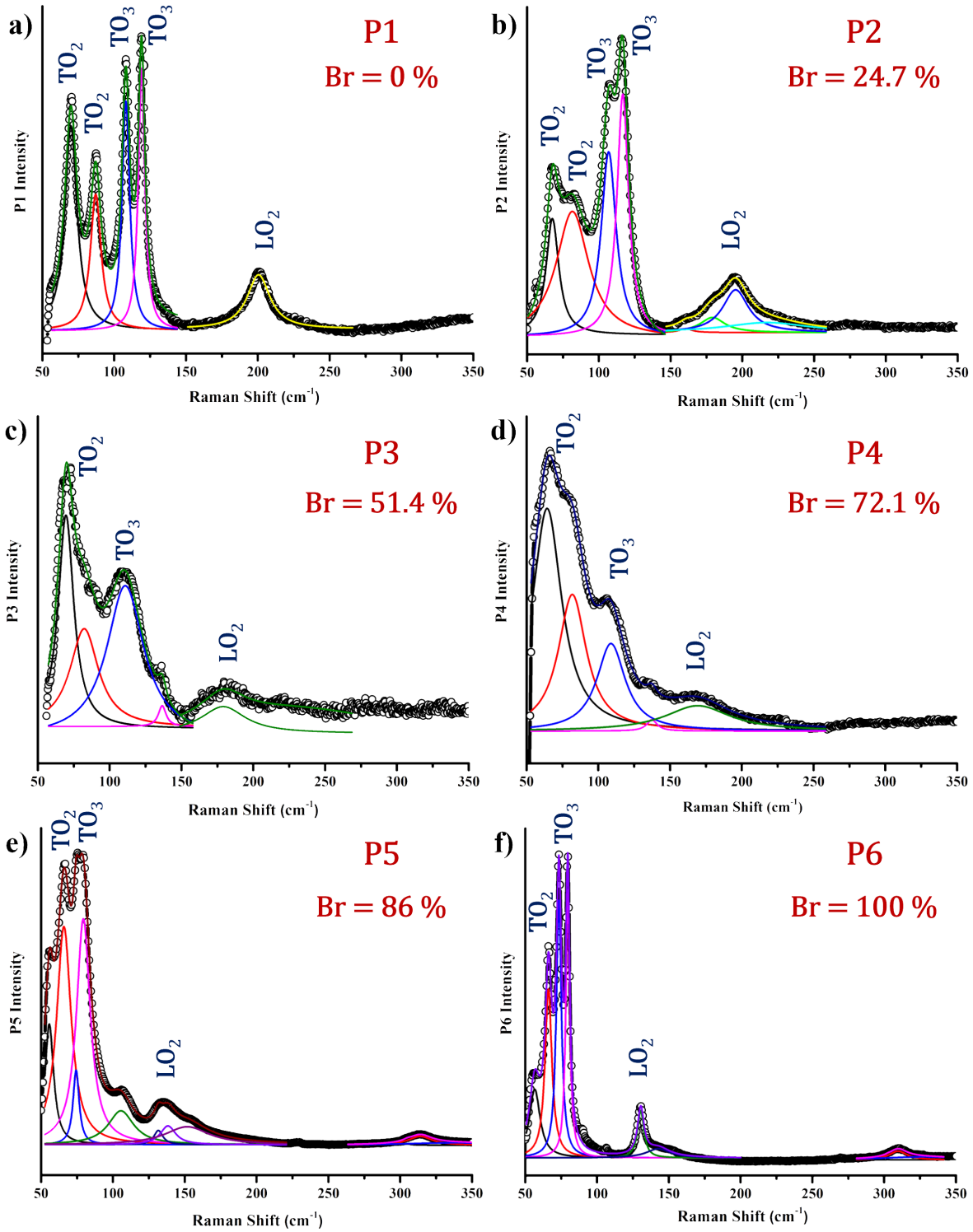

Figure 3.4: Raman spectra at 77 K for P1 to P6 NCs

TO_2 modes lie very close to the laser cut-off region used (50 cm^{-1}) thus suppressing the modes, especially in the case of $CsPbBr_3$. However, at cryogenic temperatures, these modes are expected to upshift due to the hardening of the mode. Although one of the two TO_2 modes is visible at 66 cm^{-1}, another one remains still suppressed due to the cut-off limit. It is noteworthy, that the LO_1 phonon may subsume in the intense TO_2 phonons in the spectrum [15]. The assignment of the normal Raman modes becomes crucial because of a new peak that appears below 273 K, which will be discussed in Chapter 3B. In the next section, we will be looking at how homogeneously alloyed are these nanocrystals which helps in understanding the local structural changes, ion migrations, and phase segregation in these LHPs.

3.4.2.2 Structural Homogeneity in P1-P6 NCs

The overall structural homogeneity of the NCs can be determined using the LO_2 mode, which belongs to the Cs^+ motion. The A-site in this group of perovskites under study does not vary, but the effect of changing octahedra composition will have a direct influence on the structure due to different octahedral tilt [18]. Figure 3.5 displays the peak positions shifts depending on the changing compositions. It is evident that the single $L0_2$ mode gradually shifts from 200 to 132 cm^{-1} upon moving from P1 to P6. This further confirms that these nanocrystals are alloyed to form solid solutions. In the case of any phase segregation or more than one phases in the system would have resulted in new peaks in addition to modes arising from parent NCs. However, LO_2 mode for a specific composition appeared in a defined region which is between P1 (200 cm^{-1}) and P6 (130 cm^{-1}) underscoring the formation of a solid solution.

3.4.2.3 Nature of Octahedra in P1-P6 NCs

By changing the anion composition, the local environment of the Pb atom is the most prone to get affected. Thus, the understanding of the Raman modes associated with the octahedra (TO_2 mode) will be of great importance to comment upon. However, in this case, all of the TO_2 modes in all compositions lie close to the cut-off region and thus have varying backgrounds. Hence, a cumulative fit of the spectra obtained at 77 K from P1

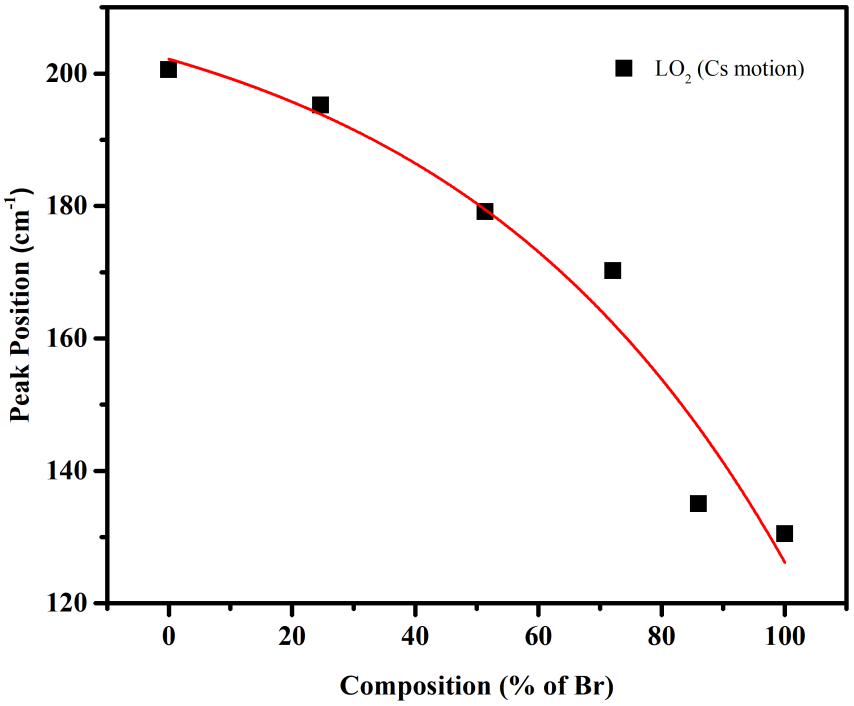

Figure 3.5: Raman peak position of the LO_2 mode for NCs of varying compositions

to P6 along with their respective curve fitting is shown in Figure 3.4. The nature of the octahedral mode (TO_2) in the mixed halide systems P2 to P5 show significant spectral differences. The spectral shape of TO_2 mode in P2 NCs (25 % Br) resembles closely to the modes of P1 NCs and the TO_2 mode in P5 NCs (86 % Br) resembles well with the modes of P6 NCs. Upon moving towards larger mixing of the anions, i.e. for P3 (50 % Br) and P4 (70 % Br) NCs, the TO_2 modes become degenerate and diffused and they do not resemble a $PbCl_6$ or $PbBr_6$ type octahedra. Also, the broadening of the mode in these cases is quite high, which may also suggest more than one solid solution.

To understand the result, the effect of doping in the system must be visualized. At lower levels of doping in the case of P2 and P5, the addition of Br or Cl will result in tensile or compressive stress respectively because of the size mismatch. However, in P2 (or P5) NCs the stress created will be small because of majority of Cl (or Br) anions in the NCs accompanied by a small lowering of energy (or increase in energy) observed in the mode. As a result, the nature of octahedra remains largely Cl-like (or Br-like) with only a few of the octahedra belonging to the minor component being Br-like (or

Cl-like). This effect is observed as the broadening in the modes as compared to the width observed in the pure counterparts and any new phase may have subsumed in the major component. However, the effect of doping becomes pronounced in higher concentration of mixing, i.e. for P3 and P4. In such a scenario, the tensile stress will start increasing in P3 and compressive stress will start increasing in P4. Because of high concentration of both the anions, the system will experience a differential stress overall resulting in a deconvulted peak observed in Figure 3.4c & d. Consequently, there will be lesser numbers of pure octahedra, and more mixing with two or three different anions shown in Figure 3.6. Recently, in $MAPb(Cl/Br)_3$, highly disordered local Pb environments were found to be related to altering bond lengths and angles around it [9]. This consequence is evident in P3 especially (P4 also to a large extent), where the peaks become highly broad and diffused even at 77 K, and thus requires a better resolution spectrometer or a much lower temperature than 77 K. This observation underpins the presence of pure $PbCl_6$ and $PbBr_6$ octahedra in the case of P2 and P5 NCs respectively in addition to possibilities 1 and 5 from Figure 3.6 respectively. However, possibilities 2, 3, and 4 will be prevalent in P3 and P4 resulting in more random doping. The extent of alloying cannot be predicted with this data but the presence of solid solutions is definite. It is noteworthy, that Figure 3.6 only represents most possibilities of randomly distributed halides about the Pb centre and not all of them.

3.5 Conclusion

The Raman spectra of the synthesized $CsPbX_3$ NCs of various compositions were assigned and discussed in detail. The mixed halide systems were found to be homogeneous and alloyed from the PL, XRD, and Raman Studies. The LO_2 mode of the NCs red-shifted systematically with changing composition due to increasing effective mass on going from P1 to P6 NCs. The presence of a single-mode suggested the formation of a solid solution. The TO_2 mode in P2 and P5 NCs were found to be Cl-rich and Br-rich respectively, resembling the octahedra close to their pure counterparts. However, broadened and diffused nature of the TO_2 mode in the case of P3 and P4 NCs suggested the formation of more than one type of octahedra, however, extent of alloying cannot be discussed.

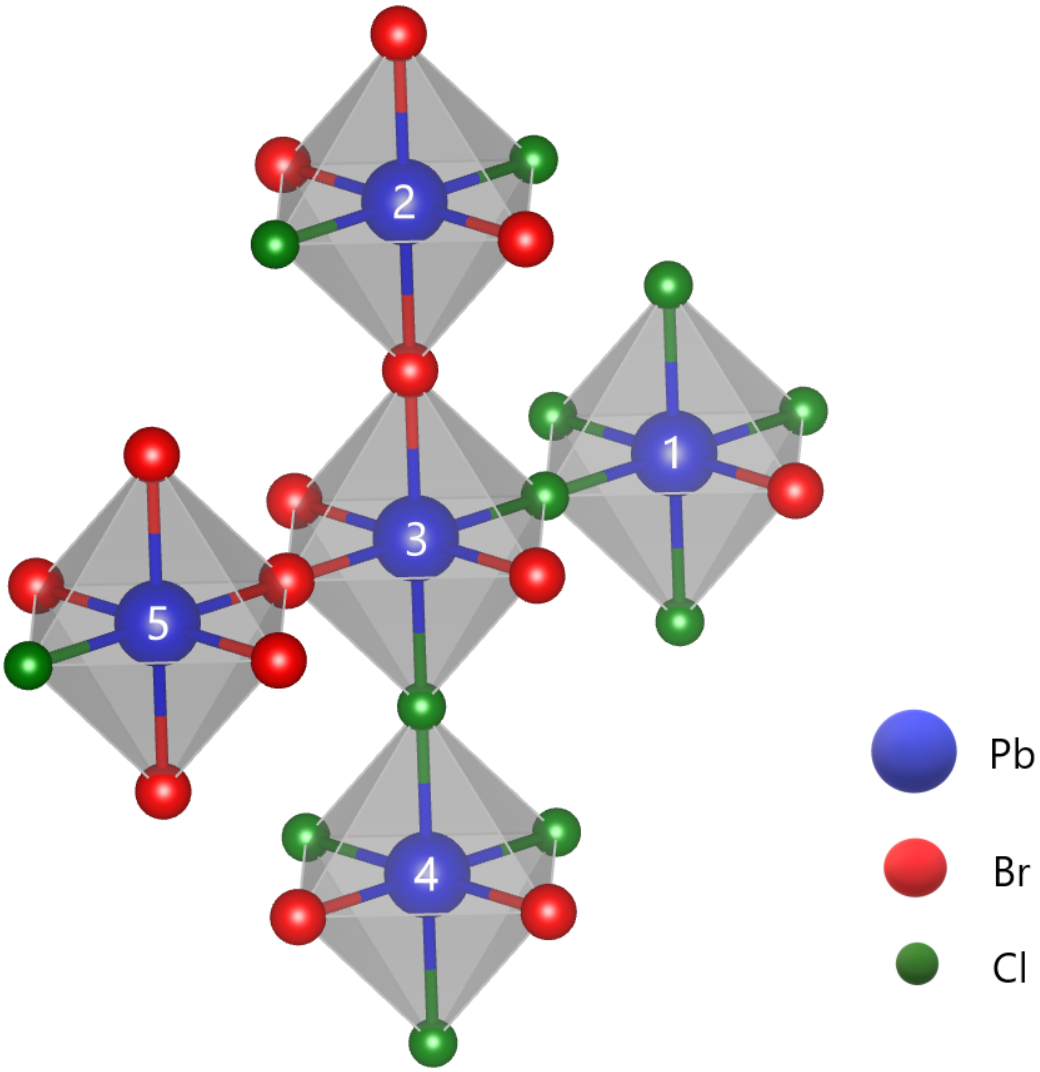

Figure 3.6: Possibilities of Pb environment in the mixed halide (Cl/Br) composition. Inspiration drawn from [9]

With this understanding of the structure from Raman spectra of these mixed NCs, we move to Chapter 3B where, an unusual mode will be discussed at 248 K.

Chapter 3B

Probing Polaronic Behaviour in Undoped and Mn-doped $CsPbX_3$ (X = Br, Cl) NCs through a Photoinduced Raman mode[‡]

Summary

The present chapter deals with understanding the structure modifications of the perovskite octahedral framework which largely affect associated distortions. Mn-doped and undoped $CsPbX_3$, were investigated via micro-Raman spectroscopy and density functional theory (DFT) Calculations for polaron formation. A new vibrational lattice mode at 132 cm^{-1} revealed the presence of polaronic distortion upon photoinduction. From the DFT studies, it was shown that the polaronic states were dominated by the B-site cation in the perovskite structure, but he strong covalent overlap of the halide was the one which determined its stability. This elucidation to map polaronic signatures with excellent spatial resolution using traditional Raman spectroscopy can be used as a simple tool to understand the structural changes, their impacted electronic properties and thus design superior devices using its in-situ applications.

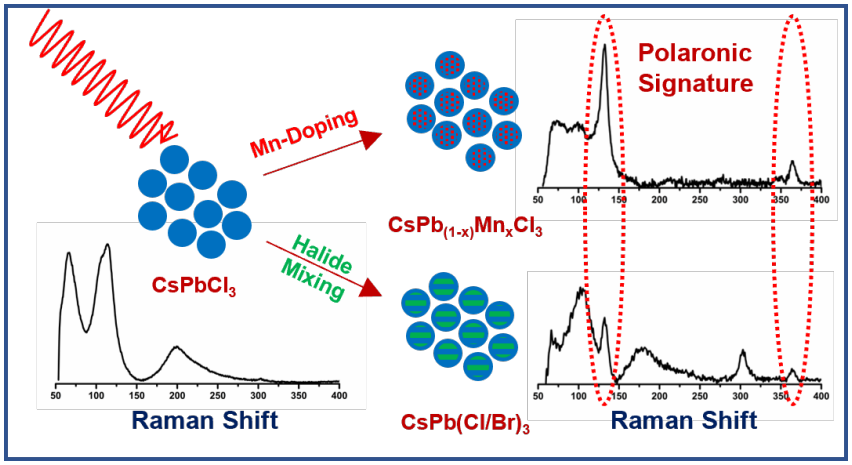

[‡]**Priyanka Jain**, Madhulika Mazumder, K. R. Pradeep, Ranjani Viswanatha, Swapan K. Pati, and Chandrabhas Narayana *ACS Applied Materials & Interfaces* 2022 **14** (4), 5567-5577 DOI: 10.1021/acsami.1c20321

3.6 Motivation for the work

Some of the most intriguing features of LHPs are their large carrier diffusion length and long carrier lifetimes making them excellent materials for photovoltaic applications. There are numerous hypotheses and studies that researchers are working on to understand why these properties exist in these materials and to design better systems to overcome their shortcomings like phase-segregation, thermal instability, non-radiative recombination, and so on. Some of the widely accepted and reported mechanisms include lattice distortions which could be intrinsic, coupled with charge carriers forming polarons, [19, 20, 21] local polar fluctuations [22] and Rashba effect [23, 24].

Polaron formation occurs when charge carriers are being protected by the surrounding lattice cloud which reduces the interaction of charge carriers and hence their recombination. This phenomenon allows the charge carrier to attain large carrier lifetimes with limited mobility due to an increase in effective mass [25]. Numerous ultrafast spectroscopic techniques have been implemented in especially hybrid organic-inorganic perovskites to probe charge carrier dynamics and structural fluctuations for polaron formation such as time-resolved terahertz spectroscopy (TRTS)[26], temperature dependent transient absorption (TA), and time-resolved photoluminescence (TRPL)[27, 28], time-domain Raman Spectroscopy[29], time-resolved optical and x-ray photo-absorption (TR-XAS)[30, 31], and time-resolved optical Kerr effect (TR-OKE) in combination with first principles and *ab-initio* calculations [32]. Recent mid-IR TA Spectroscopy underscored that charge-lattice interactions influence band-edge recombination and thus optical properties of Hybrid Organic-Inorganic Perovskites (HOIPs) [33]. Additionally, a quenching of photoluminescence quantum yield (PLQY) was observed. Consequently, the authors emphasize that structure modifications can hugely affect the electronic properties of halide perovskites. More recently, using TR-XAS, photo-induced spectral changes in Br K-edge and Pb L_3 edge of $CsPbBr_3$ resulting from polaron distortion dominated by asymmetric Pb-Br bond shortening have been discussed quantitatively [34]. The authors highlight the importance of local structural techniques in looking at the electronic and structural changes in LHPs. Consequently, there is a need to: 1) understand how structure modification of perovskite inorganic framework affects carrier lattice interactions that lead to polaron formation. 2) use more local probes for triggering structural distortions driving

polaron formation which directly influences electronic properties of the perovskites and hence, can be tuned for specific applications.

With this motivation, we use micro-Raman spectroscopy and DFT calculations to probe phonon behavior in Cs-based LHPs ($CsPbX_3$) and their Mn-doped counterparts which can be strongly influenced by charge-lattice interactions. Firstly, we display a new Raman mode at 132 cm^{-1} and a few second-order phonons in all these compositions because of photoinduction and discuss its origin. We argue from our observations, *ab-initio* calculations, and electronic structure calculations that the new mode is an implication of polaron formation in these systems. Secondly, we carefully examine the stability of the optical mode in question on various compositions of $CsPbX_3$ as described. Finally, we correlate the impact of the structural modifications on the stability of polaronic states in doped and undoped $CsPbX_3$.

3.7 Results and Discussions

Synthesis, purification, and characterisations of the NCs under study was discussed in Chapter 3A. In this chapter, some of those NCs along with Mn-doped counterparts of the same will be focussed as listed in Table 3.3 The Raman spectroscopic measurements were carried out with respect to temperature for P1, P2, P3, P6, MP1, MP2, and MP3 NCs on at least 10 different spots on the same sample (∼3 mm diameter).

$CsPbX_3$ (X=Cl,Br)	Composition of Br	Mode Assignments		
		TO_2	TO_3	LO_2
P1	0.0	70, 87	108, 119	200
P2	24.7	68, 82	106, 117	195
P3	51.4	69, 82	111, 137	179
P6	100	66	73, 80	130

Table 3.3: Compositions of NCs along with Band Assignments

In Chapter 3A, it was seen that upon going from P1 to P6 NCs, all the normal modes systematically red-shifted and were structurally homogeneous following the general trend

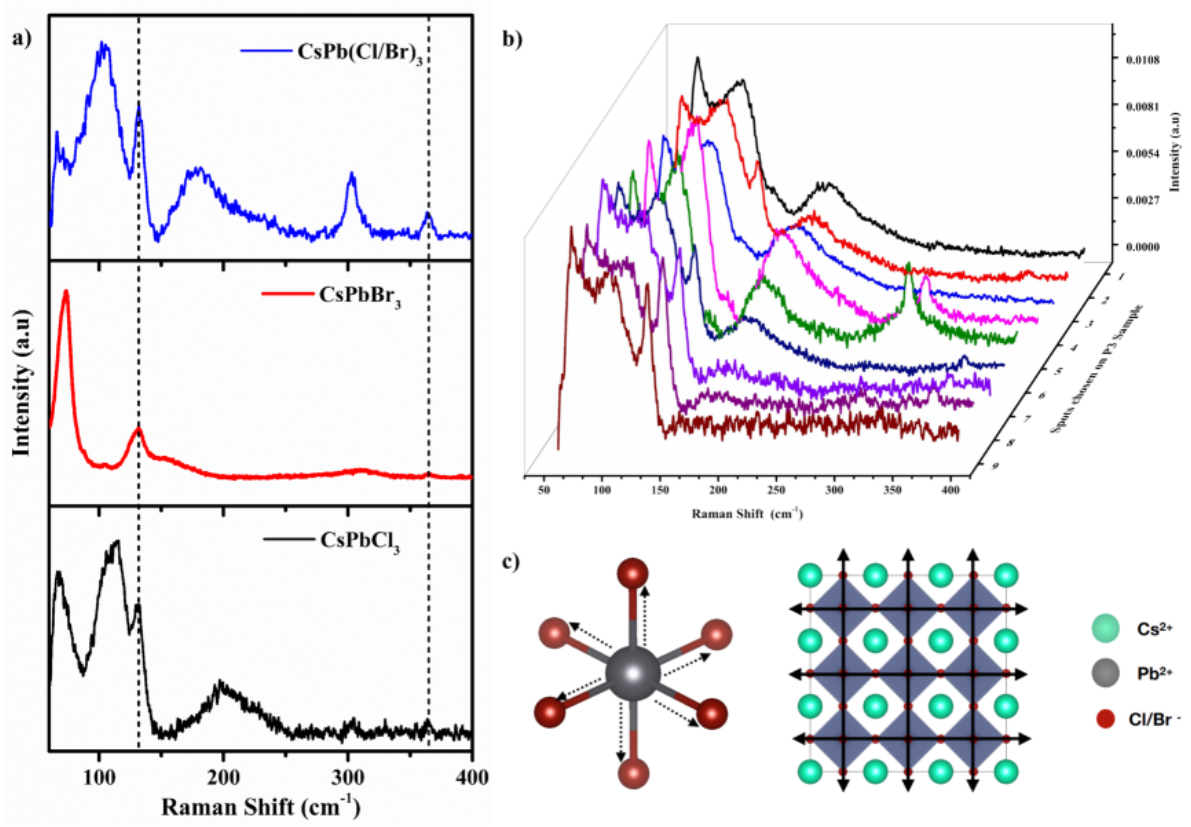

Figure 3.7: a) Raman spectra of $CsPbX_3$ NCs at 248 K for different compositions. Evidence of an unusual new mode irrespective of its halide composition. b) Raman spectra of P3 at 248 K recorded on multiple spots showing inhomogeneity in the intensity of the new mode at 132 cm^{-1}. c) Phonon vibration modes arising from Pb-X stretching in $CsPbX_3$

of alloyed compositions. However, additional peaks appear upon recording the spectra from 298 K through 77 K. A new mode at 132 cm^{-1} starts appearing below 273 K for chloride, bromide, and mixed $CsPbX_3$ NCs as shown in Figure 3.7a. To assign the 132 cm^{-1} peak as a normal Raman mode, it is possible to overlook it as the 126 cm^{-1} peak, corresponding to LO_2 mode in the case of $CsPbBr_3$. However, the peak is not the same as the LO_2 mode for the following reasons:

1) The **position of the peak does not shift** upon changing the composition of the system unlike what is expected from normal modes.

2) The peak was observed even in the case of pure $CsPbCl_3$ NCs and thus cannot solely be related to pure $CsPbBr_3$ spectra.

It is relevant to note that, in Figure 3.7a spectra shown are obtained from a single coordinate from the microscopic image of a drop-casted sample spot. However, during the experiment, Raman spectra have been recorded at multiple x, y coordinates in a single dried spot as shown in Figure 3.7b. These are weakly scattering systems because of their nano-sizes and near cubic geometry. As a result, the data can be noisy, and because all the intense modes lie close to the cut-off region, there is a possibility of obtained backgrounds being different. Thus, all the obtained spectra were area normalized, as can be seen from Figure 3.7b, the normalized intensity of all spots look fairly similar. Also with area normalization, we believe that each spot has roughly the same number of NCs being illuminated under the laser probe irrespective of the thickness on the spot. The intensity and appearance of the new 132 cm^{-1} peak vary with changing coordinates and is thus argued to be a local effect. A localized effect is not surprising considering the laser spot size of only $\sim$ 2 μm with high power density. Throughout this work henceforth, we would be looking at the Raman spectra obtained at 248 K because at this temperature in almost all samples the peak feature of the mode is well-defined. The peak may not be completely resolvable and be present as a shoulder to the TO_2 mode at higher temperatures. Additionally, the mode is absent at 295 K or higher because of dominating thermal effects. Since such a peculiar peak is not reported before in these systems, we try to understand its origin by extrapolating observed properties of LHPs using other spectroscopic tools.

It has been well-established for a few years now, that photoinduction in LHPs can lead to induced vibrations, structural distortions, and polaron formation as a result of charge carrier interaction with the lattice [35, 36]. Therefore, the new peak could arise as a result of structural distortion in the lattice, which cannot be explained by factor group analysis. Recently, Puppin et al. provided an experimental value for effective mass using Angle-Resolved Photo-Emission Spectroscopy (ARPES) for $CsPbBr_3$ crystal [37]. The authors have recorded an effective mass of more than 50 % of the bare mass because of large Fröhlich polarons at 18.2 meV using calculations. Yet another report on microscopic studies done on $CsPbBr_3$ using TR-XAS has shown that photoinduced lattice activates LO phonon mode at 18 meV by strong electron-phonon coupling [34]. Both these recent experimental evidence report an activated LO phonon mode at 145 cm^{-1} (= 18 meV), very close to our observed vibration at 132 cm^{-1}. Hence, we conjecture that the

photoinduced mode at 132 cm^{-1} (and the corresponding 364 cm^{-1}) occurs resulting from polaron formation in these systems. The activated LO mode has been suggested to be arising as a result of Pb-Br stretching mode by electron-phonon coupling. In fact, the octahedral distortions are argued to be responsible for polaron formation in LHPs, with Pb-X stretching mode as the major component. [38, 35]. However, in this work we study a range of these LHPs, with varying compositions of Br but no consequent shift in the peak position of the new mode is observed from P1 to P4 which is expected normally with composition variation. The same peak signature in both P1 and P4 suggests that the activated phonon mode may not be arising from purely a Pb-X stretching mode. Consequently, we argue, it is either the Cs ion or the Pb ion motion responsible for this polaronic mode. Large polar fluctuations have earlier been monitored by the Raman central peak and discussed to be due to Cs head-to-head motion along with Br expansion in $CsPbBr_3$ and $CH_3NH_3PbBr_3$ crystals [22]. Hence, we suggest that the unusual new peak at 132 cm^{-1} is a result of Cs/Pb displacement coupled with the halide ion. The strength of the coupling between the halide motion and the cation displacement may determine the stability and occurrence of this photoinduced mode and thus the stability of the polaron. More conclusive evidence for the origin of the mode is obtained from first principles calculations.

The $CsPbX_3$ perovskites can crystallize in cubic (Pm-3m), tetragonal (I4/mcm), and orthorhombic phases (Pnma). However, it is well established that the cubic geometry exists only at elevated temperatures[39, 40, 41]. AIMD simulations at 300 K, suggest that both the systems undergo tetragonal distortion of the Pb-X(Cl/Br) octahedra significantly. (Figure 3.7c) After 60 ps of simulation, the structures retained the 3D network of corner-shared $[PbX_6]^{4-}$ octahedra, along with the Cs+ ions inhabiting interstitial sites. However, the Pb-Cl bond length was found to decrease from 2.86 Å to 2.67 Å, whereas the Pb-Br bond is elongated from 3.00 Å to 3.20 Å. This proves that the $[PbX_6]^{4-}$ octahedra is easily prone to lattice deformation. Experimentally, these deformations can get activated by photogenerated processes [42]. The deformation potential allows for the formation of polaronic states, due to enhanced electron-phonon coupling[43, 44, 34]. The lattice parameters of the optimized 3x3x1 supercell are tabulated in Table 3.5. The phonon modes were obtained from DFPT calculations at the Γ point. Cubic $CsPbX_3$ does not exhibit any Raman mode. However, we observed that the extent of tetrago-

nal distortion influences the appearance of the Raman active modes. Distortion of the $[PbX_6]^{4-}$ octahedra in the form of elongating/shortening the Pb-X bonds as listed in Table 3.4, resulted in the appearance of the 132 cm^{-1} mode.

Pb-Cl bond length elongation	VBM(eV)	Pb-Br bond length elongation	VBM (eV)
0%	-0.929	0%	-0.72
4%	-0.573	6%	-0.47
11%	-0.478	13%	-0.36

Table 3.4: Pb-X bond elongation and corresponding VBM levels

The electronic structure calculations provide a more detailed idea about the interacting electrons in the system and carrier dynamics. It was observed from the band structures, that for both $CsPbCl_3$ and $CsPbBr_3$ the Valence Band Maximum (VBM) and the Conduction Band Minimum (CBM) lie on the R point of the Brillouin Zone, thus rendering them direct bandgap semiconductors. This is in agreement with previous reports of LHPs [45, 46, 47, 48]. The projected density of states reveals that the nature of bonding in Pb-X is strongly covalent, with the valence states majorly comprised by Pb and Cl/Br electrons.

Since charge carriers are localized in valence band states with strong halide character, [49] thus the interplay of this photoinduced vibration and charge carrier will determine the fate of the polaron. Additionally, a peak at 364 cm^{-1} is observed along with the presence of the 132 cm^{-1} peak. It is fascinating to note that the peak at 364 cm^{-1}

System	(a) (Å)
$CsPbCl_3$	5.733
$CsPbBr_3$	6.002
$CsPbMnCl_3$	5.530
$CsPbMnBr_3$	5.788
$CsPbCl_2Br$	5.712
$CsPbClBr_2$	6.012

Table 3.5: Lattice Parameters of unit cell obtained from Geometry optimization

is observable only when a fairly intense 132 cm^{-1} mode appears. The 364 cm^{-1} peak corresponds to the second-order phonon resulting from a combination of the polaronic mode and a Raman mode because its intensity is directly influenced by the strength of the 132 cm^{-1} peak. Additionally, there are a few other new peaks that originate such as around 300 cm^{-1}, and above 500 cm^{-1} in the case of Mn-doped systems, however these peaks can arise due to second-order nature making it difficult to observe them theoretically. Thus, without loss of generality, we can discuss the phenomenon in this article by focusing on only the polaronic mode at 132 cm^{-1}. It is noteworthy to mention that we use a continuous-wave laser and thus can only probe long-lived charge carriers and no transient states [42]. Steady-state carrier-lifetime measurements have shown up to 3 ms and diffusion length up to 650 μm which are consistent with the polaronic nature of these carriers as well [50].

3.7.1 Polaronic behavior in undoped $CsPbX_3$

Our Raman studies present the traces of the polaronic mode in pure as well as mixed halide compositions, but there exists a spatial in-homogeneity related to the mode in the sample space and the stability of the mode is thus not always conducive. As opposed to the normal modes of the system, where peak positions are associated with the composition, here only the occurrence of polaronic mode varies with compositions, hence needs to be carefully examined. For this reason, a stack plot recorded at multiple spots (x, y coordinates on single drop-casted sample) as shown in Figure 3.8a, clearly maps the probability of the polaronic mode over the sample space marked by the star (132 cm^{-1}) and diamond (364 cm^{-1}). A closer look at the peak positions fitted over the same in Figure 3.8b reveals the weak presence (8-14 %) of the new vibration in P1. Whereas in the case of P4, the prominence goes up to 50 % of the time along with the strength of the peak. (Figure 3.8d) In the case of the latter P4 system, it is necessary to distinguish the polaronic peak from the normal mode that appears at 126 cm^{-1} as the two may overlap in a broad peak (Figure 3.8c). Nevertheless, the two peaks are well variegated upon fitting of these curves. Furthermore, the second-order mode at 364 cm^{-1} is observed only when a sharp 132 cm^{-1} mode exists. Therefore, the mode at 364 cm^{-1} can be used as a marker to confirm not only the presence of the induced vibrational mode in P4 NCs but

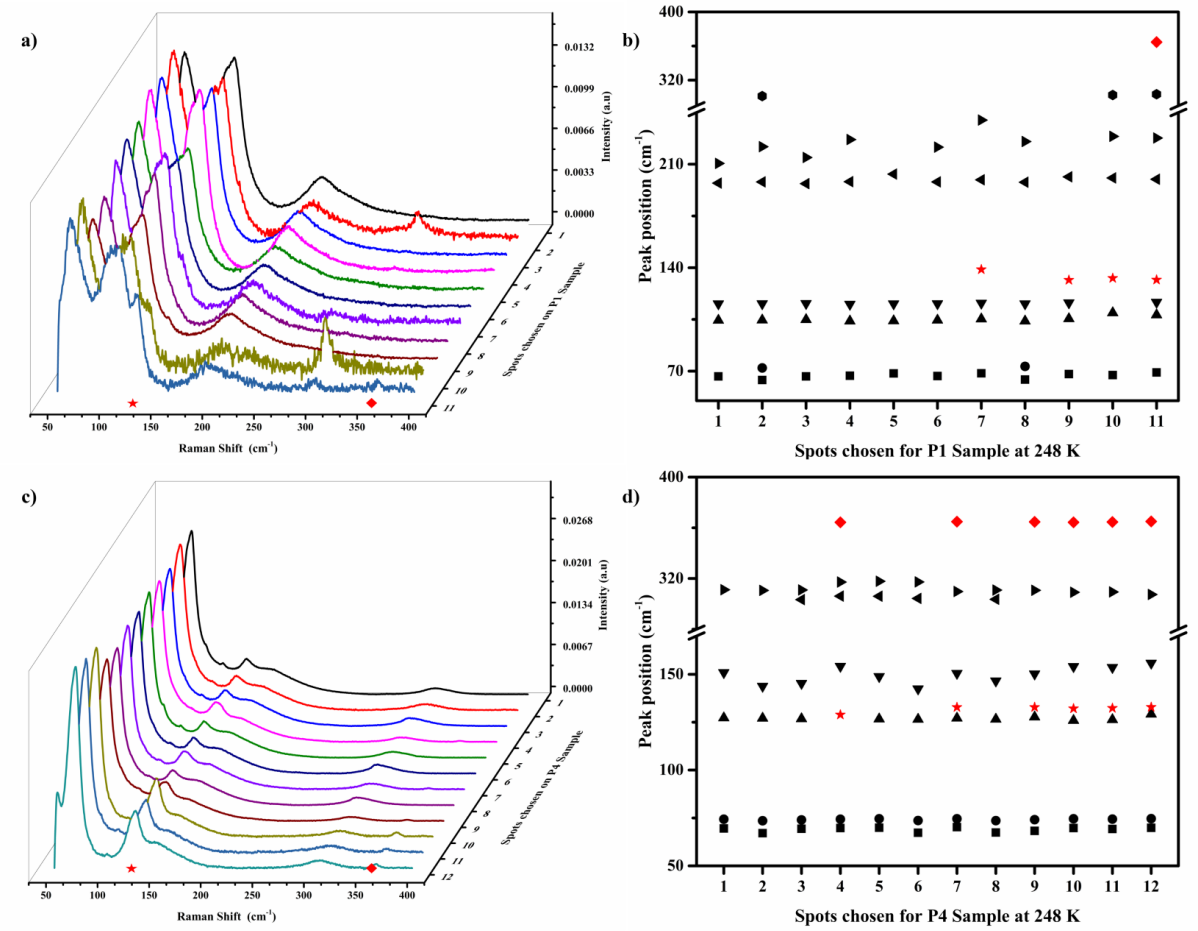

Figure 3.8: Behavior of the polaronic mode in undoped NCs a) and b) Raman spectra of P1 at 248 K recorded on multiple spots and their corresponding peak positions of all modes. c) and d) Raman spectra of P4 at 248 K recorded on multiple spots and their corresponding peak positions of all modes. Star and Diamond symbols in red color depict the polaronic mode (132 and 364 cm^{-1}) and their mapping on both the samples.

the strength of the polaronic feature in all the systems under consideration. From this observation, one may suggest that it is the presence of Br that stabilizes the polaronic mode as opposed to Cl which can be intuitively related to size-mismatch in the case of Pb-Cl as compared to Pb-Br and relatively higher polarizability of Br. As a result, the possibility of surface defects is much larger for Cl as compared to Br. Soetan et al. have proved from their studies on mixed halide perovskites that upon increasing Cl content to $CsPbBr_3$, a rise in radiative recombination of charge carriers and increased Auger losses over trap-assisted recombination is observed. [51]. Because of the above reasons, it is possible that Br couples more strongly with the distortions occurring along the cationic sites.

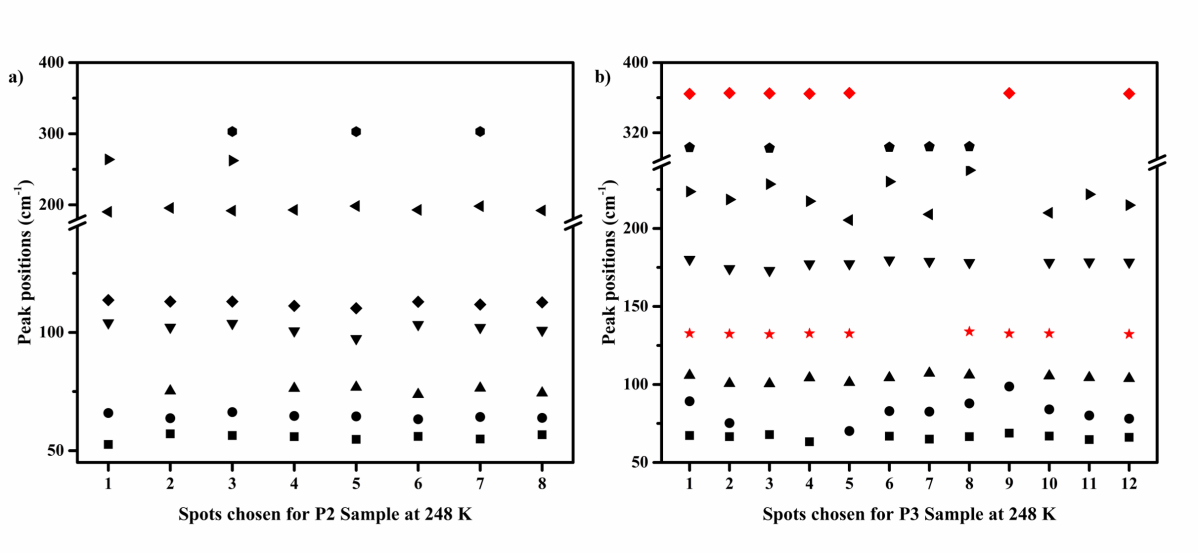

Figure 3.9: Peak positions of all modes for P2, and P3 at 248 K showing spot variation in especially the 132 cm^{-1} mode.

With this anticipation, the mixed halide systems were expected to display a stronger polaronic signature with increasing Br concentration. However, from Figure 3.11a, P2, with 25 % Br content, we do not observe a clear 132 cm^{-1} mode. It is plausible that additional strains may get introduced with the incorporation of Br which counters the distortion in the lattice. [52]. Hence, resulting in a weak to no signature of polaron for P2 NCs. Nevertheless, as we increase the concentration of Br in the mixed systems, i.e. in the case of P3, not only do we observe a strong feature of the new vibration but also homogeneity in 132 cm^{-1} peak over spots ameliorates. As shown in Figure 3.11b, nearly 60-70 % of the spot spectra display the polaronic mode along with the strong 364 cm^{-1} marker as well. This observation of the polaronic mode in P3 supersedes even the pure Br system, P4. The above results indicate that not only does Br addition to the lattice stabilize the polaronic mode, but the presence of Cl may create the possibility of increased distortion in the lattice. At this composition, Br plays a significant role in stabilizing the polaronic mode observed.

3.7.2 Polaronic behavior in Mn-doped $CsPbX_3$

Doping of LHPs has been proven to be an effective method to improve stability, PLQY, enhanced charge transport, and thus improved electronic properties [53]. Amongst many,

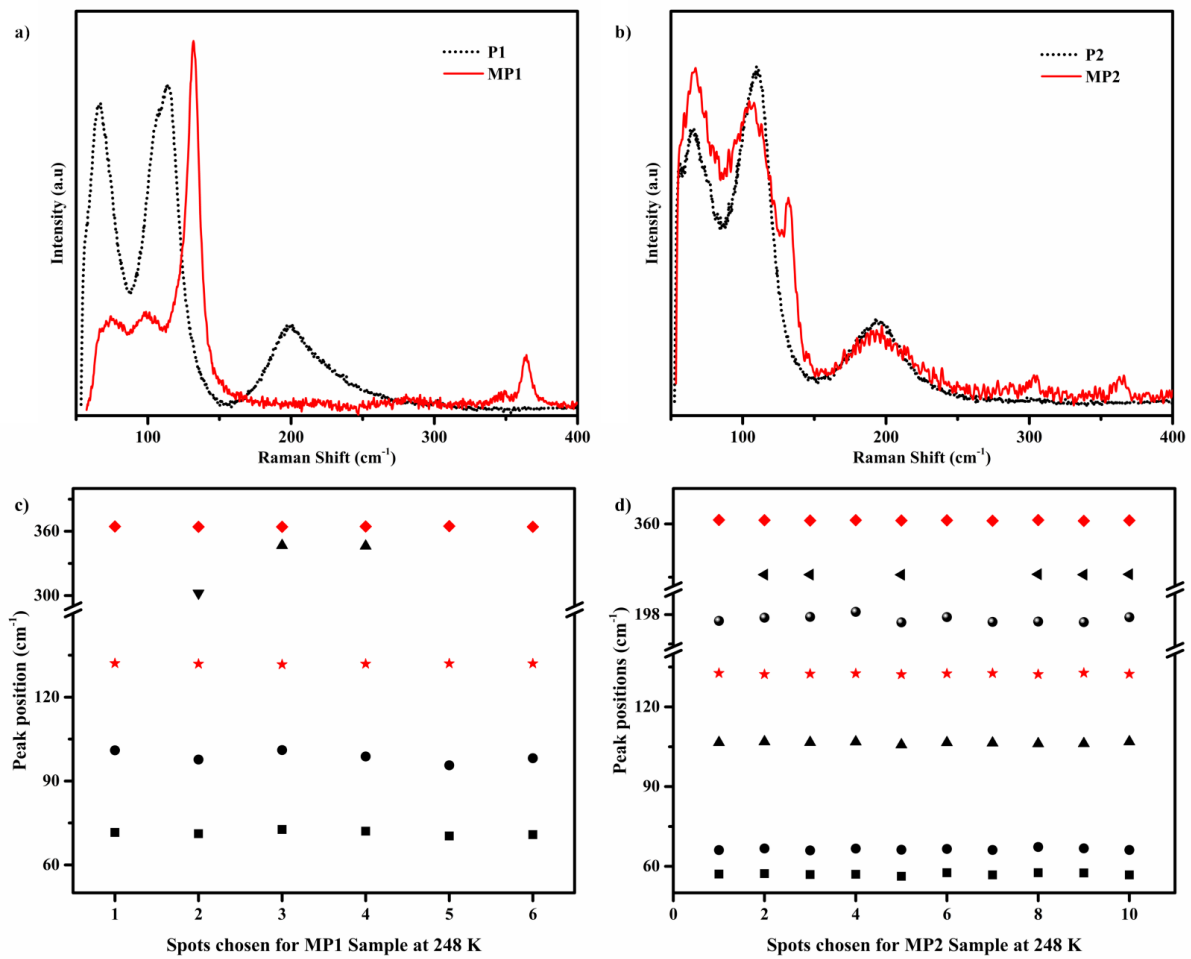

Figure 3.10: Raman spectra of Mn-doped and Undoped $CsPbX_3$ NCs at 248 K a) Mn-doped $CsPbCl_3$ (MP1) with its undoped (P1) counterpart for comparison. b) Mn-doped $CsPb(Cl/Br)_3$, where Br= 25 % (MP2) and its undoped (P2) counterpart for comparison c) Peak positions of all modes for MP1, and d) MP2 at 248 K over a range of spots. Star and Diamond symbols depict the polaronic mode (132 and 364 cm^{-1}).

Mn-doping has drawn a lot of attention because of an extra emission channel around 590 nm because of energy transfer between host and dopant resulting in increased radiative recombination in the systems [48]. Since the inorganic framework of the LHPs plays an important role in polaron formation, the role of Mn as dopant if any will be interesting to observe. In this work, upon Mn-doping (roughly between 1-5 %) of these $CsPbX_3$, surprising results were discovered. In both the Cl-rich systems, Mn-doped P1 (MP1) and Mn-doped P2 (MP2) as shown in Figure 3.10a and 3.10b, the polaronic mode is remarkable as a strong intense peak contrasting to the undoped counterparts, incapable of stabilizing the long-lived polarons.

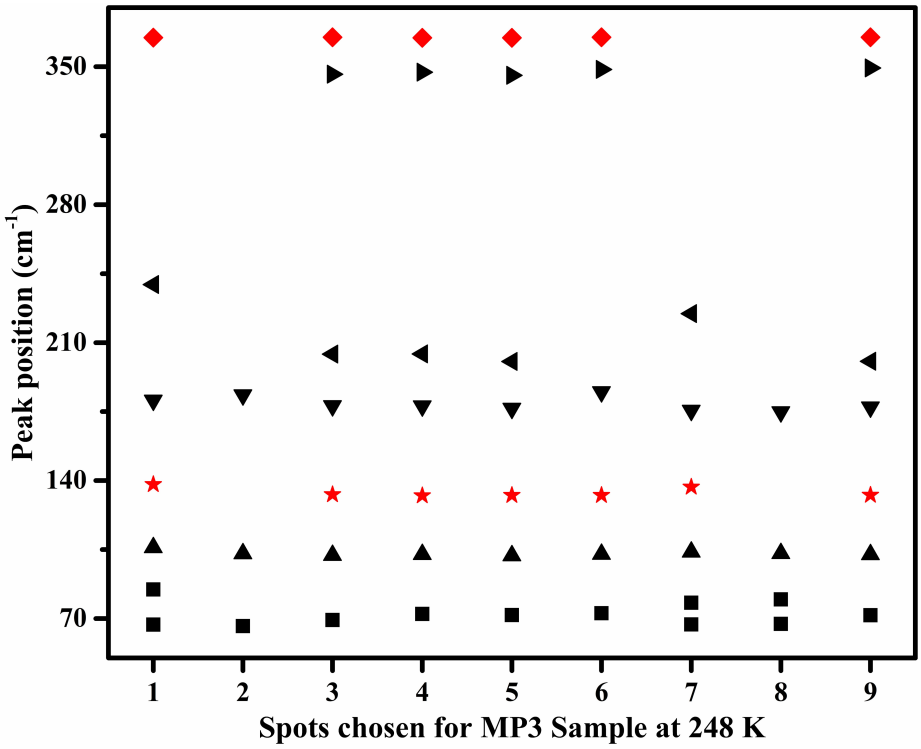

Figure 3.11: Peak positions of all modes for MP3 at 248 K showing spot variation in 132 cm^{-1} mode

The most interesting behavior of the polaronic mode was observed in the case of MP1. All spots not only feature a strong polaronic mode but bleaching of all normal modes is also observed as compared to P1. (Figure 3.10a and 3.10c). In addition to that, where the polaronic signature was absent in the P2 system, MP2 displays strong evidence of the polaronic mode throughout the sample space but unlike MP1, no bleaching of other Raman modes was observed. (Figure 3.10b and 3.10d). MP1 and MP2 not only have contrasting results with respect to their undoped counterparts, but also upon comparison with each other. In the earlier section, it was speculated that Br is strongly coupling to the polaronic mode and thus impacting its stability. However, when we observe the Mn-doped samples, even though MP2 displays clear and significant features of the mode, but it is weaker than MP1. Subsequently, the MP3 system shows a similar enhancement in polaronic mode stabilization as the other systems but no different as compared to the polaronic mode signature observed in the P3 sample (Figure 3.11). These riveting results in the Mn-doped systems indicate a possibility of a shift in the charge density upon doping which strongly influences the polaronic nature of the inorganic framework in question. Overall, Mn-doping stabilizes the polaronic mode, but the effects are more

pronounced in Cl-rich systems than with Br-incorporation. One of the previous works by Arunkumar *et al.* [54] has shown that upon Mn-doping between 5-10 %, the covalent character increases in the (Pb/Mn)-Cl bond as opposed to the usual more electrostatic bond. As a result, the distortion in the lattice increases which leads to polaron formation. They also emphasized that when Cl is replaced with a Br system, the Mn concentration required to stabilize the polaron increases to up to 70 %. This argument can be well extended in this article's context, where the Br-rich systems show lesser influence of Mn-doping on photo-activated mode as compared to P1 and P2 systems with dramatic effects. The theoretical calculations carried in the next section delves deeper to underpin the above discussed arguments.

3.7.3 Computational Analysis

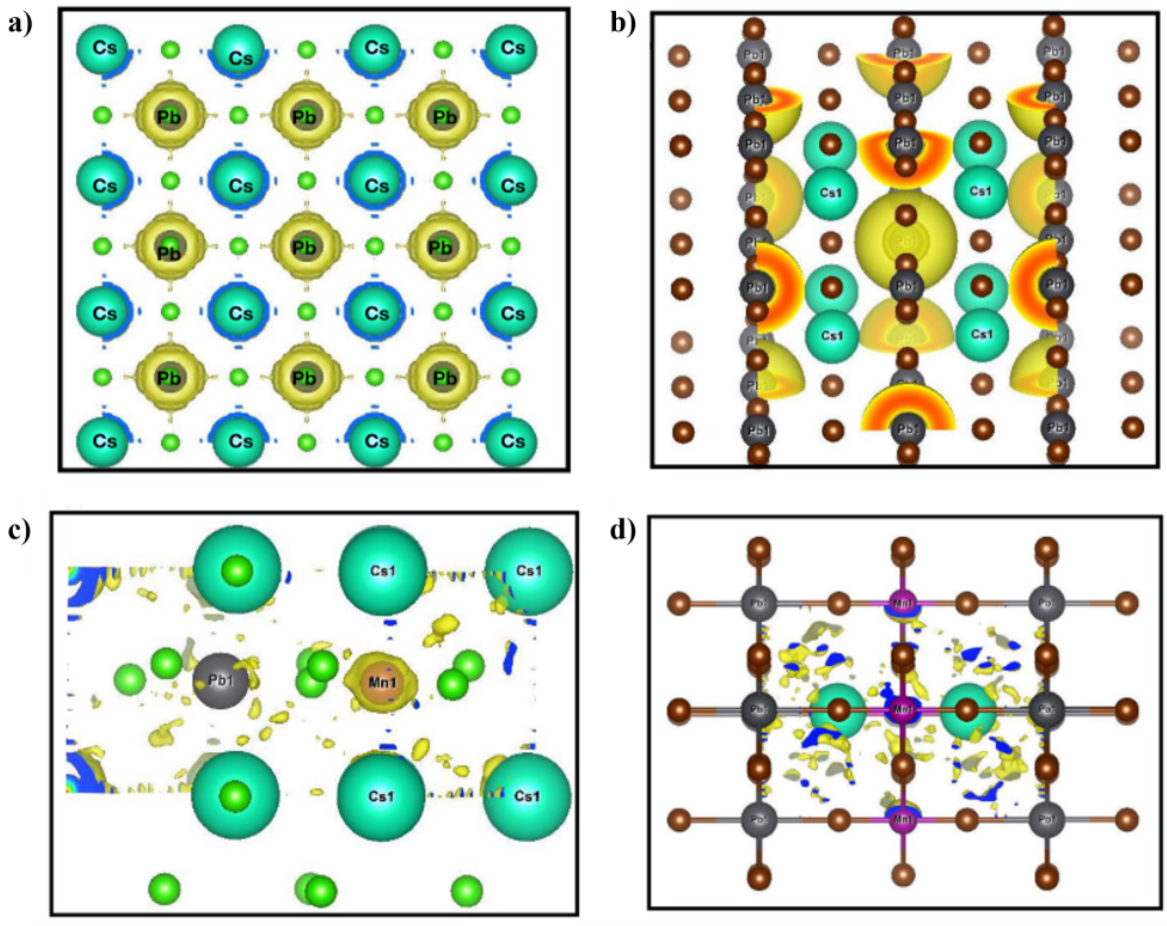

Figure 3.12: Charge density plots for pure a) $CsPbCl_3$ b) $CsPbBr_3$ and Mn-doped c) $CsPbMnCl_3$ and d) $CsPbMnBr_3$ systems. Isosurface value was 0.025 / $Å^3$.

From the HSE calculations, the polaronic state was identified from the projected density of states, at the edge of the VBM, mainly comprised by the Pb 6s orbitals, thus confirming the presence of an electron polaron centered around the Pb atom in undoped NCs, namely P1 and P6. The sharp peak arising from the polaronic state was found to shift towards the Fermi level, with an increase in Pb-X distortion. (See Table 3.4 for VBM energy levels). It is important to note that the VBM also showed a greater extent of overlap between Pb and Br 2p orbitals, than between Pb and Cl 2p orbitals. Therefore, the polaronic state is stabilized more, by the Pb-Br bond than the Pb-Cl bond. These results can be best visualized by charge density plots which confirm that stronger polarons are formed in the $CsPbBr_3$ system compared to the $CsPbCl_3$ systems as shown in Figure 3.12a and 3.12b.

In contrast to the pure $CsPbX_3$ systems, the Mn-doped systems do not show the same polaronic behavior. It is inferred that the electron polaron forms over the Mn atoms and not on the Pb atoms. Moreover, polaron formation is favored in the $CsPbMnCl_3$ systems, more than the $CsPbMnBr_3$ systems as can be seen in the charge density plots in Figure 3.12c and 3.12d. The projected density of states analysis confirms that the electronic density of Cl is higher than Br in the valence edge states, overlapping with Mn 3d orbitals, which indicates that the extent of covalent overlap between Mn-Cl bonding is stronger in comparison with the Mn-Br bond. The Mn-Cl bond thus stabilizes the electron polaron formation over the Mn center. For the mixed halide systems, $CsPbCl_xBr_{3-x}$, it is found that the polaron formation is favored over the Pb atom center. The results confirm that the concentration of Br plays affects the polaron formation energy. A higher concentration of Br stabilizes the polaron to a larger extent.

3.7.4 Structural effects in polaron formation

Substitution of anions and cations can dramatically shift the carrier dynamics because of the large structural impact to stabilize the system, consequently affecting electronic states which are involved in charge transport and recombination [55]. In systems like $CsPbCl_3$, where there is weak to negligible coupling of Cl with the Pb states, the activated phonon is sporadically observed, owing to the large Cl vacancies which decrease the overall quantum yield. Nevertheless, these weak to strong polaron signatures can be achieved with Br

incorporation in $CsPbCl_3$. Despite $CsPbBr_3$ NCs stabilized the polaronic mode strongly, it is the mixed halide P3 system, which displayed a more homogeneous behavior of the induced vibration. These polaronic signature observed in Raman spectroscopy correlates well with the increase in stability of the Cl perovskite with Br incorporation, resulting in higher quantum yield [56] and can be associated with higher radiative recombination routes due to polaron formation. Swarnkar et al. argued that B-site cations have a significant influence in shaping the optoelectronic properties of these perovskite systems [57]. Indeed, upon Mn-doping pronounced results were observed. Here, we have successfully displayed the switch in the appearance of 132 cm^{-1} mode from weak to strong, as the polaronic state shifts from being Pb-dominated to Mn-dominated in Mn-doped systems. Upon Mn-doping, not only is the polaronic mode observed in these systems which was absent or had negligible contribution in the undoped counterparts, but the spatial homogeneity also improves drastically. Moreover, from previous reports it is suggested that the doping of bivalent ions occupy defective crystal vacancies and improve the short-range ordering in the lattice [58]. Hence, the overall stability of a large polaron would increase in the lattice over a greater number of unit cells locally. Therefore, in order to obtain a stronger polaronic signature among the two methods i.e., partial replacement of Cl with Br and Mn doping, Mn doping (origin of polaronic state) is preferred. There are also numerous reports which have shown an increase in carrier lifetime and increase in PLQY in Mn-doped $CsPbCl_3$ thus making it a good candidate for photovoltaic applications [54, 53]. Our studies provide useful insight into the origins of the long recombination lifetimes observed in Mn-doped $CsPbCl_3$ underpinning a stabilized polaron formation. The clear experimental evidence of an activated phonon mode due to polaronic origin can be used as a marker to understand the structure and property relationship in these LHPs, which is fundamental for using them as potential materials for optoelectronic applications. Although there are numerous sophisticated techniques that can probe these polaronic formations and stability in-depth we believe that a simple technique like Raman spectroscopy can be used as a tool for mapping polaronic signatures *in-operando* in such a family of materials.

3.8 Conclusions

In summary, a series of $CsPbX_3$ and their Mn-doped counterparts were studied using micro-Raman spectroscopy and first principles DFT calculations. An appearance of a new Raman peak at 132 cm^{-1} and a second-order component at 364 cm^{-1} at varying compositions of the LHPs was discussed. From our Raman and first principles calculations, it is underscored that the persisting knowledge of the Pb-X stretching modes playing a dominant role in polaron formation in LHPs seems rather incomplete [35]. Although new Raman modes appear from tetragonal distortion, it is corroborated now that a strong covalent overlap of the B-site cation, which is responsible for polaronic state, with the halide ion can lead to stabilizing the induced vibration, and indirectly stabilizing the polaronic state. In other words, the primary polaronic state arises due to Pb/Mn displacement, but the coupling with Br/Cl determines the stability of the vibration. $CsPbX_3$ NCs with Cl-rich anions displayed the weakest polaronic signatures, while the incorporation of Br mediated the polaron stability. The vibrational mode was affected strongly upon Mn-doping resulting in shifting of the polaronic state to Mn from Pb. Our studies on the doped and undoped $CsPbX_3$ have looked at understanding how modifications to the structure of the perovskite lattice affect the carrier-phonon interaction through an activated new Raman mode.

References

[1] L. Protesescu, S. Yakunin, M. I. Bodnarchuk, F. Krieg, R. Caputo, C. H. Hendon, R. X. Yang, A. Walsh, and M. V. Kovalenko, "Nanocrystals of cesium lead halide perovskites (cspbx3, x= cl, br, and i): novel optoelectronic materials showing bright emission with wide color gamut," *Nano letters*, vol. 15, no. 6, pp. 3692–3696, (2015).

[2] M. V. Kovalenko, L. Protesescu, and M. I. Bodnarchuk, "Properties and potential optoelectronic applications of lead halide perovskite nanocrystals," *Science*, vol. 358, no. 6364, pp. 745–750, (2017).

[3] Y. Zhao and K. Zhu, "Organic–inorganic hybrid lead halide perovskites for optoelectronic and electronic applications," *Chemical Society Reviews*, vol. 45, no. 3, pp. 655–689, (2016).

[4] R. E. Beal, D. J. Slotcavage, T. Leijtens, A. R. Bowring, R. A. Belisle, W. H. Nguyen, G. F. Burkhard, E. T. Hoke, and M. D. McGehee, "Cesium lead halide perovskites with improved stability for tandem solar cells," *The journal of physical chemistry letters*, vol. 7, no. 5, pp. 746–751, (2016).

[5] A. Swarnkar, A. R. Marshall, E. M. Sanehira, B. D. Chernomordik, D. T. Moore, J. A. Christians, T. Chakrabarti, and J. M. Luther, "Quantum dot–induced phase stabilization of α-cspbi3 perovskite for high-efficiency photovoltaics," *Science*, vol. 354, no. 6308, pp. 92–95, (2016).

[6] M. C. Brennan, S. Draguta, P. V. Kamat, and M. Kuno, "Light-induced anion phase segregation in mixed halide perovskites," *ACS Energy Letters*, vol. 3, no. 1, pp. 204–213, (2017).

[7] W. Rehman, D. P. McMeekin, J. B. Patel, R. L. Milot, M. B. Johnston, H. J. Snaith, and L. M. Herz, "Photovoltaic mixed-cation lead mixed-halide perovskites: links between crystallinity, photo-stability and electronic properties," *Energy & Environmental Science*, vol. 10, no. 1, pp. 361–369, (2017).

[8] B. A. Rosales, L. Men, S. D. Cady, M. P. Hanrahan, A. J. Rossini, and J. Vela, "Persistent dopants and phase segregation in organolead mixed-halide perovskites," *Chemistry of Materials*, vol. 28, no. 19, pp. 6848–6859, (2016).

[9] A. Karmakar, A. M. Askar, G. M. Bernard, V. V. Terskikh, M. Ha, S. Patel, K. Shankar, and V. K. Michaelis, "Mechanochemical synthesis of methylammonium lead mixed–halide perovskites: unraveling the solid-solution behavior using solid-state nmr," *Chemistry of Materials*, vol. 30, no. 7, pp. 2309–2321, (2018).

[10] M. Liao, B. Shan, and M. Li, "In situ raman spectroscopic studies of thermal stability of all-inorganic cesium lead halide (cspbx3, x= cl, br, i) perovskite nanocrystals," *The journal of physical chemistry letters*, vol. 10, no. 6, pp. 1217–1225, (2019).

[11] M. Ledinský, P. Lóper, B. Niesen, J. Holovský, S.-J. Moon, J.-H. Yum, S. De Wolf, A. Fejfar, and C. Ballif, "Raman spectroscopy of organic–inorganic halide perovskites," *The journal of physical chemistry letters*, vol. 6, no. 3, pp. 401–406, (2015).

[12] P. KR, D. Acharya, P. Jain, K. Gahlot, A. Yadav, A. Camellini, M. Zavelani-Rossi, G. Cerullo, C. Narayana, S. Narasimhan, *et al.*, "Harvesting delayed fluorescence in perovskite nanocrystals using spin-forbidden mn d states," *ACS Energy Lett.*, vol. 5, no. 2, pp. 353–359, (2019).

[13] K. Pradeep and R. Viswanatha, "Doped or not doped? importance of the local structure of mn (ii) in mn doped perovskite nanocrystals," *Mater. Res. Bull.*, vol. 141, p. 111374, (2021).

[14] H. Lee, S. Gaiaschi, P. Chapon, D. Tondelier, J.-E. Bouré, Y. Bonnassieux, V. Derycke, and B. Geffroy, "Effect of halide ion migration on the electrical properties of methylammonium lead tri-iodide perovskite solar cells," *The Journal of Physical Chemistry C*, vol. 123, no. 29, pp. 17728–17734, (2019).

[15] D. M. Calistru, L. Mihut, S. Lefrant, and I. Baltog, "Identification of the symmetry of phonon modes in cspbcl 3 in phase iv by raman and resonance-raman scattering," *J. Appl. Phys.*, vol. 82, no. 11, pp. 5391–5395, (1997).

[16] C. Carabatos-Nédelec, M. Oussaïd, and K. Nitsch, "Raman scattering investigation of cesium plumbochloride, cspbcl3, phase transitions," *J. Raman Spectrosc.*, vol. 34, no. 5, pp. 388–393, (2003).

[17] L. Zhang, Q. Zeng, and K. Wang, "Pressure-induced structural and optical properties of inorganic halide perovskite cspbbr3," *J. Phys. Chem. Lett.*, vol. 8, no. 16, pp. 3752–3758, (2017).

[18] M. M. Karim, A. M. Ganose, L. Pieters, W. Winnie Leung, J. Wade, L. Zhang, D. O. Scanlon, and R. G. Palgrave, "Anion distribution, structural distortion, and symmetry-driven optical band gap bowing in mixed halide cs2snx6 vacancy ordered double perovskites," *Chemistry of materials*, vol. 31, no. 22, pp. 9430–9444, (2019).

[19] C. M. Iaru, J. J. Geuchies, P. M. Koenraad, D. Vanmaekelbergh, and A. Y. Silov, "Strong carrier–phonon coupling in lead halide perovskite nanocrystals," *ACS Nano*, vol. 11, no. 11, pp. 11024–11030, (2017).

[20] D. Meggiolaro, F. Ambrosio, E. Mosconi, A. Mahata, and F. De Angelis, "Polarons in metal halide perovskites," *Adv. Energy Mater.*, vol. 10, no. 13, p. 1902748, (2020).

[21] L. Zhou, C. Katan, W. Nie, H. Tsai, L. Pedesseau, J. J. Crochet, J. Even, A. D. Mohite, S. Tretiak, and A. J. Neukirch, "Cation alloying delocalizes polarons in lead halide perovskites," *J. Phys. Chem. Lett.*, vol. 10, no. 13, pp. 3516–3524, (2019).

[22] O. Yaffe, Y. Guo, L. Z. Tan, D. A. Egger, T. Hull, C. C. Stoumpos, F. Zheng, T. F. Heinz, L. Kronik, M. G. Kanatzidis, *et al.*, "Local polar fluctuations in lead halide perovskite crystals," *Phys. Rev. Lett.*, vol. 118, no. 13, p. 136001, (2017).

[23] T. Etienne, E. Mosconi, and F. De Angelis, "Dynamical origin of the rashba effect in organohalide lead perovskites: A key to suppressed carrier recombination in perovskite solar cells?," *J. Phys. Chem. Lett.*, vol. 7, no. 9, pp. 1638–1645, (2016).

[24] F. Zheng, L. Z. Tan, S. Liu, and A. M. Rappe, "Rashba spin–orbit coupling enhanced carrier lifetime in ch3nh3pbi3," *Nano Lett.*, vol. 15, no. 12, pp. 7794–7800, (2015).

[25] F. Zheng and L.-w. Wang, "Large polaron formation and its effect on electron transport in hybrid perovskites," *Energy Environ. Sci.*, vol. 12, no. 4, pp. 1219–1230, (2019).

[26] E. Cinquanta, D. Meggiolaro, S. G. Motti, M. Gandini, M. J. Alcocer, Q. A. Akkerman, C. Vozzi, L. Manna, F. De Angelis, A. Petrozza, *et al.*, "Ultrafast thz probe of photoinduced polarons in lead-halide perovskites," *Phys. Rev. Lett.*, vol. 122, no. 16, p. 166601, (2019).

[27] W. Tao, C. Zhang, Q. Zhou, Y. Zhao, and H. Zhu, "Momentarily trapped exciton polaron in two-dimensional lead halide perovskites," *Nat. Commun.*, vol. 12, no. 1, pp. 1–8, (2021).

[28] F. Thouin, A. R. Srimath Kandada, D. A. Valverde-Chávez, D. Cortecchia, I. Bargigia, A. Petrozza, X. Yang, E. R. Bittner, and C. Silva, "Electron–phonon couplings inherent in polarons drive exciton dynamics in two-dimensional metal-halide perovskites," *Chem. Mater.*, vol. 31, no. 17, pp. 7085–7091, (2019).

[29] M. Park, A. J. Neukirch, S. E. Reyes-Lillo, M. Lai, S. R. Ellis, D. Dietze, J. B. Neaton, P. Yang, S. Tretiak, and R. A. Mathies, "Excited-state vibrational dynamics toward the polaron in methylammonium lead iodide perovskite," *Nat. Commun.*, vol. 9, no. 1, pp. 1–9, (2018.

[30] C. Liu, H. Tsai, W. Nie, D. J. Gosztola, and X. Zhang, "Direct spectroscopic observation of the hole polaron in lead halide perovskites," *J. Phys. Chem. Lett.*, vol. 11, no. 15, pp. 6256–6261, (2020).

[31] B. Guzelturk, T. Winkler, T. W. Van de Goor, M. D. Smith, S. A. Bourelle, S. Feldmann, M. Trigo, S. W. Teitelbaum, H.-G. Steinrück, A. Gilberto, *et al.*, "Visualization of dynamic polaronic strain fields in hybrid lead halide perovskites," *Nat. Mater.*, vol. 20, no. 5, pp. 618–623, (2021).

[32] K. Miyata, T. L. Atallah, and X.-Y. Zhu, "Lead halide perovskites: Crystal-liquid duality, phonon glass electron crystals, and large polaron formation," *Sci. Adv.*, vol. 3, no. 10, p. e1701469, (2017).

[33] K. T. Munson and J. B. Asbury, "Influence of dynamic disorder and charge–lattice interactions on optoelectronic properties of halide perovskites," *J. Phys. Chem. C*, vol. 125, no. 10, pp. 5427–5435, (2021).

[34] O. Cannelli, N. Colonna, M. Puppin, T. C. Rossi, D. Kinschel, L. M. Leroy, J. Löffler, J. M. Budarz, A. M. March, G. Doumy, *et al.*, "Quantifying photoinduced polaronic distortions in inorganic lead halide perovskite nanocrystals," *J. Am. Chem. Soc.*, (2021).

[35] K. Miyata, D. Meggiolaro, M. T. Trinh, P. P. Joshi, E. Mosconi, S. C. Jones, F. De Angelis, and X.-Y. Zhu, "Large polarons in lead halide perovskites," *Sci. Adv.*, vol. 3, no. 8, p. e1701217, (2017).

[36] D. Ghosh, E. Welch, A. J. Neukirch, A. Zakhidov, and S. Tretiak, "Polarons in halide perovskites: A perspective," *J. Phys. Chem. Lett.*, vol. 11, no. 9, pp. 3271–3286, (2020).

[37] M. Puppin, S. Polishchuk, N. Colonna, A. Crepaldi, D. Dirin, O. Nazarenko, R. De Gennaro, G. Gatti, S. Roth, T. Barillot, *et al.*, "Evidence of large polarons in photoemission band mapping of the perovskite semiconductor cspbbr 3," *Phys. Rev. Lett.*, vol. 124, no. 20, p. 206402, (2020).

[38] H.-G. Duan, V. Tiwari, A. Jha, G. R. Berdiyorov, A. Akimov, O. Vendrell, P. K. Nayak, H. J. Snaith, M. Thorwart, Z. Li, *et al.*, "Photoinduced vibrations drive ultrafast structural distortion in lead halide perovskite," *J. Am. Chem. Soc.*, vol. 142, no. 39, pp. 16569–16578, (2020).

[39] M. C.K., "Crystal structure and photoconductivity of cesium plumbohalides," *Nature*, vol. 182, p. 1436, (1958).

[40] L. A. J. S-Y, "Twin structure by ^{133}cs nmr in ferroelastic $cspbcl_3$ crystal," *Solid State Commun.*, vol. 110, no. 3, pp. 131–136, (1999).

[41] R. P.-P. J. Gonzalez-Carrero, S; Galian, "Organic-inorganic and all-inorganic lead halide nanoparticles," *Opt. Express*, vol. 21, no. 2, p. A285, (2016).

[42] T. Ivanovska, C. Dionigi, E. Mosconi, F. De Angelis, F. Liscio, V. Morandi, and G. Ruani, "Long-lived photoinduced polarons in organohalide perovskites," *J. Phys. Chem. Lett.*, vol. 8, no. 13, pp. 3081–3086, (2017).

[43] J. T. Devreese and A. S. Alexandrov, "Fröhlich polaron and bipolaron: Recent developments," *Rep. Prog. Phys.*, vol. 72, no. 6, p. 066501, (2009).

[44] J. Yin, P. Maity, M. De Bastiani, I. Dursun, O. M. Bakr, J.-L. Brédas, and O. F. Mohammed, "Molecular behavior of zero-dimensional perovskites," *Sci. Adv.*, vol. 3, no. 12, p. e1701793, (2017).

[45] R. J. Worhatch, H. Kim, I. P. Swainson, A. L. Yonkeu, and S. J. Billinge, "Study of local structure in selected organic–inorganic perovskites in the pm-3m phase," *Chem. Mater.*, vol. 20, no. 4, pp. 1272–1277, (2008).

[46] T. V. Vu, A. Lavrentyev, B. Gabrelian, K. D. Pham, O. Parasyuk, N. Denysyuk, and O. Khyzhun, "Electronic structure and optical constants of cspbcl3: The effect of approaches within ab initio calculations in relation to x-ray spectroscopy experiments," *Mater. Chem. Phys.*, vol. 261, p. 124216, (2021).

[47] H. Chen, M. Li, B. Wang, S. Ming, and J. Su, "Structure, electronic and optical properties of cspbx3 halide perovskite: A first-principles study," *J. Alloys Compd.*, vol. 862, p. 158442, (2021).

[48] D. Ricciarelli, E. Mosconi, B. Merabet, O. Bizzarri, and F. De Angelis, "Electronic properties and carrier trapping in bi and mn co-doped cspbcl3 perovskite," *J. Phys. Chem. Lett.*, vol. 11, no. 14, pp. 5482–5489, (2020).

[49] F. G. Santomauro, J. Grilj, L. Mewes, G. Nedelcu, S. Yakunin, T. Rossi, G. Capano, A. Al Haddad, J. Budarz, D. Kinschel, *et al.*, "Localized holes and delocalized electrons in photoexcited inorganic perovskites: Watching each atomic actor by picosecond x-ray absorption spectroscopy," *Struct. Dyn.*, vol. 4, no. 4, p. 044002, (2017).

[50] Y. Chen, H. Yi, X. Wu, R. Haroldson, Y. Gartstein, Y. Rodionov, K. Tikhonov, A. Zakhidov, X.-Y. Zhu, and V. Podzorov, "Extended carrier lifetimes and diffusion

in hybrid perovskites revealed by hall effect and photoconductivity measurements," *Nat. Commun.*, vol. 7, no. 1, pp. 1–9, (2016).

[51] N. Soetan, A. Puretzky, K. Reid, A. Boulesbaa, H. F. Zarick, A. Hunt, O. Rose, S. Rosenthal, D. B. Geohegan, and R. Bardhan, "Ultrafast spectral dynamics of cspb (br x cl1–x) 3 mixed-halide nanocrystals," *ACS Photonics*, vol. 5, no. 9, pp. 3575–3583, (2018).

[52] J. Ibaceta-Jaña, R. Muydinov, P. Rosado, H. Mirhosseini, M. Chugh, O. Nazarenko, D. N. Dirin, D. Heinrich, M. R. Wagner, T. D. Kühne, *et al.*, "Vibrational dynamics in lead halide hybrid perovskites investigated by raman spectroscopy," *Phys. Chem. Chem. Phys.*, vol. 22, no. 10, pp. 5604–5614, (2020).

[53] C.-H. Lu, G. V. Biesold-McGee, Y. Liu, Z. Kang, and Z. Lin, "Doping and ion substitution in colloidal metal halide perovskite nanocrystals," *Chem. Soc. Rev.*, vol. 49, no. 14, pp. 4953–5007, (2020).

[54] P. Arunkumar, H. B. Cho, K. H. Gil, S. Unithrattil, Y. H. Kim, and W. B. Im, "Probing molecule-like isolated octahedra via phase stabilization of zero-dimensional cesium lead halide nanocrystals," *Nat. Commun.*, vol. 9, no. 1, pp. 1–11, (2018).

[55] K. T. Munson, E. R. Kennehan, G. S. Doucette, and J. B. Asbury, "Dynamic disorder dominates delocalization, transport, and recombination in halide perovskites," *Chem*, vol. 4, no. 12, pp. 2826–2843, (2018).

[56] Q. A. Akkerman, V. D'Innocenzo, S. Accornero, A. Scarpellini, A. Petrozza, M. Prato, and L. Manna, "Tuning the optical properties of cesium lead halide perovskite nanocrystals by anion exchange reactions," *J. Am. Chem. Soc.*, vol. 137, no. 32, pp. 10276–10281, (2015).

[57] A. Swarnkar, W. J. Mir, and A. Nag, "Can b-site doping or alloying improve thermal- and phase-stability of all-inorganic cspbx3 (x= cl, br, i) perovskites?," *ACS Energy Lett.*, vol. 3, no. 2, pp. 286–289, (2018).

[58] S. Seth, T. Ahmed, A. De, and A. Samanta, "Tackling the defects, stability, and photoluminescence of cspbx3 perovskite nanocrystals," *ACS Energy Lett.*, vol. 4, no. 7, pp. 1610–1618, (2019).

Chapter 4

Zeolitic Imidazolate Frameworks

4.1 Introduction

Zeolitic imidazolate frameworks (ZIFs) are a class of metal-organic frameworks (MOFs) that resemble the well-known zeolites in their geometrical similarities. ZIFs for a metal-linker (M-L) bond with the M-L-M torsional angle being 145° similar to the Si-O-Si angle of zeolites. ZIFs are not only porous materials but also possess high chemical and thermal stability [1, 2]. Hence, they became popular for various applications such as gas storage and separation [3, 4], catalysis [5], sensing [6], and drug delivery [7]. ZIFs are composed of metals such as Zn, Co, Fe and functionalized organic linkers of imidazole, providing porosity of various sizes, rigid yet flexible, and tailored steric and electronic properties [6]. The ZIF systems being more dynamic materials as opposed to the rigid zeolite analogues ameliorates in phenomenon such as gate opening, breathing, and significant structural changes upon application of temperature, pressure, and guest molecules [8, 9]. This puts these materials under the umbrella of stimuli-responsive materials.

Amongst the well-known ZIF systems, ZIF-8 is undoubtedly the most studied and well-explored material because of its facile synthesis [10] as well as high chemical and thermal stability. It is composed of Zn as the metal and 2-methyl imidazole (MIm) as the linker system. The ZIF-8 crystallizes in a cubic symmetry with space group $I\bar{4}3m$ shown in Figure 4.1, with large cage of 12 Å, connected by a six-membered ring (6MR) and a 4MR. One of the major response shown by ZIF-8 is gate-opening [11] making

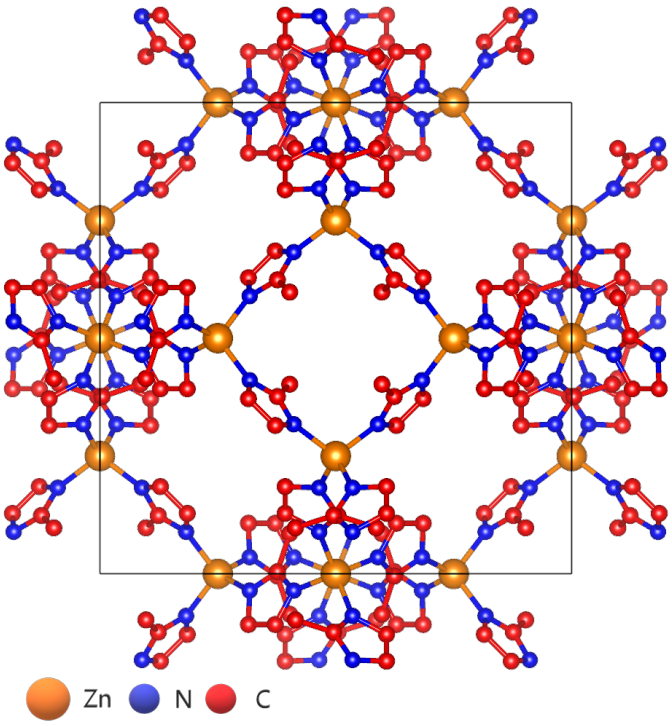

Figure 4.1: Structure of ZIF-8 redrawn from CCDC No. 1560435

the uptake of gases such as CH_4 possible inspite of high kinetic diameter. The gate opening was also observed alone by N_2 adsorption at 77 K. The soft nature of ZIF-8 also lead to loss of crystallinity upon subjecting to uniaxial mechanical pressure [12]. Riveting findings of ZIF-8 initially led to a bloom of research and interest in the material with various stimuli that could induce structural changes and explain the mechanism [13, 14, 15, 16]. A substantial part of the ZIF-8 research includes how the linker dynamics govern guest adsorption, with conflicting reports on if all probes (such as Ar, CO_2, N_2) can induce adsorption [17] and how sudden/continuous the transition is [18]. In this regard, experimental reports on N_2 adsorption showed a gradual gate opening below 150 K with a fully open phase at 110 K using temperature scanning SCXRD and Raman spectroscopy [19]. The Raman investigations carried on ZIF-8 in our group provided extremely insightful results in this field [20]. The temperature-induced structural changes were found due to "swinging of the imidazole linkers". The structural changes around 150 K were marked by the softening of the Zn-N stretching and C-H stretching (Me group) modes resulting in reduced steric hindrance between the methyl groups of the MIm. These spectral changes were simultaneously accompanied by characteristic peaks

originating from adsorbed N_2 and CH_4 molecules explaining the uptake of these gases beyond 150 K. Hence, in situ investigations carried on ZIF-8 using Raman spectroscopy provided the much needed microscopic picture of the structural dynamics in the presence of guest molecules. Over the years, other than ZIF-8, comprehensive Raman studies have been carried in our group using temperature, pressure, and guest molecules in a few MOFs/ZIFs systems explaining the dynamics of the framework and unusual gas uptakes [21, 22]. These gas adsorption studies affecting the structure function in the field of MOFs motivated us to further investigate other ZIF systems, for how linker dynamics and gas adsorption behaviour changes. For this purpose, two ZIF systems were chosen as follows;

1. ZIF-4, where imidazole is unsubstituted and pore size is extremely small (2 Å)
2. ZIF-67, which is isostructural to ZIF-8, but the metal ion is Co instead of Zn

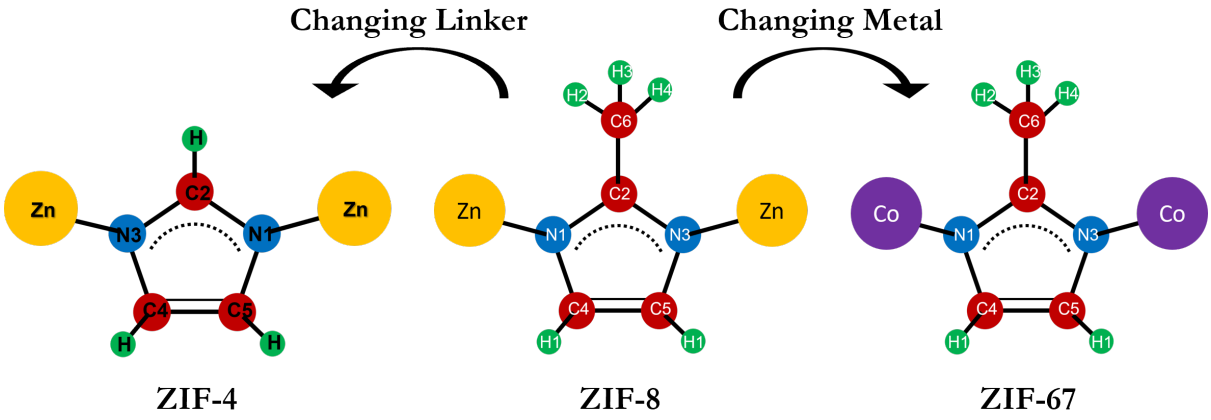

Chapter 4A

Non-covalent interactions triggering structural changes and gas uptake in ZIF-4 crystals*

Summary

ZIF-4, once believed to be inaccessible by gases, exhibits pore volume changes with external stimuli but with a limited understanding of the structural changes and adsorption mechanisms. In the present chapter, an open to narrow pore transition around 253 K in ZIF-4 under absolute guest-free environment using Raman spectroscopy was reported. Rare observations of adsorbed N_2 and CO_2 in the framework at room temperature (293 K) was discovered. The adsorption is facilitated by dispersive and quadrupolar interactions as observed from the corresponding changes in imidazole moeity. A guest-induced transition at 153 K resulting in the expansion of the framework was corroborated from the Raman spectral changes in the C-H stretching modes and low-wavenumber modes ($<$200 cm^{-1}). The adsorption of guests in ZIF-4 were proposed in the following order: C4H, C5H $>$ C2 $>$ sites near to the Im ring centre $>$ centre of cavity. Our results have immediate implications in the field of porous materials and could be vital in anticipating imperceptible structural transformations that may favour or hinder guest adsorption.

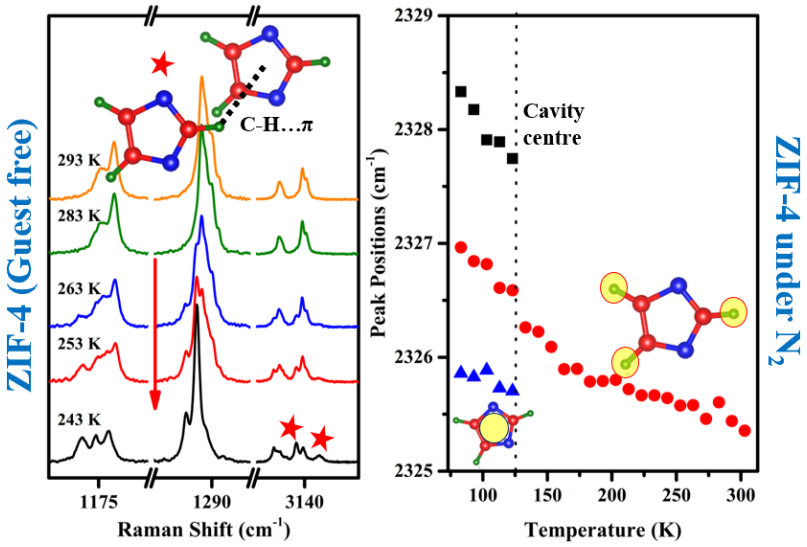

*Manuscript under preparation

4.2 Motivation for the work

ZIF-4 is a Zeolitic system, which crystallizes in an orthorhombic geometry, cag network topology with *Pbca* space group and a small pore diameter of 0.2 nm [23]. It undergoes a structural phase transition from low-density (open pore) to high density (closed pore) at 140 K [24]. ZIF-4 was intially assumed to be inaccessible to guest molecules because no N_2 absorption was observed at 77 K. Later, N_2 adsorption studies showed an anomalous step-like behavior, where the adsorption in ZIF-4 occurs at a threshold pressure of 35 KPa after which it reaches saturation. However, upon desorption, some of the nitrogen molecules remained trapped in the pore [25]. Hence, two types of phase changes have been reported for nitrogen adsorption at 77 K, where the framework undergoes a transition from a low pore to expanded pore and then from an expanded pore to open pore [26]. The significance of structural flexibility was underscored when reports of adsorption of C_2 and C_3 hydrocarbons was shown under ambient conditions [27]. Despite detailed synchrotron XRD studies, adsorption, and neutron studies, the resulting phases and mechanism differ between studies and methodologies. Moreover, the sites of gas adsorption in ZIF-4 are not well-studied and the literature is limited.

In our studies, we present the microscopic picture of the changes in the ZIF-4 framework under vacuum and guest (N_2, CO_2, and Ar) adsorption using Raman spectroscopy. The study focuses on the role of imidazole (Im) and its molecular changes under various perturbations (especially vaccum conditions act as a control for differing between temperature-induced and guest-induced transitions) to understand the structural changes and the adsorption sites in ZIF-4. Hence, highlighting the mechanism of gas adsorption in ZIF-4 crystals. Interestingly, we observed a new transition around 253 K under guest-free conditions resulting in a contraction of the pore in the synthesized crystal. This transition can be reversed by the introduction of guest molecules in the given temperature regime. Gas adsorption study shows signature of N_2 and CO_2 molecules even under ambient conditions (293 K, 1 atm), which has not been reported before for ZIF-4. The N_2 adsorption under ambient conditions is not reported for any ZIF system to the best of our knowledge. In addition, we also identified a guest-induced gate-opening process under N_2 and Ar molecules around 153 K which resulted in opening up of new sites inside the pore characterised by significant changes in the low-wavenumber Raman spectral region, Im

molecular modes, and N_2 vibrational modes. The obtained results were confirmed using well-accepted adsorption isotherms and first-principle calculations as well. The critical Raman spectral analysis obtained for ZIF-4 under no guest and guests (N_2, Ar, CO_2) conditions ensued in determining the adsorption sites for guest molecules experimentally for the first time.

4.3 Experimental Section

4.3.1 Synthesis of ZIF-4 microcrystals (mZIF-4)

mZIF4 were prepared using a solvothermal process. The temperature conditions were slightly modified from the reported literature [1, 25]. $Zn(NO_3)_2.4H_2O$, Im, and N, N dimethyl Formamide (DMF) were obtained from Sigma-Aldrich (Merck). All chemicals and reagents were used without any further purifications. In a beaker, $Zn(NO_3)_2.4H_2O$ (0.476 g, 1.8 mmol) was dissolved in 21 mL of DMF using a magnetic stirrer. To it, Im (0.35 g, 5.1 mmol) dissolved in 21 mL of DMF was added and stirred until homogeneous for about 10 minutes. The solution was then poured in a PTFE/Teflon vial, closed using the threaded lid, and placed in an isothermal oven at 85°C for 48 hrs. The solution was cooled naturally after two days and decanted to obtain transparent crystals. The crystals were dispersed and filtered using DCM (40 mL X 3) and further washed using DMF (40 mL X 3). The obtained product was then air dried for 1 hr (Yield=12.6 %).

The product obtained constituted of solvent within its pores, namely DMF and water molecules. The crystals were desolvated using a vacuum oven at 120°C overnight or more. The crystal structure remains intact as confirmed by XRD. The desolvated crystals (ZIF-4(DS)) were used for all Raman measurements under different gases and vacuum conditions.

4.3.2 Characterisations

Synchrotron XRD measurements were carried out at Xpress beamline of the Elettra, Trieste, Italy with photons of $\lambda = 0.4957$ Å and a PILATUS3S-6M detector. Brunauer-

Emmett-Teller (BET) adsorption measurements of ZIF4-DS crystals were measured with a Quantachrome Autosorb iQ2 unit. Before the BET measurement, the samples were degassed at 393 K under vacuum for 12 h. Thermogravimetric (TGA) data was acquired with a TA Q-50 unit. Morphological analysis was carried out using Zeiss Gemini SEM500. Dielectric properties were measured on a 0.26 mm thick disc of 5 mm diameter, coated with silver paste on both sides to give contacts, while controlling the temperature using Physical Property Measurement System (PPMS).

4.3.3 Raman Measurements

All Raman Spectroscopic measurements were carried using a He-Ne laser of 633 nm excitation wavelength and a grating of 1800 grooves/mm. The laser was focused using a 50 X objective lens (NA = 0.5) with ∼5 mW power at the sample. The accumulation time for each spectrum recorded was 60 s. Each spectrum was accumulated twice for reproducibility. Prior to the experiment, the sample was evacuated in a vacuum oven at 120 °C for 12 hours. The pre-evacuation step is necessary because we observed N_2 peak (ν_1 = 2326 cm^{-1}) under Ar and CO_2 atmosphere when this step was skipped. Hence, it is important to remove off the N_2 molecules (from air) which may have strongly bound to the ZIF-4(DS) system.

Samples were mounted on the stage and heated to 373 K. The sample was then activated at 373 K temperature for about 45 minutes to get rid of any absorbed moisture and other species during loading of the sample. The chamber was then purged for ten minutes with a particular gas (N_2, Ar, CO_2) using an external gas line connected to the Linkam stage. The stage was then brought to 293 K and the gas atmosphere was maintained at ∼1 atm. Raman studies that were carried under vacuum required no additional steps other than the pre-evacuation step discussed above.

For each experiment, Raman spectra were recorded at every 10 K temperature step. All spectra recorded were smoothened using Savitzky Golay (5 points) method, background subtracted, and then area-normalized with respect to the total integral area. Background subtraction was carried by a two-step process. In the first step, the spectral region from 50-300 cm^{-1} was subtracted using an exponential background as it lies close

to the Rayleigh cut-off which decays exponentially. In the second step, the spectral region from 500-3200 cm^{-1} was subtracted manually by creating a baseline.

For Chapter 4, gaussian calculations were carried out using Gaussian 16 [28] for assignments of all the modes due to lack of complete picture in the literature. However, to maintain the flow of reading, the details have been placed in Appendix A.

4.4 Results and Discussions

4.4.1 Structural characterisation of ZIF-4(DS)

Figure 4.2a shows the Rietveld refined synchrotron diffraction data of the desolvated compound at 300 K. The analysis of this data confirmed that this compound crystallizes in orthorhombic structure with space group *Pbca* similar to the previously reported results [24]. The lattice parameters and the reliability factors obtained from the refinement are shown in Table 4.1. The obtained crystal structure of ZIF-4(DS) is shown in Figure 4.2b. It has an elongated narrow pore (np) surrounded by a six-membered ring on opposite faces, with four-membered ring as the bridge structure [23]. The diameter of the largest window is 0.2 nm and the largest cavity is 0.49 nm. This structure contains two inequivalent Zn atoms, each of which is connected to four Im linkers. However, one pore constitutes of only two of these Im linkers, and the other two are part of another pore. Consequently, the Im linkers are in different environments. This structural understanding explains the multiplicity in almost all the modes obtained in the Raman spectra of ZIF-4(DS), which will be discussed subsequently.

The TGA data shows that both the samples of ZIF-4 with and without solvent have water molecules (Figure 4.3). In the case of ZIF-4(DS), it could be adsorbed from the atmosphere thus making the activation step essential before doing the Raman measurement. ZIFs are commonly hydrophobic, however, water (kinetic diameter = 0.26 nm) adsorption is favorable in few ZIFs spontaneously due to the Lewis acidic nature of C-H of imidazoles [29]. The desolvated sample starts decomposing at 450 °C as compared to the as-synthesized sample which begins to decompose at ∼600 °C suggesting the importance of solvent molecules in stabilizing the structure of the ZIF-4 molecules [30]. The

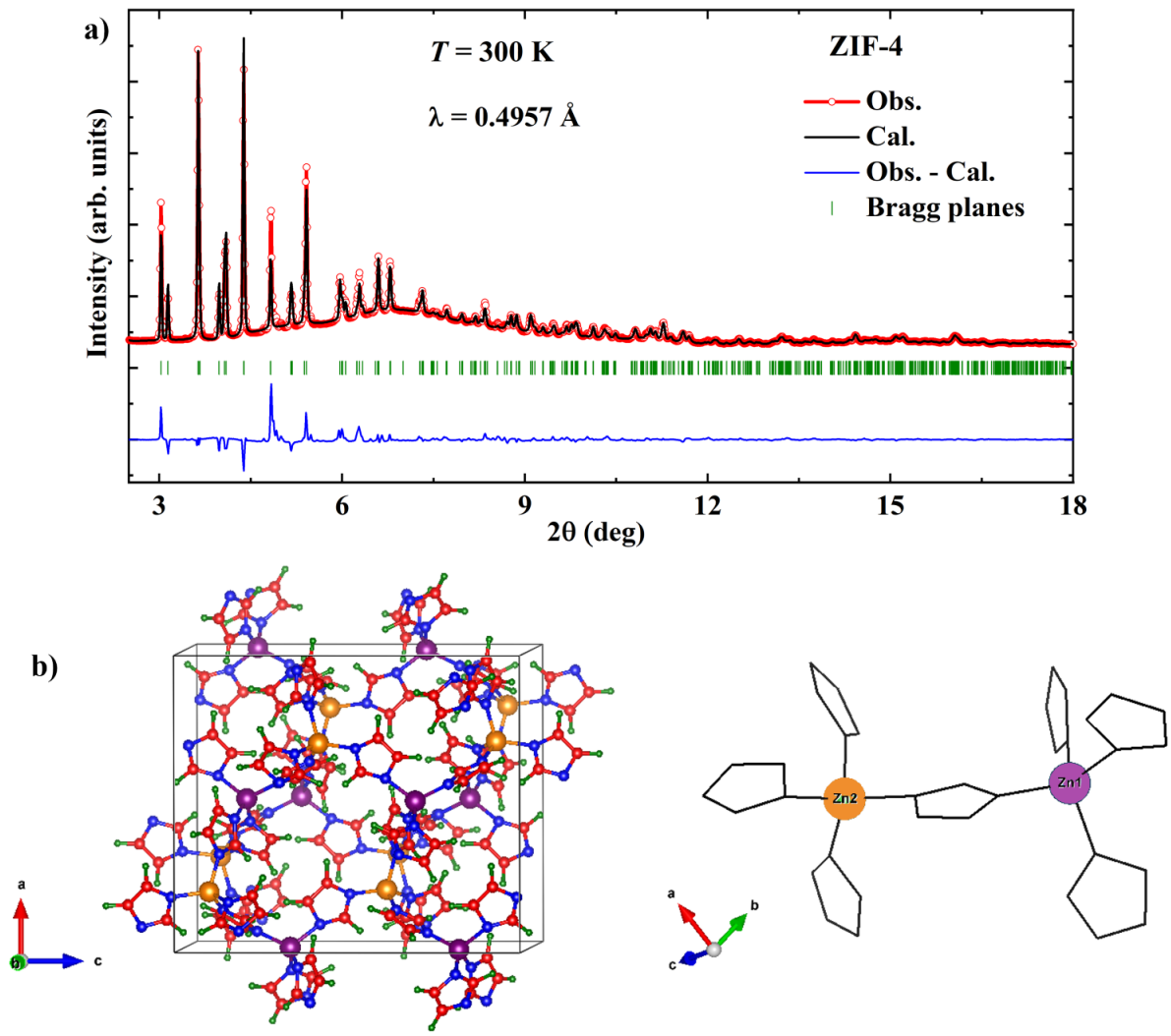

Figure 4.2: a) Rietveld refinement for the ZIF-4(DS) obtained under ambient conditions. b) Crystal structure obtained after refinement. The structure shows presence of two inequivalent Zn atoms in the structure with tetrahedral coordination with the Im linkers. *Refinement was carried out by Dr. Premakumar Yanda at JNCASR.*

ZIF-4(DS)	
Space group	*Pbca*
a [Å]	15.4969[16]
b [Å]	15.5316[15]
c [Å]	18.0870[20]
R_p/R_{wp}/GOF	2.94 %/5.27 %/ 0.87

Table 4.1: Lattice parameters and the reliability factors from the Rietveld refinement of ZIF-4(DS)

textural and morphological characterisations were carried using SEM measurements. The crystals form flower-like arrangement with crystallite sizes ranging from few micrometres to tens of micrometres (Figure 4.4a).

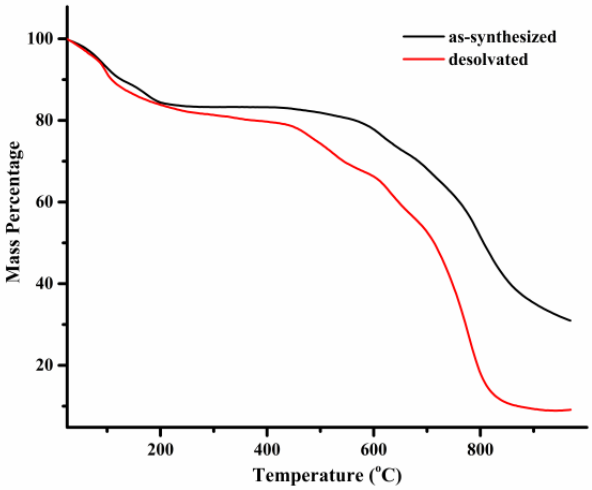

Figure 4.3: Thermogravimetric Analysis (TGA) data for ZIF-4 as-synthesized (black curve) and desolvated one (red curve). Decomposition temperature commences at 450 °C for desolvated one and at 600 °C for the as-synthesized sample.

ZIF-4 is amongst the certain group of MOFs that show gate-opening behavior at the increasing pressure of guest molecules [31, 30]. However, unlike other MOFs and ZIFs, it does not have bulky ligands wherein the steric repulsions or at-times repulsive interactions are generally the driving force for such gate-opening behavior. In ZIF-4, the rigid unit modes described by collective low-frequency vibrations play a significant role in entropy-stabilized open pore structures and dispersion stabilised closed pore structures

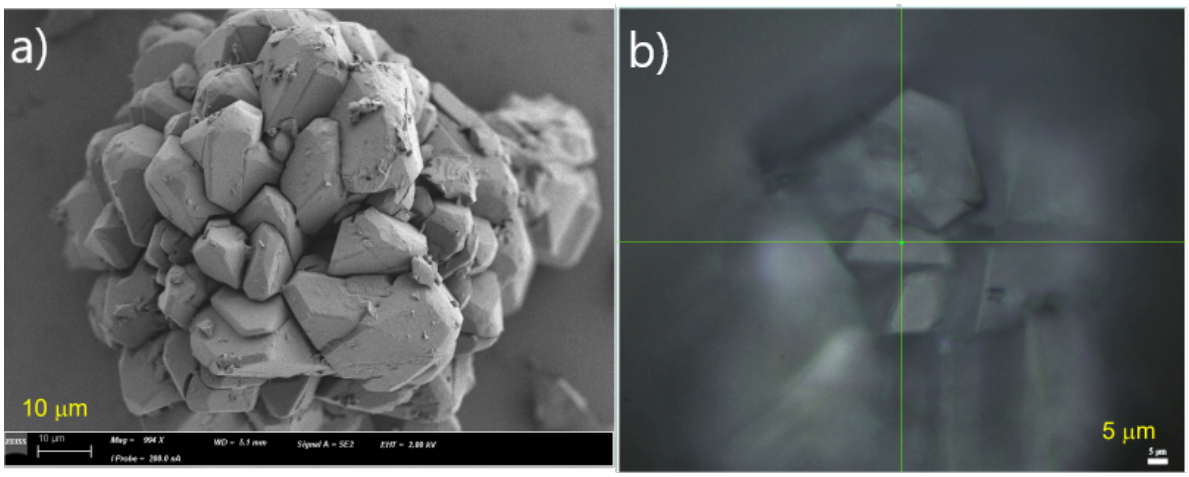

Figure 4.4: Size and texture of the ZIF-4(DS) crystals as observed under. a) SEM image obtained on a Si substrate and b) Image under the optical microscope. The green cross bar represents the laser spot.

[32]. To gain insights into microscopical structural changes of the framework leading to phase transitions in ZIF-4(DS), we studied it as a function of temperature, and in presence/absence of different guest molecules using Raman scattering as the primary tool.

4.4.2 Room Temperature Raman Spectra of ZIF-4(DS)

Raman spectra were collected by focussing 633 nm laser beam through the 50 X objective (N.A = 0.5) on one of the outgrown crystallites shown in Figure 4.4b. The room temperature (RT = 293 K) Raman spectrum of ZIF-4(DS) crystal shown in Figure 4.5, is dominated by the intense modes in the fingerprint region ∼1000-1500 cm^{-1} and high wavenumber region ∼3000 cm^{-1}. Raman spectral analysis was partially carried based on previous publications on vibrational studies of imidazole, its derivatives, and other ZIF systems [33, 34, 20, 35]. However, for more detailed analysis and understanding of low frequency modes, we performed density functional theory (DFT) calculations on a model system composed of four imidazoles coordinated to zinc atoms (details in Appendix A). The detailed peak assignments obtained for ZIF-4 are listed in the Table 4.2 and Appendix Table A.1.

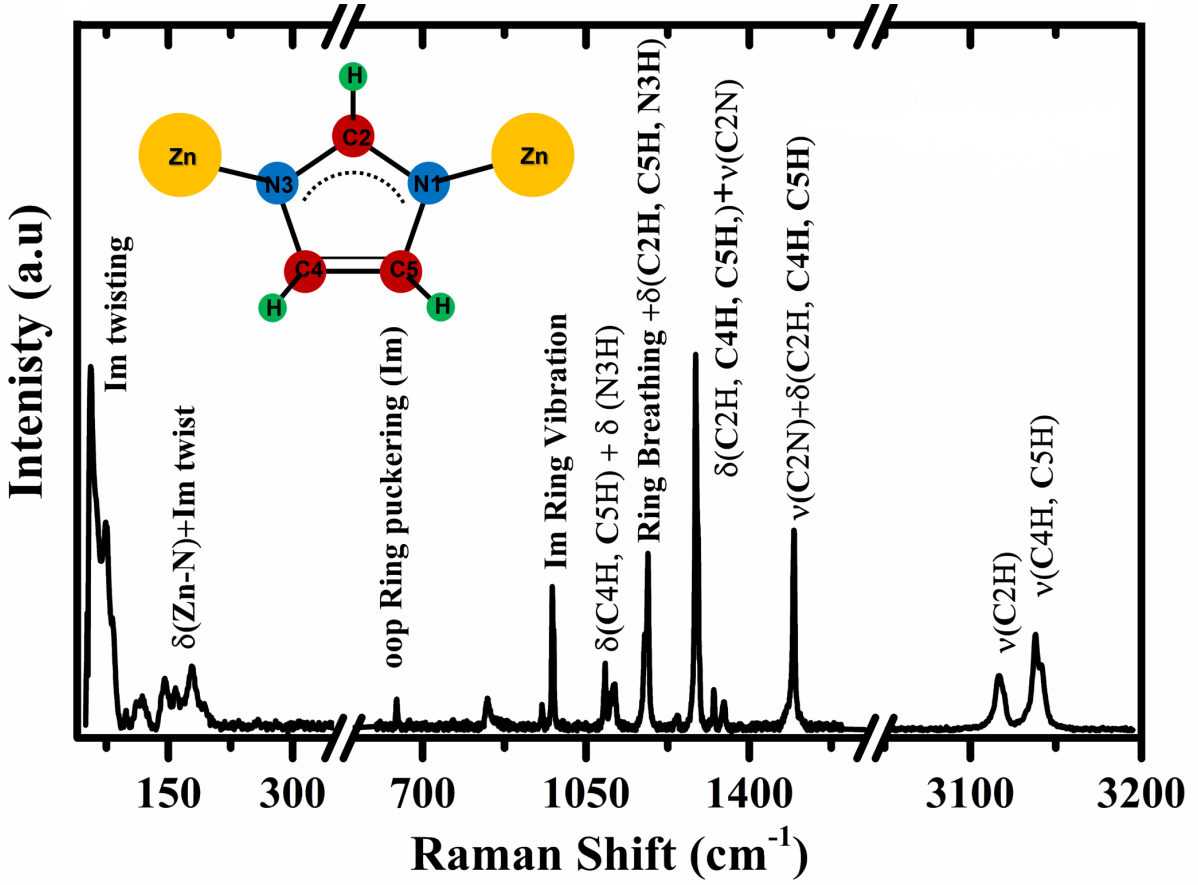

Figure 4.5: Raman spectra obtained for ZIF-4(DS) at 293 K. Schematic representation of M-Im-M for the nomenclatures used in assigning the modes.

Experimental wavenumber (cm^{-1})	**Band Assignments [23, 33]**	**Peak assignments based on computational data†**
62 75 84 98	6-Membered and 4-Membered Ring deformations (Ligand Rocking)	4 Imdz ring twisting wrt Zn-N axis
111 119	Not assigned	Not assigned
146	Not assigned	Ring δ_{oop} (4 Im)
159	n Zn-N	Ring δ_{oop} (4 Imdz) leads to lattice vibration

†ν = stretching; sym = symmetric, asym = asymmetric, δ = bending; r = rocking, t = twisting, w = wagging, s = scissoring, oop = out-of-plane

179		
643 645	δ_{oop} Ring	oop Ring puckering (Im), lattice vib
839	γ_{asym} C-H	δ_w (C2H, in-sync C4H, C5H)
955 977 980	Ring deformation	Im ring vibration
1086 1088 1091	d C-H (ar)	δ_s (C4H, C5H)+ δ (N3H)
1102 1107 1111	Ring deformation + δ (C-H)	δ (C2H, N3H)+ ν (C5N1)+ ν (C4N3)
1176 1183	ν_{asym}(C2N1+C4N3+C4C5) + γ N-H	Im ring breathing + δ_r (C2H, C5H, N3H)
1285 1287 1290 1294	ν C-N + δ C-H	δ_r (C2H, C4H, C5H, N3H) + n(N3C2N1)
1323	ν_{asym} (C2N3,C5N1) + δ_w (C4H, C2H, C5H)	δ_w (C4H, C5H) + ν_{asym} (Im)
1345	Not assigned	
1495	ν_{asym}(C4C5+C2N3+N1C2) + δ(C5H+C2H)	ν_{asym}(N1C2N3) + δ_r (C2H, C4H, C5H)
3119	ν C-H (ar)	ν_{asym} (C4H, C5H)
3138		ν (C2H)
3142		ν_{sym} (C4H, C5H)

Table 4.2: Peak Assignments for all the modes obtained at 293 K

The most intense peaks are observed around i) 1280 cm^{-1} corresponding to C-H rocking and N-C-N stretching modes, ii) 1180 cm^{-1} corresponding to imidazole ring breathing

and C-H bending modes, iii) 1480 cm^{-1} corresponding to N-C-N stretch and C-H bending modes, iv) 3100 cm^{-1} corresponding to C-H stretching modes, while the low-wavenumber region is dominated by vibrational peaks around 65-80 cm^{-1} region attributed to collective imidazole twisting vibrations, metal-ligand bonds and lattice vibrations.

4.4.3 Effect of temperature on ZIF-4(DS)

4.4.3.1 Raman spectral changes on ZIF-4(DS) with temperature

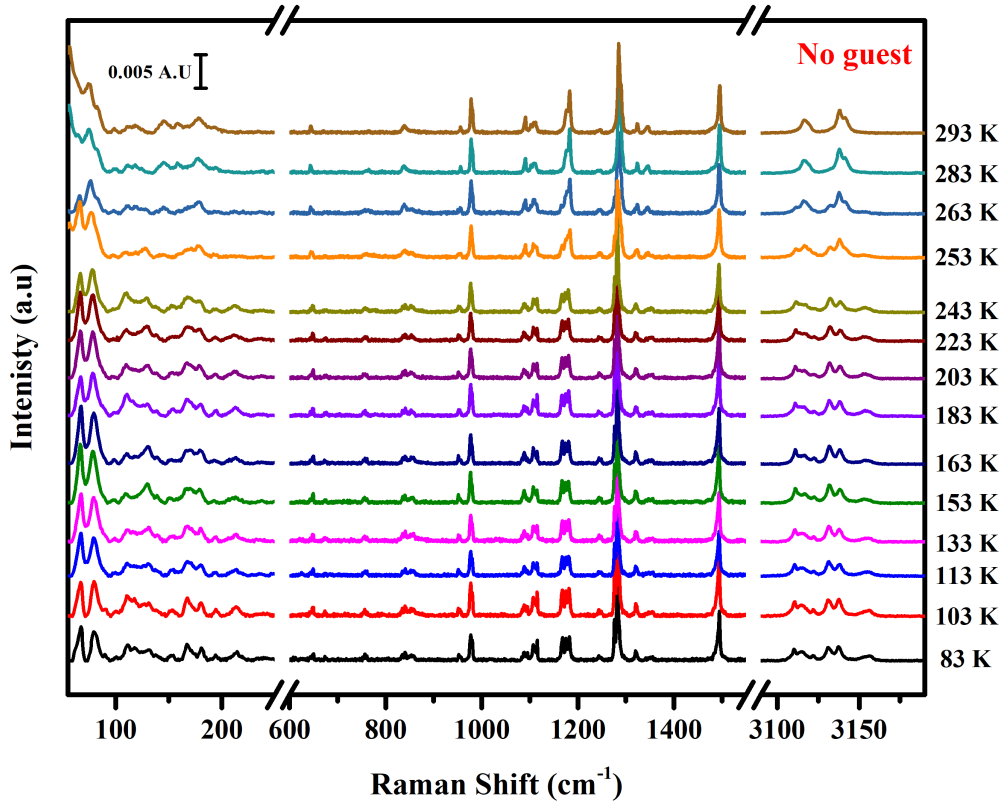

Figure 4.6: Temperature dependent Raman spectra for desolvated ZIF-4 under Vacuum

To understand the influence of only temperature on ZIF-4 (DS) crystals, Raman spectral measurements were carried out in vacuum. To the best of our knowledge, this is a first vibrational spectroscopy's report of a completely guest-free measurement on a ZIF system. ZIF-4(DS) crystals were pre-evacuated and loaded onto the platform of the cryostation s50. The cryo-stage was allowed to cool to 83 K in 150 minutes. Raman spectra were collected on two separate crystals at every 10 K going from 83 to

293 K. Figure 4.6 presents the stack plot of Raman spectra of ZIF-4(DS) collected at various temperatures. A noticeable shift in most of the vibrational modes was observed as temperature was raised from 83 K to 293 K around 253 K but not the reported open to close pore transition around 140 K by Wharmby *et al.*. Clear spectral changes in the temperature range between 273-253 K indicate a probable structural transition. Upon a closer look and peak fitting, significant changes were observed especially in the Im stretching and bending vibrations in the region 3000 cm^{-1}, 1280 cm^{-1} and 1180 cm^{-1}.

From Figure 4.7a - 4.7c, in the 273-253 K, we observe a reduced degeneracy in C-H stretching modes and Im ring expansion vibrations, whereas an increase in degeneracy in the in-plane C-H rocking modes. Such unambiguous changes in vibrational modes clearly suggest a structural re-organization or transition. In absence of any guest molecules, at low temperatures ∼253 K, there is reduced kinetic energy of system and the lattice is in a compressed state and hence have a high framework density. In such compact lattice, dispersion interactions start dominating over vibrational entropy at low temperatures [32]. These interactions may result into electron density redistribution or change in dipole moment in selective C-H modes. In the case of ZIF-4(DS), several types of dispersive interactions such as C-H$\cdots\pi$, $\pi\cdots\pi$, and C-H$\cdots$H-C interactions may become significant at low temperatures thereby reducing the degeneracy in imidazoles. Because all imidazoles do not experience similar changes in their environment on the account of being inherently different, the lifting in degeneracy occurs. Such differences between the Im ring moiety makes the analysis of especially the C-H stretching modes rather complex as observed in Figure 4.7d between 3120-3131 cm^{-1}. Hence, we focus on the clear changes in the spectral region. From the Raman plots, we observe a decrease in intensities in the C-H stretching modes (Figure 4.7a), new peak at 3150 cm^{-1} (Figure 4.7d marked by red circles), and a red-shift in the C-H rocking modes in the temperature studied regime (Figure 4.7b and 4.7e). Previously, such blue-shifts in stretching modes and red-shifts in the bending modes followed by decrease in their intensities have been associated with different types of H-bonding in a system. It is possible that in order to prevent the pore from collapsing such intra-framework interactions like C-H$\cdots\pi$ H-bonding may appear and could lead to the spectral shifts that were observed [36, 37]. Additionally, below 273 K, the ring breathing modes coupled with C2-H and C5-H bending modes at 1176 and 1185 cm^{-1} red-shift by 5-10 cm^{-1} and split into 1166, 1174, and 1180 cm^{-1} along with

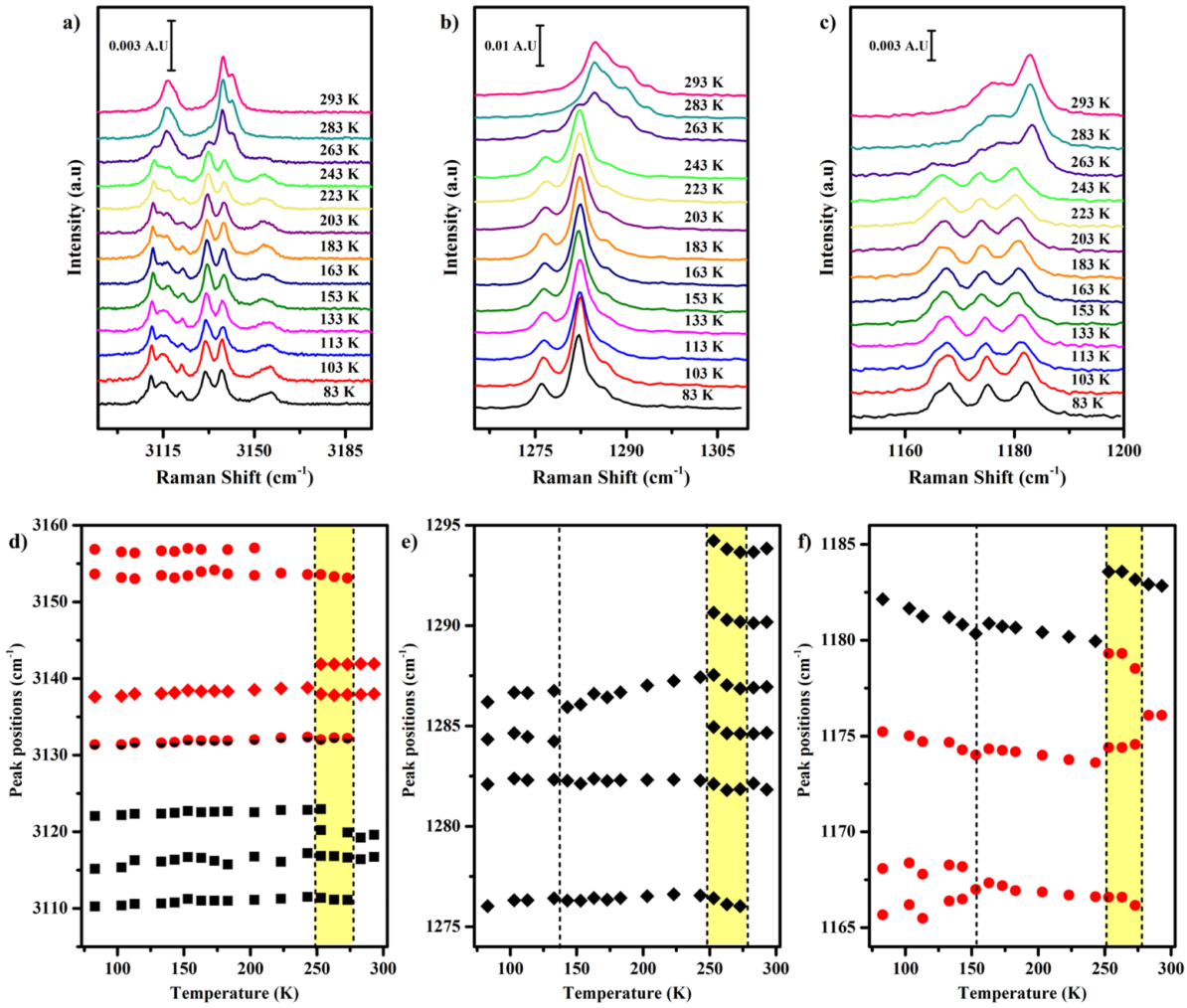

Figure 4.7: In the top panel from a) to c) shows the temperature-dependent Raman spectra obtained for ZIF-4(DS) under vacuum for selected regions. The bottom panel from d) to f) displays peak positions versus temperature for the selected regions. a) & d) Symmetric and anti-symmetric C2-H, C4-H, C5-H stretching modes, b) & e) C2-H, C4-H, & C5H rocking modes with N3-C2-N1 str c) & f) Im ring breathing with δ (C2-H, C5-H) modes.

decrease in their peak intensities (Figure 4.7c and 4.7f) suggesting an increase towards a more non-planar geometry, thus lowering the symmetry and hence activation of more number of modes [38]. A further slope change and splitting of the mode of 1166 cm^{-1} is observed around 150 K suggesting further reorganization of the Im ring moieties due to intra-framework interactions. Therefore, these results underpin a change in orientation or a tilt in the angles of the Im moiety with respect to each other resulting from C-H$\cdots\pi$ and $\pi\cdots\pi$ interactions.

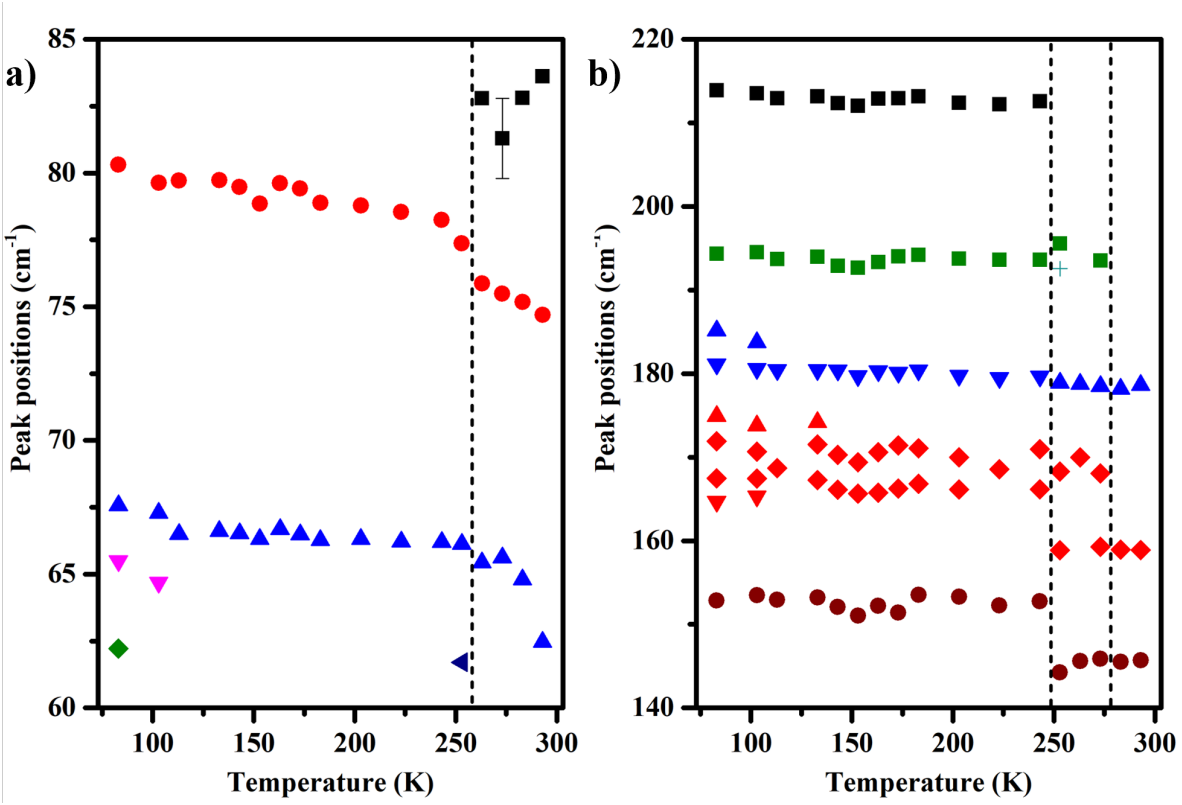

Figure 4.8: Peak positions versus temperature for ZIF-4(DS) under vacuum a) Im twisting symmetric and asymmetric b) Zn-N bending coupled with Im twisting.

The rigid unit modes have unique spectral signatures upon changes in the lattice occurring due to deformation of the network, rotation of linkers, or gas adsorption (discussed in Chapter 1, Section 1.3.4) In this case, at 293 K, three Im ring twisting modes are observed at 63 cm^{-1} corresponding to asymmetric Im ring twisting and at 75 and 84 cm^{-1} corresponding to symmetric Im ring twisting modes. However, below 273 K, the Im twisting mode at 63 cm^{-1} increases in intensity and blue-shifts while the 75 and 84 cm^{-1} become degenerate, although their peak intensifies underscoring the closing of the pore (Figure 4.6 and 4.8a). Similar kind of intensity correlations in asymmetric and sym-

metric linker twisting in ZIF-8 has been previously associated with pore volume changes [39]. Simultaneously, all the modes in the range of 100-200 cm^{-1} corresponding to Zn-N bending modes and Im ring twisting blue-shift (Figure 4.8b). These stiffened, sharp, and reduced number of Im ring twisting modes underpins the fact that there is an increase in intramolecular interactions resulting in the closing of the pore. The ring deformation modes of ZIF-4(DS) at 980 cm^{-1} presented in Figure 4.9 do not show any noticeable change suggesting absence of linker deformations upon lowering of temperature. These spectral changes strongly suggest the dominant role of linker rotation or tilt leading to dispersive interactions indicating a transition from open to narrow pore in ZIF-4(DS) below 253 K.

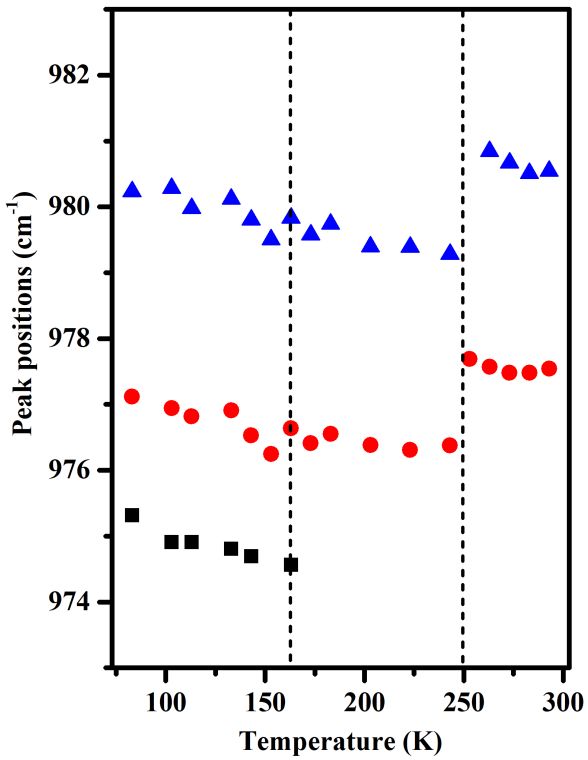

Figure 4.9: Peak positions versus temperature for ZIF-4(DS) under vacuum in the 980 region (δ_s C4-C5 + δ (C2N1+C2N3) + ν Zn-N)

4.4.3.2 Dielectric studies on ZIF(DS)

Dielectric studies were carried to further confirm any changes in the molecular orientation of the molecule. Microscopically, dielectric loss is dependent on ionic displacement, dipolar reorientation, and electronic polarizations [14]. In many dielectric materials including

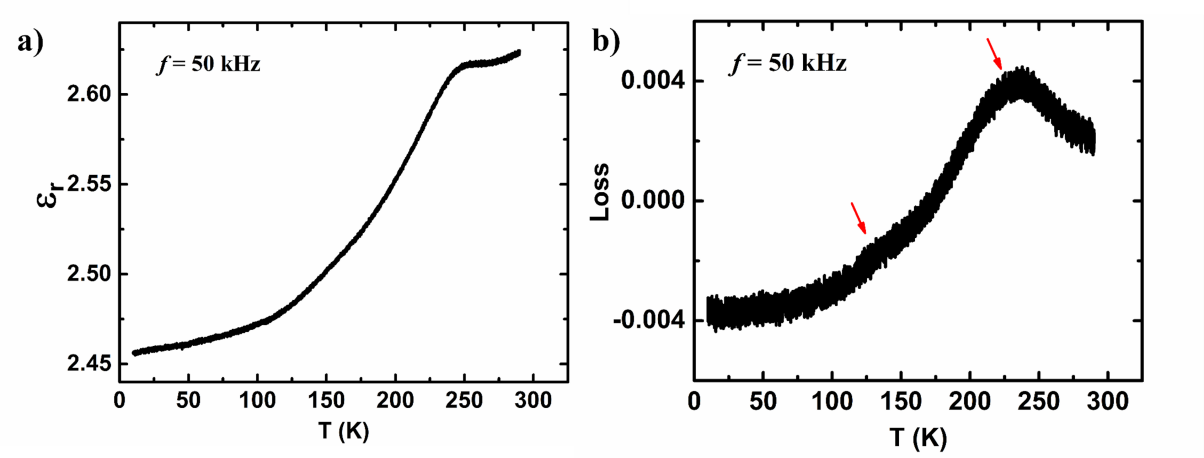

Figure 4.10: a) Dielectric constant of ZIF-4 (DS) with temperature. b) Dielectric loss of ZIF-4 (DS) disc with temperature. The arrows mark the transition region of dipolar rearrangement.

porous materials, a dielectric switching occurs due to dipolar reorientation. When the pore of any MOF/ZIF is empty, the dielectric response of the system is low and hence, we would expect a low dielectric constant. Dielectric measurements carried out on a pellet of thickness 0.26 mm and diameter 15 mm of ZIF-4(DS) yields a value of dielectric constant, $\varepsilon_r \sim 2.45$ at 50 kHz, as shown in Figure 4.10a ($\varepsilon_r = 2.33$ for ZIF-8 at 100 kHz [40]). From the dielectric loss plot as seen in the Figure 4.10b, we observe two temperature ranges ~230 K and 140 K over which a broad relaxation occurs. Both these dielectric transitions corresponded well with our low-temperature Raman studies carried under vacuum. Since there is no first-order structure phase transition in ZIF-4(DS), we do not expect sharp variations in the dielectric studies. Changes in the slope observed in our measurements indicate alterations in dipole and orientational polarizations associated with transitions in framework [40, 41]. Recently, in ZIF-90, similar dipolar relaxations in the dielectric loss behaviour under vacuum was observed which was associated with twisting dynamics of imidazolate-2-carboxyaldeyde linker in the material confirming soft porosity in the material [41].

It is interesting to note that, this open-to-narrow pore transition around 253 K has not been reported before in the ZIF-4 crystals. Previously, Gandara *et al.* [26] and Wharmby *et al.* [24], have discussed the high density to low density phase transition in ZIF-4 crystals of size ~600 μm at 140 K leading to a 23 % volume contraction. However, in our Raman

studies, we do not observe any detectable changes in that temperature regime under guest free conditions. The authors mentioned that the reported volume contraction can vary from 23 % to as low as 1 % depending upon the size of the crystal, and since our crystals were relatively small (∼10 - 20 μm), we do not detect any volume contraction. From our Raman spectroscopy studies under vacuum with the support of dielectric measurements, we suggests that for ZIF-4(DS) system, Im ring reorientation facilitated by a dominant C-H$\cdots\pi$ interactions occurs around 253 K and a second transition due to a tiny volume contraction around 150 K occurs thereby resulting in open-pore → narrow-pore → closed-pore phase transitions. To obtain a microscopic picture on the gas adsorption behaviour with ZIF-4(DS), temperature-dependent Raman measurements under guest conditions were performed.

4.4.4 Structural changes on ZIF-4(DS) under Guest Atmosphere

After a pre-evacuation step in a vacuum oven overnight at 393 K to remove any adsorbed gases and moisture, the sample was loaded on Linkam THMS600 and activated again at 373 K for 45 minutes to remove any gases/moisture that may have adsorbed into sample during the loading process. The chamber was then purged for ten minutes with the gas (N_2, Ar, or CO_2) of interest using an external gas line connected to the Linkam stage. The stage was then cooled to 293 K while maintaining the gas atmosphere at 1 atm. Raman spectra were recorded at every 10 K step from 293 to 77 K with multiple accumulations for accuracy.

4.4.4.1 Raman spectral changes in N_2 and Ar atmosphere

Figure 4.11 shows the stack plot for the temperature evolution of the Raman spectra under different gases, N_2 and Ar. Inherently both the gases are inert in nature, however N_2 gas adsorption behaviour seen from BET isotherm in literature is intriguing as discussed in the introduction [25]. Thus, carrying the measurements and analysing the data with using Ar as a control system in addition to vacuum conditions would provide a better understanding of the spectral changes specific to the N_2 molecules versus spectral changes with guests in general. Upon glancing at the stack plots shown in Figure 4.11, it is evident

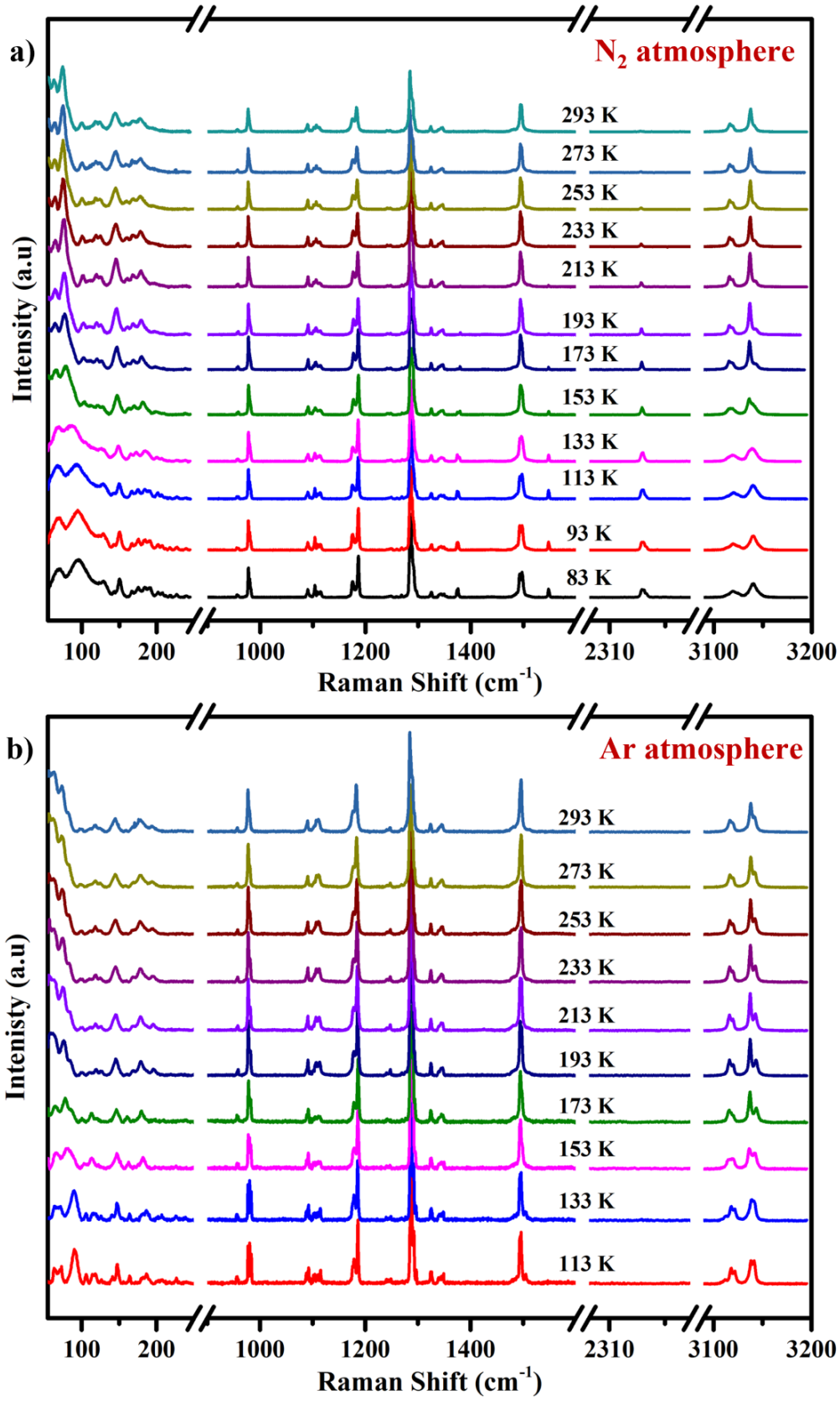

Figure 4.11: Temperature dependent Raman spectra for ZIF-4(DS) under a) Nitrogen and b) Argon atmosphere.

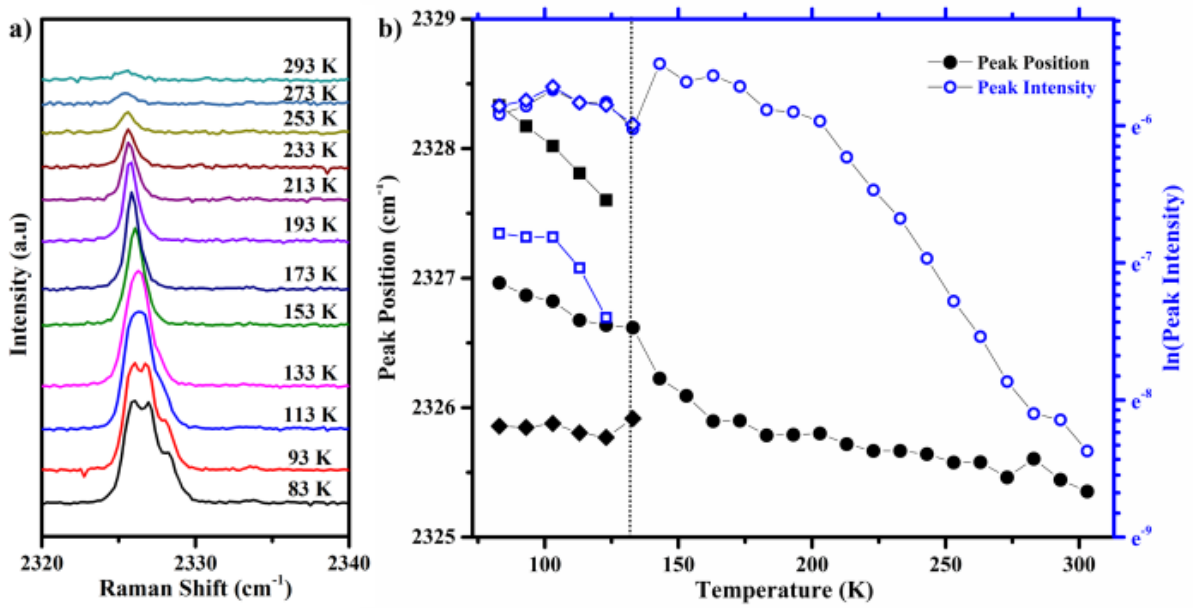

Figure 4.12: a) Temperature dependent Raman spectra obtained for ZIF-4(DS) under N_2 atmosphere showing the ν_1 stretching mode of adsorbed N_2. b) Peak positions versus temperature (black curves) plot showing three types of adsorptions and the intensity plot of the same (blue curve).

that in both conditions, no drastic Raman spectral changes in the temperature regime of 273-253 K as seen under guest-free conditions. This suggests that, the guest molecules are compensating for the transition by interacting with the framework. Secondly, there are a few differences observed between the two gases, namely presence of the ν_{N-N} stretching mode in the 2300 cm^{-1} region which is absent in Ar for obvious reasons. Additionally, in case of both the gases, spectral changes are observed below 173 K, although the nature of the spectral changes differ such as differences in peak features, broadening and others. We delve deeper into the analysis by focussing on specific regions for both gas adsorption and structural changes subsequently.

N_2 adsorption evolution with temperature using the ν_{N-N} stretching mode

The most fascinating feature in these measurements were the detection ν_{N-N} peak at 2326 cm^{-1} under ambient conditions (293 K, 1 atm). This peak is red-shifted from that of free N_2 molecules observed at 2331 cm^{-1}, suggesting entrapped N_2 molecules weakly adsorbed or physisorbed to the ZIF system (Also the possibility to detect free nitrogen at 293 K

is negligible) [42, 19]. From Figure 4.12, we notice that this peak blue-shifts while its intensity increases with decreasing temperature. At 133 K and 113 K, two distinct peaks appear. At 83 K, these peaks can be well-resolved into 2326, 2327, 2328 cm^{-1}. All these peaks are red-shifted from the 2331 cm^{-1} stretching mode observed for free N_2 molecules. Three distinct peaks observed for N_2 in ZIF-4 strongly indicate the presence of three different adsorption sites. The first adsorption, marked by the 2326 cm^{-1} peak occurs due to the dispersive interaction of the nitrogen molecules with the Im ring moiety and has been discussed in detail later. As the temperature is lowered, the density of the free N_2 molecules increases and multilayer formation may commence. Because of this adsorption stress, further expansion of the framework is triggered and hence the structural changes in the Im molecular modes were also observed below 153 K (will be discussed in the following sections). Such kinds of adsorption-induced deformation leading to structural changes, gate-opening or swelling of the pore is well-reported for soft porous crystals [43]. Therefore, the transition observed in our studies around 153 K is facilitated by the guest molecules only. Subsequently, the emergence of the new peak at 2325 cm^{-1} mode suggests opening of a new adsorption site. Concomitantly, we observe Raman structural changes which is discussed in detail in a later section. Finally, a third peak at 2328 cm^{-1} is indicative of a third site in the expanded structure where the N_2 molecules are weakly bound. No distinctive spectral changes in the Raman spectra were observed upon with the appearance of this peak. It is because of the expanded structure, that the guest molecules can finally occupy the cavity which may not be accessible in a narrow pore form at higher temperatures with low gas concentration. We will be referring to the ν_{N-N} position as the adsorption peaks observed at 83 K in the next section to explain the Raman spectral changes associated with the first two adsorptions of the guests. However, before that the BET isotherm for N_2 adsorption is presented motivated by the ν_{N-N} mode at 293 K.

N_2 Adsorption isotherm

The adsorption-desorption isotherm curve was obtained for N_2 adsorption of ZIF-4(DS). As shown in Figure 4.13, an uptake of 4 cc/g of N_2 gas on the ZIF-4(DS) at 298 K was obtained. This observation in BET isotherm has not been reported and confirms room temperature adsorption of N_2 on ZIF-4(DS). This uptake increased from 4 cc/g to 12 cc/g

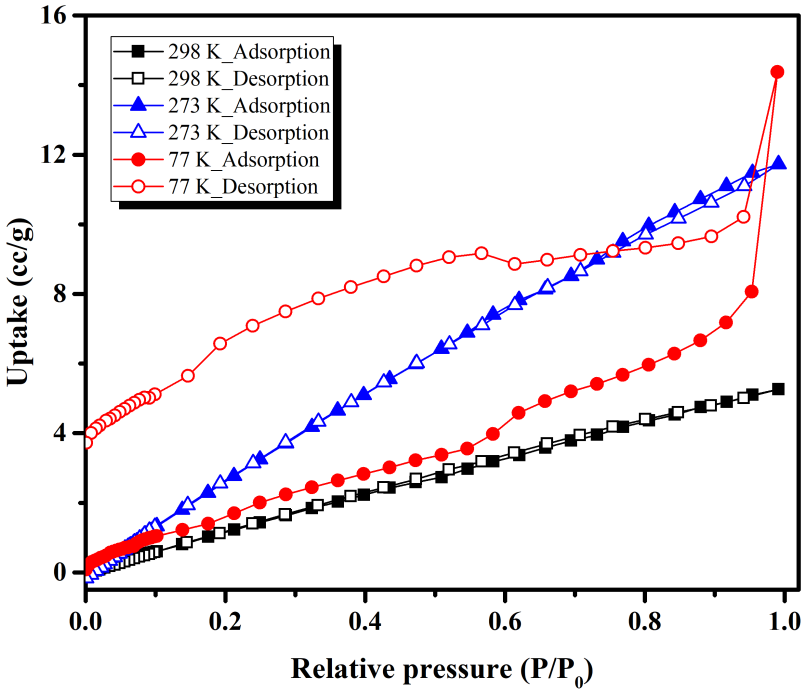

Figure 4.13: Adsorption-desorption isotherm of N_2 on ZIF-4(DS) obtained at 298, 273, and 77 K.

when recorded at 298 and 273 K respectively suggesting a sequential increase. However, the uptake of N_2 at 77 K holds an anomalous curve with a step 0.6-0.7 atm almost resembling the reported curve, where a step is observed around 0.35 atm [26]. Intriguingly, the uptake of the gas obtained is higher at 273 K than 77 K. The most plausible reason is the difference in the configuration of the ZIF-4(DS) framework at different temperature. The Raman studies carried in guest-free conditions established an open to narrow pore transition around 253 K upon lowering of temperature. Consequently, the N_2 adsorption obtained at 273 K is congruous to the open-pore configuration of ZIF-4(DS) whereas the adsorption occurs in a closed-pore framework at 77 K.

Structural changes associated with the first N_2 adsorbed peak at 2327 cm^{-1}

Since N_2 molecule signals were observed even under ambient conditions, the absence of open to narrow pore transition of ZIF-4 framework could be expected in the temperature region 273-253 K observed under no-guest conditions. Indeed, Figure 4.14 confirms the assumption since the C-H stretching modes around 3000 cm^{-1}, C-H rocking modes around

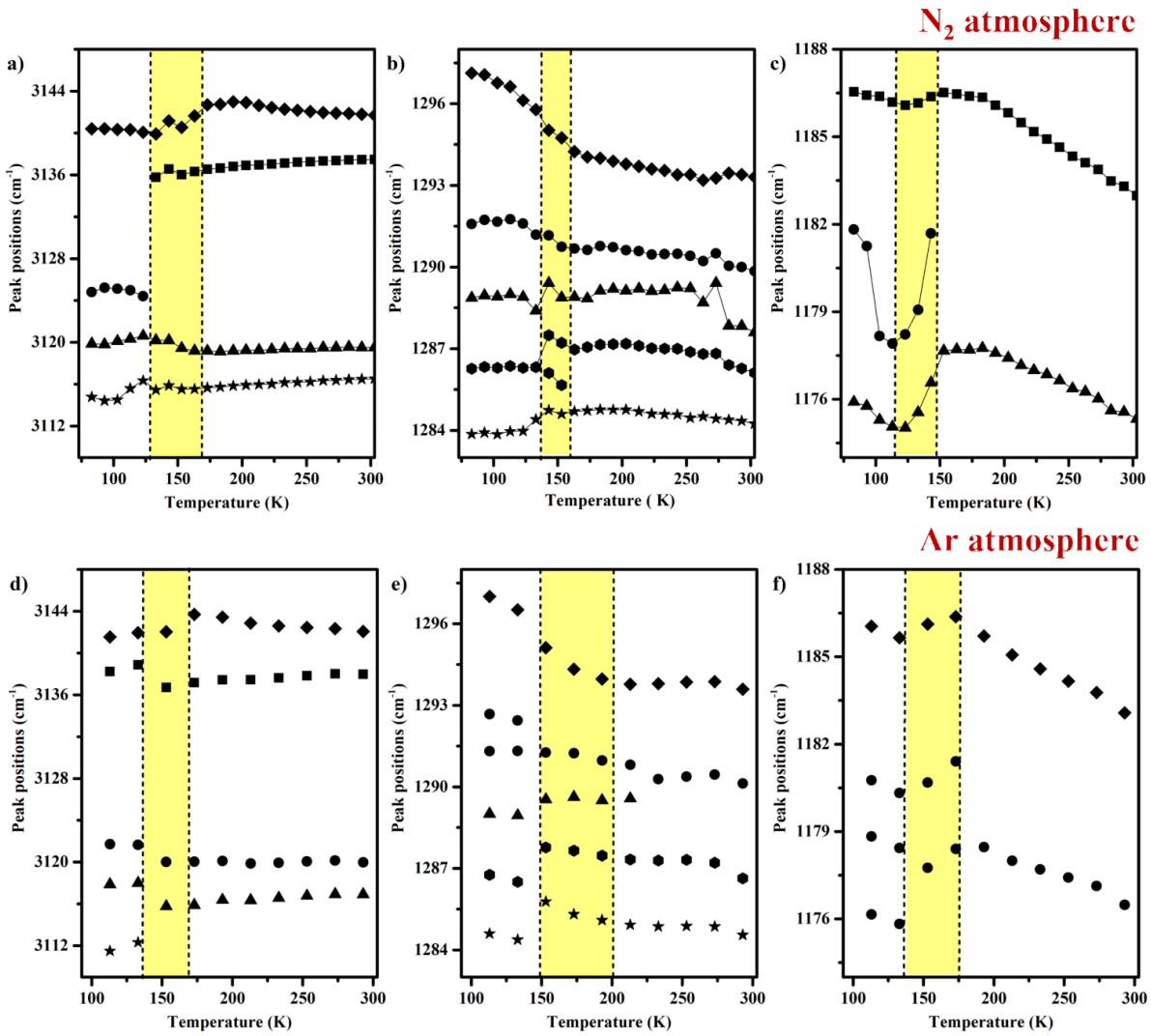

Figure 4.14: Peak positions versus temperature for ZIF-4(DS) for selected regions. a) & d) Symmetric and anti-symmetric C2-H, C4-H, C5-H stretching modes, b) & e) C2-H, C4-H, & C5H rocking modes with N3-C2-N1 stretching c) & f) Im ring breathing with δ (C2-H, C5-H) modes under N_2 & Ar atmospheres respectively.

1280 cm^{-1}, and even the ring expansion modes around 1180 cm^{-1} do not shift in position or any degeneracy lifting/suppressing under N_2 or Ar atmosphere in that temperature range. This suggests that in presence of gas molecules the structure remains intact, and stability is imparted from the host-guest interactions as opposed to intramolecular interactions within ZIF-4 network under vacuum conditions. Resemblance in the ambient Raman data in both vacuum and guest conditions suggests physisorption or Van der Waals such as dispersion interactions of guest (N_2, Ar) molecules with the framework.

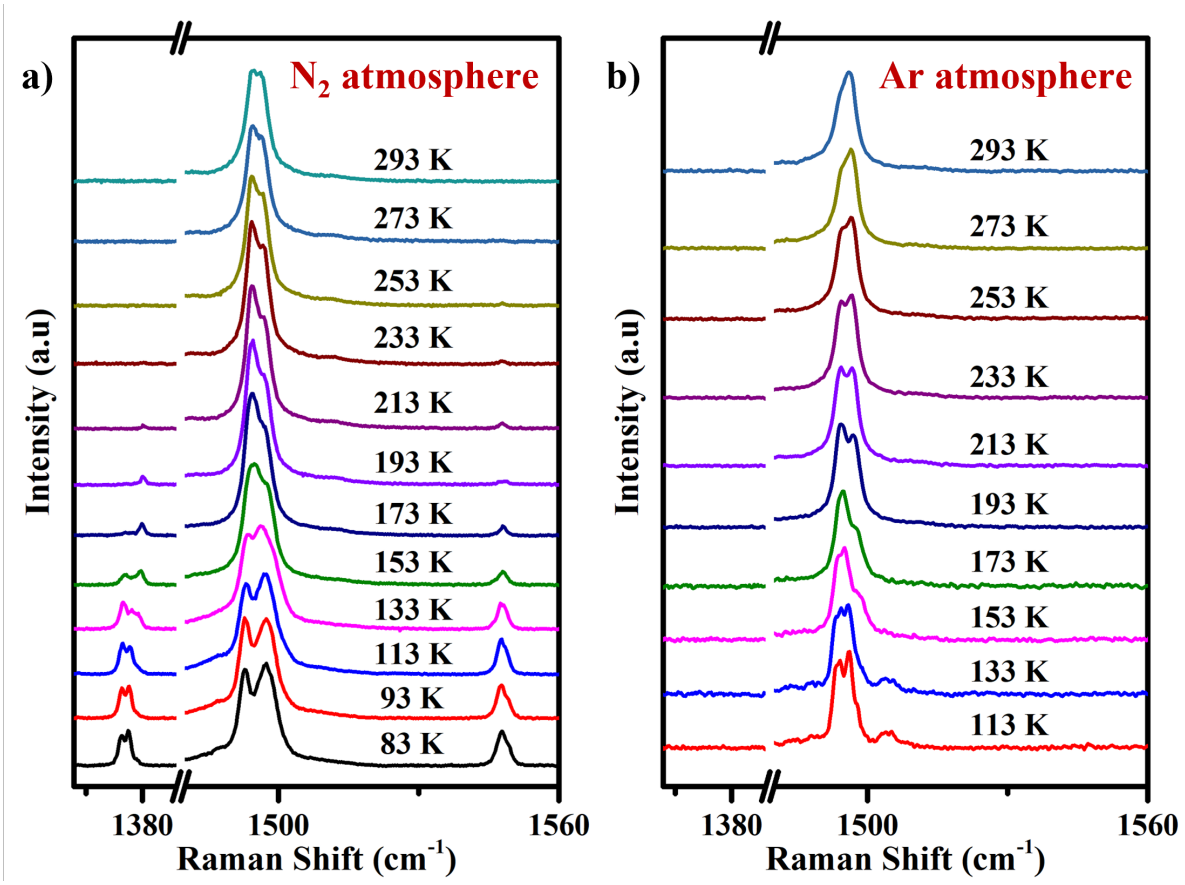

Figure 4.15: The temperature dependent Raman spectra obtained for ZIF-4(DS) for deformation mode of N1C2N3 stretch and C-H rocking (~1490 cm^{-1}) under a) N_2 gas and b) Ar gas. New modes appeared under N_2 atmosphere ~1550 cm^{-1} and ~1380 cm^{-1}. The changes in the intensity ratios in both a) and b) for the deformation mode is clear.

Interestingly, subtle spectral changes were observed from 293 K up to 160 K indicating of a dynamic gas interaction with the framework shown in Figure 4.15. A shifting trend in the 1490 cm^{-1} region, corresponding to the deformation mode of N1-C2-N3 stretch and all C-Hs rocking, of its peak line shapes was observed with lowering in temperature.

The trend in this region is evident for both the gas molecules N_2 and Ar, although the patterns are different. This result strongly suggests the interaction of the C-H centres with the gas molecules. Since, the predominant interactions will be dispersion interactions owing to the inert nature of the gases, the C-H and π cloud can be the only interacting sites [44]. However, any twist or change in the π centre would have resulted in elongation/compression of bonds [44] causing a peak shifts or broadening in the mode. The spectral changes observed here, points towards the shifting environment around the C-H centres.

Concomitantly, under N_2 atmosphere two new modes appear, one from 253 K at 1550 cm^{-1}, corresponding to C4=C5 stretching mode (refer to Appendix Table A.1) and another mode at 223 K corresponding to asymmetric C-N stretching mode shown in Figure 4.15a [45]. Because there existed an expected open-to-narrow pore transition at this point, more of adsorption sites are occupied to maintain the open pore of the framework. Moreover, an increase in the number of C-H wagging modes around 840 cm^{-1} was observed shown in Figure 4.16 indicating a lifting in its degeneracy [46]. This change in degeneracy may occur due to the presence of gas molecules which hinder the framework interactions or coupling of the modes.

These spectral changes were absent in the case of Ar visible in Figure 4.15b other than the trend with temperature being different. N_2 being diatomic can interact with the ligand in two different orientations – T-shaped interaction through its centre of mass and head-on interaction with either of the nitrogen in contrast to a single geometry possible for interaction of Ar atoms with the framework [47]. Because of multiple sites of interactions with N_2, the earlier Raman inactive modes become more polarizable because of changing environment around the C4, C5 centre and C2 centre subsequently. It is noteworthy, that the activation of the C4-C5 stretching mode strongly suggests the preference of C4 (or C5) for N_2 adsorption.

Structural changes associated with the second N_2 adsorbed peak at 2326 cm^{-1}

Figure 4.14a, b, and c show the Raman spectral changes in ZIF-4 upon N_2 incorporation at temperatures below 173 K. The C-H stretching modes reduce in intensity and peaks

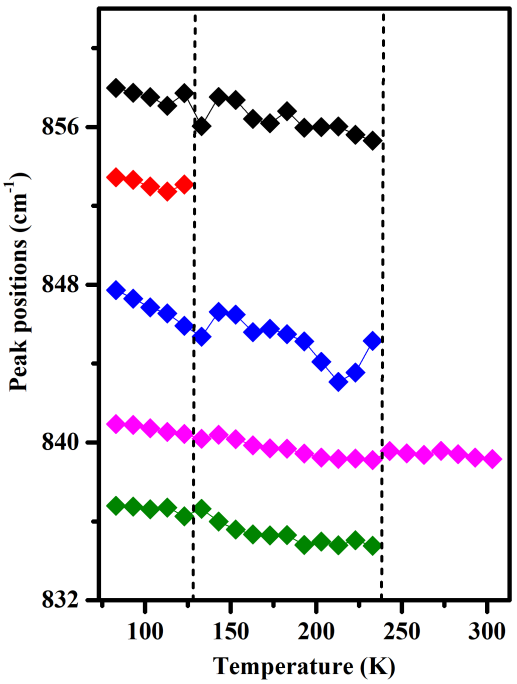

Figure 4.16: Peak position versus temperature plot for C-H wagging modes under N_2 atmosphere.

broaden (Figure 4.11a). Additionally, the C4-H and C5-H stretching modes (∼3140 cm^{-1}) become degenerate while the C2-H and C-H antisymmetric stretching modes (∼3120 cm^{-1}) lose degeneracy (Figure 4.14a). Furthermore, the peaks in the temperature regime from 1176-1186 cm^{-1} (Im ring breathing) display an anomalous behaviour shown in Figure 4.14c), wherein there is an increase in the number of modes, softening of the modes below 153 K up to 123 K and then stiffen until 83 K. Since, this region is associated with Im ring breathing, the rotation/tilting of the Im ring will greatly influence the number and behaviour of the modes. Alongside, the peaks around 1280 cm^{-1} (N3-C2-N1 stretch and C-H rocking modes) undergo a gradual but substantial change in the intensity ratio of the peaks. The number of modes in the temperature region of 153-123 K increases, and transitions beyond 123 K shown in Figure 4.14b. The peculiar pattern of the modes mentioned above especially in the region of 153-123 K, suggest a dynamic behaviour of the framework (and no sharp transition) coming from soft porosity, wherein the Im molecules may tilt/twist to expand the structure in a way to incorporate more guest molecules. The softening of the Im ring breathing modes, decrease in intensity and broadening of

C-H stretching mode, and a gradually transforming pattern (both intensities and peak positions) in the C-H rocking modes in the temperature regime is a direct consequence of significant breathing of the Im and gate-opening effects because of heightened host-guest interactions.

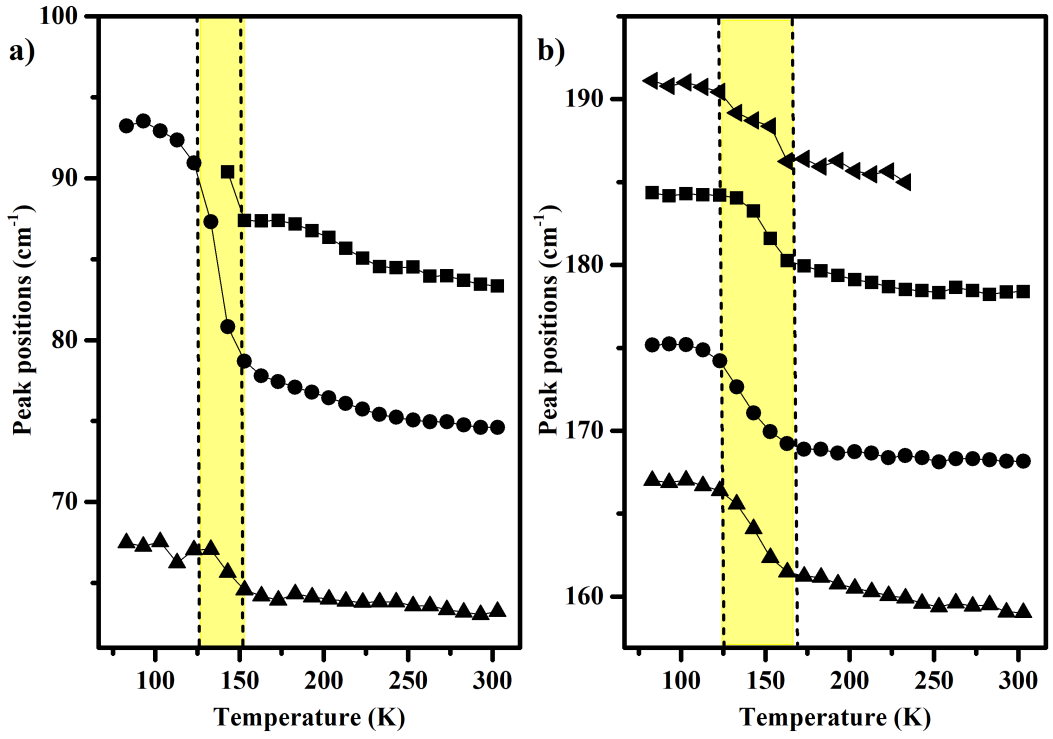

Figure 4.17: Peak positions versus temperature for ZIF-4(DS) under N_2 in the low-wavenumber region a) Im twisting modes b) Zn-N bending coupled with Im twisting.

As we lower the temperature, the density of the gas molecules increases causing an increased pressure around the ZIF crystals. However, the blue-shift below 123 K in the 1176-1186 cm^{-1} region suggests bond stiffness and locking of the Im molecules in one orientation upon guest incorporation. To confirm this, we look at the rigid-unit modes, where a gradual blue-shift along with decreasing intensity is observed in the temperature regime 153-123 K shown in Figure 4.17 suggesting opening of the pore. The Im ring twisting modes (65-95 cm^{-1}) blue-shift by 5-10 cm^{-1} shown in Figure 4.17a and their FWHM increases significantly (Figure 4.11a and 4.18). Furthermore, the Zn-N bending coupled with Im twisting modes in the region 150-200 cm^{-1} blue-shift by 5 cm^{-1} shown in Figure 4.17b suggesting a rigid framework accomplished after incorporating

guest molecules. Significant broadening in the rigid unit modes and C-H stretching modes under N_2 indicates stronger interaction with the framework mainly due to an additional quadrupolar moment on the molecule. Consequently, dipole-quadrupole interactions (also quadrupole-quadrupole) are possible between C-H centres and N_2 (it's centre of mass or one of the N atoms) or between the Im centre of mass and the quadrupole of N_2. As a result, N_2 binds strongly within the pores of ZIF-4(DS). This understanding of the interactions explains the pore-filled state (incomplete removal of N_2 from the crystals) observed upon desorption of N_2 in the BET isotherm.

In the low temperature region below 193 K, the Raman spectral behaviour under argon atmosphere is very similar to what was seen under N_2 atmosphere shown in Figure 4.14d, e, and f. This indicates that primarily, it is the flexibility of the Im ring molecules, which allows all gases to access the pore channels upon gate-opening and dispersive interactions between the guest and host molecules favour this adsorption. It is visible from the stack plots in Figure 4.11, the peaks become well-defined below 133 K whereas the data obtained under N_2 clearly shows broad features persisting even at 77 K from ∼153 K. A more quantitative view is explained in Figure 4.18. The C-H stretching modes under Ar undergo a small increase of ∼2 cm^{-1} in the transition regime but restore to the same or lower value after the transition. Whereas in the case of N_2, peak broadens in the range of ∼4-6 cm^{-1} and continues to remain broad until 83 K (Figure 4.18b). Similar but more drastic effects were observed in the low-wavenumber region, where the Im twisting modes were broadened by almost 15-20 cm^{-1}, even masking the peaks in the region 100-120 cm^{-1} under N_2 (Figure 4.18d). However, when we look at the peak behavior in Ar, not only does the broadening is less, beyond the transition regime, few peaks become sharper and intense (Figure 4.18c).

From the Raman spectral changes associated with the structural changes in ZIF-4 and N_2 peak behaviour, it is confirmed that the initial open-to-narrow pore transition observed under vacuum is absent due to gas filling inside the ZIF-4 pore. However, a guest-induced transition occurs around 153 K, which expands the ZIF-4 structure and opening new adsorption sites, incorporating more guest molecules with stronger interaction depending on the polarizability of the guest molecule. In the next section, CO_2 adsorption and the corresponding spectral changes in ZIF-4(DS) will be highlighted.

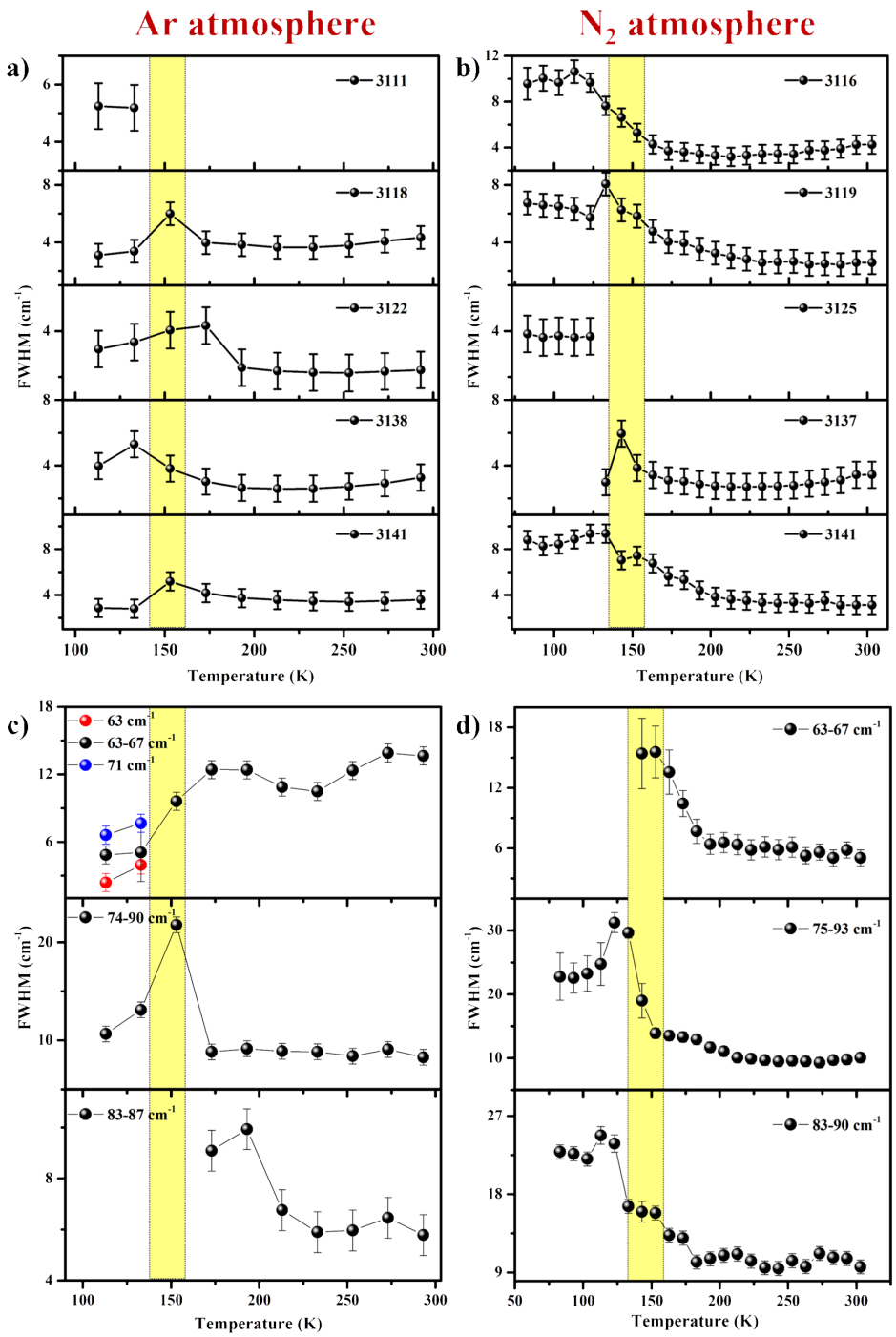

Figure 4.18: FWHM versus temperature plots. The top panel displays for the C-H stretching modes (a & b). The bottom panel displays width for peaks for the collective Im vibrations c) & d). Plots a) & c) were obtained from Raman spectra of ZIF-4(DS) obtained under Ar and Plots b) & d) under N_2.

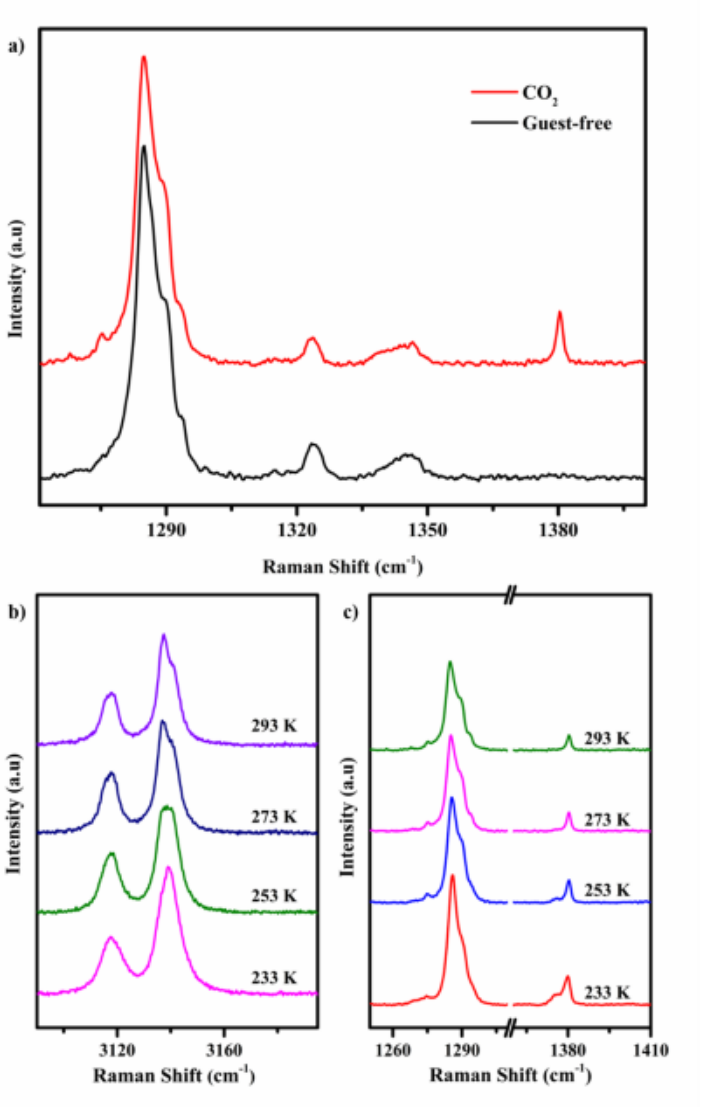

Figure 4.19: a) Raman spectra of ZIF-4(DS) under CO_2 and vacuum showing characteristic fermi-resonance ν_1 at 1276 and 1380 cm^{-1}. b) & c) Temperature-dependent spectra obtained under CO_2 atmosphere for selected regions.

4.4.4.2 ZIF-4(DS) under CO_2 atmosphere

Upon subjecting the ZIF-4(DS) system to CO_2, dramatic results can be noted at 293 K. Firstly, like N_2 gas, at 293 K, the Fermi resonance modes at 1276 cm^{-1} and 1380 cm^{-1} of CO_2 signature are identifiable in the Raman spectra obtained under vacuum (Figure 4.19a). Again, like other gases, CO_2 is entrapped within the pore, as the modes are red-shifted from the free CO_2 molecules fermi resonance modes at 1278 and 1385 cm^{-1}. Overall, as compared to the Raman spectra obtained under vacuum, N_2, and Ar conditions, all peaks are broadened, degenerate and reduced intensity shown in Figure

4.20. Additionally, a much sharper and intense signature of CO_2 at 293 K, as opposed to N_2 was observed. These results suggest a stronger interaction of the molecule with CO_2 than N_2 in the ZIF-4 framework. It is well-expected considering the higher quadrupole moment on CO_2 (-14 X 10^{-40} Cm^2) compared to N_2 (-4.65 X 10^{-40} Cm^2) [48]. The impact of the CO_2 interaction is clear as well in the symmetric Im twisting modes (80 cm^{-1}) reducing in number, intensity dropping and broadening as seen from Figure 4.20. Upon lowering the temperature, a dynamical relation in peak intensities of the C4-H and C5-H stretching modes around 3140 cm^{-1} is observed (Figure 4.19b). This trend suggests the interaction between π center at the C4-C5 of the Im ring and π-cloud on CO_2, C-H$\cdots$O H-bonding, or dipole$\cdots$induced-dipole interactions [49]. Since, the C-H stretching modes do not show a noticeable shift, a weaker H-bonding is expected.

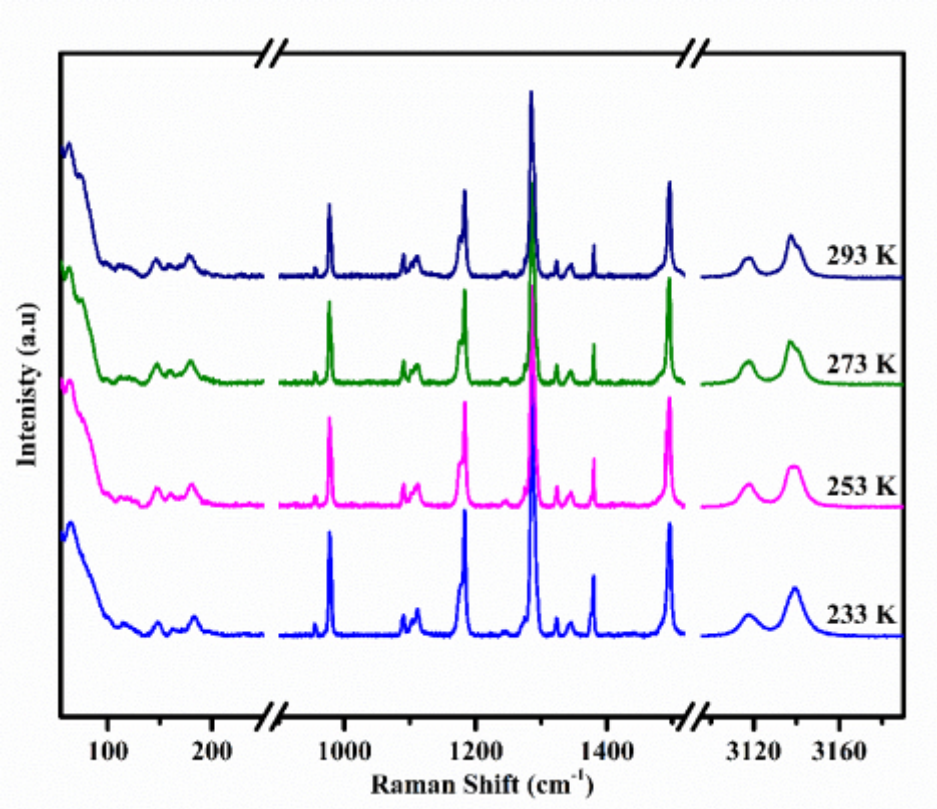

Figure 4.20: Temperature dependent Raman Spectra for ZIF-4 (DS) under CO_2 atmosphere

It is to be noted here that, we are well above the gate-opening temperature here and it is the strong interaction of this gas with the host, that drives this gas adsorption. Further splitting of the 1380 cm^{-1} observed from 273 K is indicative of multiple site adsorptions

for CO_2 also (Figure 4.19c). Below 213 K, data quality goes down because of increased condensation of CO_2 onto the stage.

4.4.5 Adsorption sites of ZIF-4

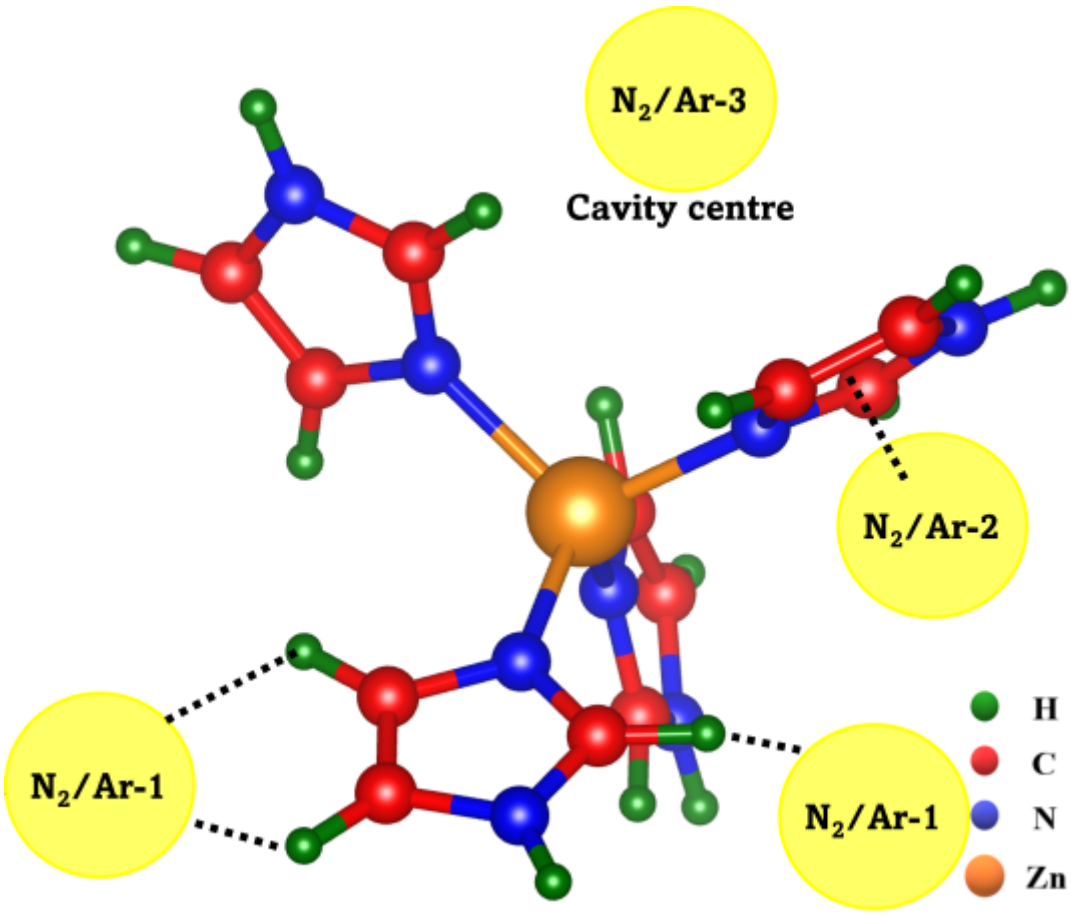

Figure 4.21: Proposed Adsorption sites in ZIF-4

From the critical analysis from our experimental studies carried under vacuum and guest conditions, we propose the following possible adsorption sites in ZIF-4 shown in Figure 4.21. The most preferential site (first adsorption site) in the system exists close to the C-H centres of the Im ring moiety. From Raman studies, these centres were found to be highly influenced by the presence of guest molecules. Between the C-H centres, the activation of C4-C5 stretching mode suggested the preference of the C4-H(or C5-H) being preferred over the C2-H for adsorption. Additionally, in this temperature regime around 253 K, in the absence of guest molecules, we observe evidence of dominant C-

H$\cdots\pi$ interactions in the framework [50, 36, 37]. These interactions originate primarily from the C-H centres of the system to prevent the pore from collapsing. Hence, upon guest incorporation, these C-H centres would be the first to be perturbed.

The second adsorption site is close to the aromatic ring centre of Im moiety. At 153 K, Im ring breathing mode is greatly affected due to the dispersive interactions between host and guest under both N_2 and Ar atmosphere. In addition, in the case of N_2, quadrupolar interactions also play a significant role. It is noteworthy, that the broadening in C-H stretching region suggest that the gas interaction is mainly with C-H centres of Im.

The third and last adsorption site is the centre of the cavity, which may be inaccessible until ZIF-4 is sufficiently expanded at low temperatures under high adsorption stress of gases. Since the N_2 peak is still red-shifted (2328 cm^{-1}) from the free N_2 peak (at 2331 cm^{-1}), the guest adsorption is again driven by dispersive interactions with the host framework. These results corroborate well with the adsorption sites of ZIF-8, where the most energetically favoured site is near the Im rings stabilized by dispersive interactions as opposed to the other MOFs, where it lies closer to their metallic clusters [51]. Also, it should be noted that, unlike ZIF-8 and ZIF-7, ZIF-4 is un-substituted, and thus steric hindrance playing a role for preferential adsorption of one gas over the other is ruled out. However, the flexibility of the Im ring and these non-covalent interactions discussed in detail facilitate the guest uptake irrespective of size and polarity of the gas.

4.5 Conclusions

In summary, we have discussed in detail the structural changes and adsorption behaviour of ZIF-4 crystals upon perturbation with temperatures and various gases. From the Raman spectroscopic studies, we observed a new phase transition around 253 K, where the system goes from an open pore to narrow pore transition. These results were further confirmed by dielectric measurements and BET isotherm. This narrow pore was found to be stabilised predominantly by C-H$\cdots\pi$ interactions within the framework. No substantial change was observed in Raman spectra upon the existing 140 K open-to-closed pore transition owing to the small size of the crystal. Further, upon gas uptake, immediately dispersive interactions mediate the adsorption of the gases inside the pore, which is

marked by the signature peaks of the gases used (N_2 and CO_2) and specific changes in the Im molecular modes (1490 cm^{-1} region). Most striking feature of the studies is the signature peaks of gases except Ar at 293 K itself, which is quite rare. This gas uptake results in absence of the open to narrow pore transition observed under vacuum. However, an additional guest-induced (or adsorption-induced) phase transition was observed around 153 K, where the ZIF-4 goes from an open to expanded pore, incorporating more guest molecules, stabilized by dispersive and quadrupole interactions depending on the gas. Sharp shifts, peak broadening, and intensity changes in both Im ring molecular modes and the rigid unit modes (associated with breathing and gate-opening effect) show strong dependence of the gas uptake. The strongly bound N_2 adsorption behaviour explains the pore-filled structure of ZIF-4, where all the molecules do not leave the framework upon desorption. Finally, based on our results, the preferential adsorption sites and its mechanism has been proposed which is mainly near the C-H centres of the Im ring moiety governed by the dispersive interactions in the ZIF-4(DS) system synthesized.

Chapter 4B

Role of Metal Ion influencing N_2 adsorption in ZIF-67 using Raman Spectroscopy[‡]

Summary

Owing to the limited understanding of the structure-property relationship of ZIF-67, this chapter presents the Raman investigations under N_2 atmosphere addressing this aspect. Two types of adsorption were observed, where one of them is associated with the $Co^{2+}\cdots N_2$ adduct formation from ambient conditions. Later, this interaction facilitates the gate-opening around 153 K, suggested by the appearance of N_2 physisorption signature mode. Concomitant spectral changes were revealed in the two temperature regions, especially the modes associated with Co-N bending. Fundamental understanding of the adsorption mechanism in ZIF-67 using Raman studies, described the higher uptake of various gases in ZIF-67 than ZIF-8, inspite a stiffer Co-N bond as opposed to the Zn-N.

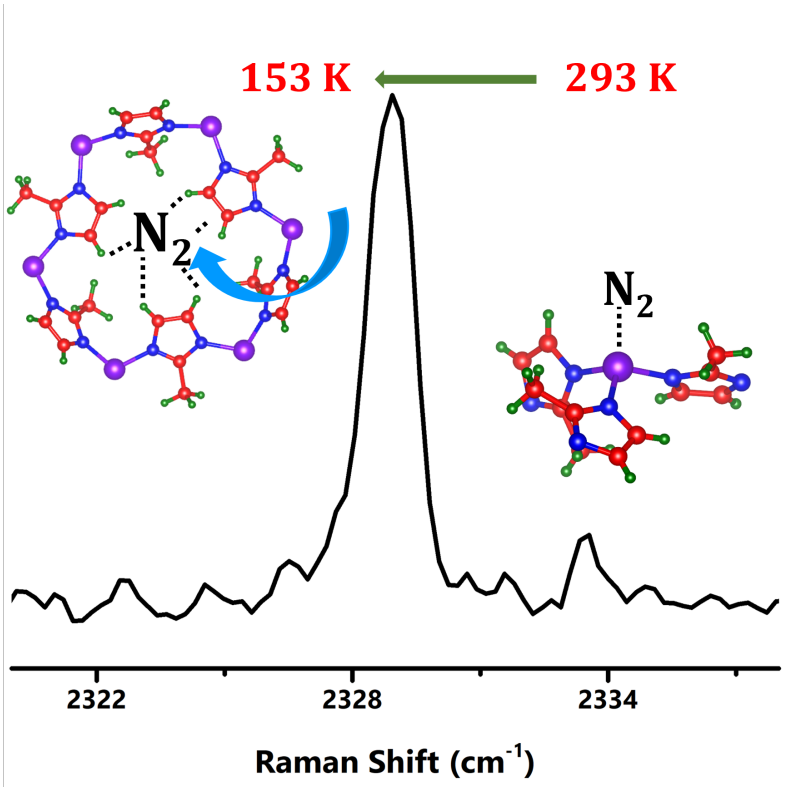

[‡] *Manuscript under preparation*

4.6 Motivation for the work

ZIF-67 is a Co-based ZIF with methylimidazole (MIM) as the linker, which makes it isostructural to the popular ZIF, ZIF-8 (Zn-based). Although isostructural, there are various differences in the properties of the two materials such as different thermal stability, surface area, diffusion rate for gases, and others [45, 52, 53]. Despite these differences, the studies discussing the influence of metal ion, especially from a structural point of view is limited. In literature, there are interesting aspects related to ZIF-67 gas adsorption. Because of the stiffer Co-N bond, the pore volume and flexibility is slightly less as compared to ZIF-8 [52]. But, the uptake of various gases such as N_2, CO_2, and CH_4 are reported to be slightly higher as compared to ZIF-8 [54]. Additionally, the stiffness of the Co-N provides restricted ligand flipping motion, hence resulting in a better selectivity of small molecules [55]. The presence of unsaturated Co^{2+} ion at the surface of ZIF-67 makes it susceptible to interaction with various species such as superoxo anion formation, susceptibility towards oxygen [56]. All these properties make ZIF-67 intriguing and a microscopic picture of the structural/framework behaviour with guest molecules will truly highlight the role of metal ions in making it different from ZIF-8.

4.7 Experimental section

4.7.1 Synthesis of ZIF-67

To prepare ZIF-67, a modified procedure was used [57]. In a beaker, 6 g of 2-MIM and 40 mL methanol (MeOH) were dissolved. Subsequently, 3 g of $Co(NO_3)_2{\cdot}6H_2O$ was added to another beaker containing 40 mL of MeOH. An immediate colour change was observed from deep orange-brown to deep purple upon rapid addition of the former solution to the latter solution. This resultant mixture was stirred for 2 hours and then aged without stirring for 24 hours under ambient temperature. Post-aging, visible precipitates were observed at the bottom of the beaker, which was transferred to 50 ml centrifugation tubes. The particles were centrifuged at 8500 rpm for 5 min. The supernatant was discarded, the residue was washed with methanol (25 ml X 3), and the centrifugation process was repeated. The residue was oven-dried at 120 °C for 12 hours in a vacuum oven to obtain

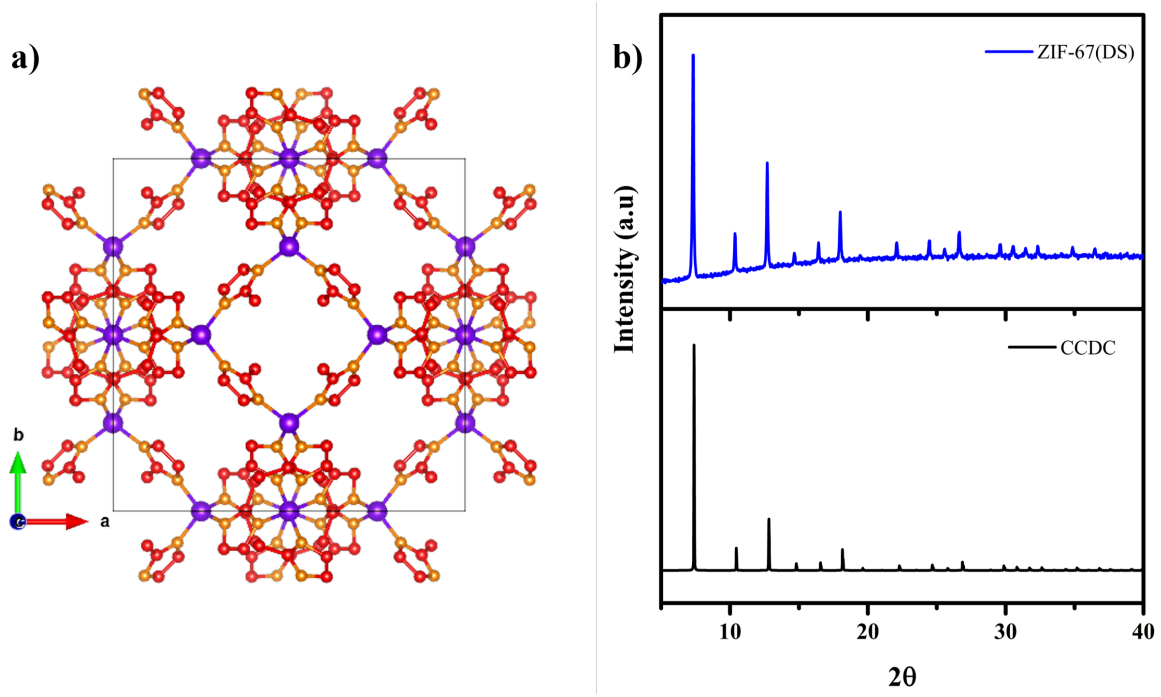

Figure 4.22: a) Structure of ZIF-67 at 298 K redrawn from CCDC file No. 1429244 b) XRD pattern of the desolvated ZIF-67 obtained stacked with reported XRD pattern

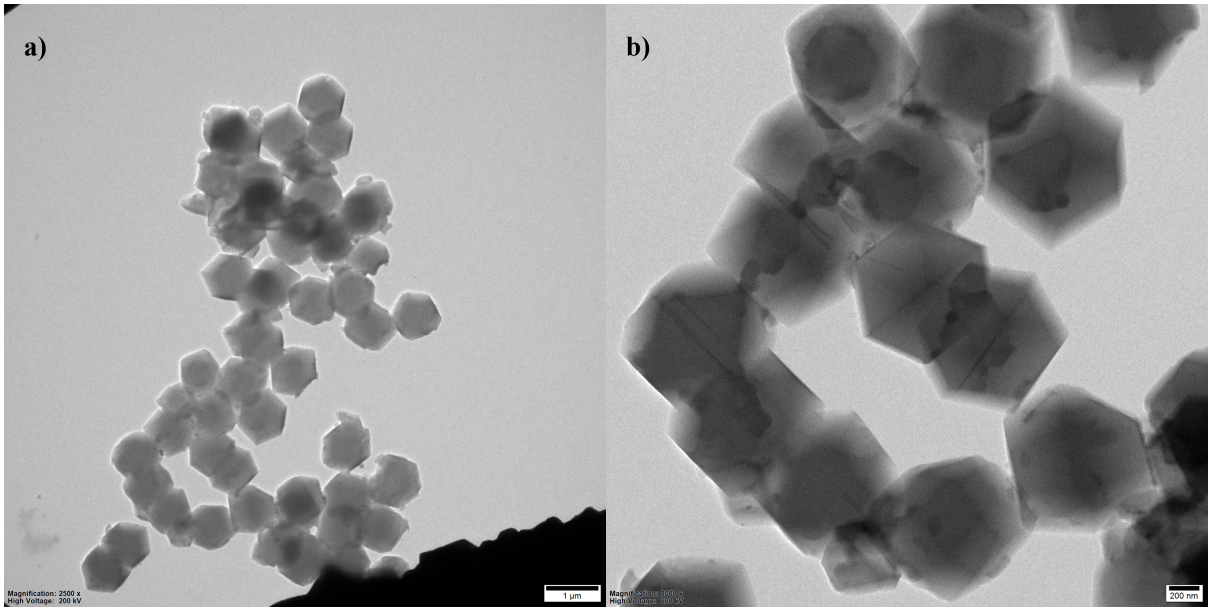

Figure 4.23: a) and b) shows the TEM image of the prepared ZIF-67 sample

solvent-free particles. The ZIF-67(DS) product was further used for characterisation and experiments.

4.7.2 Characterisation studies

The XRD pattern of the synthesized ZIF-67(DS) nanoparticles resembled the reported structure shown in Figure 4.22 and was redrawn from CCDC No. 1429244. The size and morphology of the nanoparticles were confirmed from the TEM images shown in the Figure 4.23. The particle was uniformly distributed with a size between 500-600 nm and possessed a well-defined rhombic dodecahedral shape.

4.8 Results and discussions

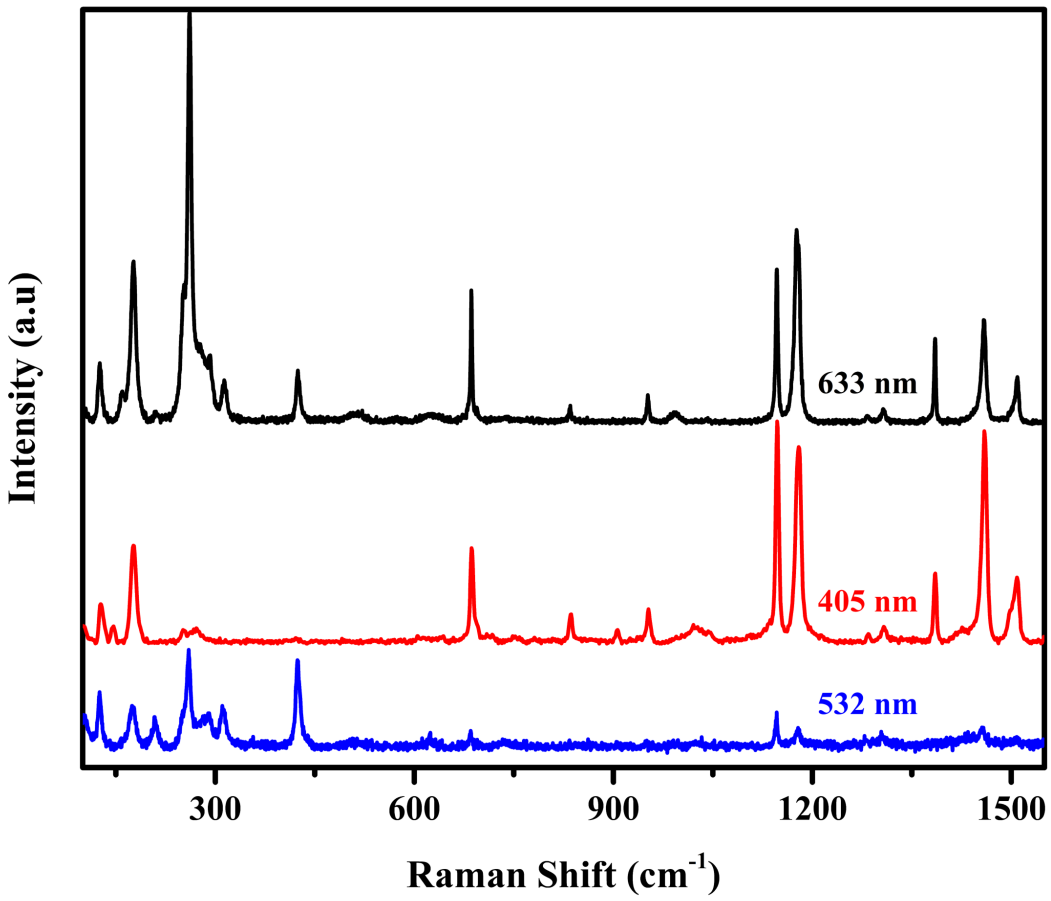

Figure 4.24: Raman spectra obtained for ZIF-67(DS) at various wavelengths under ambient conditions

4.8.1 Raman spectrum of ZIF-67 under ambient conditions

Raman spectral measurements were carried out on the ZIF-67(DS) sample with various wavelengths to optimize the best parameters for the measurements. In the process, it was found that, upon illuminating the sample with $\lambda = 633$ nm, all observed Raman peaks were present (Figure 4.24). However, upon illumination with $\lambda = 405$ & 532 nm, certain modes were absent. This observation hinted at the presence of resonant Raman in the latter cases. Indeed from the literature, it was realized that absorption maxima for ZIF-67 appear at 565 nm and 537 nm generated due to the higher-lying, $^4A_2$(F) to $^4T_1$(P) d-d ligand field transitions and of Co^{2+} being in a tetrahedral environment [58]. As a result, the Raman peaks associated with the metal ion contribution were enhanced in the case of $\lambda = 532$ nm. This result is of great significance here because although ZIF-67 is isostructural to ZIF-8, it differs in the metal ion. Hence, in order to understand the role of the metal ion with structural changes with temperature and gas adsorption on ZIF-67, it is primary to focus on the modes affected by the vibrations involving Co. The modes between 200-430 cm^{-1} have contributions involving Co^{2+} ion. Additionally, the linker molecular modes are similar to ZIF-8 and corroborate well with our data. Within these molecular modes, the bands associated with the C-N stretching modes (at 1176 and 1180 cm^{-1}) lower in energy as compared to ZIF-8 (at 1180 and 1187 cm^{-1}) because of the stiffer Co-N bond over the Zn-N bond causing the C-N bond to elongate.

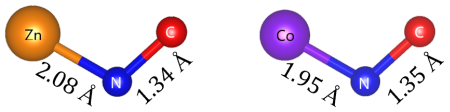

The low-wavenumber modes especially the ones involving the metal ion were assigned using gaussian calculation on a small fragment shown in Figure A.2 similar to chapter 4A. All details of the calculation is discussed in the Appendix A itself. The assignments for ZIF-67(DS) are listed in the Table 4.3, A.2, and Figure 4.25. In this chapter, the focus remains only on the modes important for the discussion as follows: ≈ 3130 cm^{-1} corresponding to C-H stretching modes, and the low-wavenumber region around 65-80 cm^{-1} belonging to the RUMs. Additionally in this chapter, the spectral changes in the region 250-420 cm^{-1} (Table 4.3 for precise assignments), corresponding to the bending of Co-N along with the bending of the ligand often accompanied by Me libration will be

discussed.

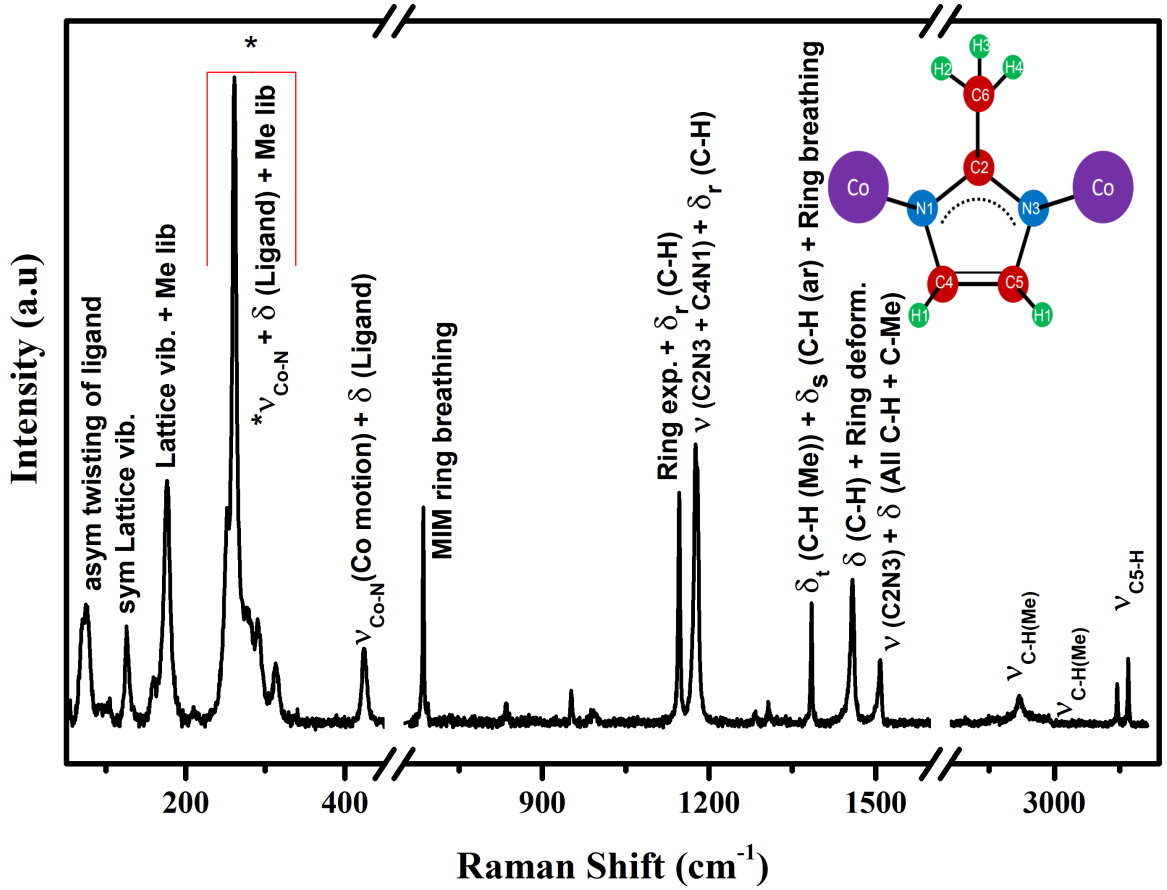

Figure 4.25: Raman spectrum of ZIF-67(DS) obtained under ambient conditions with peak assignments

Table 4.3: Peak assignments listed for ZIF-67(DS) in comparison with ZIF-8 assignments in literature and the computational assignments carried in the present work.

Experimental wavenumber (cm^{-1})	**Band Assignments[23, 20]**	**Peak assignments based on computational data**
70	Strong Me Rotation, asym twisting	asym twisting pivoting on N1
76	MIM Rocking and Me Rotation, asym twisting	asym twisting pivoting on C2

Experimental wavenumber (cm^{-1})	**Band Assignments**	**Peak assignments based on computational data[§]**
126	NA	sym Lattice vibration pivoting on N1
159	NA	Me libration
176	δ(N-Zn-N)+$\nu(Zn-N)$(Tetrahedral Deformation)	Lattice vibration + Me libration
251 261	δ(MIM) + δ_{oop}(Me)	δ_{Co-N} + sym δ_t(MIM) + Me libration
278 292	ν_{Co-N}	δ_{Co-N} + asym δ_t(MIM) pivoting on C2
314		δ_{Co-N} + sym $\delta_t(MIM)$ pivoting on C2 + Me libration
424 426	ν_{Co-N} or δ_{MIM} (Co-N-C & N-C-Me)	δ_{Co-N} (Co motion) + sym $\delta_t(Im)$ + Me libration
681 686 694	In ring puckering, $\delta_{oop}H$	ip Ring breathing
835	δ_{oop} (C4, C5-H)	Ring deformation+ δ_{Co-N}
952	δ_{oop} (C2)	δ_w C-H(Me) + $\delta_t(C-H)$ + Ring deformation
993	NA	δ_{oop}(C-Me) + δ_w C-H(Me)
1146	ν_{C5-N}	Ring expansion+δ_r(C5-H)
1176	$\nu_{C-N} + \delta_w(N-H)$	$\delta_w(C-H) + \delta(C-Me) + \delta_{Co-N} + \nu(C2N1)$
1180	ν_{C-N}	δ_r C-H + ν(C5N3+C4N1)
1283	NA	δ_r(C-H) + Ring breathing (C4N3+C2N1) + δ_{Co-N}

[§] ν = stretching; sym = symmetric, asym = asymmetric, δ = bending; r = rocking, t = twisting, w = wagging, s = scissoring, oop = out-of-plane

Experimental wavenumber (cm^{-1})	**Band Assignments**	**Peak assignments based on computational data[§]**
1385	δ_{Me}	δ_t C-H(Me) + δ_s C-H + Ring breathing
1459	δ_{C-H}	δ_wC-H(Me) + δ_r C-H+ν(C-Me+N1C5+N3C4)
1502	ν (C2N3+C4N3+C5N1) + δ_w(N-H)	δ(C-H+C-Me) + ν(C2N3) + δ_r(C5H+C4H+N3H)
1509	NA	δ(C-H+C-Me) + ν(C4C5+C2N3) + δ_r(C5H+N3H)
2933	ν_{C-H}(Me)	ν_{C-H}(Me)
3119	ν_{C-H}(ar)	ν(C4-H)
3141		ν(C5-H)

4.8.2 Temperature evolution of Raman spectra of ZIF-67(DS) under N_2 atmosphere

For all temperature-dependent Raman studies under guest molecules, linkam (THMS600) stage was used. After a pre-evacuation step in a vacuum oven overnight at 373-393 K to remove any adsorbed gases and moisture, the sample was activated at the temperature for about 45 minutes at 373 K after loading on the linkam stage too. These steps were necessary to ensure, no adsorbed gases or moisture would interfere with the Raman measurements which will also be evident with mighty mite spectral differences. The chamber was then purged for ten minutes with N_2 gas using an external gas line connecting to the linkam stage. The stage was brought to 293 K and the gas atmosphere was maintained approximately at 1 atm. Spectra were recorded at every 10 K step from 293 K to 77 K with multiple accumulations for accuracy. The temperature evolution is shown in the stack plot 4.26 which broadly reveals spectral changes in the C-H stretching regions and the RUM region of the ZIF-67(DS).

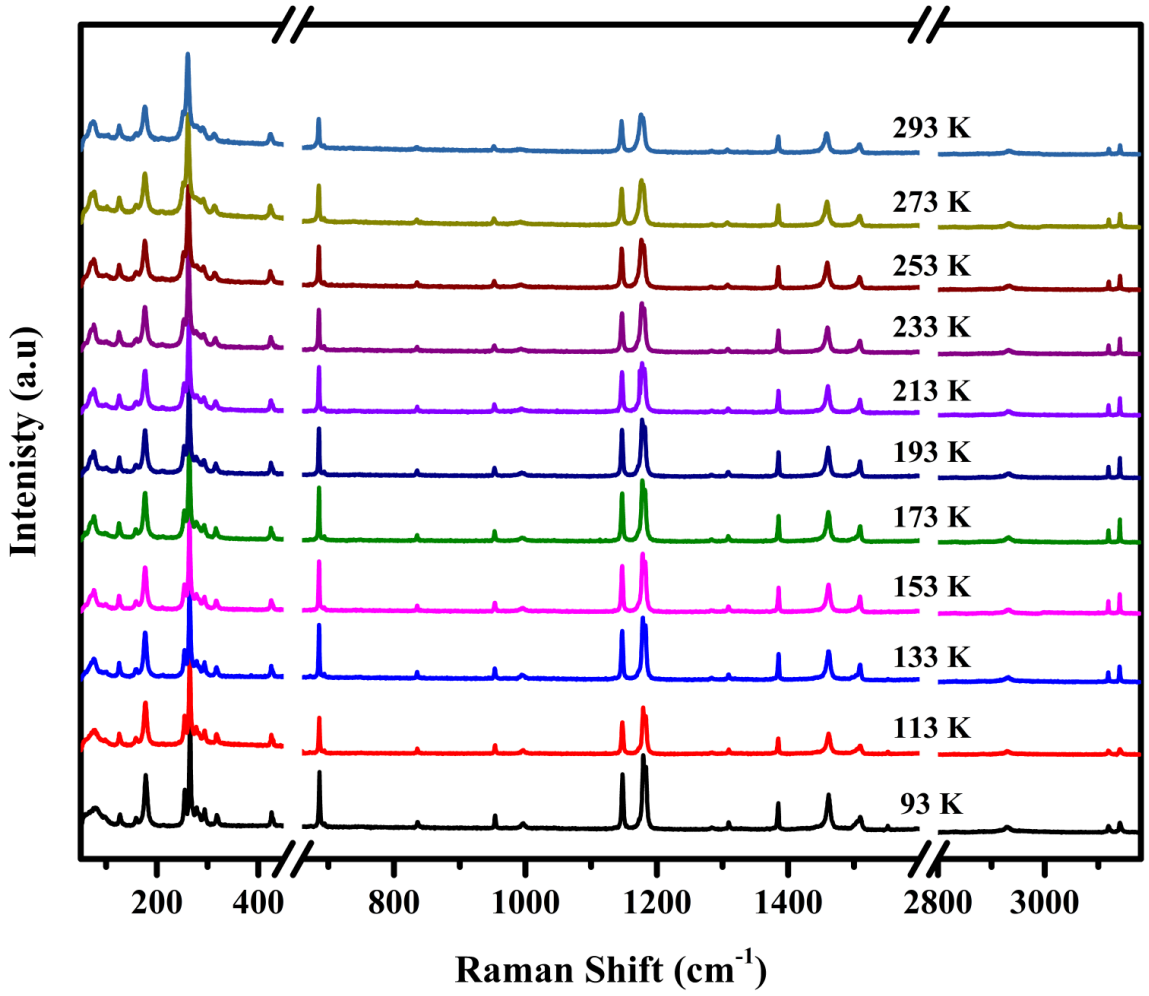

Figure 4.26: Raman spectra obtained for ZIF-67(DS) in the temperature regime from 293 to 93 K

4.8.3 Raman spectral changes in ν_{N-N} in ZIF-67 with temperature

The most important result obtained from the studies carried on ZIF-67(DS) was the presence of two types of N_2 characteristic peaks in the Raman spectra from the sample.

- At 2329 cm^{-1}
- At 2333 cm^{-1}

The peak at 2333 cm^{-1} is intriguing for two reasons. Firstly, it appears under ambient conditions from 293 K. Although the peak is tiny, and often such peaks are considered to be a spike (1-pixel peak), the result is reproducible and consistent over different experi-

ments carried out. Secondly, the peak is a blue-shifted mode from the free N_2 peak (2331 cm^{-1}) unlike what was observed in the case of chapter 4A. This feature is unique and the appearance of this peak again is only possible due to adsorption of the N_2 to the sample. This adsorption was further confirmed from BET measurements, where it is clear from the inset of the Figure 4.27b that at 298 K, ZIF-67(DS) adsorbs $\approx$ 3 cc/g of N_2.

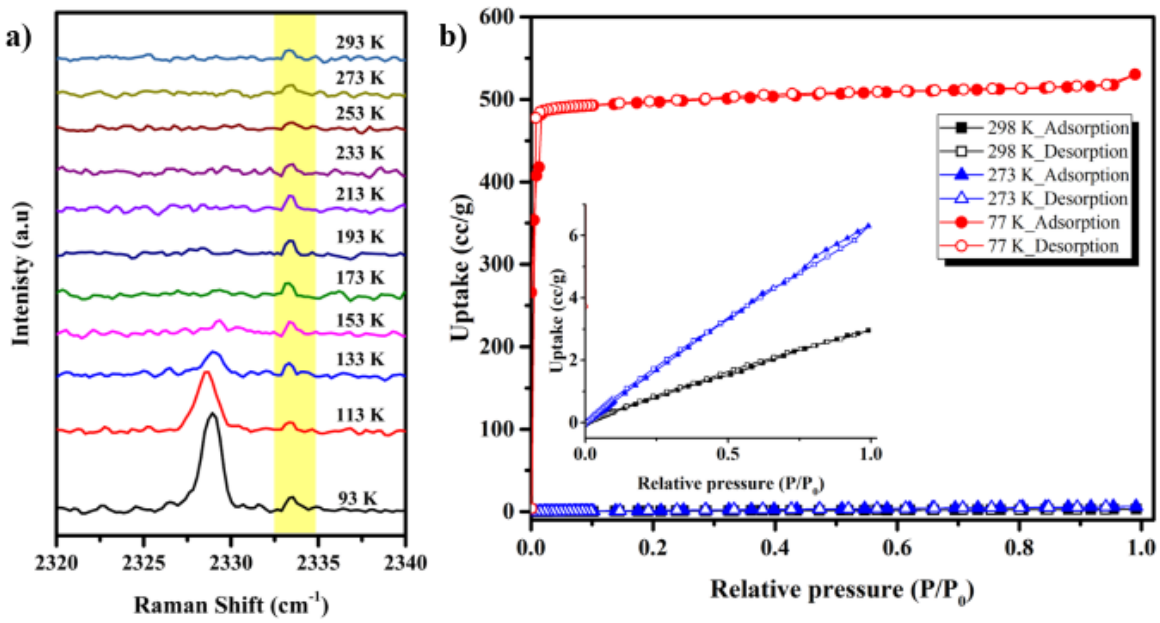

Figure 4.27: a) Temperature evolution of Raman spectra of ZIF-67(DS) under N_2 in the region 2200-2400 cm^{-1} b) BET adsorption isotherm of ZIF-67(DS) at three temperatures 298, 273, and 77 K. The inset displays the uptake of gas at 298 and 273 K

The origin of this new peak comes from the presence of unsaturated Co^{2+} in ZIF-67(DS) [45, 59]. As a result of which an adduct, $Co^{2+}\cdots N_2$, formation occurs. Such an adduct results in a blue-shift of the N-N stretching mode upon interaction with the MOF framework [46, 60, 61]. This peak was also absent in ZIF-4(DS) discussed in chapter 4A, where the Zn centre was saturated. Moreover, the intensity of this peak only increases up to 213 K owing to a limited number of such unsaturated centres. The impact of this type of adsorption on the structure will be discussed subsequently.

The second type of adsorption was observed from 153 K similar to the case of ZIF-8 by Kumari *et al.* [20]. The ν_{N-N} at 2329 cm^{-1} arises due to physisorption upon entrapping the N_2 molecules with gate-opening of the framework. The sequential increase in intensity can be correlated with the increased uptake of the gas molecules at low temperatures.

The high uptake of gas observed at 77 K in Figure 4.27b underscores the inference of Raman results as well.

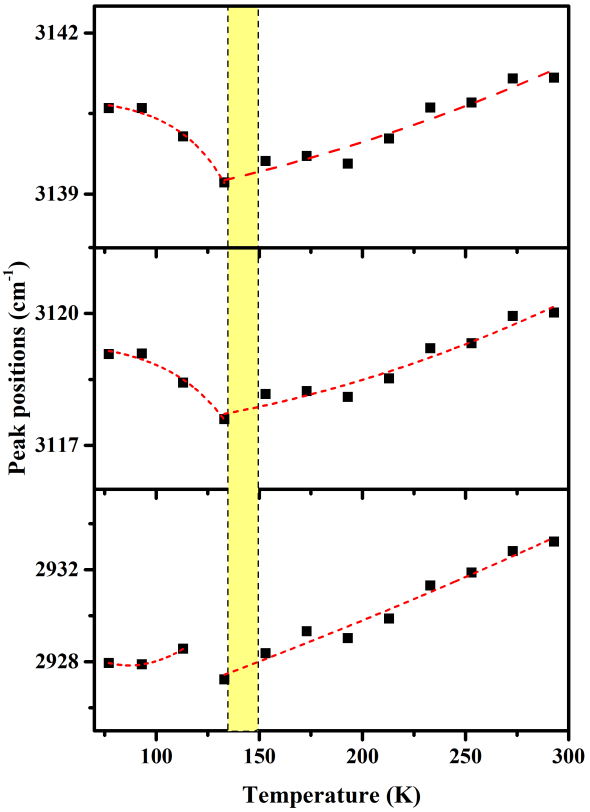

Figure 4.28: Temperature evolution of the Raman changes in the C-H stretching regions for ZIF-67(DS)

4.8.4 Structural changes in ZIF-67(DS) upon N_2 adsorption

The nature of both types of adsorption observed was either low in intensity or weak in nature. In other words, the peak observed at 2333 cm^{-1} from the adduct formation is a stronger interaction as opposed to the physisorption because of entrapping of N_2 molecules inside the pore at 2329 cm^{-1}. However, the number of unsaturated Co^{2+} will be limited. Hence, strong signatures from the molecular modes are not expected, but the trends provide crucial understanding. The C-H stretching modes, both associated with the aromatic rings and the methyl group soften upon lowering the temperature from 293 K shown in Figure 4.28. This observation opposes the general trend, where gradual stiffening of the modes is expected upon lowering the temperature. Chavan *et al.* has shown from IR studies that the coordinately unsaturated Ni^{2+} in CPO-27-Ni resulted in

a $Ni^{2+}...N_2$ adduct formation [46]. As a result of the quadruple nature of N_2, it interacted not only with the Ni ion, but with the neighbouring O atoms as well. Moreover, these interactions resulted in a significant distortion around the Ni centre. Therefore, by virtue of the quadrupole moment on N_2 and adduct formed with the unsaturated Co^{2+} in ZIF-67(DS), the polarised N_2 interacts with the C-H oscillators, resulting in slight elongation of the bond. Upon further lowering of temperature shown in Figure 4.28, the modes begin to harden beyond 153 K, where the second peak also appears at 2329 cm^{-1} marking the gate opening which will be confirmed in the subsequent paragraph.

Low-wavenumber modes In the Figure 4.29, the trend of peak positions with respect to the modes involving Co as a function of temperature is presented. In all of the plots, two transition regions have been highlighted, one at $\sim$ 233 K and another at $\sim$ 153 K, corresponding well with the two types of adsorption observed for ZIF-67(DS). The intensity of the 2333 cm^{-1} saturates around 213 K, whereas the second mode at 2329 cm^{-1} appears only beyond 153 K. Moreover, an unusual slope was observed shown in Figure 4.29c, where the mode at 312 cm^{-1}, corresponding to Co-N bending coupled with MIM symm twisting and Me libration, undergoes a blue-shift of $\approx$ 4 cm^{-1} in a small temperature region between 293 to 233 K. With the formation of the adduct, electrostatic interactions are predominant, resulting in a blue-shifting mode causing a distortion around metal centres in the framework [46]. This mode undergoes a slope change beyond 233 K followed by another slope change around 153 K, where most of the low-wavenumber modes show saturation in peak positions. These spectral changes are indicative of the framework softening before the gate-opening around 153 K and further locking of the framework upon guest incorporation.

The gate-opening in the case of ZIF-67 was further confirmed by the spectral changes of the rigid unit modes, at 70 and 76 cm^{-1} corresponding to the asymmetric twisting of the MIM. The intensity of the modes below 100 cm^{-1} decreases along with the broadening of the mode shown in Figure 4.30a, similar to the pattern discussed in the case of ZIF-4(DS). The decrease in the intensity underpins an open structure along with all the other spectral changes of the adsorbed N_2 as well as framework changes discussed. Additionally, broadening of these RUMs suggests N_2 interacting to the linker moieties, which is, in turn, confirmed from the activation of the mode at 1550 cm^{-1} corresponding to C4=C5

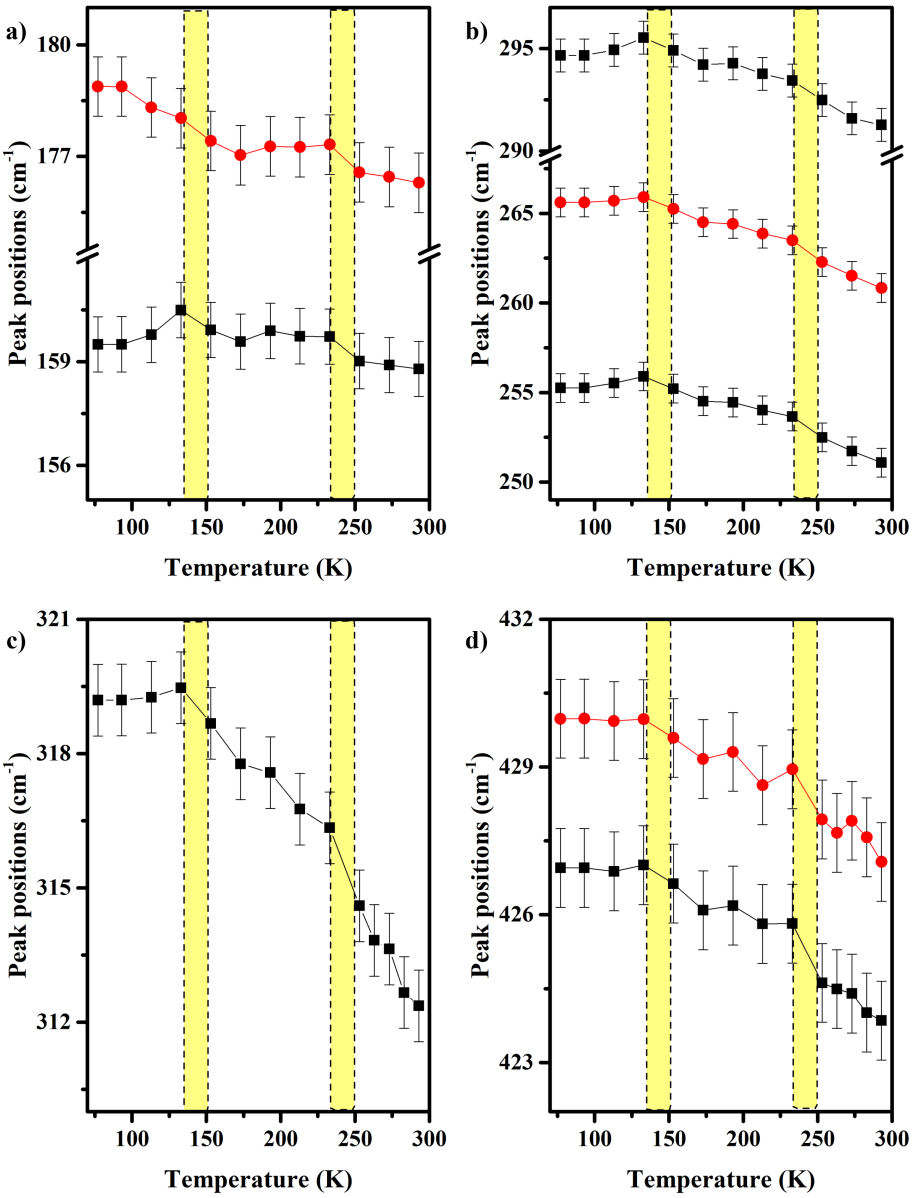

Figure 4.29: Temperature evolution of peak positions of low-wavenumber modes a) Lattice vibration + Me libration b), c), & d) δ_{Co-N} + sym and asym δ_t(MIM) (See Table 4.3 for details).

stretching vibration shown in Figure 4.30b. Because of the presence of multipole and quadruple interactions of N_2, the environments around C4-H and C5-H centres become inequivalent resulting in degeneracy lifting of the earlier absent mode. Inside the pore, N_2 interactions is predominantly with the C-H centres of the MIM.

The Raman results underscores the formation of the $Co^{2+}\cdots N_2$ to be facilitating the gate-opening of ZIF-67, in spite of a stiffer Co-N bond. This underpins a higher uptake of

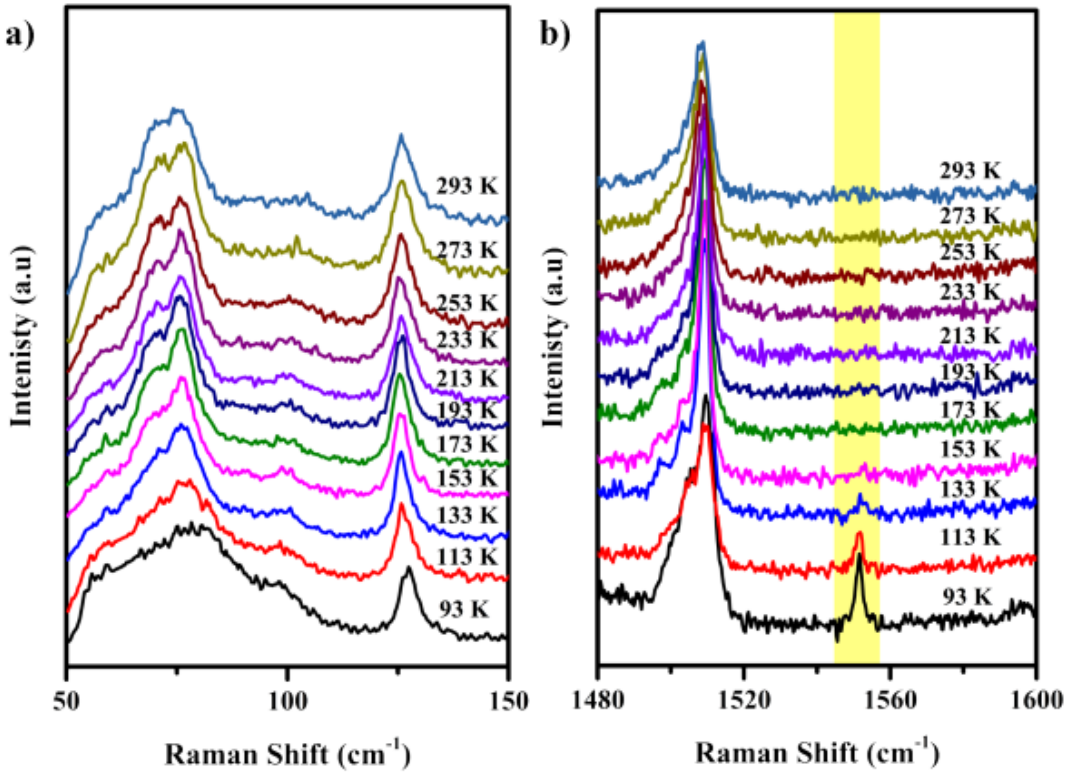

Figure 4.30: Temperature evolution of the Raman spectra a) Rigid Unit Modes b) Activation of C=C stretching mode at 1550 cm^{-1}

N_2 molecules for ZIF-67(DS) over ZIF-8 and other gases as well. For example, propylene uptake by ZIF-67 was observed at a threshold pressure at both 273 and 298 K, but only at the lower temperature for ZIF-8. Moreover, The uptake of CO_2 (condenses way above the gate-opening) has been reported at 273 K, however why this adsorption occurred still remained under survey [62]. Indeed, the BET isotherm presented in this work as well, (Figure 4.27b) showed a low uptake of the gas, but using Raman spectroscopy here, the origin behind it could be understood [63].

4.9 Conclusion

In this chapter, Raman investigations were carried out on ZIF-67(DS) over a temperature range from 293 to 93 K under N_2 atmosphere. Two types of adsorption were observed here, where the first one was associated with the presence of unsaturated Co^{2+} ion resulting in $Co^{2+} \cdots N_2$ adduct formation. Because of this continuous softening of C-H modes and blue-shifts in metal-linker modes was observed. From Raman studies, it was under-

scored that the increased affinity of N_2 towards ZIF-67 as compared to ZIF-8 observed in literature is related to a more distorted metal centre as well as polarized N_2 despite a stiffer Co-N bond. The second adsorption occurred as a result of entrapped N_2 around 153 K. Spectral changes in the molecular modes, decrease in intensity of the RUMs, and activation of C4=C5 stretching mode confirmed the gate-opening effects in ZIF-67(DS) with a predominant C4-H and C5-H dispersive interaction with the guest. The study amplifies the fundamental understanding of one of the intriguing properties displayed by the material.

In Chapter 4, a very concrete and interesting study using Raman spectroscopy was able to mark important differences in the role of the linker as well as metal ion between varying ZIF systems. The structural changes with and without guest molecules in ZIF-4(DS) highlighted the role of non-covalent interactions as a key role. On one hand, in the absence of guest, intra-framework interactions comes to the rescue to prevent the pore from collapsing, on the other hand, heightened guest-framework interactions which are mainly dispersive in nature mediate the adsorption of the guest molecules. With a detailed and controlled experiment for the first time, adsorption sites in the ZIF-4 were identified experimentally. This knowledge was further extended to ZIF-67 for both understanding adsorption sites as well as molecular changes with temperature.

References

[1] K. S. Park, Z. Ni, A. P. Côté, J. Y. Choi, R. Huang, F. J. Uribe-Romo, H. K. Chae, M. O'Keeffe, and O. M. Yaghi, "Exceptional chemical and thermal stability of zeolitic imidazolate frameworks," *Proceedings of the National Academy of Sciences*, vol. 103, no. 27, pp. 10186–10191, (2006).

[2] C. Zhang and W. J. Koros, "Zeolitic imidazolate framework-enabled membranes: challenges and opportunities," *The Journal of Physical Chemistry Letters*, vol. 6, no. 19, pp. 3841–3849, (2015).

[3] B. Chen, Z. Yang, Y. Zhu, and Y. Xia, "Zeolitic imidazolate framework materials: recent progress in synthesis and applications," *Journal of Materials Chemistry A*, vol. 2, no. 40, pp. 16811–16831, (2014).

[4] V. M. A. Melgar, J. Kim, and M. R. Othman, "Zeolitic imidazolate framework membranes for gas separation: A review of synthesis methods and gas separation performance," *Journal of Industrial and Engineering Chemistry*, vol. 28, pp. 1–15, (2015).

[5] A. Bavykina, N. Kolobov, I. S. Khan, J. A. Bau, A. Ramirez, and J. Gascon, "Metal–organic frameworks in heterogeneous catalysis: recent progress, new trends, and future perspectives," *Chemical reviews*, vol. 120, no. 16, pp. 8468–8535, (2020).

[6] J. Zhang, Y. Tan, and W.-J. Song, "Zeolitic imidazolate frameworks for use in electrochemical and optical chemical sensing and biosensing: a review," *Microchimica Acta*, vol. 187, no. 4, pp. 1–23, (2020).

[7] M. Ibrahim, R. Sabouni, and G. A Husseini, "Anti-cancer drug delivery using metal organic frameworks (mofs," *Current medicinal chemistry*, vol. 24, no. 2, pp. 193–214, (2017).

[8] S. A. Moggach, T. D. Bennett, and A. K. Cheetham, "The effect of pressure on zif-8: Increasing pore size with pressure and the formation of a high-pressure phase at 1.47 gpa," *Angewandte Chemie International Edition*, vol. 48, no. 38, pp. 7087–7089, (2009).

[9] S. Aguado, G. Bergeret, M. P. Titus, V. Moizan, C. Nieto-Draghi, N. Bats, and D. Farrusseng, "Guest-induced gate-opening of a zeolite imidazolate framework," *New Journal of Chemistry*, vol. 35, no. 3, pp. 546–550, (2011).

[10] Y. Pan, Y. Liu, G. Zeng, L. Zhao, and Z. Lai, "Rapid synthesis of zeolitic imidazolate framework-8 (zif-8) nanocrystals in an aqueous system," *Chemical Communications*, vol. 47, no. 7, pp. 2071–2073, (2011).

[11] D. Fairen-Jimenez, S. Moggach, M. Wharmby, P. Wright, S. Parsons, and T. Duren, "Opening the gate: framework flexibility in zif-8 explored by experiments and simulations," *Journal of the American Chemical Society*, vol. 133, no. 23, pp. 8900–8902, (2011).

[12] K. W. Chapman, G. J. Halder, and P. J. Chupas, "Pressure-induced amorphization and porosity modification in a metal- organic framework," *Journal of the American Chemical Society*, vol. 131, no. 48, pp. 17546–17547, (2009).

[13] S. Sharma, K. Sudarshan, A. Yadav, S. Jha, D. Bhattacharyya, and P. Pujari, "Investigation of compression-induced deformations in local structure and pore architecture of zif-8 using ftir, x-ray absorption, and positron annihilation spectroscopy," *The Journal of Physical Chemistry C*, vol. 123, no. 36, pp. 22273–22280, (2019).

[14] A. Knebel, B. Geppert, K. Volgmann, D. Kolokolov, A. Stepanov, J. Twiefel, P. Heitjans, D. Volkmer, and J. Caro, "Defibrillation of soft porous metal-organic frameworks with electric fields," *Science*, vol. 358, no. 6361, pp. 347–351, (2017).

[15] Y. Hu, H. Kazemian, S. Rohani, Y. Huang, and Y. Song, "In situ high pressure study of zif-8 by ftir spectroscopy," *Chemical Communications*, vol. 47, no. 47, pp. 12694–12696, (2011).

[16] J. Choi, J. Im, K. Noh, J. Kim, T. Vogt, and Y. Lee, "Universal gas-uptake behavior of a zeolitic imidazolate framework zif-8 at high pressure," *The Journal of Physical Chemistry C*, vol. 123, no. 42, pp. 25769–25774, (2019).

[17] H. Tanaka, S. Ohsaki, S. Hiraide, D. Yamamoto, S. Watanabe, and M. T. Miyahara, "Adsorption-induced structural transition of zif-8: a combined experimental and simulation study," *The Journal of Physical Chemistry C*, vol. 118, no. 16, pp. 8445–8454, (2014).

[18] M. E. Casco, J. Fernández-Catalá, Y. Cheng, L. Daemen, A. J. Ramirez-Cuesta, C. Cuadrado-Collados, J. Silvestre-Albero, and E. V. Ramos-Fernandez, "Understanding zif-8 performance upon gas adsorption by means of inelastic neutron scattering," *ChemistrySelect*, vol. 2, no. 9, pp. 2750–2753, (2017).

[19] J.-P. Zhang, A.-X. Zhu, and X.-M. Chen, "Single-crystal x-ray diffraction and raman spectroscopy studies of isobaric n 2 adsorption in sod-type metal–organic zeolites," *Chemical Communications*, vol. 48, no. 93, pp. 11395–11397, (2012).

[20] G. Kumari, K. Jayaramulu, T. K. Maji, and C. Narayana, "Temperature induced structural transformations and gas adsorption in the zeolitic imidazolate framework zif-8: A raman study," *The Journal of Physical Chemistry A*, vol. 117, no. 43, pp. 11006–11012, (2013).

[21] G. Kumari, N. Patil, V. S. Bhadram, R. Haldar, S. Bonakala, T. K. Maji, and C. Narayana, "Understanding guest and pressure-induced porosity through structural transition in flexible interpenetrated mof by raman spectroscopy," *Journal of Raman Spectroscopy*, vol. 47, no. 2, pp. 149–155, (2016).

[22] P. Kanoo, S. K. Reddy, G. Kumari, R. Haldar, C. Narayana, S. Balasubramanian, and T. K. Maji, "Unusual room temperature co 2 uptake in a fluoro-functionalized mof: insight from raman spectroscopy and theoretical studies," *Chemical Communications*, vol. 48, no. 68, pp. 8487–8489, (2012).

[23] M. R. Ryder, B. Civalleri, T. D. Bennett, S. Henke, S. Rudić, G. Cinque, F. Fernandez-Alonso, and J.-C. Tan, "Identifying the role of terahertz vibrations in metal-organic frameworks: from gate-opening phenomenon to shear-driven structural destabilization," *Physical review letters*, vol. 113, no. 21, p. 215502, (2014).

[24] M. T. Wharmby, S. Henke, T. D. Bennett, S. R. Bajpe, I. Schwedler, S. P. Thompson, F. Gozzo, P. Simoncic, C. Mellot-Draznieks, H. Tao, *et al.*, "Extreme flexibility in a zeolitic imidazolate framework: Porous to dense phase transition in desolvated zif-4," *Angewandte Chemie*, vol. 127, no. 22, pp. 6547–6551, (2015).

[25] T. D. Bennett, D. A. Keen, J.-C. Tan, E. R. Barney, A. L. Goodwin, and A. K. Cheetham, "Thermal amorphization of zeolitic imidazolate frameworks," *Angewandte Chemie*, vol. 123, no. 13, pp. 3123–3127, (2011).

[26] J. Gandara-Loe, A. Missyul, F. Fauth, L. L. Daemen, Y. Q. Cheng, A. J. Ramirez-Cuesta, P. I. Ravikovitch, and J. Silvestre-Albero, "New insights into the breathing phenomenon in zif-4," *Journal of Materials Chemistry A*, vol. 7, no. 24, pp. 14552–14558, (2019).

[27] M. Hartmann, U. Bóhme, M. Hovestadt, and C. Paula, "Adsorptive separation of olefin/paraffin mixtures with zif-4," *Langmuir*, vol. 31, no. 45, pp. 12382–12389, (2015).

[28] R. Gaussian09, M. Frisch, G. Trucks, H. Schlegel, G. Scuseria, M. Robb, J. Cheeseman, G. Scalmani, V. Barone, B. Mennucci, *et al.*, "Gaussian, inc., wallingford ct," (2009).

[29] V. Timón, M. L. Senent, and M. Hochlaf, "Structural single and multiple molecular adsorption of co2 and h2o in zeolitic imidazolate framework (zif) crystals," *Microporous and Mesoporous Materials*, vol. 218, pp. 33–41, (2015).

[30] P. Iacomi and G. Maurin, "Responzif structures: Zeolitic imidazolate frameworks as stimuli-responsive materials," *ACS Applied Materials & Interfaces*, vol. 13, no. 43, pp. 50602–50642, (2021).

[31] A. Sławek, J. M. Vicent-Luna, B. Marszałek, B. Gil, R. E. Morris, W. Makowski, and S. Calero, "Gate-opening mechanism of hydrophilic–hydrophobic metal–organic frameworks: Molecular simulations and quasi-equilibrated desorption," *Chemistry of Materials*, vol. 30, no. 15, pp. 5116–5127, (2018).

[32] K. T. Butler, P. Vervoorts, M. G. Ehrenreich, J. Armstrong, J. M. Skelton, and G. Kieslich, "Experimental evidence for vibrational entropy as driving parameter of

flexibility in the metal–organic framework zif-4 (zn," *Chemistry of Materials*, vol. 31, no. 20, pp. 8366–8372, (2019).

[33] L. M. Markham, L. C. Mayne, B. S. Hudson, and M. Z. Zgierski, "Resonance raman studies of imidazole, imidazolium, and their derivatives: the effect of deuterium substitution," *The Journal of Physical Chemistry*, vol. 97, no. 40, pp. 10319–10325, (1993).

[34] M. Majoube, M. Henry, L. Chinsky, and P. Turpin, "Preresonance raman spectra for imidazole and imidazolium ion: interpretation of the intensity enhancement from a precise assignment of normal modes," *Chemical physics*, vol. 169, no. 2, pp. 231–241, (1993).

[35] M. J. Wójcik, J. Kwiendacz, M. Boczar, Ł. Boda, and Y. Ozaki, "Theoretical and spectroscopic study of hydrogen bond vibrations in imidazole and its deuterated derivative," *Chemical Physics*, vol. 372, no. 1-3, pp. 72–81, (2010).

[36] S. D. Hamann and M. Linton, "The influence of pressure on the infrared spectra of hydrogen-bonded solids. i. compounds with oh—o bonds," *Australian Journal of Chemistry*, vol. 28, no. 12, pp. 2567–2578, (1975).

[37] S. D. Hamann and M. Linton, "The influence of pressure on the infrared spectra of hydrogen-bonded solids. iii. compounds with nh... x bonds," *Australian Journal of Chemistry*, vol. 29, no. 8, pp. 1641–1647, (1976).

[38] S. Guha, W. Graupner, R. Resel, M. Chandrasekhar, H. Chandrasekhar, R. Glaser, and G. Leising, "Tuning intermolecular interactions: A study of the structural and vibrational properties of p-hexaphenyl under pressure," *The Journal of Physical Chemistry A*, vol. 105, no. 25, pp. 6203–6211, (2001).

[39] W. Zhang, J. Maul, D. Vulpe, P. Z. Moghadam, D. Fairen-Jimenez, D. M. Mittleman, J. A. Zeitler, A. Erba, and M. T. Ruggiero, "Probing the mechanochemistry of metal–organic frameworks with low-frequency vibrational spectroscopy," *The Journal of Physical Chemistry C*, vol. 122, no. 48, pp. 27442–27450, (2018).

[40] S. Eslava, L. Zhang, S. Esconjauregui, J. Yang, K. Vanstreels, M. R. Baklanov, and E. Saiz, "Metal-organic framework zif-8 films as low-κ dielectrics in microelectronics," *Chemistry of Materials*, vol. 25, no. 1, pp. 27–33, (2013).

[41] S. Balšiūnas, M. Šimėnas, D. Pavlovaitė, M. Kinka, F.-K. Shieh, K. C.-W. Wu, J. Banys, and R. Grigalaitis, "Low-frequency dipolar dynamics and atmospheric effects in zif-90 metal–organic framework," *The Journal of Physical Chemistry C*, vol. 123, no. 1, pp. 631–636, (2018).

[42] E. N. Gribov, D. Cocina, G. Spoto, S. Bordiga, G. Ricchiardi, and A. Zecchina, "Vibrational and thermodynamic properties of ar, n 2, o 2, h 2 and co adsorbed and condensed into (h, na)-y zeolite cages as studied by variable temperature ir spectroscopy," *Physical Chemistry Chemical Physics*, vol. 8, no. 10, pp. 1186–1196, (2006).

[43] F.-X. Coudert, A. Boutin, A. H. Fuchs, and A. V. Neimark, "Adsorption deformation and structural transitions in metal–organic frameworks: from the unit cell to the crystal," *The Journal of Physical Chemistry Letters*, vol. 4, no. 19, pp. 3198–3205, (2013).

[44] P. H. Kowalski, A. Krzemińska, K. Pernal, and E. Pastorczak, "Dispersion interactions between molecules in and out of equilibrium geometry: Visualization and analysis," *The Journal of Physical Chemistry A*, (2022).

[45] C. Wu, D. Xie, Y. Mei, Z. Xiu, K. M. Poduska, D. Li, B. Xu, and D. Sun, "Unveiling the thermolysis natures of zif-8 and zif-67 by employing in situ structural characterization studies," *Physical Chemistry Chemical Physics*, vol. 21, no. 32, pp. 17571–17577, (2019).

[46] S. Chavan, F. Bonino, J. G. Vitillo, E. Groppo, C. Lamberti, P. D. Dietzel, A. Zecchina, and S. Bordiga, "Response of cpo-27-ni towards co, n 2 and c 2 h 4," *Physical Chemistry Chemical Physics*, vol. 11, no. 42, pp. 9811–9822, (2009).

[47] J. Vekeman, N. Faginas-Lago, I. G. Cuesta, J. Sánchez-Marín, and A. S. D. Merás, "Nitrogen gas on graphene: Pairwise interaction potentials," in *International Conference on Computational Science and Its Applications*, pp. 563–578, Springer, (2018).

[48] C. Graham, J. Pierrus, and R. Raab, "Measurement of the electric quadrupole moments of co2, co and n2," *Molecular Physics*, vol. 67, no. 4, pp. 939–955, (1989).

[49] A. G. Kontos, G. E. Romanos, C. M. Veziri, A. Gotzias, M. K. Arfanis, E. Kouvelos, V. Likodimos, G. N. Karanikolos, and P. Falaras, "Correlating vibrational properties with temperature and pressure dependent co2 adsorption in zeolitic imidazolate frameworks," *Applied Surface Science*, vol. 529, p. 147058, (2020).

[50] J. Joseph and E. D. Jemmis, "Red-, blue-, or no-shift in hydrogen bonds: a unified explanation," *Journal of the American Chemical Society*, vol. 129, no. 15, pp. 4620–4632, (2007).

[51] J. Pérez-Pellitero, H. Amrouche, F. R. Siperstein, G. Pirngruber, C. Nieto-Draghi, G. Chaplais, A. Simon-Masseron, D. Bazer-Bachi, D. Peralta, and N. Bats, "Adsorption of co2, ch4, and n2 on zeolitic imidazolate frameworks: experiments and simulations," *Chemistry–A European Journal*, vol. 16, no. 5, pp. 1560–1571, (2010).

[52] D. K. Panchariya, R. K. Rai, E. Anil Kumar, and S. K. Singh, "Core–shell zeolitic imidazolate frameworks for enhanced hydrogen storage," *ACS omega*, vol. 3, no. 1, pp. 167–175, (2018).

[53] D. M. Polyukhov, A. S. Poryvaev, A. S. Sukhikh, S. A. Gromilov, and M. V. Fedin, "Fine-tuning window apertures in zif-8/67 frameworks by metal ions and temperature for high-efficiency molecular sieving of xylenes," *ACS Applied Materials & Interfaces*, vol. 13, no. 34, pp. 40830–40836, (2021).

[54] K. Zhou, B. Mousavi, Z. Luo, S. Phatanasri, S. Chaemchuen, and F. Verpoort, "Characterization and properties of zn/co zeolitic imidazolate frameworks vs. zif-8 and zif-67," *Journal of Materials Chemistry A*, vol. 5, no. 3, pp. 952–957, (2017).

[55] P. Krokidas, M. Castier, S. Moncho, D. N. Sredojevic, E. N. Brothers, H. T. Kwon, H.-K. Jeong, J. S. Lee, and I. G. Economou, "Zif-67 framework: a promising new candidate for propylene/propane separation. experimental data and molecular simulations," *The Journal of Physical Chemistry C*, vol. 120, no. 15, pp. 8116–8124, (2016).

[56] G. Saracco, S. Vankova, C. Pagliano, B. Bonelli, and E. Garrone, "Outer co (ii) ions in co-zif-67 reversibly adsorb oxygen from both gas phase and liquid water," *Physical Chemistry Chemical Physics*, vol. 16, no. 13, pp. 6139–6145, (2014).

[57] J. Shao, Z. Wan, H. Liu, H. Zheng, T. Gao, M. Shen, Q. Qu, and H. Zheng, "Metal organic frameworks-derived co 3 o 4 hollow dodecahedrons with controllable interiors as outstanding anodes for li storage," *Journal of Materials Chemistry A*, vol. 2, no. 31, pp. 12194–12200, (2014).

[58] B. Pattengale, S. Yang, J. Ludwig, Z. Huang, X. Zhang, and J. Huang, "Exceptionally long-lived charge separated state in zeolitic imidazolate framework: implication for photocatalytic applications," *Journal of the American Chemical Society*, vol. 138, no. 26, pp. 8072–8075, (2016).

[59] J. C. Tan, T. D. Bennett, and A. K. Cheetham, "Chemical structure, network topology, and porosity effects on the mechanical properties of zeolitic imidazolate frameworks," *Proceedings of the National Academy of Sciences*, vol. 107, no. 22, pp. 9938–9943, (2010).

[60] A. Zecchina, C. O. Areán, G. T. Palomino, F. Geobaldo, C. Lamberti, G. Spoto, and S. Bordiga, "The vibrational spectroscopy of h 2, n 2, co and no adsorbed on the titanosilicate molecular sieve ets-10," *Physical Chemistry Chemical Physics*, vol. 1, no. 7, pp. 1649–1657, (1999).

[61] K. I. Hadjiivanov, D. A. Panayotov, M. Y. Mihaylov, E. Z. Ivanova, K. K. Chakarova, S. M. Andonova, and N. L. Drenchev, "Power of infrared and raman spectroscopies to characterize metal-organic frameworks and investigate their interaction with guest molecules," *Chemical Reviews*, vol. 121, no. 3, pp. 1286–1424, (2020).

[62] G. Zhong, D. Liu, and J. Zhang, "The application of zif-67 and its derivatives: adsorption, separation, electrochemistry and catalysts," *Journal of Materials Chemistry A*, vol. 6, no. 5, pp. 1887–1899, (2018).

[63] E. Andres-Garcia, J. López-Cabrelles, L. Oar-Arteta, B. Roldan-Martinez, M. Cano-Padilla, J. Gascon, G. M. Espallargas, and F. Kapteijn, "Cation influence in adsorptive propane/propylene separation in zif-8 (sod) topology," *Chemical Engineering Journal*, vol. 371, pp. 848–856, (2019).

Chapter 5

Dendronic Raman Markers*

Summary

SERS has been well-established as a viable tool for bio-diagnostics but is often limited by the sensitivity of analyte and practical applicability of the substrate. In this chapter, an analyte strategy with the assistance of simple coupling chemistry was developed. Dendronic-Raman markers with thiophenols in the periphery were synthesized using a stepwise process of protection, DCC coupling and de-protection. A 10^2 fold enhancement in SERS detection was observed upon going from a mono-thiophenol (MT) to a tetra-thiophenol (TT). By constraining the analyte molecule into a dendronic framework, the probability of SERS to occur at a much lower concentration compared to a single Raman active molecule was increased. This strategy broadens the applicability of SERS, as these analyte molecules can be just mixed or drop-casted on any kind of SERS substrate.

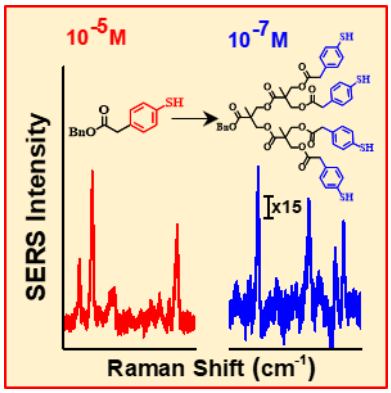

*Priyanka Jain, Robi Sankar Patra, Sridhar Rajaram, Chandrabhas Narayana, *Designing dendronic-Raman markers for sensitive detection using surface-enhanced Raman spectroscopy* RSC Adv., 2019,**9**, 28222-28227

5.1 Introduction

Sensitive detection for biological applications especially diagnostics has been a widespread area of interest. Most disease states commence with slight changes in the cellular processes which magnify with disease progression [1]. Thus, early diagnosis and regular monitoring become paramount for enhancing treatment efficacy. In view of this, there have been numerous reports exploiting SERS for disease diagnostics [2, 3, 4, 5]. SERS has been extensively used for its ability to get a molecular signature and trace detection of analytes [6, 7, 8, 9]. With the possibility of customized miniaturized Raman spectrometers [10], Surface Enhanced Raman Spectrometer becomes a very important tool for bio-diagnostics.

For early diagnosis, where the biological analyte concentration is low, detecting a Raman reporter labelled to a biomolecule becomes advantageous. Various strategies have been applied to functionalize a Raman reporter to a specific linker that can target specific biomolecules [11, 12, 13]. Cao et al. performed a multiplexed detection of oligonucleotide targets using gold nanoparticles (AuNPs) labelled with oligonucleotides and dye molecules [2]. Later, Ranga et al. developed a high sensitivity assay for HIV-1 subtype detection using Surface Enhanced Resonant Raman Spectroscopy (SERRS) [14]. These assays were highly specific and manifested high sensitivity up to the femtomolar level. However, early diagnosis of disease progression requires this limit to be pushed further.

The overall sensitivity of these strategies is influenced by the signal obtained from the Raman marker. SERS signal intensity has mainly been enhanced by substrate engineering to maximize the interaction of Raman reporters with the surface of the substrate [15, 16, 17]. However, the processes involved in engineering the substrate are cumbersome and may not be scalable. To achieve ultra-sensitive SERS detection, other techniques including analyte modification along with hotspot engineering is important [18]. In our quest to detect low levels of viral RNA (Target probe), we hypothesized that a stronger signal could be obtained when multiple Raman markers are attached to a detector strand (Capture probe) as opposed to a single Raman marker as shown in Figure 5.1. Before this can be reduced to practice, the level of enhancement that can be obtained by attaching multiple Raman markers to an analyte has to be determined. To prove this, we chose to

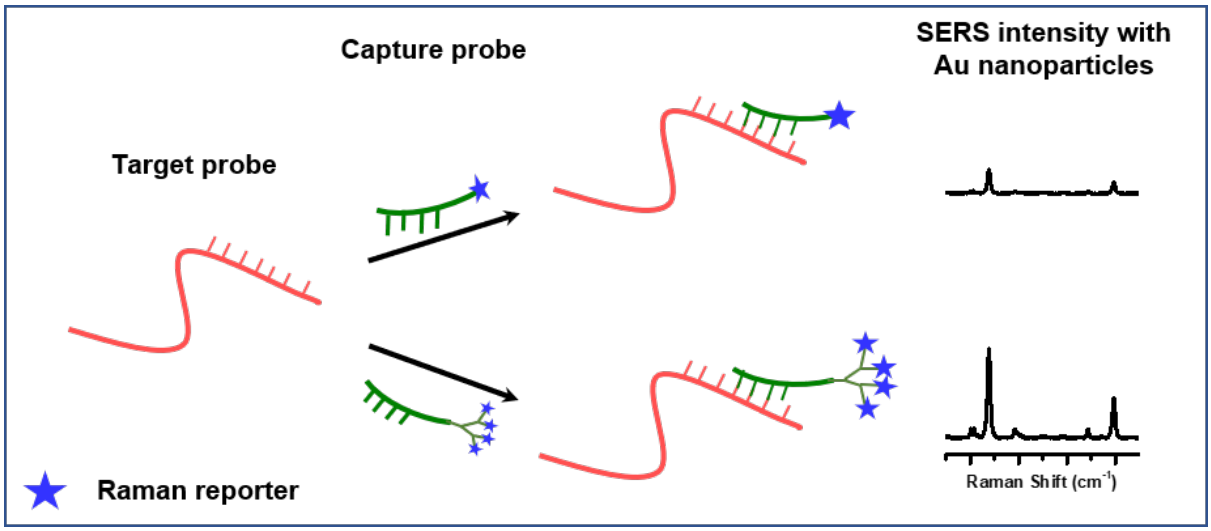

Figure 5.1: Proposed hypothesis for the SERS based oligonucleotide assay

determine the detection limit of Raman markers attached to the periphery of a dendron.

Dendrons are macromolecules that are highly branched and monodisperse in nature. A large number of functional groups can be introduced in the periphery of the dendrons with precise structural control [19, 20, 21]. We chose the 2,2-bis(methylol)-propionic acid (Bis-MPA) dendron as a scaffold for connecting the oligo and the Raman marker. The oligo can be potentially linked to the focal point of the dendron, while signal enhancement can be achieved by attaching multiple copies of the Raman marker in the periphery. As a proof of principle, we have synthesized a Bis-MPA dendron with a benzyl group in the focal point and thiophenol as the Raman reporter on the periphery. This would clarify the potential for signal enhancement that is possible with multiple Raman markers. Other Raman markers will be explored in future. The analyte with the tetra-thiophenol substitution was detectable consistently up to a 10^{-7} M concentration, which was a 100-fold enhancement of detection concentration when compared to a mono thiophenol. In addition, these results were obtained using simple colloidal AuNPs as SERS substrate. The nanoparticles were prepared using the kinetic seeded-growth method [22].

5.2 Experimental Section

General Information All glassware was dried in an oven overnight at 120 °C prior to using. Standard Schlenk techniques were used for carrying out reactions under argon

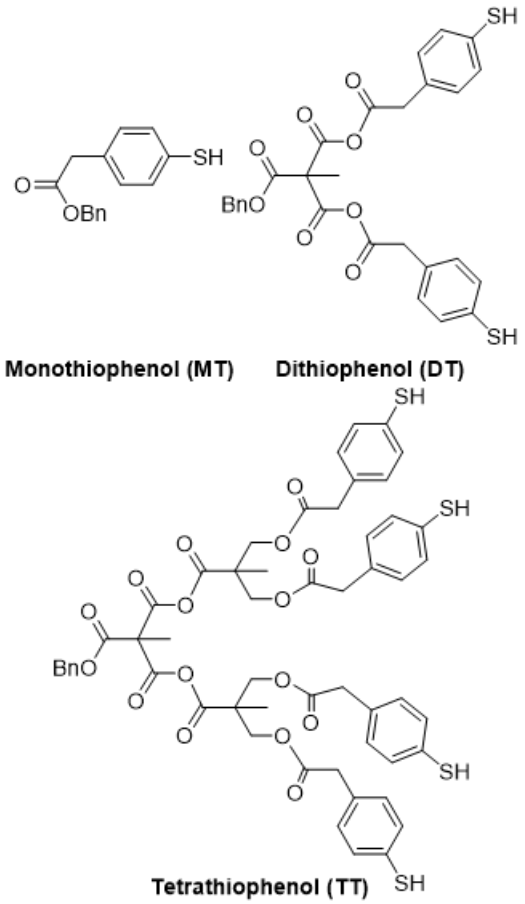

Figure 5.2: Structures of the dendronic Raman markers

atmosphere and thin layer chromatography (Merck TLC silica gel 60 F254) was used for monitoring. Silica gel of mesh size 230–400 was used for performing flash column chromatography. ^{1}H and ^{13}C NMRs was recorded on a Fourier transform NMR spectrometer (400 MHz for ^{1}HNMR and 125 MHz for ^{13}CNMR). Residual solvent peak: $CDCl_3$ (^{1}H NMR: 7.27 ppm, ^{13}H ^{1}H NMR: 77.16 ppm) were used as a reference for reporting chemical shifts in parts per million (ppm). IR was recorded using Frontier MIR/FTIR Spectrometer. Mass spectrometry was carried out using the Q-TOF instrument for HRMS and Autoflex speed instrument for MALDI. All Raman and SERS measurements were done on LabRam HR Evolution using a He-Ne laser of 633 nm excitation wavelength and 50 X objective lens. Absorption spectra of AuNPs colloidal solution were recorded using a quartz cell in a lambda 900 spectrometer. TEM measurements were performed on a carbon-coated copper grid using a JEOL 3010 with an operating voltage of 300 keV.

5.2.1 Synthesis of Bis-MPA thiophenol derivatives

Synthesis of Bis-MPA dendrons was carried out as reported in the literature [23, 24] Thiophenol (TP) was chosen as the Raman-active counterpart in the dendronic structure owing to the high affinity of thiol molecules towards Au [25]. Even though it is a relatively poor scatterer when compared with dyes like rhodamine 6G, we chose it for the ease-of-synthesis. The structures of the TP derivatives are shown in Figure 5.2. Coupling of 4-S-trityl mercapto phenylacetic acid with benzyl alcohol using DCC (N,N'-dicyclohexylcarbodiimide) yielded the trityl protected mono-thiophenol derivative. Similarly, coupling with the Bis-MPA derived diol and the G1 dendron gave the protected di- and tetra- thiophenol derivatives, respectively. The three derivatives were de-protected using trifluoroacetic acid (TFA) and triisopropylsilane (TIPS) to yield the corresponding thiophenol derivatives. Details of synthesis and characterisation of the Bis-MPA dendronic Raman markers are as follows:

1. Compounds reported in literature

Synthesis of Bis-MPA dendrons was carried out as reported in the literature [23, 24, 26] shown below.

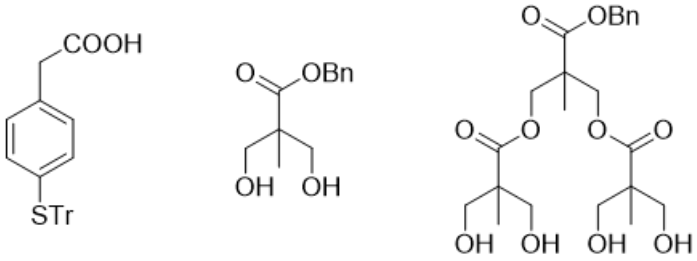

2. Synthesis of trityl MT derivative (5)

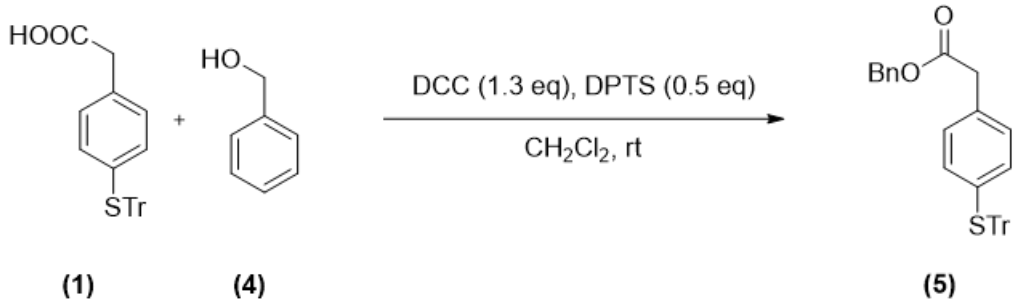

Procedure In a 10 mL two-necked round bottom flask, compound 1 (100 mg, 0.22 mmol) and 4-(Dimethylamino)pyridinium 4-toluenesulfonate (DPTS) (30 mg, 0.12 mmol) were taken and the flask was purged with argon. Benzyl alcohol (100 μL, 0.9 mmol) was added to this flask followed by dichloromethane (DCM) (1.5 mL). A solution of N, N'-dicyclohexyl carbodiimide (DCC) (65 mg, 0.317 mmol) in DCM (1 mL) was added dropwise at room temperature. Immediate precipitation of white residue occurred upon DCC addition. The reaction mixture was monitored for completion by TLC. After 2 hours, the reaction mixture was concentrated and further purified using flash column chromatography.

Column Chromatography About 60 mL of silica was taken and packed into a column using hexanes. The crude compound obtained from the reaction was adsorbed over 2 mL of silica and loaded onto the column. The column was initially eluted with hexanes and 12 fractions of 25 mL each were collected. The compound started eluting in 5 % EtOAc/hexanes (25 mL fractions). Fractions 16 through 19 were collected, concentrated and dried under high vacuum to obtain 100 mg of product (yield = 82 %).

Characterisation White solid; R_f: 0.33 in 10 % EtOAc/hexanes. ^{1}H NMR (400 MHz, $CDCl_3$) δ 7.41-7.16 (m, 20H), 6.94-6.89 (m, 4H), 5.10 (s, 2H), 3.54 (s, 2H). ^{13}C NMR^{1}H (125 MHz, $CDCl_3$): 40.9, 66.6, 70.8, 126.7, 127.7, 128.1, 128.25, 128.55, 129.0, 130.0, 133.3, 133.6, 134.8, 135.8, 144.5, 171.0. IR: 3056, 3035, 2924, 1732, 1445, 1329, 1151, 958, 737, 697 cm^{-1}. HRMS (ESI) m/z (M-Na)$^+$ Calculated for $C_{34}H_{28}O_2S$ 500.1810, Found 500.1683.

3. Synthesis of MT derivative (MT)

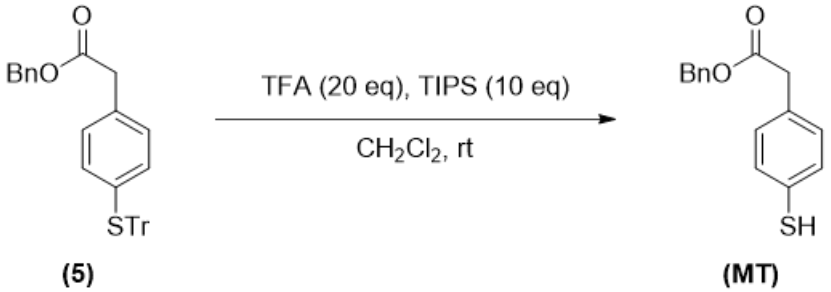

(5) **(MT)**

Procedure In a 5 mL Schlenk tube, compound 5 (111 mg, 0.22 mmol) was added and the tube was evacuated and then filled with argon. This process was repeated twice more. To the Schlenk tube, a mixture of trifluoroacetic acid (TFA) (340 μL, 4.45 mmol) and DCM (1.4 mL) was injected under ice-cold conditions. The reaction mixture became deep yellow during addition. A mixture of triisopropylsilane (TIPS) (228 μL, 1.12 mmol) and DCM (1 mL) was added dropwise to the reaction. The reaction mixture turned pale slowly. The reaction was brought to room temperature and monitored via TLC. After completion (3 hours), the reaction was quenched using a few drops of water. The volatile components were removed by distillation under reduced pressure. The crude material was purified using flash column chromatography.

Column Chromatography About 60 mL of silica was packed into a column using 2 % EtOAc/hexanes. The crude compound obtained from the reaction was adsorbed on 2 mL of silica and loaded onto the column. The compound was eluted with 3 % EtOAc/hexanes and 15 mL fractions were collected (20 fractions), concentrated and dried under high vacuum to obtain 40 mg of product (yield = 78 %).

Characterisation Yellowish-white solid; R_f: 0.23 in 10 % EtOAc/hexanes. ^{1}H NMR (400 MHz, $CDCl_3$) δ 7.36-7.33 (m, 5H), 7.25-7.15 (dd, J = 7.5Hz, 7.7Hz, 8H), 5.13 (s, 2H), 3.62 (s, 2H), 3.44 (s, 1H). ^{13}C NMR^{1}H (125 MHz, $CDCl_3$): 40.8, 66.7, 128.2, 128.3, 128.6, 129.5, 129.7, 130.0, 131.5, 136.0, 170.0. IR: 3065, 3036, 2957, 2561, 1724, 1600, 1494, 1016, 1002, 738, 701 cm^{-1}. HRMS (ESI) m/z (M-Na)$^+$ Calculated for $C_{15}H_{14}O_2S$ 258.0715 Found: 258.0607.

4. Synthesis of trityl DT derivative (6)

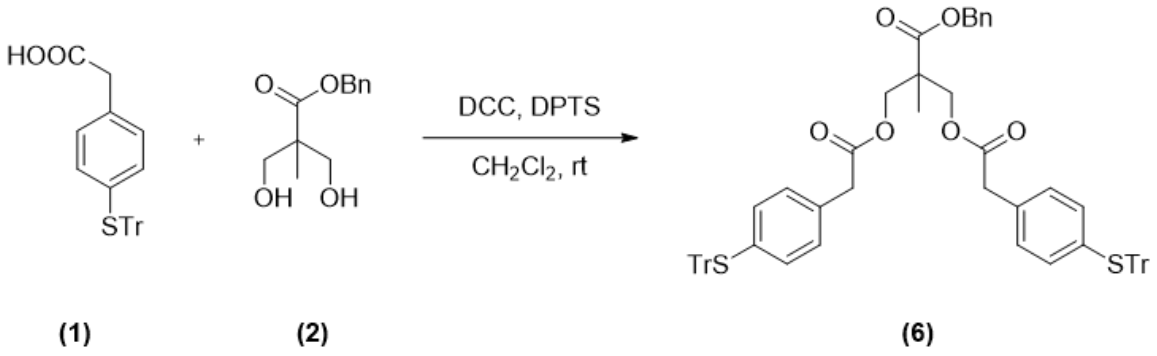

(1) **(2)** **(6)**

Procedure A 10 mL Schlenk tube was charged with compound 2 (65 mg, 0.29 mmol), compound 1 (300 mg, 0.73 mmol) and DPTS (73 mg, 0.29 mmol). The Schlenk tube was purged with argon. The compounds were dissolved in DCM (2 mL). A solution of DCC (72 mg, 0.35 mmol) in DCM (2 mL) was added dropwise at room temperature. Immediate precipitation of white residue occurred upon DCC addition. The reaction mixture was stirred till completion and monitored using TLC. After 3 hours, the reaction was removed from stirring, concentrated and further purified using flash column chromatography.

Column Chromatography Approximately 70 mL of silica was taken in a column and packed with 10 % EtOAc/hexanes. The crude product was dissolved in a minimum amount of DCM and adsorbed on 3 mL of silica. The silica was dried under vacuum and loaded on the column. The column was then eluted with 10 % EtOAc/hexanes and 25 mL fractions each was collected (10 fractions). The pure material eluted in 12 % EtOAc/hexanes. Fractions 20 through 34 were collected. The fractions were concentrated and dried under high vacuum to obtain 230 mg of product. (yield = 79 %)

Characterisation White flaky solid, R_f: 0.37 in 12 % EtOAc/hexanes. ^{1}H NMR (400 MHz, $CDCl_3$) δ 7.42-7.16 (m, 35H), 6.89-6.81 (m, 8H), 5.00 (s, 2H), 4.17-4.10 (dd, J = 11Hz, 4H), 3.37 (s, 4H), 1.06 (s, 3H). ^{13}C NMR^{1}H (125 MHz, $CDCl_3$): 17.6, 40.8, 46.4, 65.6, 66.8, 70.7, 126.7, 127.9, 128.1, 128.4, 128.6, 129, 130.0, 133.0, 133.5, 134.5, 144.5, 165.5, 170.5. IR: 3084, 3054, 3029, 1738, 1733, 1594, 1444, 1129, 1016, 1002, 806, 739, 697 cm^{-1}. MALDI m/z (M-Na)$^+$ Calculated for $C_{66}H_{56}O_6S_2$ 1008.352 Found: 1031.693.

5. Synthesis of DT derivative (DT)

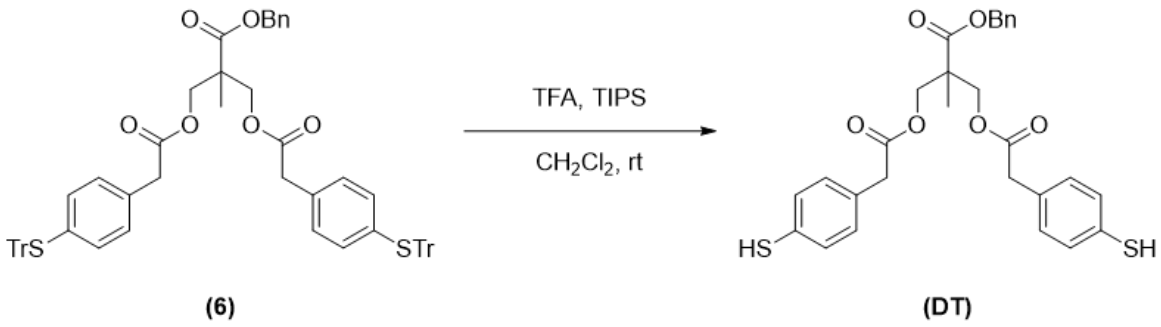

(6) (DT)

Procedure The procedure described in step 3 was used for the deprotection of compound 6. Ten equivalents of TIPS were used in the reaction.

Column Chromatography About 60 mL of silica was taken and packed using 5 % EtOAc/hexanes. The crude compound obtained from the reaction was adsorbed on 2 mL of silica and loaded onto the column. The column was eluted with 5 % EtOAc/hexanes and 15 mL fractions were collected (20 fractions). The pure compound was eluted in 15 % EtOAc/hexanes. Fractions 42 through 52 were collected, concentrated and dried under high vacuum to obtain 35 mg of product (yield = 67 %).

Characterisation Colourless viscous liquid; R_f: 0.1 in 20 % EtOAc/hexanes. ^{1}H NMR (400 MHz, $CDCl_3$) δ 7.42-7.28 (m, 5H), 7.20-7.19 (d, J = 8Hz, 4H), 7.07-7.05 (d, J = 8Hz, 4H), 5.06 (s, 2H), 4.23-4.15 (dd, J = 11Hz, 4H), 3.47 (s, 4H), 3.42 (s, 2H), 1.15 (s, 3H). ^{13}C NMR ^{1}H (125 MHz, $CDCl_3$): 17, 40, 46, 65, 66, 127.7, 128, 128.4, 128.6, 129.6, 130, 131.1, 135.5, 170, 172. IR: 3062, 3028, 2988, 2557, 1725, 1599, 1494, 1154, 1134, 1098, 1008, 803, 733, 695 cm^{-1}. HRMS (ESI) m/z (M-H_2O) Calculated for $C_{28}H_{28}O_6S_2$ 524.1327 Found: 524.1637

6. Synthesis of trityl TT derivative (7)

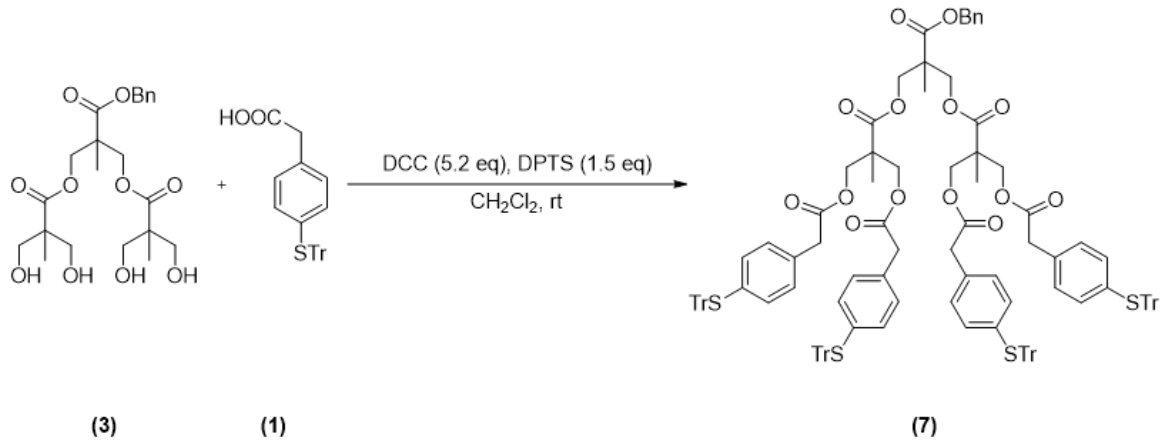

(3) (1) (7)

Procedure A 10 mL Schlenk tube was charged with compound 3 (182 mg, 0.40 mmol), compound 1 (816 mg, 1.99 mmol) and DPTS (150 mg, 0.60 mmol). The Schlenk tube was purged with argon. The compounds were dissolved in DCM (3 mL). A solution of DCC (427 mg, 2.06 mmol) and DCM (3 mL) was added dropwise at room temperature. The reaction mixture was monitored using TLC and stirred till completion. After 48 hours, the reaction mixture was concentrated and further purified using flash column chromatography.

Column Chromatography About 40 mL of silica was taken and packed using 10 % EtOAc/hexanes. The crude compound obtained from the reaction was adsorbed on 1 mL of silica and loaded onto the column. The column was eluted with 10 % EtOAc/hexanes and 15 mL fractions were collected (13 fractions). The pure compound was eluted in 20 % EtOAc/hexanes. Fractions 26 through 32 were collected, concentrated and dried under high vacuum to obtain 500 mg of product (yield = 62 %).

Characterisation White solid; R_f: 0.17 in 30 % EtOAc/hexanes. ^{1}H NMR (400 MHz, $CDCl_3$) δ 7.38-7.36 (d, J = 7.6Hz, 30H) 7.22-7.14 (m, 35H), 6.88-6.81 (dd, J = 8.2Hz, 7.9Hz, 16H), 5.08 (s, 2H), 4.15-3.98 (m, 12H), 3.40 (s, 8H), 1.11 (s, 3H), 0.94 (s, 6H). ^{13}C NMR ^{1}H (125 MHz, $CDCl_3$): 17.6, 24.9, 25.8, 33.9, 40.5, 46.4, 46.6, 65.3, 65.7, 67.1, 70.7, 126.7, 127.7, 127.9, 128.4, 129.0, 130.0, 133.2, 133.5, 134.6, 144.5, 170.5, 171.8, 171.9. IR: 3084, 3030, 2930, 1738, 1626, 1594, 1580, 1444, 1239, 1218, 1125, 1016, 1003, 907, 732, 696 cm^{-1}. MALDI m/z $(M\text{-}Na)^+$ Calculated for

$C_{130}H_{112}O_{14}S_4$ 2025.697 Found: 2025.612.

7. Synthesis of TT derivative (TT)

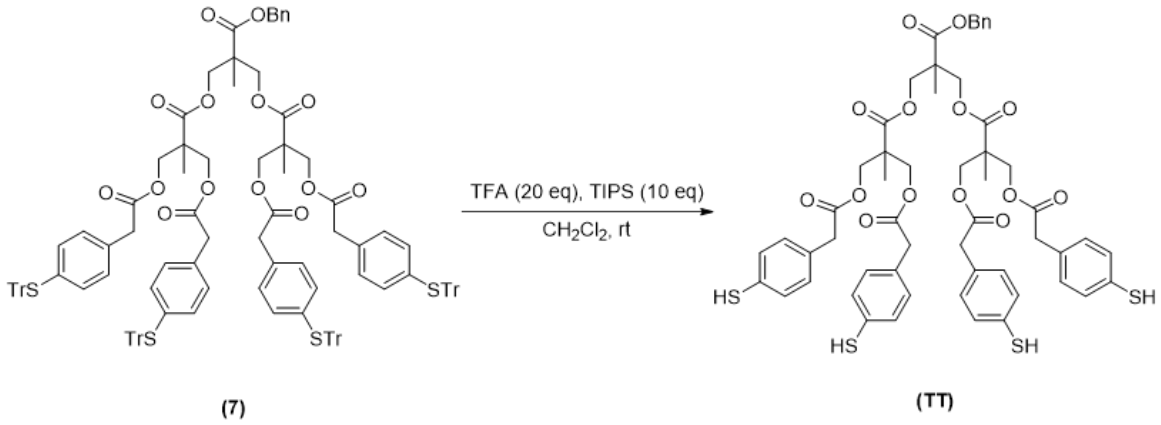

Procedure The procedure described in step 3 was used for the de-protection of compound 7. Ten equivalents of TIPS were used in the reaction.

Column Chromatography About 50 mL of silica was taken and packed using 5 % EtOAc/hexanes. The crude compound obtained from the reaction was adsorbed on 2 mL of silica and loaded onto the column. The column was eluted with 5 % EtOAc/hexanes followed by 30 % EtOAc/hexanes and 40 % EtOAc/hexanes. (15 mL fractions each) Fractions 58 through 70 were collected, concentrated and dried under high vacuum to obtain 35 mg of product (yield = 56 %).

Characterisation Colourless viscous liquid; R_f: 0.1 in 30 % EtOAc/hexanes. ^{1}H NMR (400 MHz, $CDCl_3$) δ 7.32 (s, 5H), 7.21-7.19 (d, J = 7.9Hz, 8H), 7.09-7.07 (d, J = 7.7Hz, 8H), 5.12 (s, 2H), 4.17-4.05 (m, 12H), 3.51 (s, 8H), 3.43 (s, 4H), 1.14 (s, 3H), 1.04 (s, 6H). ^{13}C NMR ^{1}H (125 MHz, $CDCl_3$): 17.4, 17.6, 40.4, 46.4, 46.6, 65.3, 65.7, 67.1, 127.8, 128.4, 128.5, 128.7, 129.7, 130.0, 131.1, 135.4, 170.6, 171.8, 171.9. IR: 3028, 2980, 2566, 1731, 1600, 1494, 1237, 1218, 1126, 1099, 1015, 908, 802, 732, 698 cm^{-1}. HRMS (ESI) m/z $(M\text{-}Na)^+$ Calculated for $C_{54}H_{56}O_{14}S_4$ 1056.2553 Found 1056.2347.

5.2.2 ^{1}H NMR of the dendronic Raman Markers

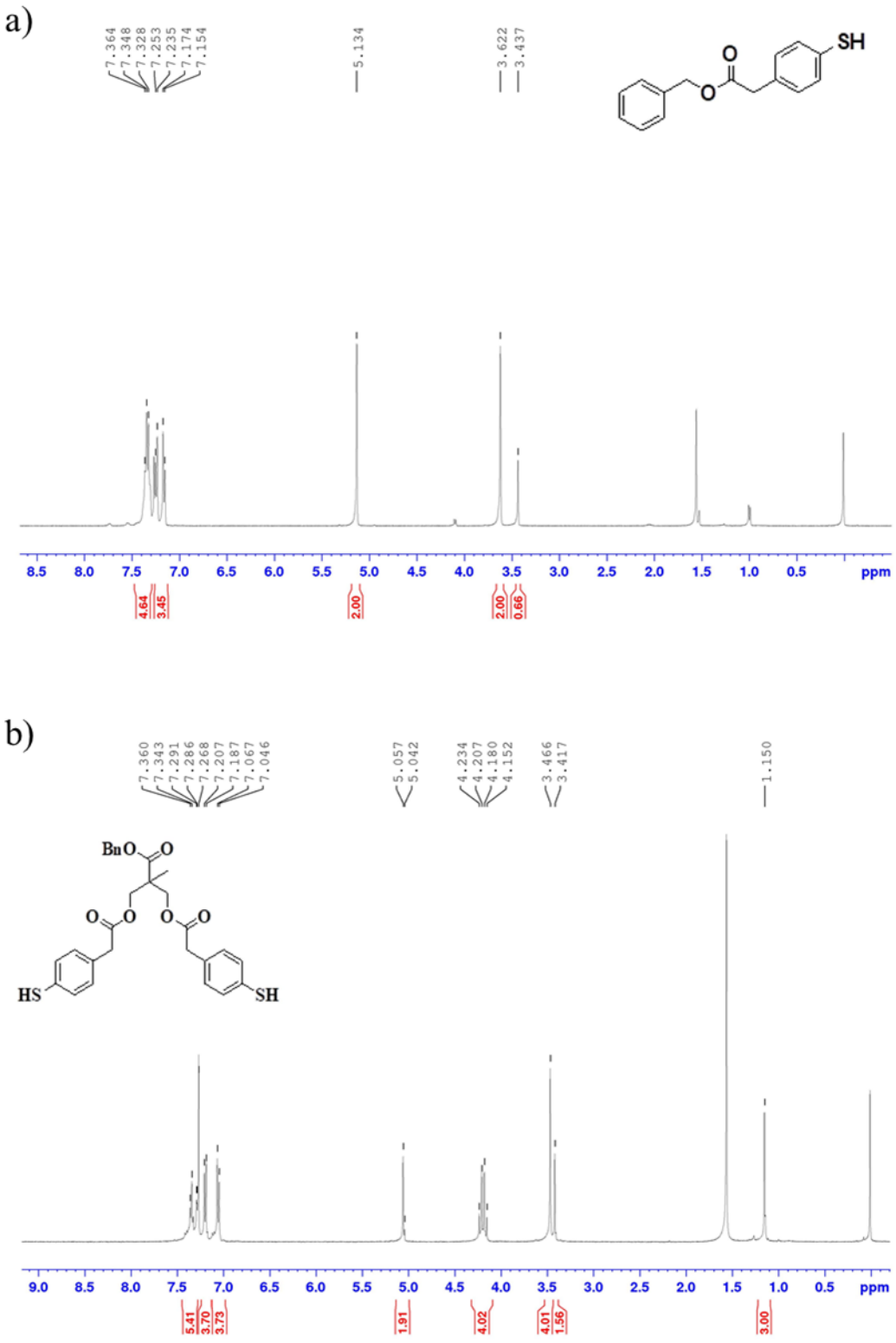

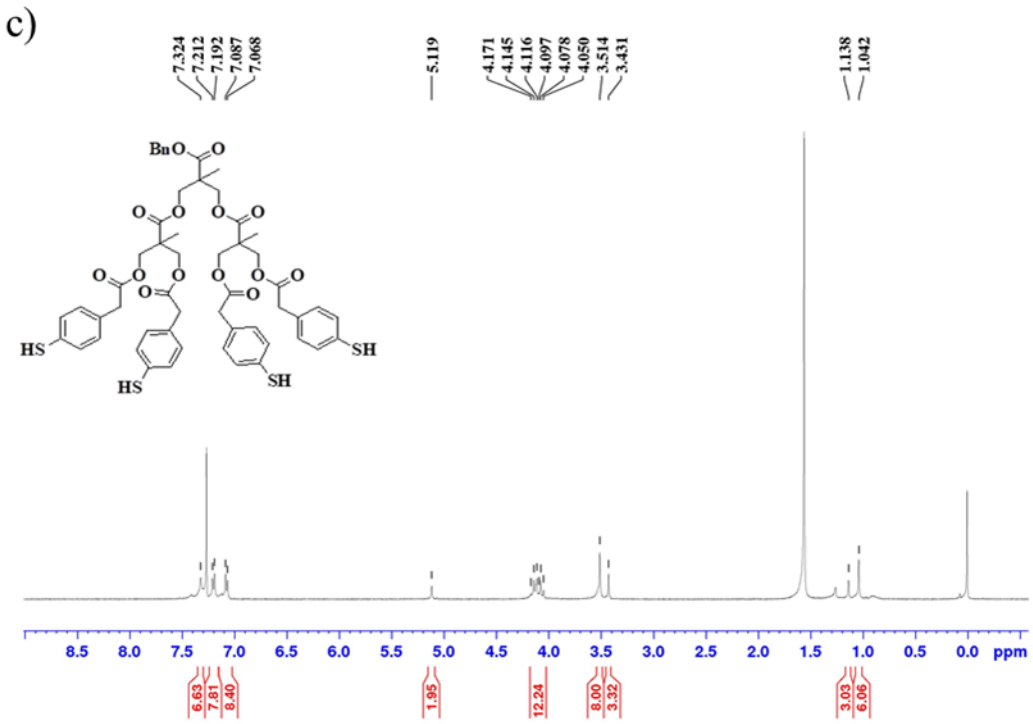

5.2.3 Synthesis of Gold nanoparticles (AuNPs)

The colloidal gold nanoparticles were prepared by using the method given by Bastus et al [22]. Briefly, a 2.2 mM sodium citrate solution (150 mL) was heated in an oil-bath vigorous stirring. 1 mL of $HAuCl_4$ (25 mM) was injected upon boiling. The solution was stirred for about 10 minutes. Light pink Au seeds were immediately prepared, and the solution was cooled to 90 °C for further growth of seeds. 1 mL of $HAuCl_4$ was injected twice. An interval of 30 minutes was maintained post every injection. 55 mL of the solution was pipetted out, followed by the addition of 53 mL water and 2 mL sodium citrate solution (60 mM). This solution served as the seed for the next batch of AuNPs and was repeated till batch 10. AuNPs of size 60-70 nm gave the best SERS enhancement with the analyte molecules and were chosen for the studies. (Figure 5.3)

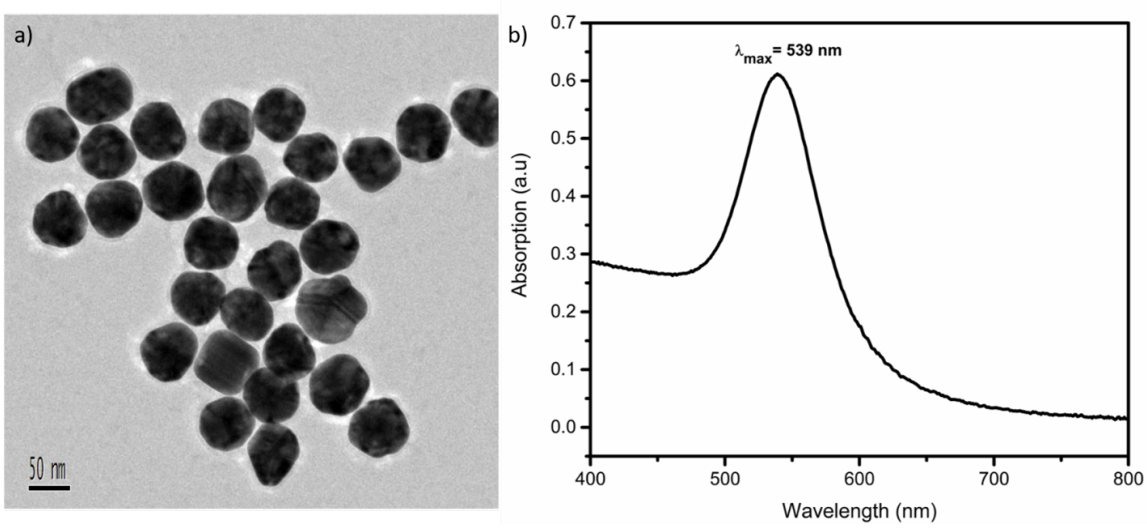

Figure 5.3: a) TEM image obtained for the AuNPs synthesized of average size 60 nm. b) Extinction spectra of the obtained AuNPs.

5.2.4 SERS Studies

In our SERS study, the molecules (MT, DT and TT) are incubated with the Au nanoparticle solution in the ratio of 1:100 by volume for one hour. Post-incubation, these colloidal solutions were centrifuged (8 min at 7500 rpm) to form a pellet (residue from centrifugation) generating hotspots for the nanoparticles irrespective of the analyte molecules. The supernatant was decanted and 10 μL of the residue was dropped on a siliconized glass substrate. The tiny microdroplet (or pellet) is then irradiated with a laser source of about 1-2 μm spot size thus, probing an average number of hotspots. Although these hotspots have a non-uniform distribution, [27] we obtain a similar reproducible average. It is to be noted that, not all hotspots generated are occupied by the analyte molecules considering the ratio of the analyte to the nanoparticle. Such colloidal nanoparticles also lead to random orientations of the analyte molecules on their surface and these hotspots [28]. Thus increasing the number of Raman markers per detector probe increases the chance of each probe getting detected. This idea will be used to explain our results in the next section.

5.3 Results and Discussion

Figure 5.4a shows the SERS spectra of benzyl 4-mercapto phenylacetic acid (**MT**) at various concentrations. The MT system was detectable up to 10^{-5} M concentration as expected and seen in previous reports [21, 29]. The peaks at 1006, 1018, 1080, and 1595 cm^{-1} are characteristic peaks of TP molecule and assigned to in-plane ring deformation, in-plane ring deformation and C-C symmetric stretch, C-C asymmetric stretch and C-S stretch, and C-C symmetric bending modes respectively [30, 31]. For comparing with the other systems chosen for this study, we normalized all spectra with respect to 1078 cm^{-1} peak. All spectra shown in Figure 5.4 are background corrected with respect to the AuNPs and solvents used. It is to be noted that the origin of the peak around 1540 cm^{-1} (marked by * in Figure 5.4a) is unclear and suspected to come from the ethanol and citrate ions interaction with AuNPs. The SERS studies were then extended to di-thiophenol (**DT**) and tetra-thiophenol (**TT**) derivatives, shown in Figure 5.4b and 5.4c respectively. In the case of DT, only a nominal increase in signal enhancement was observed. On the other hand, TT displays a steep enhancement of the detection limit and is detectable up to a concentration of 10^{-7} M concentration. A 10^2-fold increase in detection limit was recorded consistently. It is important to understand these results in order to develop better strategies based on them.

Although a comprehensive theory of SERS has not been developed yet, it is now well accepted that signal enhancement in SERS occurs due to electromagnetic enhancement and chemical enhancement [32, 33]. Further increase in signal intensity can be obtained by the formation of hotspots [34]. In this scenario, it is unlikely that all Raman markers contribute to the SERS signal, which makes hotspots generation quite significant, especially in a low concentration regime. Tailoring the substrate provides more opportunity for such an environment in a tiny region and is advantageous when having static detection of analytes [35, 36]. However, in the case of detection under flow conditions, this will be difficult to achieve without intricate SERS structures in the flow chambers. Here, we need to remember the process used for hotspot generation discussed previously.

The molecules in question will have similar fundamental interaction with the nanoparticles (Au-SH) but will vary in the number of analytes per hotspot. By confining a large

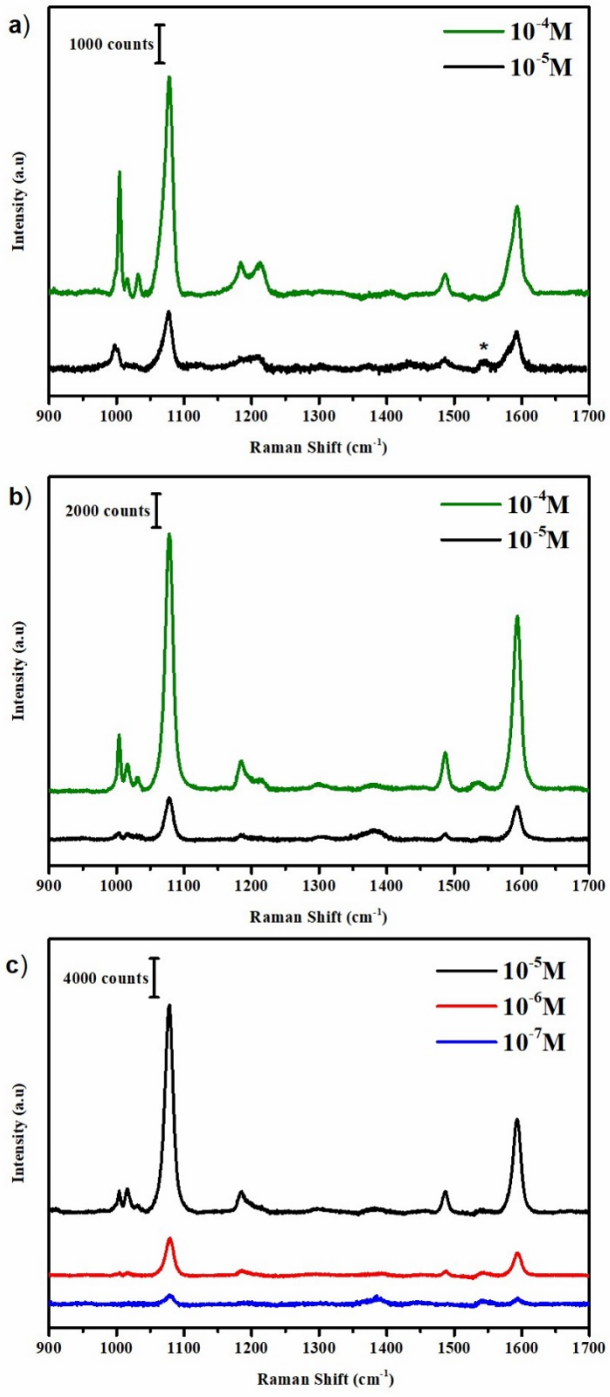

Figure 5.4: a) SERS spectrum of benzyl-4-mercapto phenylacetic acid (MT) solution at different concentrations. b) SERS spectrum of di-thiophenol (DT) derivative solution at different concentrations. c) SERS spectrum of tetra-thiophenol (TT) derivative solution at different concentrations. The laser wavelength used was 633 nm with 3 mW power at the sample and 10 s acquisition time.

number of TP molecules into a dendronic framework, we increase the possibility of hotspot occupancy as seen in the top view of Figure 5.5. Labels 1, 2 and 4 mark the possible number of active sites interacting with the AuNPs for TT derivatives under hotspot conditions. It is to be noted that, all the possibilities will not exist simultaneously under the same hotspot conditions because compared to the neighbouring metallic surface, the surface area of a hotspot is very small [27]. Hence, Figure 5.5 depicts the various random possibilities of the TT derivative occupying hotspot (depending on the TP ring orientation which is discussed subsequently). In the case of MT and DT derivatives, the odds of occupying hotspots are lesser compared to the TT derivative because the chances of unbound TPs for TT derivative are higher compared to the former derivatives. These unbound TPs can bind to other nanoparticles in the hotspots once formed due to pelletisation. This is the reason, we do not observe a large increase in the SERS signal of the DT derivative whereas, it increases drastically for the TT derivative.

A 100-fold enhancement in the detection limit of the analyte molecule supports our argument that not all Raman markers contribute to the SERS signal equally. These results emphasize that the possibility of having Raman markers in the right environment increases non-linearly with an increase in the number of Raman markers confined per analyte giving a large SERS enhancement. While both the number and orientation of the analyte which is proximal to the nanoparticles and its hotspots affect the SERS signal, in the low concentration regime (where only a few analytes are present) constraining the TP molecules into a dendronic system drastically influences this number orienting in the right position.

In order to obtain an understanding of the orientations of the three systems under SERS conditions, we look through the well-known fundamental modes associated with TP. Carron et al. determined the orientation of the benzene ring by looking at the ring vibrations classified as a_1, a_2, b_1 & b_2, assuming a C_{2v} symmetry [37]. The SERS spectra contain mostly peaks of the a1 modes at 1003, 1078, 1184, 1485 and 1593 cm^{-1} whereas; the a_2 and b_1 modes obtained were very weak making them unsuitable for analysis. The a_1 modes include a linear combination of polarizability tensors α_{xx}, α_{yy}, α_{zz}, hence making it difficult to include for analysis to determine orientation. However, the a_1 mode associated with only the phenyl ring breathing could be used for determining the orientation [37].

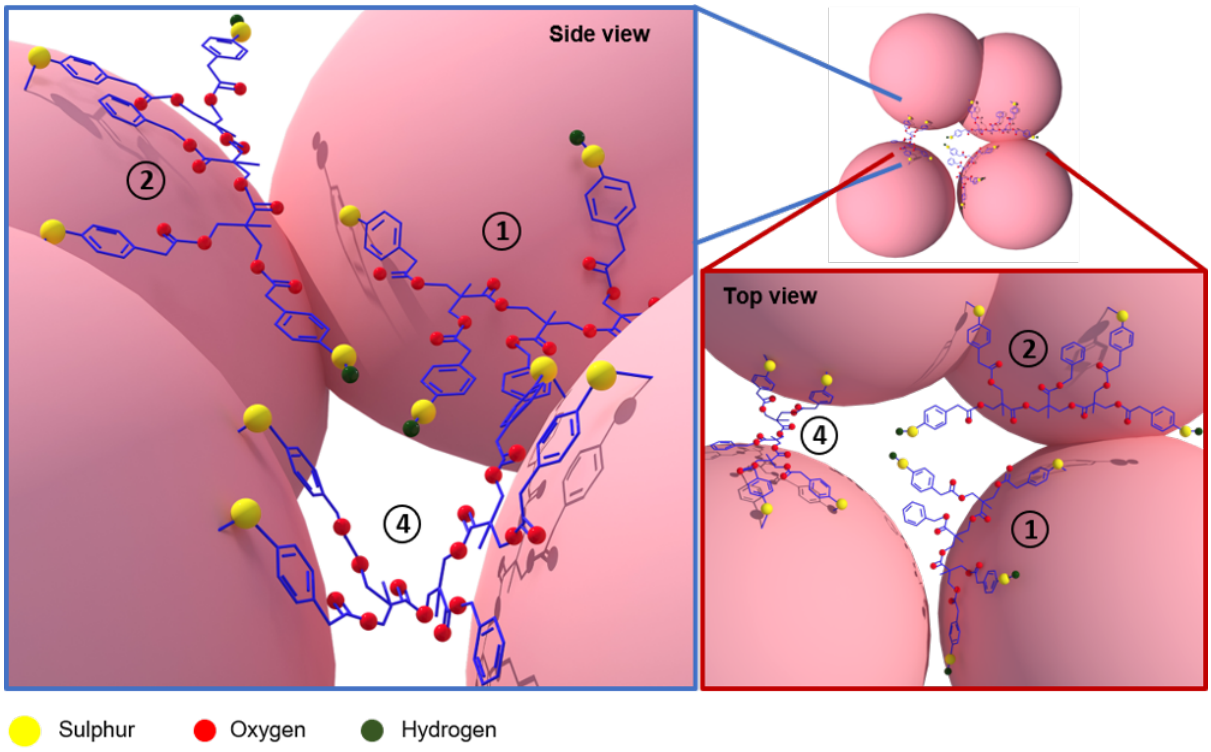

Figure 5.5: Possible orientations and interaction of TT derivative with the nanoparticles. Labels 1, 2 and 4 depict the number of active sites which may bind to the nanoparticle under different hotspot conditions for the TT derivative.

According to the surface selection rule, the in-plane bending modes would be quite strong for a perpendicular orientation with respect to the nanoparticle surface and vice versa [38]. Li et al. concluded that the in-plane modes at 1021(ν_{18a}) and 988 cm^{-1} (ν_{12}) were strongly related to the orientation of the adsorbed 4-mercaptophenyl boronic acid (MPBA) molecule and consider them to be orientation-sensitive marker bands [39].

With this knowledge, we closely look at the 1006 cm^{-1} band (normalized w.r.t 1078 cm^{-1}) corresponding to the ν_{12} mode in the case of MT which downshifts to 1004 cm^{-1} in the case of DT and TT. From Table 5.1, we clearly observe the decrease in the intensity of ν_{12} mode with an increasing number of TP molecules. For TT derivative, the signal intensity of the 1004 cm^{-1} is 0.1 indicating a nearly flat orientation on the surface of the AuNPs. At 10^{-5} M concentration, a near flatter orientation of the TT derivative compounded with multiple Raman markers indicates a lower coverage per unit area of AuNPs as compared to when in a perpendicular orientation. However, we observe a much-enhanced SERS signal at the same point which indicates more number of molecules

sitting in hotspot conditions because of the dendronic geometry as shown in the side view of Figure 5.5. In this concentration regime, an MT system (where the active molecules are all independent, less in number and not constricted) will have a lesser probability of occupying such hotspots as they would tend to spread out resulting in a poor signal being observed. Dendronic geometry not only increases the probability of obtaining a SERS signal thus, pushing the detection limit by 100-fold but also allows the molecules to occupy more hotspots sites due to their constrained framework.

	Concentration	I_{1004}/I_{1078}
MT	10^{-4}	0.5
DT	10^{-4}	0.2
TT	10^{-5}	0.1

Table 5.1: SERS intensities of 1004 $cm^{-1}(\nu_{12})$ mode for synthesized thiophenol derivatives

The scheme envisaged in this letter to demonstrate SERS signal enhancement for trace detection by using multiple Raman markers, can be performed on any SERS substrates or nanoparticles and can be adapted in both static and dynamic systems. Here, the experiment was carried out just by mixing the two solutions, centrifuging and dropping on a glass slide with no prior sample preparation. The obtained spectra are a result of these "non-ideal" molecules and conditions used, thereby making the strategy extremely promising. This can be improved by using much better SERS markers thereby, lowering the detection limit (femto to attomolar concentrations). It also shows that this is a better solution than just tailoring the SERS substrates to provide better hotspot conditions. Since it is a chemical strategy, the analyte can always be modified to better scattering dye molecules like Rhodamine 6G. Such dye molecules would require a more sophisticated purification technique than normal column chromatography; they inherently give better SERS enhancement for a single molecule itself.

5.4 Conclusions

We have developed an analyte strategy for the improved detection of biomarkers. The model system was synthesized using a simple coupling reaction carried between the Bis-

MPA dendrons and TP molecules yielded the thiophenol and tetrathiophenol Raman markers. From the SERS studies, a 10^2-fold enhancement in the detection limit was observed as we go from an MT system to a TT system using simple Au colloidal nanoparticles. It is proposed that, by bringing the analyte molecule into a dendronic framework, we increase the probability of at least one of the four Raman markers to achieve a signal and push the detectable concentration by 100 times. The applicability of the strategy is widened by the ease of investigation on any kind of SERS substrate in future. Alternatively, any type of biomarkers like rhodamine 6G can be linked to the dendrons for further enhancement. A facile synthesis with an oligonucleotide can be carried on these molecules by de-protecting the other end of the dendronic system, thus making them a superior biomarker strategy in the future.

References

[1] T. J. Moore, A. S. Moody, T. D. Payne, G. M. Sarabia, A. R. Daniel, and B. Sharma, "In vitro and in vivo sers biosensing for disease diagnosis," *Biosensors*, vol. 8, no. 2, p. 46, (2018).

[2] Y. C. Cao, R. Jin, and C. A. Mirkin, "Nanoparticles with raman spectroscopic fingerprints for dna and rna detection," *Science*, vol. 297, no. 5586, pp. 1536–1540, (2002).

[3] S. S. Dasary, A. K. Singh, D. Senapati, H. Yu, and P. C. Ray, "Gold nanoparticle based label-free sers probe for ultrasensitive and selective detection of trinitrotoluene," *Journal of the American Chemical Society*, vol. 131, no. 38, pp. 13806–13812, (2009).

[4] M. Kahraman, E. R. Mullen, A. Korkmaz, and S. Wachsmann-Hogiu, "Fundamentals and applications of sers-based bioanalytical sensing," *Nanophotonics*, vol. 6, no. 5, pp. 831–852, (2017).

[5] L.-J. Xu, Z.-C. Lei, J. Li, C. Zong, C. J. Yang, and B. Ren, "Label-free surface-enhanced raman spectroscopy detection of dna with single-base sensitivity," *Journal of the American Chemical Society*, vol. 137, no. 15, pp. 5149–5154, (2015).

[6] E. J. Blackie, E. C. Le Ru, and P. G. Etchegoin, "Single-molecule surface-enhanced raman spectroscopy of nonresonant molecules," *Journal of the American Chemical Society*, vol. 131, no. 40, pp. 14466–14472, (2009).

[7] M. Fleischmann, P. J. Hendra, and A. J. McQuillan, "Raman spectra of pyridine adsorbed at a silver electrode," *Chemical physics letters*, vol. 26, no. 2, pp. 163–166, (1974).

[8] K. Kneipp, H. Kneipp, and J. Kneipp, "Surface-enhanced raman scattering in local optical fields of silver and gold nanoaggregates from single-molecule raman spectroscopy to ultrasensitive probing in live cells," *Accounts of chemical research*, vol. 39, no. 7, pp. 443–450, (2006).

[9] S. Nie and S. R. Emory, "Probing single molecules and single nanoparticles by surface-enhanced raman scattering," *science*, vol. 275, no. 5303, pp. 1102–1106, (1997).

[10] G. Kumar and C. Narayana, "Adapting a fluorescence microscope to perform surface enhanced raman spectroscopy.," *Current Science (00113891)*, vol. 93, no. 6, (2007).

[11] K. Faulds, R. Jarvis, W. E. Smith, D. Graham, and R. Goodacre, "Multiplexed detection of six labelled oligonucleotides using surface enhanced resonance raman scattering (serrs)," *Analyst*, vol. 133, no. 11, pp. 1505–1512, (2008).

[12] J.-M. Li, C. Wei, W.-F. Ma, Q. An, J. Guo, J. Hu, and C.-C. Wang, "Multiplexed sers detection of dna targets in a sandwich-hybridization assay using sers-encoded core–shell nanospheres," *Journal of Materials Chemistry*, vol. 22, no. 24, pp. 12100–12106, (2012).

[13] L. Sun, C. Yu, and J. Irudayaraj, "Surface-enhanced raman scattering based nonfluorescent probe for multiplex dna detection," *Analytical Chemistry*, vol. 79, no. 11, pp. 3981–3988, (2007).

[14] U. Ranga, C. Narayana, and J. Narayana, "High sensitivity assay for molecular typing of biological sample, probes and a kit thereof," July 24 (2012). US Patent 8,227,590.

[15] M. P. Cecchini, V. A. Turek, J. Paget, A. A. Kornyshev, and J. B. Edel, "Self-assembled nanoparticle arrays for multiphase trace analyte detection," *Nature materials*, vol. 12, no. 2, pp. 165–171, (2013).

[16] P. A. Mosier-Boss, "Review of sers substrates for chemical sensing," *Nanomaterials*, vol. 7, no. 6, p. 142, (2017).

[17] S. Shanmukh, L. Jones, J. Driskell, Y. Zhao, R. Dluhy, and R. A. Tripp, "Rapid and sensitive detection of respiratory virus molecular signatures using a silver nanorod array sers substrate," *Nano letters*, vol. 6, no. 11, pp. 2630–2636, (2006).

[18] H. K. Lee, Y. H. Lee, C. S. L. Koh, G. C. Phan-Quang, X. Han, C. L. Lay, H. Y. F. Sim, Y.-C. Kao, Q. An, and X. Y. Ling, "Designing surface-enhanced raman scattering (sers) platforms beyond hotspot engineering: emerging opportunities in analyte manipulations and hybrid materials," *Chemical Society Reviews*, vol. 48, no. 3, pp. 731–756, (2019).

[19] P. Antoni, D. Nyström, C. J. Hawker, A. Hult, and M. Malkoch, "A chemoselective approach for the accelerated synthesis of well-defined dendritic architectures," *Chemical communications*, no. 22, pp. 2249–2251, (2007).

[20] A. Carlmark, C. Hawker, A. Hult, and M. Malkoch, "New methodologies in the construction of dendritic materials," *Chemical Society Reviews*, vol. 38, no. 2, pp. 352–362, (2009).

[21] M. V. Walter and M. Malkoch, "Simplifying the synthesis of dendrimers: accelerated approaches," *Chemical Society Reviews*, vol. 41, no. 13, pp. 4593–4609, (2012).

[22] N. G. Bastús, J. Comenge, and V. Puntes, "Kinetically controlled seeded growth synthesis of citrate-stabilized gold nanoparticles of up to 200 nm: size focusing versus ostwald ripening," *Langmuir*, vol. 27, no. 17, pp. 11098–11105, (2011).

[23] T. Jiang, R. Liu, X. Huang, H. Feng, W. Teo, and B. Xing, "Colorimetric screening of bacterial enzyme activity and inhibition based on the aggregation of gold nanoparticles," *Chemical communications*, no. 15, pp. 1972–1974, (2009).

[24] S. Castelar, J. Barbera, M. Marcos, P. Romero, J.-L. Serrano, A. Golemme, and R. Termine, "Supramolecular dendrimers based on the self-assembly of carbazole-derived dendrons and triazine rings: liquid crystal, photophysical and electrochemical properties," *Journal of Materials Chemistry C*, vol. 1, no. 44, pp. 7321–7332, (2013).

[25] F. Sun, D. D. Galvan, P. Jain, and Q. Yu, "Multi-functional, thiophenol-based surface chemistry for surface-enhanced raman spectroscopy," *Chemical Communications*, vol. 53, no. 33, pp. 4550–4561, (2017).

[26] N. Feliu, M. V. Walter, M. I. Montañez, A. Kunzmann, A. Hult, A. Nyström, M. Malkoch, and B. Fadeel, "Stability and biocompatibility of a library of polyester

dendrimers in comparison to polyamidoamine dendrimers," *Biomaterials*, vol. 33, no. 7, pp. 1970–1981, (2012).

[27] E. C. Le Ru, E. Blackie, M. Meyer, and P. G. Etchegoin, "Surface enhanced raman scattering enhancement factors: a comprehensive study," *The Journal of Physical Chemistry C*, vol. 111, no. 37, pp. 13794–13803, (2007).

[28] W. Xu, X. Ling, J. Xiao, M. S. Dresselhaus, J. Kong, H. Xu, Z. Liu, and J. Zhang, "Surface enhanced raman spectroscopy on a flat graphene surface," *Proceedings of the National Academy of Sciences*, vol. 109, no. 24, pp. 9281–9286, (2012).

[29] G. Kumari and C. Narayana, "New nano architecture for sers applications," *The Journal of Physical Chemistry Letters*, vol. 3, no. 9, pp. 1130–1135, (2012).

[30] S. Li, D. Wu, X. Xu, and R. Gu, "Theoretical and experimental studies on the adsorption behavior of thiophenol on gold nanoparticles," *Journal of Raman Spectroscopy*, vol. 38, no. 11, pp. 1436–1443, (2007).

[31] M. Osawa, N. Matsuda, K. Yoshii, and I. Uchida, "Charge transfer resonance raman process in surface-enhanced raman scattering from p-aminothiophenol adsorbed on silver: Herzberg-teller contribution," *The Journal of Physical Chemistry*, vol. 98, no. 48, pp. 12702–12707, (1994).

[32] E. Le Ru and P. Etchegoin, *Principles of Surface-Enhanced Raman Spectroscopy: and related plasmonic effects*. Elsevier, (2008).

[33] B. N. J. Persson, K. Zhao, and Z. Zhang, "Chemical contribution to surface-enhanced raman scattering," *Physical review letters*, vol. 96, no. 20, p. 207401, (2006).

[34] X. Wang, M. Li, L. Meng, K. Lin, J. Feng, T. Huang, Z. Yang, and B. Ren, "Probing the location of hot spots by surface-enhanced raman spectroscopy: toward uniform substrates," *ACS nano*, vol. 8, no. 1, pp. 528–536, (2014).

[35] Q. Yu, S. Braswell, B. Christin, J. Xu, P. M. Wallace, H. Gong, and D. Kaminsky, "Surface-enhanced raman scattering on gold quasi-3d nanostructure and 2d nanohole arrays," *Nanotechnology*, vol. 21, no. 35, p. 355301, (2010).

[36] Q. Yu, P. Guan, D. Qin, G. Golden, and P. M. Wallace, "Inverted size-dependence of surface-enhanced raman scattering on gold nanohole and nanodisk arrays," *Nano letters*, vol. 8, no. 7, pp. 1923–1928, (2008).

[37] K. T. Carron and L. G. Hurley, "Axial and azimuthal angle determination with surface-enhanced raman spectroscopy: thiophenol on copper, silver, and gold metal surfaces," *The Journal of Physical Chemistry*, vol. 95, no. 24, pp. 9979–9984, (1991).

[38] M. Moskovits, "Surface selection rules," *The Journal of Chemical Physics*, vol. 77, no. 9, pp. 4408–4416, (1982).

[39] S. Li, Q. Zhou, W. Chu, W. Zhao, and J. Zheng, "Surface-enhanced raman scattering behaviour of 4-mercaptophenyl boronic acid on assembled silver nanoparticles," *Physical Chemistry Chemical Physics*, vol. 17, no. 27, pp. 17638–17645, (2015).

Chapter 6

Summary and outlook

In this thesis, Raman spectroscopy has been used as the primary tool to explore various aspects such as structure, electronic properties, and the surface phenomenon of popular class of materials, which usually requires more than one tool to be used for the same. The relevance and critical analysis of subtle but important changes in the Raman spectra have been employed to explain structural transformations and different types of interactions in the material making it a very versatile technique.

Usually, materials are designed or sometimes derived from naturally existing ones to exhibit interesting properties for applications to solve many issues of mankind such as the need for more sustainable energy sources, technological advancement, diagnostics etc. Great progress is being made every day in all directions, however, it is necessary to build a good foundation for structure-property relationships to design better materials and molecules. In this aspect, many techniques are used with X-ray diffraction as a gold standard for structure determination, however, it lacks in explaining the phenomenon related to lighter atoms such as hydrogen and minute changes locally, or electronic transitions that can substantially alter the properties. Here, Raman spectroscopy being a local probe can amplify such alterations from intrinsic as well as extrinsic perturbations.

The first part of the thesis deals with perovskite nanocrystals, which are an interesting class of materials that exhibit exceptional properties such as high photoluminescence quantum yields, wide-tunability, defect tolerance along solution processability making them promising candidates for optoelectronic applications. In this thesis, local struc-

tural homogeneities and inhomogeneities have been highlighted explaining solid solution formation, nature of octahedra, and polaron formation in doped and undoped $CsPbX_3$ mixed halide NCs. The most interesting discovery was this new induced Raman peak indirectly evidencing polaron formation in this group of materials using the traditional Raman spectroscopy. From the studies, the B-site in a perovskite (ABX_3) was highlighted to be where the polaron formation occurs. Hence, it would be interesting to look, at how the behaviour of this polaronic mode changes, when the B-site is doped by a different cation such as Fe, Sn, or when changed altogether.

The second part of the thesis deals with zeolitic imidazolate frameworks (ZIFs), which are porous materials exhibiting fascinating structures and being widely studied for their applications in gas storage and separation, catalysis, and others. Using Raman spectroscopy, a very concrete understanding was developed of the role of the linker as well as metal ion between varying ZIF systems explaining their unusual gas uptakes and few properties. The structural transformation in these materials was associated deeply with the non-bonding interactions exhibited by them to keep their pore intact be it in the open or closed phase. After careful experiments on one of the materials, the adsorption sites were proposed experimentally (ZIF-4) and the understanding made it easier to explain the adsorption mechanism in the other ZIF (ZIF-67). However, one of the most important results belonged to obtaining an N_2 adsorption behaviour over temperature right from ambient conditions, which was critical in defining the adsorption mechanism qualitatively. Nevertheless, a quantitative understanding of the same should be of greater interest. In simple words, the obtained adsorption intensity can be quantified with temperature to obtain physical parameters such as entropy and enthalpy of adsorption. Such a methodology has been developed using IR spectroscopy known as variable temperature infrared spectroscopy, which is an absorption phenomenon. One of the major challenges here would be to quantify the intensity of photons detected concerning the adsorption occurring with the framework as Raman is a scattering process.

And finally, a small part of the thesis deals with designing new Raman markers for SERS applications in the detection of biomolecules. Using simple column chromatography a good model system was developed in pushing the detection limit of the marker by 100-fold increasing the number of Raman markers in a constrained environment. One of the

questions which can be answered is, how many molecules can be constrained in a network before the enhancement saturates? But also, in terms of chemistry, one of the challenges faced was the synthesis of dendronic Raman markers using the molecules of the fluorescent dye such as Rhodamine 6G, fluorescein owing to their purification limitation. These dye molecules are much better scattering molecules as compared to the thiol molecules. Hence, effective click chemistry involving purification through non-chromatography methods will be ideal. This will become a great way to push the detection limit to a much lower concentration as opposed to the thiol markers.

Hence, this thesis is concluded on an affirmative note that Raman spectroscopy has proven to be versatile with great potential in investigating materials possessing novel properties. The more attractive the materials, the more is the learning curve associated with them, thus opening up new avenues in science.

Appendix A

Gaussian calculations

Computational Methods Density Functional Theory (DFT) calculations were performed using Gaussian 09 programs [28]. Initial structure was obtained from the reported ZIF-4 X-ray crystal structure from CCDC No. 1047055 [24] and ZIF-67 X-ray crystal structure from CCDC No. 1429244. Calculations have been carried out on a single Zn center with four imidazolate (Im) linkers in tetrahedral positions for ZIF-4. Similar fragment was chosen for ZIF-67 with single Co centre and four methyl-imidazolate (MIM) linkers. Hydrogens were added to satisfy valency. Optimization was carried using a combined basis set of functional B3LYP: 6-31(g) on all non-metal atoms and LanL2DZ on Zn and Co atoms. To adhere to the reported structure, all four Im (or MIm) were frozen for the optimization calculations and the system was allowed to optimize. Frequency calculation was carried at the same level of theory. Raman bands obtained in the output file were visualized using gaussview 5 and analyzed for peak assignments. Different regions in the entire frequency range were scaled differently depending upon the experimental values. Unscaled frequencies generally have large difference in comparison with the experimental values. Scaling factors for both the systems were different and mentioned with their respective tables. Low frequency modes generally belong to the lattice vibrations or metal-ligand bond of the crystal structure. Our model, on account of being molecular moiety in order to reduce computational cost and time, was unable to capture those modes accurately. Hence, a large mismatch between the calculated and experimental modes were observed which necessitated the application of large scaling factors to calculated frequencies in this region. Additionally, for the case of ZIF-67, the crystal has a

cubic geometry whereas the fragment is molecular. Consequently, the difference between number of molecular modes and low-frequency vibrations observed experimentally and theoretically is significant, although all modes were analysed critically using gaussview. Hence, for the case of ZIF-67, the modes were assigned with a prior experimental knowledge from the present studies and studies carried on ZIF-8. More importantly, only an overall picture of the modes have been discussed and no serious conclusions were drawn on the basis of specific modes listed.

Some abbreviations used in labelling the assignments are as follows: ν = stretching mode; sym = symmetric, asym = asymmetric, δ = bending mode; r = rocking, t = twisting, w = wagging, s = scissoring, oop = out-of-plane, ip = in-plane.

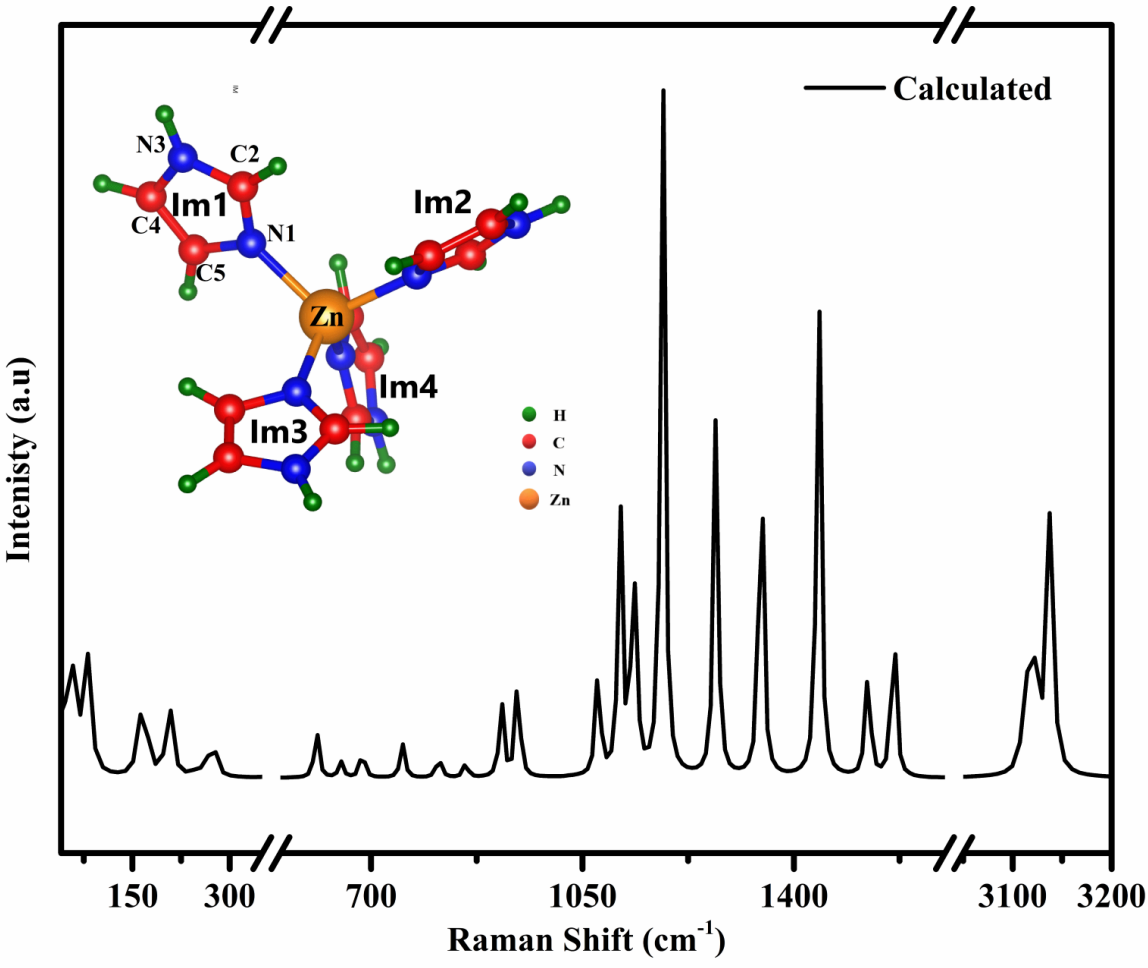

Figure A.1: Raman spectrum for ZIF-4 fragment at 298 K. The optimized structure with the appropriate labels used for assignment of the modes shown as the inset.

Computated frequencies and Raman spectrum of ZIF-4 fragment

The computed Raman spectrum is shown in Figure A.1 along with the optimized structure as the inset. A scaling factor of 1.3 was used for low-frequency vibrations, 1.02 for mid-frequency region from 600-990 cm^{-1}, 0.96 for 1000-1600 cm^{-1} and 0.945 for high-frequency region above 3000 cm^{-1}. Frequencies were obtained from each Im ring moiety for a certain vibration with a tiny shift in the frequency owing to the different environment of each Im moiety. This result was also well observed experimentally, where large multiplicity in the modes were observed for a single vibration. Hence, all the modes were analysed acknowledging the number of Im involved for each frequency as labelled in the inset of Figure A.1 and listed in Table A.1.

Table A.1: Scaled and Unscaled Raman frequencies obtained from ZIF-4 molecular fragment with band assignments and the Im fragment in the molecule involved with the vibration

Calculated Frequency Unscaled (cm^{-1})	**Calculated Frequency Scaled (cm^{-1})**	**Band Assignments**	**Imidazole (Im) involved**
24.6901	32.09713	Im ring twisting w.r.t Zn-N axis	All
28.0452	36.45876		All
30.6684	39.86892		All
33.6429	43.73577		All
35.7393	46.46109		All
37.4687	48.70931		All
40.0628	52.08164		All
43.5919	56.66947		All
56.1952	73.05376		All
111.52	144.976	Ring δ_{oop} ((Im) + Zn-N)	All
118.025	153.4325		All
119.258	155.0354		All

Calculated Frequency Unscaled (cm^{-1})	**Calculated Frequency Scaled (cm^{-1})**	**Band Assignments**	**Imidazole (Im) involved**
142.595	185.3735		All
167.607	217.8891	Im ring rotation around Zn-N axis	All
171.983	223.5779	δ (2 Im)+ δ_{oop} (2 Im) w.r.t Zn-N axis	All
176.448	229.3824		All
182.965	237.8545	ip Im Ring rotation with Zn as pivot	All
189.165	245.9145	ν_{Zn-N} with Im breathing	All
254.477	330.8201	ν_{Zn-N}, Zn atom motion along three axes's	All
255.212	331.7756		All
264.031	343.2403		All
620.686	633.09972	oop Ring puckering (Im), lattice vibration	All four with unequal contribution
621.477	633.90654		
621.774	634.20948		
623.649	636.12198		
662.275	675.5205	oop Ring puckering (Im), lattice vibration	All four with unequal contribution
663.599	676.87098		
664.269	677.55438		
665.892	679.20984		
698.652	712.62504	δ_w (N-H) against C5-N1-C2 centre	Im 3
699.253	713.23806		Im 1
699.75	713.745		Im 4
700.693	714.70686		Im 2
765.284	780.58968	δ_w (C4H, C5H anti to C2)	Two
765.923	781.24146		Two
767.956	783.31512		All
769.746	785.14092		All
823.712	840.18624	δ_w (C2H, in-sync C4H, C5H)	Im 3

Calculated Frequency Unscaled (cm^{-1})	**Calculated Frequency Scaled (cm^{-1})**	**Band Assignments**	**Imidazole (Im) involved**
828.47	845.0394	δ_w (C2H, in-sync C4H, C5H)	Im 1
829.78	846.3756		Im 4
832.791	849.44682		Im 2
872.133	889.57566	δ_t (C4H, C5H)	Two (Im 1, Im 4)
872.825	890.2815		Im 2
875.17	892.6734		Two (Im 1, Im 4)
877.99	895.5498		Im 3
934.123	952.80546	Im ring vibration	Two (Im 1, Im 3)
934.321	953.00742		Three (Im 1, Im 4, Im 3)
934.422	953.11044		Three (Im 3, Im 2, Im 1)
934.72	953.4144		Im 2
962.038	981.27876	Im ring vibration (more like deformation, Zn-N str)	All
963.769	983.04438		Two (Im 2, Im 4)
964.208	983.49216		Im 1
964.317	983.60334		Im 3
1095.38	1051.5648	ip δ C4-H, C5-H, C2-H	Three
1096.06	1052.2176		Three
1096.58	1052.7168		Two
1099.77	1055.7792		All
1133.68	1088.3328	δ_s (C4H, C5H)+ δ (N3H)	Two (Im 1, Im 4)
1134.56	1089.1776		Im 2
1135.31	1089.8976		Im 1 (other three also)
1136.68	1091.2128		Im 3 (other three also)
1155.53	1109.3088		Three

Calculated Frequency Unscaled (cm^{-1})	**Calculated Frequency Scaled (cm^{-1})**	**Band Assignments**	**Imidazole (Im) involved**
1156.7	1110.432	δ (C2H, N3H)+ ν (C5N1)+ ν (C4N3)	Three
1157.44	1111.1424		All
1161.31	1114.8576		All
1205.91	1157.6736	Im ring breathing + δ_r (C2H, C5H, N3H)	Im 4
1206.86	1158.5856		Im 2
1207.23	1158.9408		Im 1
1207.89	1159.5744		Im 3
1295.16	1243.3536	δ_r (C2H, C4H, C5H, N3H) + ν(N3C2N1)	Three
1295.76	1243.9296		Three
1296.6	1244.736		Im 2 (plus one)
1297.85	1245.936		Im 1 (All in motion)
1372.18	1317.2928	δ_w (C4H, C5H) + ν_{asym} (Im)	Two
1373.16	1318.2336		Three
1373.27	1318.3392		Three
1373.73	1318.7808		Two
1470.06	1411.2576	δ (N-H) + ν (C4-C5)	Im 4, Im 2
1470.41	1411.5936		Im 4, Im 2
1470.48	1411.6608		Im 3
1470.88	1412.0448		Im 1
1550.84	1488.8064	ν_{asym} (N1C2N3) + δ_r (C2H, C4H, C5H)	Two
1551	1488.96		Two
1551.59	1489.5264		All
1556.22	1493.9712		All
1595.98	1532.1408	ν (C4-C5) + δ_r (C4H, C5H, N3H, C2H)	Three
1596.29	1532.4384		Im 2
1596.93	1533.0528		Three
1597.91	1533.9936		Two
3292.68	3111.5826	ν_{asym} (C4H, C5H)	Im 2

Calculated Frequency Unscaled (cm^{-1})	**Calculated Frequency Scaled (cm^{-1})**	**Band Assignments**	**Imidazole (Im) involved**
3294.09	3112.91505	ν_{asym} (C4H, C5H)	Im 4
3296.2	3114.909		Im 1
3298.5	3117.0825		Im 3
3300.78	3119.2371	ν (C2H) + ν_{asym} (C4H, C5H)	Im 3
3302.97	3121.30665	ν (C2H)	Im 2
3303.13	3121.45785		Im 1
3303.86	3122.1477		Im 4
3318.69	3136.16205	ν_{asym} (C4H, C5H)	Im 2
3319.05	3136.50225		Im 4
3319.97	3137.37165		Im 1
3320.81	3138.16545		Im 3
3623.49	3424.19805	ν (N3-H)	Im 2
3624.04	3424.7178		Im 4 (other three also)
3624.6	3425.247		Im 1, Im 3
3625.29	3425.89905		All

Computated frequencies and Raman spectrum of ZIF-67 fragment

Similar to ZIF-4, the computed Raman spectrum is shown in Figure A.2 along with the optimized structure as the inset. A scaling factor of 1.3 was used for low-frequency vibrations, 0.99 for mid-frequency region from 600-1700 cm^{-1}, and 0.955 for high-frequency region above 2700 cm^{-1}. In this case too, the contributions of all the MIM were taken into consideration during analysis and listed in Table A.2.

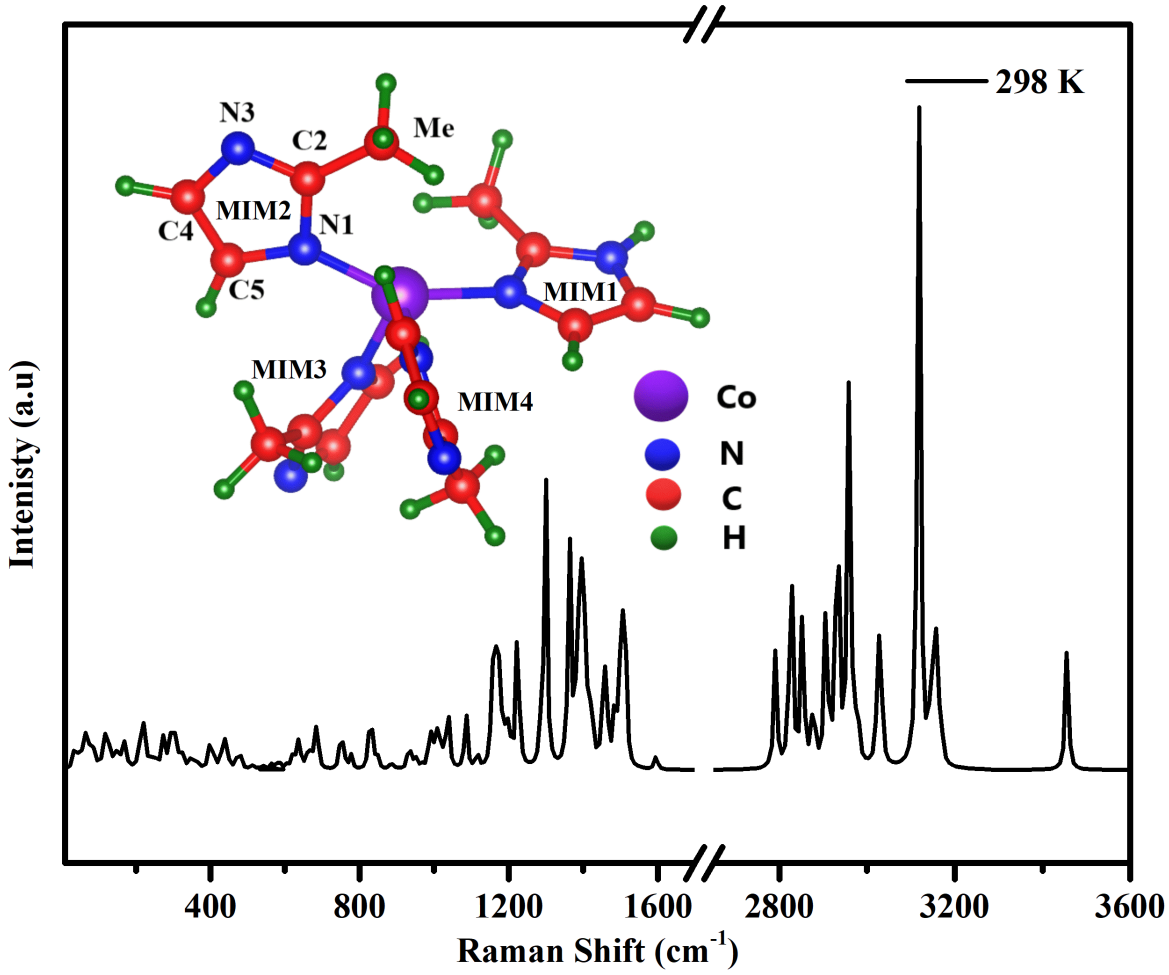

Figure A.2: Raman spectrum for ZIF-67 fragment at 298 K. The optimized structure with the appropriate labels used for assignment of the modes shown as the inset.

Table A.2: Scaled and Unscaled Raman frequencies obtained from ZIF-67 molecular fragment with band assignments and the MIM fragment in the molecule involved with the vibration

Calculated Frequency Unscaled (cm^{-1})	**Calculated Frequency Scaled (cm^{-1})**	**Band Assignments**	**Methylimidazole (MIM) involved**
28	36.4	δ_t (sym)	All
39	50.7	δ_t (asym)	All
50	65	δ_t (asym) pivoting on N1	All
58	75.4	δ_t (asym) pivoting on C2	All
64	83.2	asym lattice vibration pivoting on N1	All
69	89.7		All
89	115.7		All
98	127.4	Lattice vibration (δ_t (asym) + Me libration	All
114	148.2	δ_t (asym) + Me libration	All
120	156	Me libration	All
130	169	Lattice vibration + Me libration (MIM1, 2)	All
137	178.1	δ_{Co-N} + δ_t (asym) MIM	All
162	210.6	δ_{Co-N} + δ_t (sym) MIM + Me libration	All
168	218.4		All
173	224.9	δ_{Co-N} + δ_t (asym) MIM pivoting on C2	All
190	247		All
210	273		All
224	291.2	Me libration	MIM4
233	302.9	δ_{Co-N} + δ_t (sym) MIM pivoting on C2 + Me libration	All
236	306.8	δ_{Co-N} (sym) + δ_t (sym) MIM + Me libration (MIM3,4)	All

Calculated Frequency Unscaled (cm^{-1})	**Calculated Frequency Scaled (cm^{-1})**	**Band Assignments**	**Methylimidazole (MIM) involved**
249	323.7	δ_t Im & Me + δ_{Co-N} (asym) Me libration (N3N1 as axes)	All
268	348.4		All
271	352.3		All
280	364		All but unequal
308	400.4	δ_{Co-N} (Co-motion) + δ_t Im (symm) + Me libration	All
330	429	δ_{Co-N} + δ_w Im & Me (MIM4)	All
339	440.7	δ_{Co-N} (Co-motion) + δ_t Im& Me	All
366	475.8	ν_{Co-N} (Co-motion) + δ_t (MIM)	All
394	512.2	δ_{Co-N} + δ_r Im & Me on C2	All
397	516.1		All
416	540.8	δ_{Co-N}&ν_{Co-N} + δ_r Im & Me on C2	All but different contributions
434	564.2		
575	569.25	Imdz Ring puckering	MIM4
590	584.1		MIM2
613	606.87	Imdz Ring puckering	MIM3
629	622.71		MIM1
643	636.57	Ring puckering alogn N3C2N1	MIM4,3
652	645.48		MIM2
665	658.35	oop ring breathing	MIM2,3,4
671	664.29		MIM2,3,4
676	669.24		MIM1
692	685.08	ip ring breathing	MIM4
692	685.08		MIM4,3,2
755	747.45	Ring deformation + δ_{Co-N}	MIM2,4 in opposite direction
764	756.36		

Calculated Frequency Unscaled (cm^{-1})	**Calculated Frequency Scaled (cm^{-1})**	**Band Assignments**	**Methylimidazole (MIM) involved**
778	770.22	Ring deformation + δ_{Co-N}	MIM1
833	824.67		MIM2,3,4
840	831.6		MIM2,3,4
854	845.46		MIM3,4
892	883.08	δ_w C4H,C5H, C4C5 oop	MIM1
898	889.02		MIM4,2
942	932.58	ip Ring deformation	MIM1
958	948.42	$\delta_w(C - H_{Me})$ + δ_tC-H + Ring deformation	MIM4
964	954.36	ip δ(C4N3C2) + δC4H + δMe	MIM4,3 in opposite direction
977	967.23		
997	987.03	$\delta_w(C - H_{Me} + \delta(N3C2) + \delta(C4H) + \delta(C4N3C2)$	MIM1,3,4 in opp direction
998	988.02		
1005	994.95	C-Me oop+ $\delta_w C - H_{Me}$	MIM1
1014	1003.86		MIM3
1018	1007.82		MIM2
1020	1009.8	δ_r + ν_{Co-N} + δC5N2	MIM2
1026	1015.74		MIM4
1037	1026.63	δ_r(C4H, C5H) + ν(C4C5)	MIM2,1
1040	1029.6	Ring breathing	All
1047	1036.53	δ_s(C-H) + δ_{oop}(C-Me)	MIM 1, 4, 2
1051	1040.49		MIM1,2,3
1096	1085.04	δ_s(C-H) + ip Ring breathing	MIM2
1127	1115.73	δ_t(C-H) + δ(N-H)	MIM1
1168	1156.32	Ring expansion + δ_s(C5-H, C4-H)	MIM1

Calculated Frequency Unscaled (cm^{-1})	**Calculated Frequency Scaled (cm^{-1})**	**Band Assignments**	**Methylimidazole (MIM) involved**
1175	1163.25	Ring expansion + δ_s(C4-H, C5-H)	MIM1
1182 1183	1170.18 1171.17	$\delta_w(C-H)+\delta(C-Me)+\delta(Co-N)+\nu(c2N1)$	MIM1 MIM3
1197	1185.03	$\delta_r(C-H)+\nu(C5N3+c4N1)$	MIM3
1207	1194.93	$\delta_r(AllC-H)+\delta(C-Me)\nu(C2N1)$	MIM3
1216	1203.84	$\delta_r(C4-H,C5-H)+\delta(Co-N)\nu(C4N2)$	MIM2, 4
1221	1208.79	$\delta_s(C4-H,C5-H)+\delta(Co-N)\nu(C4N2)$	MIM2, 4
1237	1224.63	ν(C4N1+C5N3) + δ(CoN1)	MIM4,3,3
1312	1298.88	δ_r(C-H) + Ring breathing (C4N3+C2N1) + δ_{Co-N}	MIM4,3,2
1376 1379 1395 1400 1408	1362.24 1365.21 1381.05 1386 1393.92	δ_t(C-H_{Me}) + δ_s + Ring deformation	MIM4,3,2 MIM1 MIM4,3,2 MIM4,3,4 MIM4,3,3
1414	1399.86	δ_w(C-H_{Me}) + δ_r + Ring deformation	MIM4,3,2
1417	1402.83	δ_t(C-H_{Me}) + δ_s + Ring deformation	MIM4, 3, 4
1420	1405.8	δ_w(C-H_{Me}) + δ_r + Ring deformation	MIM4, 3, 3
1423 1424	1408.77 1409.76	δ_w(C-H_{Me}) + δ_r	MIM4, 3, 2 MIM2

Calculated Frequency Unscaled (cm^{-1})	**Calculated Frequency Scaled (cm^{-1})**	**Band Assignments**	**Methylimidazole (MIM) involved**
1432	1417.68	δ_t(C-H$_{Me}$) + δ_s	MIM2,3,4
1433	1418.67	δ_t(C-H$_{Me}$) + δ(C-H + N-H)	MIM1
1443	1428.57	δ_w(C-H$_{Me}$) + δ(C-H)	MIM5
1465	1450.35		MIM1
1472	1457.28	δ_w(C-H$_{Me}$) + δ(C-H) + ν(C-Me+N1C5+N3C4)	MIM4
1477	1462.23		MIM3
1497	1482.03	δ_w(C-H$_{Me}$) + δ_r(C-H)	MIM2
1508	1492.92	δ_w(C-H+C-Me) + ν(C2N3) + δ_r(C5H+C4H+N3H)	MIM4+MIM3
1511	1495.89		MIM3+MIM4
1518	1502.82		MIM2
1522	1506.78	δ_w(C-H+C-Me) + ν(C4=C5 + C2N3) + δ_r(C5H+N3H)	MIM1 vib in opp direction
1529	1513.71	δ_w(C-H+C-Me) + ν(C4=C5 + C2N1) + δ_r(C4H+N3H)	
2922	2790.51	1H νCH_{Me}	MIM3 & 4 in opposite directions
2960	2826.8		
2988	2853.54	νCH_{Me}	MIM2
3013	2877.415	1H νCH_{Me}	MIM3
3044	2907.02	2Hs νCH_{Me}	MIM1
3070	2931.85	3Hs νCH_{Me}	MIM2
3097	2957.635	2Hs νCH_{Me}	MIM4
3099	2959.545	1H νCH_{Me}	MIM2
3117	2976.735		MIM1
3120	2979.6	2Hs νCH_{Me}	MIM1
3168	3025.44		MIM4
3174	3031.17	1H νCH_{Me}	MIM2
3264	3117.12	ν C4-H	MIM3
3265	3118.075		MIM4

Calculated Frequency Unscaled (cm^{-1})	**Calculated Frequency Scaled (cm^{-1})**	**Band Assignments**	**Methylimidazole (MIM) involved**
3266	3119.03		MIM2
3295	3146.725	asym ν (C4-H, C5-H)	MIM1
3302	3153.41	ν C5-H	MIM4
3304	3155		MIM3
3308	3159.14		MIM2
3318	3168.69		MIM1
3618	3455	ν N3-H	MIM1